In situ and *Operando* Electrocatalysis: Shape-dependent Nanocatalysts for the CO_2 Reduction and the Formic Acid Oxidation

vorgelegt von
M. Sc.
Clara Irene Rettenmaier
ORCID: 0000-0001-5654-4478

an der Fakultät II - Mathematik und Naturwissenschaften
der Technischen Universität Berlin
zur Erlangung des akademischen Grades

Doktorin der Naturwissenschaften
Dr. rer. nat.

genehmigte Dissertation

Promotionsausschuss:

Vorsitzende:	Prof. Dr. Maria-Andrea Mroginski
Gutachterin:	Prof. Dr. Beatriz Roldán Cuenya
Gutachter:	Prof. Dr. Reinhard Schomäcker
Gutachterin:	Prof. Dr. María Escudero Escribano

Tag der wissenschaftlichen Aussprache: 8. Juni 2023

Berlin 2023

Acknowledgement

At this point, I want to thank everybody, who contributed to successfully compile this thesis. A work like this is not done without many people and supporters both, in the professional environment and private environment.

I would like to express my gratitude to Prof. Dr. Beatriz Roldán Cuenya, who accepted me in the group during the midst of the transition from the Ruhr-Universität Bochum to the Fritz-Haber-Institute Berlin. During my stay at the institute, I was granted invaluable access to cutting-edge techniques and instruments, as well as the chance to gain expert knowledge from a team of experts across diverse fields. The regular scientific discussions and guidance provided were of utmost importance to advance the progress in combining surface science with electrocatalysis. I feel fortunate to have had the chance to work with such a dedicated group.

Special thanks go to Prof. Dr. Schomäcker and Prof. Dr. Escudero Escribano for taking the time to read and evaluate my thesis.

I also want to thank my supervisors Dr. Rosa Arán-Ais and Dr. Arno Bergmann for fruitful discussions and guiding my projects. Deep appreciation goes to Dr. Janis Timoshenko, who selflessly brought together the different aspects and techniques of the pulse project towards a successful publication. Furthermore, I want to thank all group leaders for their supportive mentoring and valuable advice, which I found really helpful and which emphasizes the interdisciplinary nature of the Interface Science Department. Credits go to the technicians, who took care of all the little but essential things and tasks to keep the scientific work running.

This time would not have been as pleasant without the many colleagues, the PhDs and postdocs, which were caring, supporting, humorous and who have gone through ups and downs with me to eventually become good friends. I really enjoyed the time that we have spent together and I keep our time in good memories!

Next, I want to appreciate the financial and educational support of the International Max Planck Research School for elementary Processes in Phyical Chemistry (IMPRS EPPC).

Finally, I want to deeply thank my dear family and my friends for continuously supporting me during the doctorate. Thank you!

List of Publications

First Author Publications

1. **Enhanced Formic Acid Oxidation over SnO_2-decorated Pd Nanocubes**
   Clara Rettenmaier, Rosa M. Arán-Ais, Janis Timoshenko, Rubén Rizo, Hyo Sang Jeon, Stefanie Kühl, See Wee Chee, Arno Bergmann, Beatriz Roldan Cuenya
   ACS Catalysis (2020) 10, 14540-14551
   DOI: 10.1021/acscatal.0c03212

2. **Steering the Structure and Selectivity of CO_2 Electroreduction Catalysts by Potential Pulses**
   Janis Timoshenko[1], Arno Bergmann[1], Clara Rettenmaier[1], Antonia Herzog, Rosa M. Arán-Ais, Hyo Sang Jeon, Felix T. Haase, Uta Hejral, Philipp Grosse, Stefanie Kühl, Earl M. Davis, Jing Tian, Olaf Magnussen, Beatriz Roldan Cuenya
   [1]: equal contribution
   Nature Catalysis (2022) 5, 259
   DOI: 10.1038/s41929-022-00760-z

3. ***Operando* Insights into Correlating CO Coverage and Alloying with the Selectivity of Au NP decorated Cu_2O Nanocubes during the Electrocatalytic CO_2 Reduction**
   Clara Rettenmaier, Antonia Herzog, Daniele Casari, Martina Rüscher, Hyo Sang Jeon, David Kordus, Mauricio Lopez Luna, Stefanie Kühl, See Wee Chee, Alexander Duncan, Janis Timoshenko, Arno Bergmann, Beatriz Roldan Cuenya
   to be submitted

4. **The Role of undercoordinated Cu Atoms: The Electrocatalytic CO_2 Reduction Reaction on a stepped Cu(310) Single Crystal Surface**
   Clara Rettenmaier, Fabian Scholten, Beatriz Roldan Cuenya
   in preparation

Co-Author Publications

5. **Transition Metal-based Catalysts for the Electrochemical CO_2 Reduction: from Atoms and Molecules to Nanostructured Materials**
   Federico Franco, Clara Rettenmaier, Hyo Sang Jeon, Beatriz Roldan Cuenya
   Chemical Society Reviews (2020) 49 (19), 6884
   DOI: 10.1039/D0CS00835D

6. **Growth Dynamics and Processes Governing the Stability of Electrodeposited Size-Controlled Cubic Cu Catalysts**
   Philipp Grosse, Aram Yoon, Clara Rettenmaier, See Wee Chee, Beatriz Roldan Cuenya
   The Journal of Physical Chemistry C (2020) 124 (49), 26908
   DOI: 10.1021/acs.jpcc.0c09105

7. **Pt-Sn-Co Nanocubes as Highly Active Catalysts for Ethanol Electro-Oxidation**
   Rubén Rizo, Arno Bergmann, Janis Timoshenko, Fabian Scholten, Clara Rettenmaier, Hyo Sang Jeon, Yen-Ting Chen, Aram Yoon, Alexander Bagger, Jan Rossmeisl, Beatriz Roldan Cuenya
   Journal of Catalysis (2021) 393, 247
   DOI: 10.1016/j.jcat.2020.11.017

8. **Revealing the CO Coverage-Driven C-C Coupling Mechanism for Electrochemical CO_2 Reduction on Cu_2O Nanocubes via Operando Raman Spectroscopy**
   Chao Zhan, Federico Dattila, Clara Rettenmaier, Arno Bergmann, Stefanie Kühl, Rodrigo García-Muelas, Núria López, Beatriz Roldan Cuenya
   ACS Catalysis (2021) 11, 7694
   DOI: 10.1021/acscatal.1c01478

9. **Operando Investigation of Ag-decorated Cu_2O Nanocube Catalysts with Enhanced CO_2 Electroreduction toward Liquid Products**
   Antonia Herzog, Arno Bergmann, Hyo Sang Jeon, Janis Timoshenko, Stefanie Kühl, Clara Rettenmaier, Mauricio Lopez Luna, Felix T. Haase, Beatriz Roldan Cuenya
   Angew. Chem (2021) 60, 13, 7426
   DOI: 10.1002/anie.202017070

10. **Selectivity Control of Cu Nanocrystals in a Gas-Fed Flow Cell through CO_2 Pulsed Electroreduction**
    Hyo Sang Jeon, Janis Timoshenko, Clara Rettenmaier, Antonia Herzog, Aram Yoon, See Wee Chee, Sebastian Oener, Uta Hejral, Felix T. Haase, Beatriz Roldan Cuenya
    JACS (2021) 143, 19, 7578
    DOI: 10.1021/jacs.1c03443

11. **Role of the Oxide Support on the Structural and Chemical Evolution of Fe Catalysts during the Hydrogenation of CO_2**
    Mauricio Lopez Luna, Janis Timoshenko, David Kordus, Clara Rettenmaier, See Wee Chee, Adam S. Hoffman, Simon R. Bare, Shamil Shaikhutdinov, Beatriz Roldan Cuenya
    ACS Catalysis (2021) 11 (10), 6175
    DOI: 10.1021/acscatal.1c01549

12. **Dynamic Transformation of Cubic Copper Catalysts during CO_2 Electroreduction and its Impact on Catalytic Selectivity**
    Philipp Grosse, Aram Yoon, Clara Rettenmaier, Antonia Herzog, See Wee Chee, Beatriz Roldan Cuenya
    Nature Communications (2021) 12, 6736
    DOI: 10.1038/s41467-021-26743-5

13. **Size Effects and Active State Formation of Cobalt Oxide Nanoparticles during the Oxygen Evolution Reaction**
    Felix T. Haase, Arno Bergmann, Travis E. Jones, Janis Timoshenko, Antonia Herzog, Hyo Sang Jeon, Clara Rettenmaier, Beatriz Roldan Cuenya
    Nature Energy (2022) 7, 765
    DOI: 10.1038/s41560-022-01083-w

14. **Influence of the Cobalt Content in Cobalt Iron Oxides on the Electrocatalytic OER Activity**
Sascha Saddeler, Georg Bendt, Soma Salamon, Felix T. Haase, Joachim Landers, Janis Timoshenko, Clara Rettenmaier, Hyo Sang Jeon, Arno Bergmann, Heiko Wende, Beatriz Roldan Cuenya, Stephan Schulz
J. Mater. Chem. A (2021) 9, 25381
DOI: 10.1039/D1TA06568H

15. **Steering Hydrocarbon Selectivity in CO_2 Electroreduction over Soft-Landed CuOx Nanoparticle-Functionalized Gas Diffusion Electrodes**
Nick Daems, Daniel Choukroun, Pablo Merino, Clara Rettenmaier, Lien Pacquets, Arno Bergmann, Gonzalo Santoro, Luis Vázquez, Lidia Martínez, Beatriz Roldan Cuenya, Jose Martín-Gago, Tom Breugelmans
ACS Appl. Mater. Interfaces (2022) 14, 2, 2691
DOI: 10.1021/acsami.1c17998

16. **Covalent Organic Framework (COF) Derived Ni-N-C Catalysts for Electrochemical CO_2 Reduction: Unraveling Fundamental Kinetic and Structural Parameters of the Active Sites**
Changxia Li, Wen Ju, Sudarshan Vijay, Janis Timoshenko, Kaiwen Mou, David A. Cullen, Jin Yang, Xingli Wang, Pradip Pachfule, Sven Brückner, Hyo Sang Jeon, Felix T. Haase, Sze-Chun Tsang, Clara Rettenmaier, Karen Chan, Beatriz Roldan Cuenya, Arne Thomas, Peter Strasser
Angew. Chem. (2022) 134, e202114
DOI: 10.1002/anie.202114707

17. **Shape-Dependent CO_2 Hydrogenation to Methanol over Cu_2O Nanocubes Supported on ZnO**
David Kordus, Jelena Jelic, Mauricio Lopez Luna, Núria J. Divins, Janis Timoshenko, See Wee Chee, Clara Rettenmaier, Jutta Kröhnert, Stefanie Kühl, Annette Trunschke, Robert Schlögl, Felix Studt, Beatriz Roldan Cuenya
J. Am. Chem. Soc. 2023, 145, 5, 3016–3030 DOI: 10.1021/jacs.2c11540

18. **Spatially- and Chemically-Resolved Visualization of Fe Incorporation into NiO Octahedra during the Oxygen Evolution Reaction**
Fengli Yang, Mauricio Lopez Luna, Felix T. Haase, Aram Yoon, Martina Rüscher, Clara Rettenmaier, Hyo Sang Jeon, Janis Timoshenko, Arno Bergmann, See Wee Chee, Beatriz Roldan Cuenya
submitted to Nature Comm. (2023), under revisions

19. **Unveiling Specific Cu Active Sites and Reaction Intermediates for CO_2 Electro Reduction to C_2 Products by Operando Raman Spectroscopy**
Chao Zhan[1], Federico Dattila[1], Clara Rettenmaier, Fabian Scholten, Zhen Yao, Arno Bergmann, Núria López, Beatriz Roldan Cuenya
in preparation

20. **Catalysts Convert CO_2 under Pressure: An in situ X-ray Diffraction Study on Oxide-derived Cu under Potentiodynamic CO_2 Reduction Conditions**
Arno Bergmann, Antonia Herzog, Travis E. Jones, Canrong Qiu, Tian Jing, Reihaneh Amirbeigiarab, Clara Rettenmaier, Rosa M. Arán Ais, Stefanie Kühl, See Wee Chee, Olaf Magnussen, Beatriz Roldan Cuenya
in preparation

21. **Tracking the evolution of single atom catalysts for the CO_2 electrocatalytic reduction using *operando* X-ray absorption spectroscopy and machine learning**
Andrea Martini, Dorottya Hursan, Janis Timoshenko, Jose E. Ortega Aguilar, Felix Haase, Hyosang Jeon, Martina Rüscher, Clara Rettenmaier, Antonia Herzog, Beatriz Roldan Cuenya
in preparation

22. **Steering the CO_2 reduction selectivity of copper-nitrogen-doped carbon catalysts by pulsed potential electrolysis**
Dorottya Hursán, Janis Timoshenko, Hyo Sang Jeon, Eduardo Ortega, Martina Rüscher, Arno Bergmann, Aram Yoon, Uta Hejral, Antonia Herzog, Clara Rettenmaier, Felix T. Haase, Beatriz Roldan Cuenya
in preparation

23. **Reversible evolution of metal-nitrogen-doped carbon catalysts during CO_2 electroreduction: an operando X-ray absorption spectroscopy study**
Dorottya Hursán, Janis Timoshenko, Eduardo Ortega, Hyo Sang Jeon, Martina Rüscher, Antonia Herzog, Clara Rettenmaier, See Wee Chee, Beatriz Roldan Cuenya
in preparation

24. **Non-uniform effects during electrochemical CO_2 reduction on Cu foil treated with oxygen plasma**
Chao Zhan, Yu-Jie Peng, Liviu Tanase, Clara Rettenmaier, Fabian Scholten, Daniel Abou-Ras, Thomas Schmidt, Christopher Kley, Arno Bergmann, Beatriz Roldan Cuenya
in preparation

25. **Time-resolved *operando* Insights into Cu-Zn Nanocubes during the Pulsed CO_2 Electroreduction toward Ethanol**
Antonia Herzog, Hyo Sang Jeon, Martina Rüscher, Janis Timoshenko, Clara Rettenmaier, David Kordus, Uta Hejral, Earl M. Davis, F. T. Haase, Stefanie Kühl, Wiebke Frandsen, Arno Bergmann, Beatriz Roldan Cuenya
in preparation

Abbreviations

AFM	Atomic Force Microscopy
BF	Bright-Field
CE	counter electrode
CO_2RR	CO_2 reduction reaction
CTAB	hexadecyltrimethylammonium bromide
CV	Cyclic Voltammetry
DLC	Double Layer Capacitance
DF	Dark-Field
DFAFC	Direct Formic Acid Fuel Cell
EC	electrochemistry
ECSA	Electrochemical Surface Area
Ep	electropolished
EDX	Energy Dispersive X-ray Spectroscopy
EtOH	ethanol
EXAFS	Extended X-ray Absorption Fine Structure
FA	formic acid
FAOR	Formic Acid Oxidation Reaction
FC	fuel cell
fcc	face centered cubic
FE	Faradaic Efficiency
FID	Flame Ionization Detector
FT	fourier transformed
FT-IRRAS	Fourier-transformed Infrared Reflection Absorption Spectroscopy
FTIR	Fourier-transformed Infrared Spectroscopy
FWHM	full width half maximum
GC	Gas Chromatograph
HAADF	High-Angle Annular Dark Field
HPLC	High Pressure Liquid Chromatrography
HER	Hydrogen Evolution Reaction
HOR	Hydrogen Oxidation Reaction
HE-XRD	High Energy X-ray Diffraction
ICP-MS	Inductively Coupled Plasma - Mass Spectrometry
LCA	linear combination analysis
LEED	Low-Energy Electron Diffraction
NC	nanocubes
NP	nanoparticle
OCP	open circuit potential
OER	Oxygen Evolution Reaction
ORR	Oxygen Reduction Reaction
QXAFS	Quick X-ray Absorption Fine Structure
PEEK	polyetheretherketone
PTFE	hydrophobic polytetrafluoroethylene
RC	resistor-capacitor
RE	reference electrode
RF	roughness factor
RHE	reversible hydrogen electrode
SEM	Scanning Electron Microscopy
SERS	surface enhanced Raman Spectroscopy
SHE	standard hydrogen Electrode
STEM	Scanning Transmission Electron Microscopy
STM	Scanning Tunneling Microscopy
TCD	Thermal Conductivity Detector
TEM	Transmission Electron Microscopy
UHV	Ultra high Vacuum
WE	working electrode
XAFS	X-ray Absorption Fine Structure
XANES	X-ray Absorption Near Edge Structure
XAS	X-ray Absorption Spectroscopy
XAS	X-ray Auger Electron Spectroscopy
XPS	X-ray Photoelectron Spectroscopy
XRD	X-ray Diffraction

Abstract

Environmental friendly technologies for storage and reutilization energy are important for the future of humanity on earth. Scientific efforts cover not only the investigation of new technologies to close the carbon cycle, but also by advancing already existing applications such as batteries and fuel cells. Major challenges for these electrocatalytic reactions are the detailed understanding of their reaction mechanisms and increasing the performance and stability of the catalysts. In this thesis, I reveal new insights on the behavior of promising catalysts during the CO_2 reduction reaction (CO_2RR) and the Formic Acid Oxidation Reaction (FAOR). By systematically studying single crystals as well as shaped nanoparticle and bimetallic catalysts during potentiostatic and pulsed reaction conditions, correlations between the catalyst structure and the reaction performance are identified.

In the electrocatalytic CO_2RR, the role of surface Cu atoms is still not well understood. Thus, one research focus has been set to study surface-selectivity relationships by investigating the surface structure of a stepped Cu(310) single crystal and its influence on the CO_2RR. In particular, it was found that these catalysts provide mostly hydrogen and only small amounts of hydrocarbons or ethanol.

Furthermore, the presence and the role of oxide species during CO_2RR remain an elusive scientific discussion. In order to understand how oxides tune the catalytic selectivity, the use of potential pulses with different time lengths to periodically regenerate the oxide species was established. In particular, under certain pulse-length conditions, a doubled ethanol production was obtained as compared to non-pulsed conditions has been observed. The nature of the Cu species and structures responsible for this selectivity was investigated using *operando* techniques.

The role of nanocubes (NCs) decorated with a co-catalyst was investigated both, for the CO_2RR and the FAOR. Au-Cu_2O NC catalysts displayed higher C_{2+} yields than bare Cu_2O NCs. Furthermore, the type, amount and role of CuAu alloys on the CO_2RR was elucidated. Moreover, for the FAOR, Pd NCs were decorated with a SnO_2 shell, which exceeded the performance of pure Pd by reducing poisoning intermediates. By *in situ* and *operando* techniques, the structural and chemical alterations under these reaction conditions were investigated.

This thesis unveils the role of surface termination, oxides and bimetallic catalyst structures on the activity and selectivity of CO_2RR and FAOR electrocatalysts. The here presented insights contribute to a knowledge-driven design of electrocatalysts, that can be used in the future to steer the reactions towards highly-valuable products and high performances, emphasizing the importance of characterizing these catalysts under operating conditions and establishing useful structure-selectivity relationships.

Zusammenfassung

Umweltfreundliche Technologien zur Speicherung und Wiederverwendung von Energie sind wichtig für die Zukunft der Menschheit auf der Erde. Die wissenschaftlichen Bemühungen erstrecken sich nicht nur auf die Erforschung neuer Technologien um beispielsweise den Kohlenstoffkreislauf zu schließen, sondern auch auf die Weiterentwicklung bereits bestehender Anwendungen wie Batterien und Brennstoffzellen. Die größten Herausforderungen für diese elektrokatalytischen Reaktionen sind das detaillierte Verständnis von Reaktionsmechanismen und die Verbesserung von Leistung und Stabilität der Katalysatoren. In dieser Arbeit präsentiere ich neue Erkenntnisse über das Verhalten vielversprechender Katalysatoren während der CO_2 Reduktionsreaktion (CO_2RR) und der Ameisensäure Oxidationsreaktion (FAOR). Durch systematische Studien über Einkristalle sowie über kubische und bimetallische Katalysatoren unter statischen und gepulsten Reaktionsbedingungen werden Korrelationen zwischen der Katalysatorstruktur und ihrer Reaktionsleistung identifiziert.

In der elektrokatalytischen CO_2RR ist die Rolle von Cu Atomen and der Oberfläche noch nicht gut verstanden. Daher wurde ein Forschungsschwerpunkt auf die Untersuchung der Beziehungen zwischen Oberflächen und Selektivität gelegt, indem die Oberflächenstruktur eines gestuften Cu(310)-Einkristalls und deren Einfluss auf die CO_2RR analysiert wurde. Tatsächlich liefiern diese Katalysatoren hauptsächlich Wasserstoff und nur geringe Mengen an Kohlenwasserstoff oder Ethanol.

Darüber hinaus bildet die Rolle von Oxiden während der CO_2RR eine ungelöste wissenschaftliche Diskussion. Um zu verstehen, wie Oxide die katalytische Selektivität beeinflussen, wurde die Verwendung von Potenzialpulsen mit unterschiedlichen Zeitlängen zur perodischen Regeneration von Oxiden etabliert. Insbesondere wurde ein Pulslängenbereich mit verdoppelter Ethanolproduktion im Vergleich zu nicht gepulsten Bedingungen beobachtet und mit *operando* Techniken untersucht.

Die Rolle von Nanowürfeln (NCs), die mit einem co-Katalysator dekoriert sind, wurde sowohl für die CO_2RR als auch für die FAOR untersucht. Es wurde festgestellt, dass Au-Cu_2O NCs Katalysatoren mehr C_{2+} Produkte liefern als bloße Cu_2O NCs. Außerdem wurde die Art, Menge und Rolle der CuAu-Legierung bei der CO_2RR aufgeklärt. Darüber hinaus wurden für die FAOR Pd NCs mit einer SnO_2-Hülle versehen, die die Leistung von reinen Pd NCs übertraf, indem es die vergiftenden Intermediate reduzierte. Mit *in situ* und *operando* Techniken wurden die strukturellen und chemischen Veränderungen unter diesen Reaktionsbedingungen untersucht.

In dieser Arbeit wird der Einfluss der Oberflächenterminierung, der Oxide und der bimetallischen Katalysatorstrukturen für die Aktivität und Selektivität an Beispielen der CO_2RR und der FAOR bestimmt. Die hier vorgestellten Erkenntnisse tragen zu einem zukünfitgen wissensbasierten Design von Elektrokatalysatoren bei, um die Reaktionen zu wertvollen Produkten und zu hohe Leistungen zu lenken, und unterstreichen die Bedeutung der Charakterisierung dieser Katalysatoren unter Reaktionsbedingungen um nützliche Struktur-Selektivitäts-Beziehungen herzustellen.

Contents

Publications

Introduction

This introductory part provides a motivation for this work by illustrating the challenges of the climate crisis, its impact on the global energy market and its economic and technologic perspectives. Electrocatalysis is one way to alleviate climate change by generating alternative possibilities to produce, store and utilize renewable energy effectively. Introductions to the respective state-of-the-art are given for the two investigated electrocatalytic reactions, the CO_2 reduction reaction (CO_2RR) and the Formic Acid Oxidation Reaction (FAOR). Having set this basis, the scientific objective and the approach to answer specific scientific questions are illustrated. Finally, an overview over selected methods and instrumentation are provided.

1

Climate Crisis and the Role of Electrocatalytic Solutions for Synthetic Fuels

The climate crisis is the biggest threat to humanity and the biggest challenge of the 21st century.[1] The human's energy consumption and chemical needs within the last 200 years have led to an over proportional use of fossil fuels adding to the atmosphere over 400 ppm of CO_2 in 2022 compared to the pre-industrial concentration of 280 ppm, shown in Figure 1.1a.[1] The continuous increase in global temperature is now 1.1°C higher than the pre-industrial time baseline.[2] Since the atmospheric CO_2 concentration and temperature have been directly correlated throughout Earth's history,[3] the human-driven emission of CO_2 and other greenhouse gases are found to be primary drivers of climate change.[4]

The exponential increase in energy consumption since the pre-industrial times is unquestioned in Figure 1.1b, which illustrates the global direct energy consumption partitioned into the sources used to acquire the energy.[5,6] It is evident that the global amount of non-renewable power sources exceeds the renewable produced energy greatly, with a positive trend towards more renewable energy. Although, a further increase in the overall energy demand is expected in the near future, which increases the urge for finding alternative and regenerative paths for energy usage.[7]

From an economic perspective, the cost of renewable energy has been continuously decreasing.[8] In particular, solar power has demonstrated a uniform decline in prize. While fossil fuels are limited, renewable power sources such as sunlight, wind or water are abundant. From a technologic point of view, energy storage and reutilization technologies remain challenging innovations. Fossil fuels are more and more replaced by batteries and fuel cells, which provide solutions for certain applications, such as short distance transportation. However, these are not adaptable to other important fossil fuel applications such as air transportation or long term storage. Though synthetic fuels can replace the use of fossil fuels while keeping the advantages: high energy density, cheap storage and making use of already existing infrastructure for fossil fuels. In particular, aviation and shipping can benefit from synthetic fuels since a switch to alternative energy sources is technologically and economically not yet feasible. Using CO_2 as a resource for synthetic fuels might therefore be utilized to control

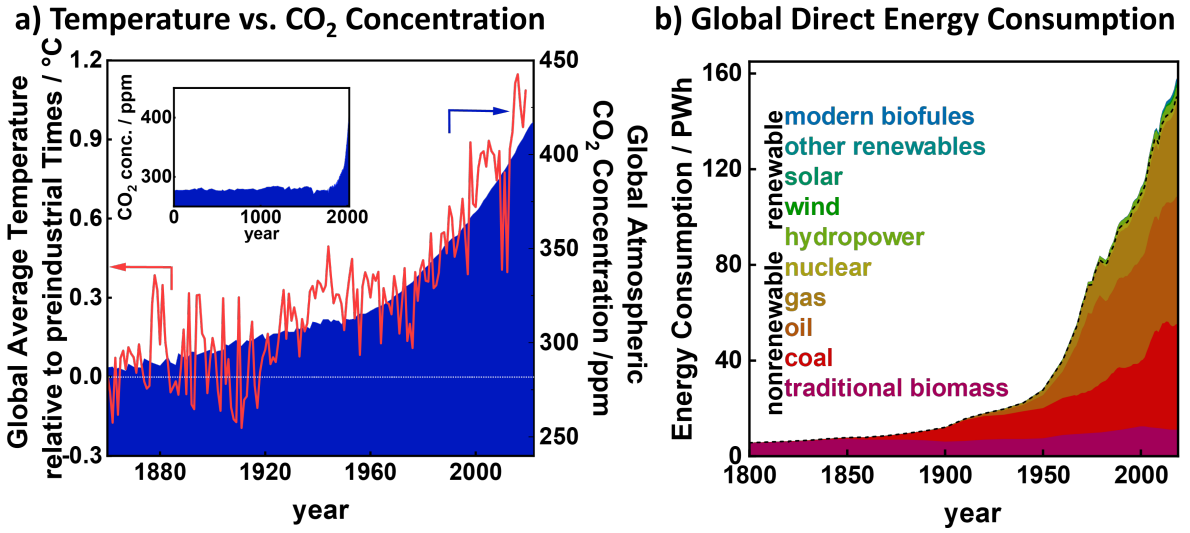

Figure 1.1: a) Global average temperature anomaly relative to the 1961-1990 average temperature compared to the global atmospheric CO_2 concentration. The inset shows the CO_2 concentration from the years 0 to 2022. b) Global direct energy consumption from pre-industrial times until 2019, divided into the sources of the utilized energies. The dashed line separates the renewable energies from the nonrenewable ones. Nuclear power was defined here as nonrenewable power source. Data reproduced from ourworldindata.org and [1, 5, 6].

CO_2 emissions in a sustainable and equitable fashion.[9]

The natural carbon cycle uses photosynthesis to convert CO_2 with the energy of the sun into biomass. However, photosynthesis is relatively inefficient to diminish the large amounts of anthropogenic produced CO_2 and is also an unfeasible source for fast energy production on demand.[10] Closing the anthropogenic carbon cycle in an artificial manner e.g. with the electrocatalytic CO_2 reduction reaction (CO_2RR) would open opportunities to produce clean and sustainable fuels and chemicals. This technology can be used flexibly and can be adapted rapidly to the needs of humanity, as illustrated in Figure 1.2.

In the future, electricity could be abundant and cheap for utilization due to sustainable wind-, solar and hydro energy plants.[9] Thus, electrochemistry is an ascending field to transform energy to valuable and industrially relevant products with many different reactions. Examples of existing and future potential technologies are the water-splitting reaction, the chloralkali electrolysis, the nitrogen reduction reaction or the CO_2RR, which is studied in this work. In order to utilize the stored energy from these chemicals, electrocatalytic oxidation reactions are used. Fuel cells comprise these oxidation reactions to turn the stored energy back into usable electricity. Fuel cell types exist already commercially, which are either powered by hydrogen directly or indirectly by reforming hydrogen-rich fuels. An additional type of fuel cells are fed directly with liquids, such as methanol or formic acid. The latter reaction of the oxidation of formic acid is also studied in this thesis. The general goals of

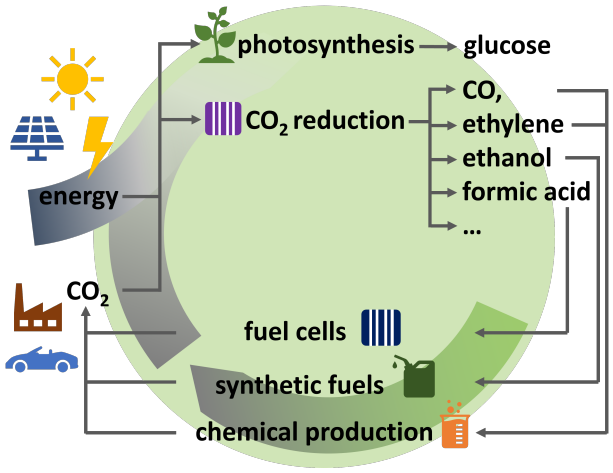

Figure 1.2: Carbon cycle for the most important technologies compared to natural photosynthesis.

this electrocatalysis research are the improvement of performance, efficiency and lifetime of the used catalysts.

The Formic Acid Oxidation Reaction (FAOR), which is explored in chapter 9, can be utilized as hydrogen donor for the automobile fuel infrastructure or as direct formic acid fuel cell in microelectronics of portable devices.[11] Formic acid as fuel for fuel cells is often compared to hydrogen and benefits from its non-flammability, low toxicity, high abundance and its higher volumetric energy density. However, the main technical challenge that hinders commercialization of direct formic acid fuel cells is the fast catalyst deactivation. Therefore, it is of utmost importance to focus on the understanding of periodic catalyst regeneration or the intrinsic prevention of the deactivation by a specific catalyst design.

Furthermore, the CO_2RR, which is studied in chapters 6, 7, 8, is about to become commercialized for syngas production (a CO/H_2 mixture), for which Ag catalysts are mainly used.[12] The syngas can then be used for commercially available hydrogenation reactions. However, the production of highly valuable hydrocarbons with sufficient yield can, to date, be only performed with copper catalysts. Copper forms commercially interesting products such as ethylene, ethanol and formic acid. Yet, the main challenges for industrial application are the multiproduct mixtures, the low single pass CO_2 consumption efficiencies and thus the high downstream separation and purification costs.[13] Thus, the major scientific challenge is to push towards a highly selective process, which can be be boosted through a knowledge-driven catalyst design and a sensitive manipulation of the applied potential as shown in this work.

It is a scientific challenge to get to understand these reactions and their respective catalysts further. In particular, the catalysts should be explored as they are under working conditions as they alter their structure and chemical state.

2

The Electrocatalytic CO_2 Reduction Reaction

The electrocatalytic CO_2 reduction reaction (CO_2RR) has become the focus for a multitude of research groups due to the economical need to improve technologies for sustainable energy conversion. The main goal is to make this reaction economically efficient by producing highly valuable chemicals, such as ethylene or ethanol. This chapter describes the basic concepts of the CO_2RR and gives a summary of the state-of-the-art on selected aspects regarding the catalyst development and strategies to tune the selectivity. In particular, a focus is set on surface facets and single crystal studies, which grounds in the understanding of active sites on the atomic level. The establishment of shaped nanoparticles are thus a direct consequence of the structure-activity relationship findings of the single crystals. Moreover, tuning the potential profile leads to a new area of parameters to manipulate the catalytic activity. Finally, bimetallic catalysts allow the controlled variation of the material properties resulting in new insights regarding the catalyst performances.

2.1 Basic Concepts of the electrocatalytic CO_2RR

The CO_2RR is a promising approach to valorize CO_2 back to energy-dense fuels or chemicals. A copper catalyst can reduce CO_2 to up to 16 different products by the transfer and storage of up to 18 electrons per each newly formed molecular bond. The competing parasitic reaction is the Hydrogen Evolution Reaction (HER). The first report about this reaction was published in 1985, showing product analysis of several metal cathodes towards $HCOO^-$, CO and CH_4.[14] Hori's studies continued by further finding ethylene,[15] ethanol and 1-propanol as products from Cu catalysts[16] and by deconvoluting electrolyte effects, suggesting the influence of the pH on the product selectivity and identifying CO as key intermediate.[17,18] The investigation of CO producing substrates modified with $HCOO^-$-producing adatoms featured variable product selectivities between both products and created the foundation for the investigation of bimetallic catalysts.[19] Further, the adsorption of CO on Cu was investigated with *in situ* Fourier-transformed Infrared Spectroscopy (FTIR).[20,21] Furthermore, systematic studies on structure sensitivity by investigating low and high index faceted Cu single crystal electrodes were performed, suggesting the high dependence of the catalyst activity

on its structure.[22–26]

The general form of the reaction is shown in equations 2.1, where the cathodic part reduces CO_2 to valuable products by consuming protons and electrons with water as the source for protons. On the anode side, the Oxygen Evolution Reaction (OER) takes place, which splits water into its elementary components. The overall reaction is described as CO_2 recycling reaction.[27]

$$\begin{aligned} &\text{cathodic:} && x\,CO_2 + n\,H^+ + n\,e^- \longrightarrow \text{product} + y\,H_2O \\ &\text{anodic:} && w\,H_2O \longrightarrow z\,O_2 + n\,H^+ + n\,e^- \\ &\text{overall:} && x\,CO_2 + y\,H_2O \longrightarrow \text{product} + z\,O_2 \end{aligned} \tag{2.1}$$

Catalysts and Product Distribution

Since the beginning of CO_2RR investigations, many different metals were examined and classified by their product distribution. $HCOO^-$ producing metals are Pb, Hg, Tl, In, Sn, Cd or Bi, while Au, Ag or Zn produce mainly CO. Ni, Fe, Pt, Pd or Ti provide mostly H_2. Cu is the only metal that is able to perform $\geq 2e^-$ electron transfers and produce hydrocarbons, aldehydes and alcohols in significant amounts.[14,28,29] Here, the product distribution correlates directly with the binding energy to *OCHO, *COOH, *CO and *H intermediates of both, the CO_2RR and the parasitic HER, which indicates the relevance of optimizing the binding energy for selective product formation. Cu as the standalone metal shows a unique negative binding energy for *CO and a positive one for *H.[28]

The different products of Cu are categorized in hydrocarbons, alcohols, aldehydes, ketons, carboxylic acids and CO. Table 2.1 shows the eleven most common products in the order of the electrons transferred to form the respective product, as well as their cathodic half cell reactions and their thermodynamic equilibrium potentials. Additional products that have been demonstrated in other studies are methanol, glyoxal, glycolaldehyde, ethylene glycol or hydroxyacetone, but are not presented here due to their insignificant production rates.[30] Hydrogen is technically not produced during CO_2RR, but occurs simultaneously during the parasitic HER. This reaction utilizes the same catalytic sites and its intermediate *H is involved in several products of the CO_2RR. Thus, the HER during the experiment is counted to the overall Faradaic efficiency.

Potential Dependency on the Product Selectivity

The formation of products under CO_2RR conditions depends on the various processes in the microenvironment around the catalytic active electrode. Charge and electron transfers occur from the electrode site to the interface of the catalyst with the electrolyte. Upon potential polarization between the working electrode (WE) and the counter electrode (CE), a double layer of adsorbed ions is formed at the catalyst interface with different binding energies of the adsorbates. Thus, the CO_2RR

Table 2.1: Electrochemical Reactions in CO_2RR with corresponding equilibrium potentials. The equilibrium potentials are Gibbs free standard energies, given vs. RHE in pH 7, at 25°C.

Product	Half Cell Reaction		E / V vs. RHE
CO	$CO_2 + 2H^+ + 2e^-$	$\longrightarrow CO + H_2O$	−0.10 V
Formate	$CO_2 + 2H^+ + 2e^-$	$\longrightarrow HCOOH$	−0.20 V
Methane	$CO_2 + 8H^+ + 8e^-$	$\longrightarrow CH_4 + 2H_2O$	0.17 V
Acetic acid	$2CO_2 + 8H^+ + 8e$-	$\longrightarrow CH_3COOH + 2H_2O$	0.11 V
Acetadehyde	$2CO_2 + 10H^+ + 10e^-$	$\longrightarrow CH_3CHO + 3H_2O$	0.06 V
Ethanol	$2CO_2 + 12H^+ + 12e^-$	$\longrightarrow C_2H_5OH + 3H_2O$	0.09 V
Ethylene	$2CO_2 + 12H^+ + 12e^-$	$\longrightarrow C_2H_4 + 2H_2O$	0.08 V
Ethane	$2CO_2 + 14H^+ + 14e^-$	$\longrightarrow C_2H_6 + 4H_2O$	0.14 V
Propionaldehyde	$3CO_2 + 16H^+ + 16e^-$	$\longrightarrow C_2H_5CHO$	0.09 V
Allylalcohol	$3CO_2 + 16H^+ + 16e^-$	$\longrightarrow C_3H_5OH$	0.11 V
Acetone	$3CO_2 + 16H^+ + 16e^-$	$\longrightarrow C_3H_6O$	−0.14 V
Propanol	$3CO_2 + 18H^+ + 18e^-$	$\longrightarrow C_3H_7OH + 5H_2O$	0.10 V
Hydrogen	$2H^+ + 2e^-$	$\longrightarrow H_2$	0 V

is very sensitive to the applied potential and the product distribution varies significantly with it. The Faradaic Efficiency (FE) of different products can be displayed as a function of the potential, where the products for one catalyst are analyzed at steady state conditions at each potential. The curves for potential dependent product analysis of synthesized Cu_2O NCs in Figure 2.1 have been set as a benchmark in this work for well performing nanoshaped catalysts. Here, a) the current transients, b) the potential dependent FEs and c) the potential dependent partial current densities are plotted.[31] Hydrogen reaches a minimum in FE at −1.0 V vs. the reversible hydrogen electrode (RHE), while at −1.05 V vs. RHE all alcohols, C_2H_4 and acetaldehydes achieve a maximum. CO is the main product at low overpotentials and reaches its minimum at the maximal measured overpotential. The same transient shape is shown for $HCOO^-$. The CH_4 transient grows exponentially with increasing overpotential. The partial current densities are shown here in the same plots to illustrate the importance of this data representation. Since the current transient increases exponentially with overpotential, the activities of the individual products, displayed as partial current densities, increase respectively. For example, a relatively high selectivity at lower overpotentials is given by CO, H_2 and $HCOO^-$ compared to higher overpotentials, but only low amounts of these products are actually produced.

Mechanistic Understanding

The mechanism of the CO_2RR has been a matter of research ever since CO_2RR was studied and thorough understanding is critical to improve and steer the selectivity. For the development of active

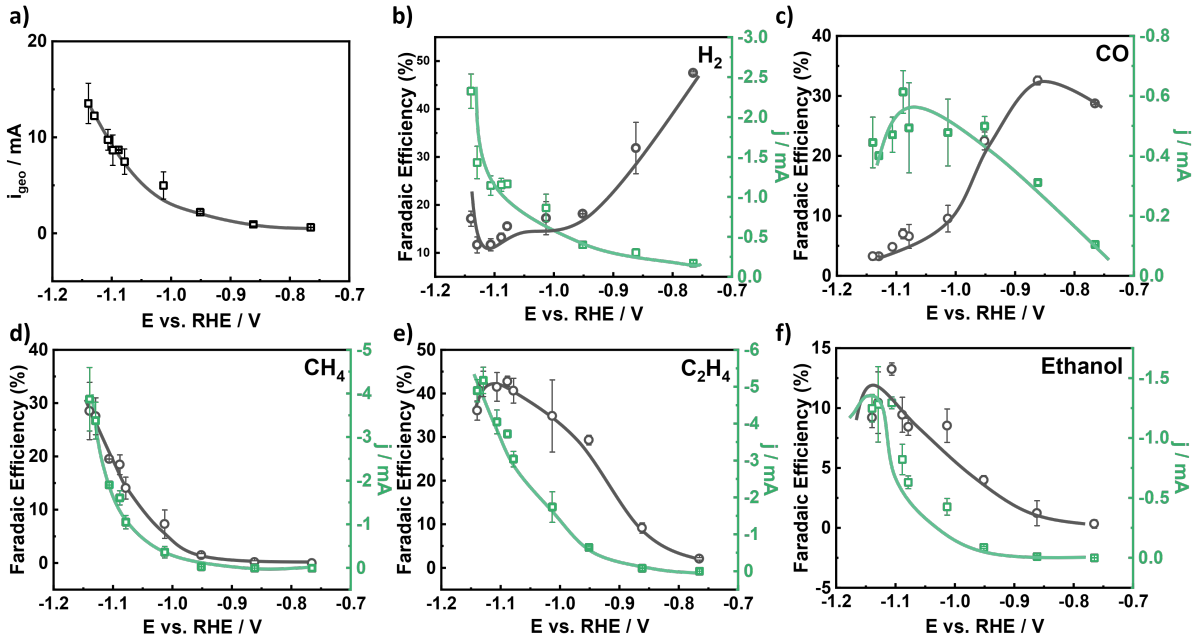

Figure 2.1: Potential dependency of the CO_2RR of Cu_2O nanocubes (NC) in 0.1 M $KHCO_3$. a) Transient of the total current density, Faradaic efficiencies and partial current densities of b) H_2, c) CO, d) CH_4, e) C_2H_4 and f) Ethanol. The data were also published in [31].

and selective catalysts, a fundamental understanding of the mechanisms is essential and new insights are yet continuously gained. Several articles focus on comprehensive summaries on the mechanistic pathways to each product, which will not be repeated here.[27,32–39] Instead, an overview is presented in Figure 2.2, which shows a simplified flowchart comprising the most important intermediates.

The reduction and adsorption of CO_2 to *CO is the rate limiting step. The *CO intermediate is key to form C_{2+} products in CO_2RR. The optimal binding energy on Cu prevents fast desorption and poisoning of the catalyst. If *CO does not desorb directly, it can react further to C_1 products or via C-C coupling to C_2 or C_3 products. Possible steps from CO_2 to CO are the formation of *COOH or *OCOH. It is widely accepted that the other intermediate, *OCOH, leads to the formation of formate with further protonation to Formic Acid as a terminal step. Methane is simply produced by a step-by-step protonation of the *CO. Ethylene can be formed via two pathways which differ in the adsorption sites after the C-C coupling. On one hand, a bridge bond *OC*C is formed, while on the other hand both C adsorb to the metal surface. From there, acetaldehyde can be formed, which itself has been also shown to be produced from the methane pathway, by insertion of a CO.[39] It has been suggested that CO is continuously produced, but remains in the local reaction environment until it is further reduced.[35] Acetaldehyde is a direct precursor of ethanol.[40] With ethanol or ethylene as products, some traces of ethane are found in the product mixture. C_3 products are mainly formed by an additional CO insertion, with propionaldehyde being the precursor for propanol.[36,37] A prior

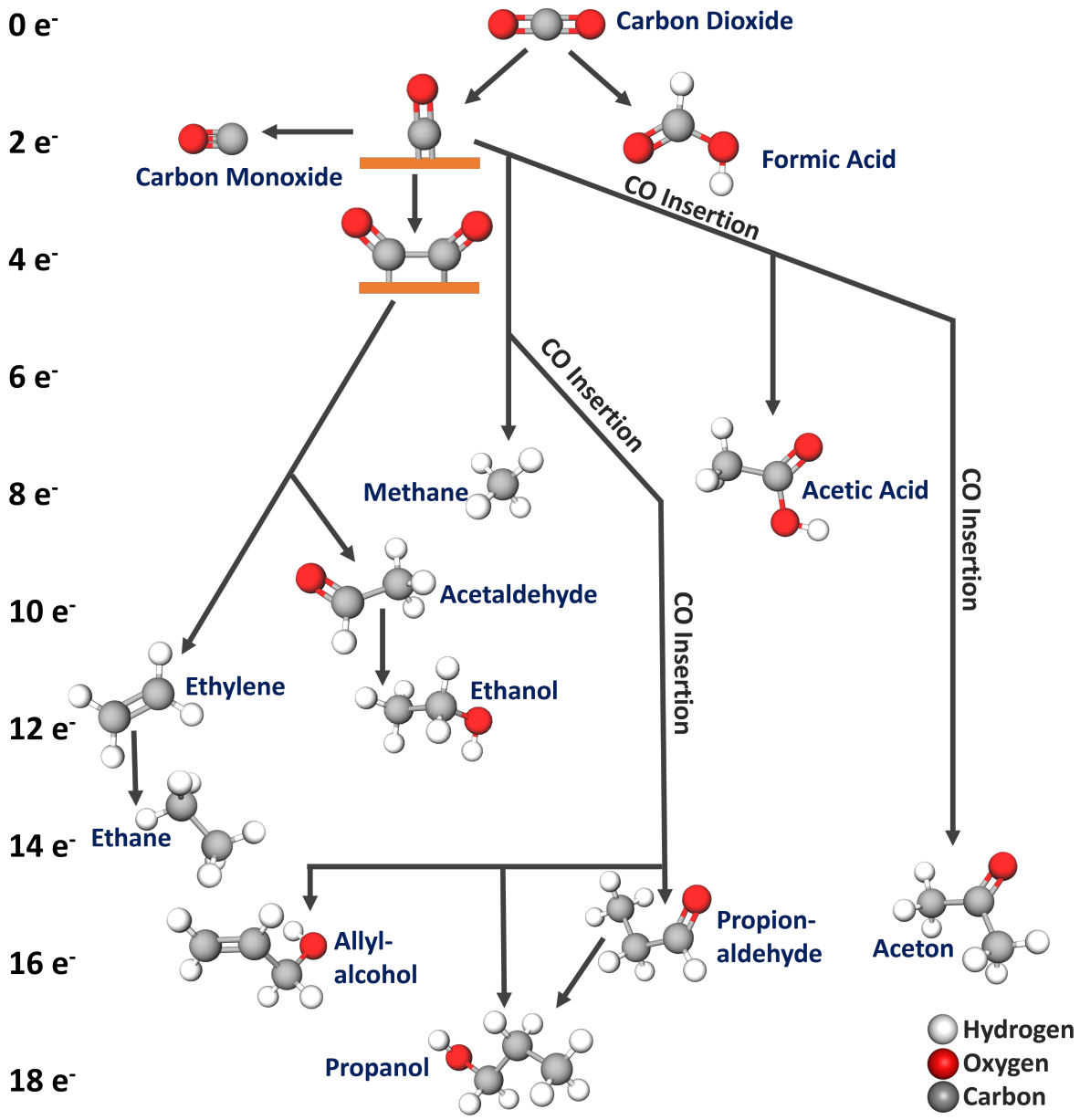

Figure 2.2: Reaction network on the Mechanistic pathways of CO_2RR to C_1, C_2 and C_3 products on copper. The possible intermediates and transition states are incomplete. Pathways were reconstructed after [27, 32–39].

branch leads to the formation of allylalcohol.[33] Aceton and Acetic Acid are often found as traces products and are formed via the glyoxal pathway.[34,35,38]

CO_2RR is a complex reaction with many parameters affecting the reaction. Numerous studies focus on the influence of certain effects on the CO_2RR. All these effects can be assigned to the following categories:

- **Catalyst Design**: size effect,[41,42] facet and morphology effect,[43–45] oxidation state,[45,46] roughness,[45] defects,[47] grain boundaries,[48] interparticle distances,[49,50] loading[51,52]
- **Support and Co-Catalysts:** bimetallics,[53,54] support effect,[45,55,56] spillover effect,[57–59] stability[55]
- **Electrolyte Design:** electrolyte anions,[60,61] additional anions,[62,63] cations,[64] pH,[65] solubility of CO_2,[66,67] electrolyte concentration[63]
- **External Conditions:** temperature,[68] pressure,[69] cell geometry[70]
- **Operating Conditions:** choice of electrochemical technique,[27] potential profile[71]

This thesis presents studies about selected effects regarding the catalyst and operating conditions, and kept all other effects as steady as possible. Therefore, summarized descriptions will be given for these in the following sections. Detailed descriptions and summmaries of the other possible effects can be found in the many comprehensive and informative review articles available, as for example [27, 72–75].

2.2 Surface Facets and Single Crystal Studies

The catalytic activity as well as the product distribution depend highly on the atomic structure of the active sites, implying a significant structure sensitivity of CO_2RR with regard to the catalyst surface. Every catalyst exhibits planar areas or facets as well as undercoordinated steps, kink edges or defect sites, whose individual contributions are challenging to deconvolute. Investigating atomically flat or well-structured stepped single crystal electrodes are the choice in order to understand structure-activity relationships on the atomic level. Low index model catalysts are single crystals exposing a certain orientation such as Cu(100), Cu(110) or Cu(111), which is illustrated in Figure 2.3a-c. High-index surfaces can be derived from the low-index surfaces with a certain step site density. Step-edges with (100) terraces and (111) or (110) steps can be modelled as Cu(S)-[$n(100)x(111)$] or Cu(S)-[$n(100)x(110)$] with a $n = 2$-8 terrace width. Figure 2.3d depicts a Cu(310) stepped surface.

Advantages of investigating well-ordered surfaces are the direct comparability to theoretical calculations since they model perfect surface structures as pre-catalyst substrates. Moreover, structure-

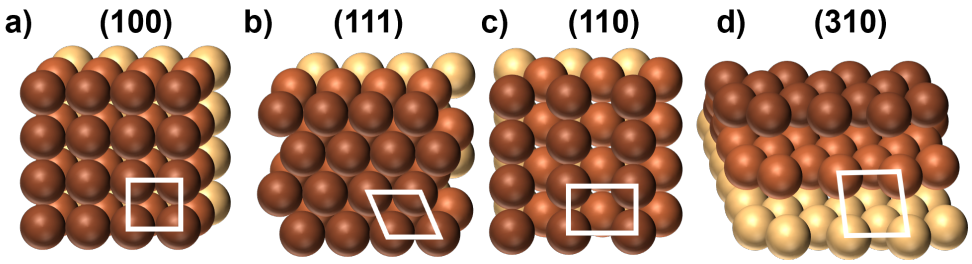

Figure 2.3: Top view schemes of the low index facets a) (100), b) (111) and c) (110). d) Scheme of the high-index surface (310). The white boxes indicate the respective unit cells.

unrelated effects can be explored with the use of reproducible well-defined surface structures.

Low-index facets have been a matter of investigation since the pioneering work of Hori[21] and form different main products dependent on the structure type. In the order Cu(100) > Cu(110) > Cu(111), C_2H_4 is produced the most on Cu(100), while CH_4 is produced the least at −1.0 V vs. RHE.[21,23,25,76–78] Along with C_2H_4, alcohols are produced the most on Cu(100).[21,78] It is suggested that the lower CO dimerization barrier on Cu(100)[79] and the high surface coverage of adsorbed CO are essential for the favored C_2H_4 formation on Cu(100).[78] Nonetheless, recent work has shown that flat (100) surfaces only produce H_2, and that defects are needed for CO_2RR.[80] The latter had been achieved in prior work through electropolishing pre-treatments.

It is widely accepted that complex atomic structures and uncoordinated sites play a major role in the structure-activity relationships. High-index facets were therefore studied complementary to the low index facets.[23–25] Figure 2.4 shows the FEs of C_2H_4, CH_4 and ethanol of stepped single crystals as a function of the crystal orientation, with Cu(100) as reference and a termination in the low-index facets Cu(111) and Cu(110). The numerous high-index facets in between are sorted by increasing number of step sites compared to terrace sites in both directions. An increase of ethylene is observed starting from Cu(100) in both directions, while only the (110) steps increase ethanol production.[25,43,81] For the methane production, the trends are opposite to ethylene production. Thus, these results indicate that short (100) terraces with steps vary the FEs significantly and an optimal selection of the terrace/step ratio can significantly enhance C_{2+} product formation. However, the mechanistic role of the individual facets, steps and edges for CO_2RR is not fully understood.

The thorough investigation of single crystals is overshadowed by challenges in reproducibility and the actual structure of the surface.[23] For example, the transfer between the surface preparation to the electrocatalytic measurement often leads to a gap, where the surface is exposed to air. Due to partial surface oxidation upon air exposure, the surface homogeneity might be disrupted since Cu is a metal with high atomic mobility at room temperature. Additionally, most electrocatalytic studies on Cu single crystals have been performed after electropolishing, which usually results in a surface textured with uncontrolled defect sites. As mentioned before, a recent study from my departement revealed

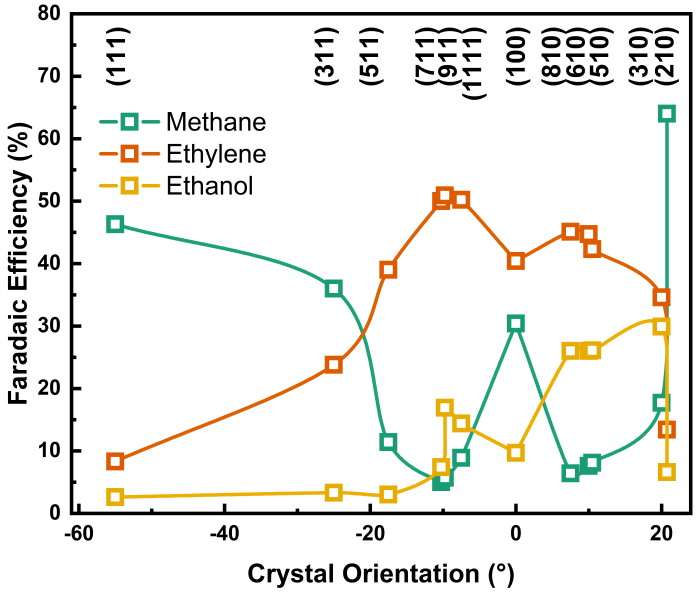

Figure 2.4: Faradaic Efficiencies of stepped Cu single crystals for Methane, Ethylene and Ethanol as a function of the crystal orientation angle with Cu(100) as reference. The high-index surfaces are sorted with termination in the low index facets Cu(111) and Cu(110). Data redrawn from [25].

that the product distribution of Ultra high Vacuum (UHV) clean, flat and atomically ordered Cu(100) and Cu(111) surfaces favored mostly parasitic H_2 evolution.[80] In contrast, by introducing controlled roughness and defects through sputtering, electropolishing or plasma treatments, a significant amount of hydrocarbons could be formed.[80] These experiments confirm that steps and defect sites might be involved as active sites for CO dimerization and formation of hydrocarbons. Furthermore, it was found that the CO binding strength correlates with the hydrocarbon selectivity, which implies that stronger CO binding sites favor C-C coupling.[80,82] Alcohols were found in trace amounts only. These results suggest that large terrace sites favor HER, while steps, edges, defects and high index facets favor C-C coupling.

It is worth to note that Cu alters its surface structure not only due exposure to air, but also upon insertion into the electrolyte and potential modification.[83] For example, the immersion of an electropolished Cu(100) into 0.1 M $KHCO_3$ at open circuit potential (OCP) led to a surface coverage with spherical particles or platelet-shaped crystallites with macro-steps. Increasing the overpotential towards CO_2RR relevant conditions led to further increase of undercoordinated Cu sites and changes in the atomically structured surface indicating high sensitivity on the experimental conditions.[83]

Therefore, single crystals provide model catalysts to study individual structures and structural alterations in a systematic way.

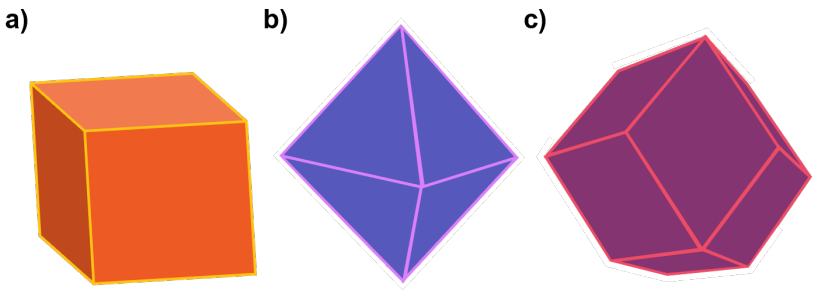

Figure 2.5: Illustration of shaped nanoparticles a) cube for (100) surfaces, b) octahedra for (111) surfaces and c) rhombododecahedra for (110) surfaces.

2.3 Shaped Nanoparticles

Catalysts that might be suitable for industrial application, need to offer high current densities, enhanced stability and low material costs. A high surface area to volume ratio on small particles leads to improved utilization of material per mass unit. Thus, the investigation of nanoparticles are the logical consequence to transfer the more fundamental understanding of facet effects to industrial relevance. Nanostructured copper, in particular nanoparticles, exhibit much higher surface to bulk ratios and can thus provide higher current densities per geometric area compared to single crystals. Moreover, nanoparticles can be engineered to fit the current mechanistic and structural understanding of optimal active sites. Preferential faceting of (100) surfaces on face centered cubic (fcc) Cu and Cu_2O results in cubic shaped particles, while octahedra or rombododecahedra expose shapes of only (111) or (110) surfaces, respectively, as illustrated in Figure 2.5. These nanoparticles can also be varied in size, which modifies the ratio of facets to edges and kinks and therefore also the density of uncoordinated sites. Thus, a change in binding energies can be induced.[27]

Efforts have been made on the synthesis and characterization of shaped Cu nanoparticles confirming the preservation of product trends up to catalysts in nanoscale.[42,84,85] Similar to the results for single crystals, it has been discussed that metallic Cu cubes dominated by (100) surfaces are highly selective for ethylene, while (111) shaped octahedra provide mostly CH_4 and Cu spheres do not provide any preferential product.[84–86] Size effects have been investigated on spherical, but also on cubic particles.[41,42] Spherical Cu nanoparticles below 15 nm produce mainly CO and H_2, with significant increase in the production rate for particles below 5 nm.[41] Cubic catalysts between 20 and 65 nm, however, were discussed to display higher selectivity for ethylene than spherical ones, with ethylene selectivity peaking at particle size of 44 nm.[42] Nonetheless, the role of residual surface ligands used for the synthesis of the distinct nanoparticle (NP) sizes is yet to be clarified.

It has to be noted that the chemical state of the synthesized catalyst is important, as oxide derived catalysts provide enhancement in C_{2+} product formation.[49,87] The motives for this phenomenon may include the increase of surface roughness, defects and grain boundaries upon progressive reduction

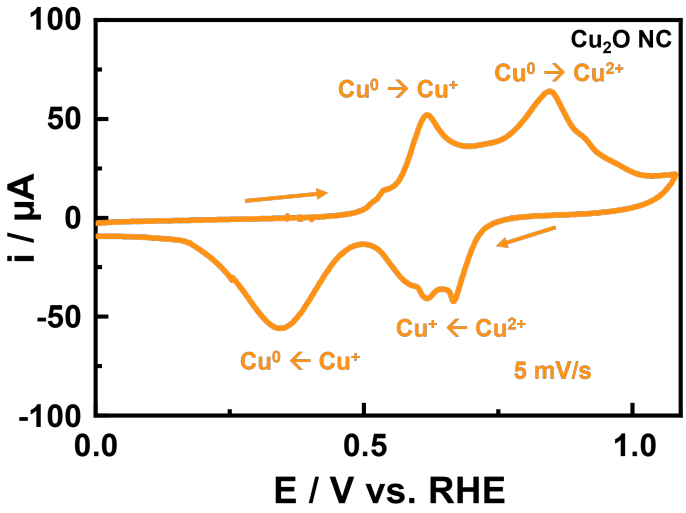

Figure 2.6: CV of Cu NCs showing the oxidation from Cu^0 to Cu^I and to Cu^{II} at 0.6 V and 0.8 V, respectively.

of the oxides, the presence of residual subsurface oxygen, or the chemical state of the active Cu species.[88–90] Additionally, by using nanoparticles, a support must be selected providing good dispersion and mechanical stability. The catalyst loading on the support can be varied, which also results in altered electrocatalytic properties by more frequent readsorption of intermediates and products.[49,91]

2.4 Pulsed Electrolysis - Tuning the Potential Profile

The manipulation of the applied potential profile is an additional option to establish a more catalytically active surface and optimize the the composition of the double layer, while modulating the electron transfer processes from the catalyst to the educt. In particular, potential pulses towards potentials, which oxidize the catalysts are of interest. Such pulses can however not only modify the chemical state, but also the surface structure. The Cyclic Voltammetry (CV) of Cu in Figure 2.6 depicts the potentials that can lead to an oxidation of the material. For example, the application of 0.6 V vs. RHE oxidizes the surface from Cu^0 to Cu^I, while the oxidation to Cu^{II} appears at 0.8 V vs. RHE.

The sole application of different static potentials usually leads to very different product selectivities. However, fast changes in the potential result in non-equilibium of the numerous processes during the CO_2RR, such as the electron transfer processes, the surface composition of the catalyst or the microenvironment of the electrolyte, including the double layer. Thus, these variations result in a different interplay between the processes, resulting in a variation of the product selectivity. Key parameters here are the choice of the upper and lower potentials and their respective pulse durations. The main advantages of pulsed electrolysis are that the catalytic processes and selectivites can be

influenced during the electrocatalytic measurements by changing the applied potential. Thus, the modification of the pulse profile benefits from the immediate response of the current and the catalytic processes and thus to possible instantaneous switches to different selectivites. Additionally, the reaction can temporarily be set "off", when external conditions are not favorable, such as an instable energy input from renewable energy or a short-term shortage of CO_2 resources.[92]

Selectivity changes due to pulsed potential application have been studied since the 1990s.[92] The catalyst deactivation was reversed and its catalytic activity was restored by stripping off any poisoning species, for instance graphitic carbon, on the surface.[93,94] Thus, pulsing leads to an increase in the lifetime and performance of the catalyst, but also to an alteration in product selectivity towards improved ethylene formation and H_2 suppression. It was furthermore suggested that restoring potential pulses may cause roughening and oxidation of the catalyst.[95,96] A surface reconstruction as a result of the oxidation during the anodic pulses was proposed to improve C_{2+} products and simultaneously suppress HER.[97] However, an enhanced CO and carbonate coverage due to pulsing could as well result in the observed selectivity trends.[98]

More recently, it was found that a mixed chemical composition on copper with Cu^0 and Cu^I on the surface contributes to a more selective ethanol production. The carbonyl intermediates are thus stabilized on the surface while protonation is prevented.[99] By investigation of the temporal evolution during a pulse it was found that the CO_2 concentration at the vicinity of the surface was restored during the anodic pulse and that the local pH was decreased.[100] Additionally, multiple pulse repetitions lead to an enhancement of the surface concentrations of adsorbed CO and H, resulting in improved C_{2+} and suppressed HER.[101] When pulses in the millisecond regime are applied, the product distribution adjusts to favor mostly H_2 and CO,[102] or promote CO and CH_4 formation. These results highlight the significant selectivity dependence on pulse duration, where the product selectivity may be switched between C_1 and C_2 products by tuning the potential profile.[103]

The investigation of potential pulses requires the consideration of several fundamental physicochemical transformation processes that occur in different time scales from the ms-range for charge processes to the s-range for the CO_2RR. This dynamic variation in responses results in new microenvironments in the electrolyte that could be beneficial for certain selectivities. Figure 2.7 illustrates the main processes categorized in charging, catalyst composition and CO_2RR and divided in its primary location. The changes are exemplified for a lower potential (purple, 1.0 V vs. RHE), where CO_2RR is occurring and an upper potential (green, 0.6 V vs. RHE), which oxidizes a Cu catalyst to Cu_2O.

A change of the applied potential in the catalyst is the fastest process, as it is the base for any other change. This catalyst charging directly affects the electrical field, which resonates through the double layer region. As a result, the ions at the vicinity of the catalyst are replaced with ions of the opposite charge of the catalyst interface. The adjustment between OH^- and H^+ results in a change in the local pH as well.[100,101]

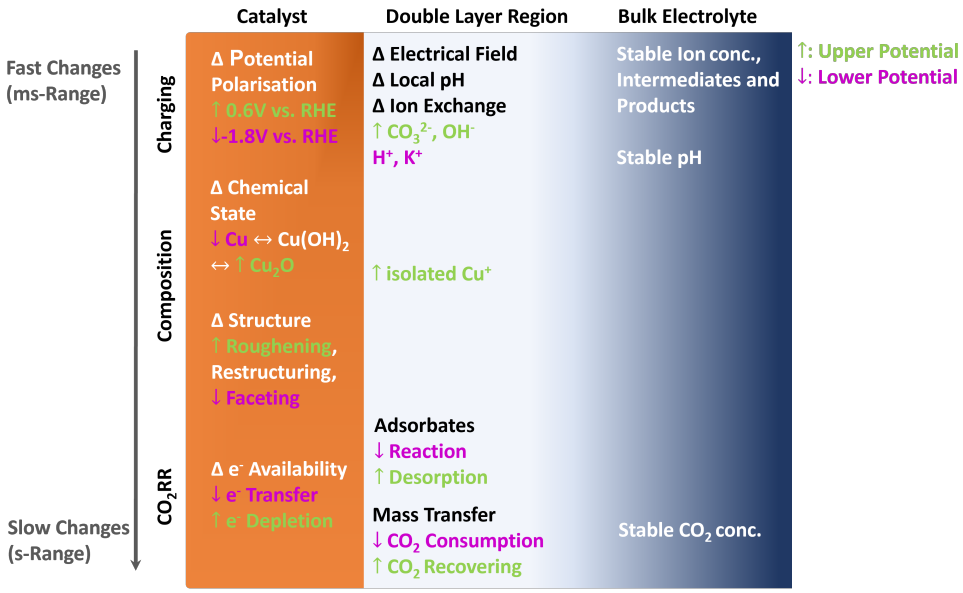

Figure 2.7: Illustration of the physicochemical transformation processes during the application of potential pulses.

Upon the application of an upper pulse of at least 0.6 V vs. RHE, the metallic catalyst surface changes promptly to Cu^{I}, as shown in the CV in Figure 2.6. As it will be seen in chapter 7, small amounts of Cu^{II} are always simultaneously formed, which could result in Cu^{I} ions in the electrolyte. Surface roughening is a direct consequence of this material loss, while the catalyst might also restructure dependent on the applied potential. At the same time, any oxidic structure gets reduced during a lower pulse.

During the application of potential pulses, the electrocatalytic CO_2RR occurs only when CO_2RR relevant conditions are applied. At this point, the Cu catalyst reduces to Cu^{0} and available electrons get transferred to adsorbates and intermediates for further reduction. Upon the catalytic reaction, the educt CO_2 is consumed and its amount, which is limited by the relatively low solubility of CO_2 in the electrolyte, diminishes close to the catalytic surface. The bulk electrolyte is usually continuously saturated with CO_2, while the CO_2 close to the surface is consumed during CO_2RR. Thus, mass transport of dissolved CO_2 from the bulk electrolyte to the vicinity of the electrode depends on diffusion, migration and convection. Furthermore, adsorbates that do not react further and are irreversibly bound to the surface are expected to deactivate and poison the catalyst. During an anodic pulse, CO_2RR is stopped, resulting in the recovery of the CO_2 in the double layer region, and adsorbates, intermediates but also poisoning impurities are expected to desorb. A single electron transfer is a fast process, but multiple-electron transfers are estimated to take some more time. Note here, that the optimal ethanol production found during potential pulses in chapter 7 occurs with a cathodic potential time of about 4 s.

The interplay between all those sub-processes is complex and any small variation of one process parameter might lead to an altered interaction and thus to different selectivity trends. For the investigation of pulsed CO_2RR it is therefore imperative to carefully characterize the different components of the overall pulsing process. In summary, the pulse conditions have to be chosen such that most of the electron transfer is Faradaic, while having a minimal amount of non-Faradaic processes like surface oxidation or charging. At the same time, the microenvironment of the electrolyte and the interface to the catalytic surface should be optimal for certain selectivity trends, including the CO_2 concentration at the vicinity to the surface, the modulation of the adsorbates, the local pH, the optimal surface reconstruction and the right quantity of Cu^+ species with the appropriate structure. Thus, the correlation between the pulse conditions and the resulting product distributions with the particular structure of the catalyst surface and the double layer is yet unclear.

2.5 Bimetallic Catalysts

Bimetallic catalysts merging the Cu metal with a secondary material is a large field of investigation because the combination of two metals can vary the structural, chemical and electronic properties of Cu and thus alter the product selectivity. For instance, more CO can be created with the secondary catalyst at the vicinity of the catalytically active surface, which promotes C-C coupling, and thus enhances the formation of C_{2+} products. A classification of the secondary metals according to their main products has been well established.[19,27,28,104] Metals that promote the HER, $HCOO^-$ or CO are suitable to be added to Cu as a co-catalyst because they can create intermediates that can facilitate rate limiting steps of the CO_2RR on Cu. In particular, Au, Ag and Zn show decreased CO binding strengths[29] in this order compared to Cu, while their onset potentials and correspondingly their partial current densities for CO follow a slightly different order with −0.25 V (vs. RHE) for Au, −0.4 V for Cu, −0.52 V for Ag and −0.6 V for Zn.[29,105,106] Synergistic effects promoting higher activities for CO, but also improved C_{2+} products have been demonstrated between these CO-producing metals and Cu.[107,108] The atomic structural arrangement of these co-catalysts with Cu are essential to drive activity and selectivity in certain directions. The underlying effects are electronic and strain effects, bifunctional mechanisms, tandem or sequential mechanisms or CO spillover.

In the following, structure-selectivity relationships towards CO and C_{2+} products are described on the example of Cu-Au bimetallic catalysts. The reader is referred to comprehensive literature to learn about other Cu-M catalysts.[27,109,110]

Several Cu-Au catalysts have demonstrated increased activity for CO production compared to pure Au or Cu, when an optimal Cu:Au composition is satisfied. These pre-catalysts usually show a homogeneous alloyed structure in the as-prepared state and the optimized CO formation can be attributed to (i) dipole repulsion between adsorbed CO on Cu and on Au,[77] (ii) to a bifunctional

mechanism, where the intermediates on Au are stabilized by Cu[111] and (iii) to an electronic effect, where the Au surface is compressively strained.[53] These efforts to study bimetallic catalysts serve to find better catalysts for the production of CO/H_2 mixtures, which can be further processed to valuable chemicals. Nonetheless, *operando* studies during CO_2RR on such bimetallic catalysts are still missing, since the as-prepared state of these materials is not likely preserved during operation.

Gold as co-catalyst is used as a local CO generator that increases the CO local pressure at the vicinity of a Cu surface and such increases the *CO coverage on Cu.[112,113] CO is also understood to provide facilitated surface diffusion over short distances.[27] Moreover, it is suggested that the overpotential for C_{2+} products is reduced by the presence of Au NPs on Cu material.[112] Thus, it is expected, that small amounts of Au may improve the CO_2RR of Cu towards C_{2+} products.

2.6 Conclusion

CO_2RR is a promising technology that can help to close the carbon cycle and provide valuable chemicals and fuels in a climate-neutral fashion by using CO_2 and energy from renewable resources. This complex reaction has been investigated from different perspectives, while a multitude of effects are found to be relevant. Major focus has been set to create catalysts improving the product distribution towards high valuable chemicals. However, the structures favoring specific products have not yet been well understood during operation. Thus, thorough understanding of morphological and compositional changes during the CO_2RR is pivotal. The projects in this work concerning the CO_2RR focus emphasize the role of undercoordinated Cu atoms as active sites, the role of bimetallic Cu-Au catalysts and the role of potential pulses on the selectivity.

3

The Formic Acid Oxidation Reaction (FAOR)

A fuel cell (FC) is a power generating device with low carbon emission that is defined by high thermodynamic efficiency, versatility and modularity. In near future, FCs may play a key technology for stationary and portable electronic devices. Proton exchange membrane fuel cells, fed with molecular hydrogen, serve as a benchmark for the FC technology with high power density, a reasonable weight-to-power ratio and low operating temperature. However, the low volumetric energy density of hydrogen leads to storage problems. Thus, formic acid (FA) forms an attractive alternative as it is not flammable and can be stored and transported as salt or dissolved in water. Moreover, FA is a hydrogen carrier with higher volumetric energy density than molecular H_2. The theoretical cell voltage is higher for FA (1.45 V vs. standard hydrogen Electrode (SHE)) compared to H_2 (1.23 V) or even methanol (1.23 V) or ethanol (1.14 V), resulting in high theoretical power density. Moreover, ionized FA has a low crossover through the membrane in the FC and thus high concentrations of FA can be used, which compensates for its low volumetric energy density.[114]

The overall reaction for FAOR in Direct Formic Acid Fuel Cells (DFAFCs) is described by the equations 3.1, where FA is used as fuel in the anode and O_2/air at the cathode.

$$\begin{array}{lrll} \text{anodic:} & \mathrm{HCOOH} \rightarrow \mathrm{CO_2} + 2\mathrm{H^+} + 2\mathrm{e^-} & \mathrm{E^0} & = -0.25\,\mathrm{V\ vs.\ SHE} \\ \text{cathodic:} & {}^1\!/_2\mathrm{O_2} + 2\mathrm{H^+} + 2\mathrm{e^-} \rightarrow \mathrm{H_2O} & \mathrm{E^0} & = 1.23\,\mathrm{V\ vs.\ SHE} \\ \hline \text{overall:} & \mathrm{HCOOH} + {}^1\!/_2\mathrm{O_2} \rightarrow \mathrm{CO_2} + \mathrm{H_2O} & \mathrm{E^0} & = 1.48\,\mathrm{V\ vs.\ SHE} \end{array} \tag{3.1}$$

At the anode, HCOOH gets oxidized to CO_2, generating $2e^-$ and $2H^+$. The latter ones cross through the membrane and reduce oxygen to water in the Oxygen Reduction Reaction (ORR). Typical ORR catalysts are Pt- or Pd-based.

However, the reaction suffers from severe deactivation originating from the production of poisoning species such as CO_{ads} at the catalyst's surface during FAOR. Moreover, although the FA is considered

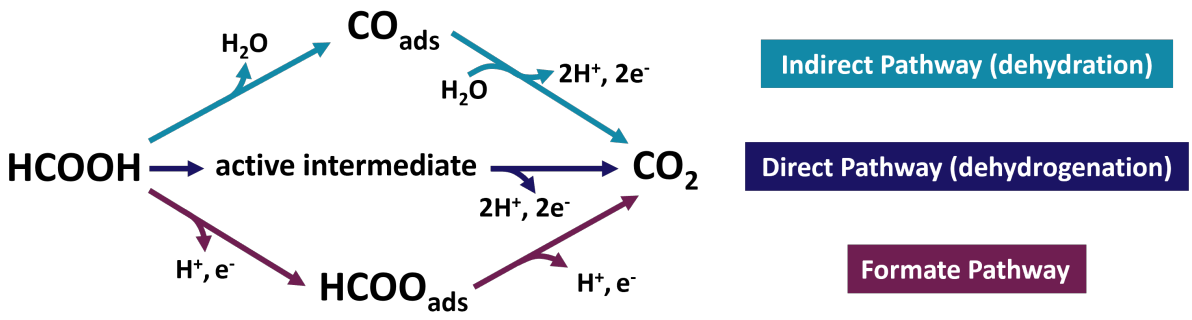

Figure 3.1: Proposed Mechanisms of the Electrocatalytic Oxidation of Formic Acid.

as small organic molecule, the oxidation process is more complicated than Hydrogen Oxidation Reaction (HOR) and not entirely understood. Thus, it is imperative to understand the reaction mechanism and to control the catalyst's surface to impede deactivation. With this, it could be possible to design catalysts rationally in order to achieve high activities with good durability and stability. Further, FAOR is considered as model reaction for other small organic molecules and mechanistic understanding may be transferred to other oxidation reactions, e.g. methanol oxidation.

3.1 Reaction Mechanism of FAOR

In the following section a brief overview of the current status of the mechanistic knowledge is presented. Please refer to the literature for deeper insight.[114–118] Note that the actual mechanism and the reactive intermediates are still under debate and are still investigated with improved *operando* techniques.[119] The commonly employed reaction pathways are described in Figure 3.1.

Since 1973, a dual-pathway mechanism is proposed containing a direct pathway, where HCOOH is oxidized by an active intermediate via dehydrogenation. Possible active intermediates are $COOH_{ads}$ or CHO_{ads}.[120] In the indirect pathway, poisonous species are produced via dehydration.[120,121] The poisonous species was later identified to be CO_{ads}[122] and can be further oxidized to CO_2 by the Langmuir-Hinshelwood mechanism.[123] A third pathway, the formate pathway, was proposed with bidentate $HCOO_{ads}$ as active intermediate species.[124,125] However, it was also suggested that bidentate adsorbed $HCOO_{b,\ ads}$ is a site-blocking spectator site,[126] and/or forms a neighboring site for monodentate adsorbed $HCOO^*_m$ and facilitates its further oxidation.[127]

Commonly, Pt- or Pd-based materials are used as catalysts for FAOR because they combine optimal conditions for both dehydrogenation steps to oxidize FA to CO_2. Other metals enable only one dehydrogenation step, while they hamper the other one. For example, the first dehydrogenation step is facilitated on under-coordinated sites (e.g. on Ru, Re, Os), while highly coordinated sites (e.g. Cu, Ag, Au) facilitate the second dehydrogenation step to CO_2.[115] The major difference of Pt and Pd

as catalysts is the abilitiy of Pd to regenerate itself by releasing the poisoning species CO_{ads}. On the other hand, Pt shows higher catalytic activities than Pd.[128]

Poisoning intermediates can be removed by catalysts with high CO oxidation activity. For Pt, it is proposed that adjacent Pt atoms are responsible for the CO_{ads} formation and thus, single Pt sites might eliminate poisoning.[129,130] For Pd, the catalyst deactivation through poisoning is mainly attributed to particle agglomeration, oxidation state changes or other CO-like toxic species. Additionally, CO may be produced by reduction of the produced CO_2 at low oxidation potentials.[116,131,132] General mitigation strategies for the deactivation are the introduction of oxyphilic active sites that facilitate CO oxidation or the elimination of certain surface sites that lead to CO_{ads}.

3.2 Synthesis of Electrocatalysts by Rational Design

Rational design of catalysts is key for establishing catalysts with optimal activity, stability and thus a high tolerance to deactivation. The optimal catalyst exhibits optimal activity and stability, but at the same time requires low material costs, high electrical conductivity and a good physical and electrochemical stability without agglomeration. By the choice of the surface structure and composition, e.g. by adding secondary metals, several effects can be distinguished. Due to the high structure sensitivity of this reaction, facet-, shape- and size effects are of outermost importance. But also by adding additional ligands or metals, several effects like bifunctional mechanism, ligand-, ensemble-, third-body-, electronic- or synergistic effects can be studied. This also involves the regulation of the electronic and surface structure by defining the atom arrangement and chemical structure. The effects that are of relevance for this thesis, are discussed in the following sections.

3.3 Monometallic Catalysts: Facet, Shape and Size Effects

The structure sensitivity of FAOR has been well studied on single crystals of Pd and Pt, since it has been found that the binding energy of FA and adsorbed intermediates depend on the surface atomic structure for these elements. The catalytic activity follows the order Pd(100) $>$ Pd(111) $>$ Pd(110), with Pd(100), showing four times higher catalytic activity than Pd(110).[133] The high catalytic performance of the (100) facets has been explained through its ability to stabilize two types of bridge formate species on its surface.[134] The translation of these facet planes to nanoparticles for fcc-structured materials is the same as explained for Cu materials in chapter 2. Shaped Pd NPs have been shown to exhibit a similar behavior compared to the single crystal work, with nanocubic nanoparticles displaying the highest catalytic activity compared to the other shapes.[135]

The size of a shaped catalyst influences the catalytic activity due to the ratio between edges and corners with low coordinated atoms and the facets with high coordination numbers, possibly affecting

the reaction- and poisoning mechanisms. Thus, the proportions of different surface atom types change with particle size[136] and therefore the catalytic activity.[134] Moreover, a high surface-to-volume ratio is favored for electrochemical reactions due to the increased surface area. However, contrary to the CO_2RR, it has been suggested that size factors are less relevant to the FAOR than the structure sensitivity of the planar facets on nanoparticles.[116]

3.4 Bimetallic Catalysts

Bimetallic catalysts combining Pd or Pt with a secondary metal have been widely employed in order to improve the catalytic activity and to mitigate deactivation through poisoning. In this regard, possible effects of bimetallic catalysts for FA can be defined in the following categories:

- **Blockage of CO adsorption sites**
  - **Geometric Effect:** The secondary metal sits on specific sites on the catalytically active material and blocks certain other facets. Thus, only the appropriate facets for adsorption of active intermediates are exposed and allows adsorption of reactants in particular orientations.[137]
  - **Third Body Effect:** The secondary metals block CO_{ads} sites and thus inhibit the possible adsorption of CO. In addition, a steric effect might facilitate the adsorption of active intermediates.[138,139]
- **Electronic Effect:** The electronic structure on the catalyst' surface and thus the binding strength of adsorbed molecules can be modified through alloying. Thus, by adjusting the d-band center of the active catalyst, the binding of the educt can be optimized.[140] Two subforms are the ligand- and the strain effects.[130]
  - **Ligand Effect:** Partial charge transfer of the two metals due to their difference in electronegativity leads to a change in the d-band center.[141,142]
  - **Strain Effect:** A metal overlayer over an alloyed NP core shifts the d-band center of the metal overlayer towards the due to lattice mismatch.[141]
  - **Ensemble Effect:** The composition of the local atomic structure around the active sites may alter the catalytic activity.[141,143]
- **Bifunctional Mechanism / Synergistic Effect:** The secondary metal acts as a cocatalyst and participates actively as an independent catalyst. For example, the second metal may provide oxygen containing species that performs water dissociation at lower overpotentials for CO removal.[144]

It should be noted that these effects overlap in their functions and are seldom studied independently of the others. Thus, the described effects are usually present in combined forms and the secondary metal can act through two or more effects.

3.5 Conclusion

The electrocatalytic FAOR has attracted great attention to be used in DFAFC. This reaction is very sensitive to surface material and structure and many effects have already been explored to identify the role of the material composition on the activity. These known structure-activity relationships can be utilized to prepare new catalysts by rational design and thus further understand the relevant parameters. As the goals are high catalytic activities and good stabilities, the optimal morphology and structural architecture can be chosen accordingly. Since bimetallic catalysts show higher catalytic activites, one has to evaluate if an alloyed structure or a discrete structure is prefered. Alloyed structures may be obtained in an ordered or an unordered form. In a discrete structure, a secondary metal ideally functions as a cocatalyst in order not to destroy the structure sensitivity of the main catalyst.

The design of novel electrocatalysts towards high-performance catalysts is essential to bridge research towards the realization of commercialization of DFAFCs, which also includes safety, activity, durability and low material cost.

4

Scientific Objective

This work addresses some of the main challenges for the CO_2RR and the FAOR. The low selectivities towards high-valuable products of the CO_2RR as well as the low performance of the FAOR due to catalyst deactivation are studied and promising options for improvements are investigated. In particular, catalyst structures and shapes, bimetallic catalysts and the manipulation of the applied potential for selected electrocatalytic reactions are explored. The main scientific questions for this work are:

A What is the role of under-coordinated Cu atoms in the CO_2RR?

B What is the role of oxide species on the selectivity in the CO_2RR?

C How do shaped NPs, combined with a secondary metal, improve catalysis, specifically the CO_2RR and the FAOR?

D How do shaped, bimetallic catalysts behave during an oxidation reaction compared to a reduction reaction?

These objectives involve several different catalysts, characterization methods under reaction conditions and different electrocatalytic reactions. In particular, the following tasks are inevitable for a full scientific approach of the above mentioned objectives:

1. **Synthesis and Characterization:** Initially, nanoparticle catalysts for the objectives **B**, **C** and **D** are synthesized and characterized with X-ray Diffraction (XRD), Transmission Electron Microscopy (TEM), Scanning Electron Microscopy (SEM), X-ray Photoelectron Spectroscopy (XPS) and Inductively Coupled Plasma - Mass Spectrometry (ICP-MS) in order to get a full picture on the shape, composition, chemical structure and its concentration. A single crystal that is used to answer objective **A**, was sputtered and annealed several times and its surface structure characterized with Low-Energy Electron Diffraction (LEED) and XPS.

2. **Electrocatalytic Characterization:** In the next step, the catalysts were studied and analyzed

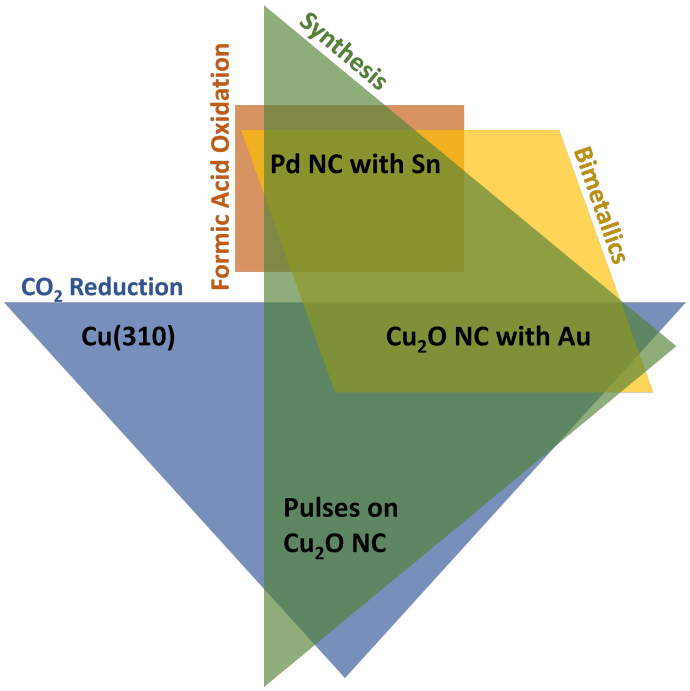

Figure 4.1: Projects categorized in catalyst structure and electrocatalytic reaction.

for the electrocatalytic reactions and conditions of interest. The electrocatalytic characterization involves the analysis of the current transients under applied potential, the product selectivity and electrochemical surface area determination.

3. **Spectroscopic Analysis under Reaction Conditions:** Afterwards, the catalytic conditions of interest were studied spectroscopically under reaction conditions with the goal to gain insights into the dynamic behavior of the nanosized electrocatalysts under operation and unveil structure-activity or structure-selectivity relationships. These correlations provide thorough understanding on the role of the chemical state of the catalyst in its activity, the effect of the secondary metal or the role of the catalytic active sites.

These scientific questions are answered in four projects, which are summarized and categorized in Figure 4.1. Each of the four projects is linked with at least two other projects in terms of catalyst structure and reaction. Below, it is further discussed how these projects address the above mentioned aspects:

Objective **A** addresses the role of under-coordinated Cu atoms under CO_2RR. This fundamental work is conceptualized with a well defined Cu(310) single crystal consisting of periodically appearing atomic steps partitioning well-defined atomic terraces. Because of the well-defined surface structure of the crystal and the high affinity to impurities, structure-selectivity relationships are investigated by characterizing the surface before and after the catalytic reaction under UHV conditions.

Objective **B**, which is dedicated to the role of oxide species on the selectivity, was approached by periodically generating oxides during CO_2RR conditions using potential pulses. Cu_2O NCs that have been pre-reduced, are used as state of the art catalyst. By repeated pulsing between CO_2RR conditions and copper oxide-generating potentials, oxides are created on the catalyst surface and correlated to the changes in selectivity. Furthermore, by changing the potential pulse lengths, the amount of oxide on the surface is controlled and further analyzed with *in situ* and *operando* time-resolved spectroscopic and diffraction methods. It was found that small amounts of oxides nearly double the ethanol production compared to static potentials.

To address objectives **C** and **D** on how shaped and bimetallic catalysts can improve the catalysis, two sets of nanocubic catalysts decorated with a secondary metal were synthesized and characterized in order to study the role of the secondary metal on shaped nanoparticles for two different reactions. Secondly, Cu_2O NCs decorated with Au were used to investigate the role of CO-producing Au on the selectivity of the Cu_2O nanocubes under CO_2RR. Thus, a correlating effect of the produced CO, the alloying between Cu an Au and the selectivity was detected. Both systems were investigated under their respective reaction conditions with several *operando* and *in situ* spectroscopic methods to understand their structure-activity relationships.

In summary, all four objectives require correlations of the catalyst structure and its activity, for which the incorporation of different techniques are required. *Operando* and *in situ* methods are key to investigate the working catalysts regardless of the type of the electrocatalytic reaction. When well defined catalytic systems such as single crystals, are used, a more simplistic approach of correlating the surface structure before and after reaction with its selectivities can be performed.

5

Methods and Instrumentation

This chapter concerns the methods and instrumentation that are used for the scientific studies throughout this thesis. A short description about synthesis procedures is followed by the instrumentation and methods used in electrocatalysis. Then, a description of the methods used in Ultra high Vacuum (UHV) follows with a short depiction of Scanning Tunneling Microscopy (STM), Low-Energy Electron Diffraction (LEED) and X-ray Photoelectron Spectroscopy (XPS) techniques. X-ray Absorption Spectroscopy (XAS) and Fourier-transformed Infrared Spectroscopy (FTIR) techniques complete the *operando* methods section before a very short depiction of other used techniques is compiled in the end.

5.1 Synthesis of Shaped Nanoparticles

Nanocatalysts with particles of uniform size and shape are of special interest for the use in catalysis, as their exposed surfaces can determine the catalytic activity. Their high surface-to-volume ratio leads to low material consumption and allows specific *operando* studies using sample-averaging methods. Among the "bottom-up" chemical synthesis methods, surfactant-free methods as well as the use of capping agents control the growth direction and dimension. Hard templating methods on the other hand confine the size and shape of the particles physically. The former method works with common surfactants such as hexadecyltrimethylammonium bromide (CTAB) or anions such as Br, I or CN^-.[145] These allow the capping of the initial nuclei through strong adsorption on specific sites, thus letting a crystal grow in selected directions.

CTAB is a cationic surfactant with a quaternary ammonium head group and a C_{16} alkyl tail. It forms a bilayer of surfactant on metal nanoparticles (typically Au, Ag and Pd).[147] On Pd, it preferably binds on (100) facets and thus assists in the formation of cubic shapes.[148] The main challenge by using this type of capping agents are their complete removal after the synthesis without destroying the well-defined morphology, which is critical for catalysis. It is suggested that residues of CTAB would block active sites for catalytic measurements.[149] In this work, a previously reported method[150] was

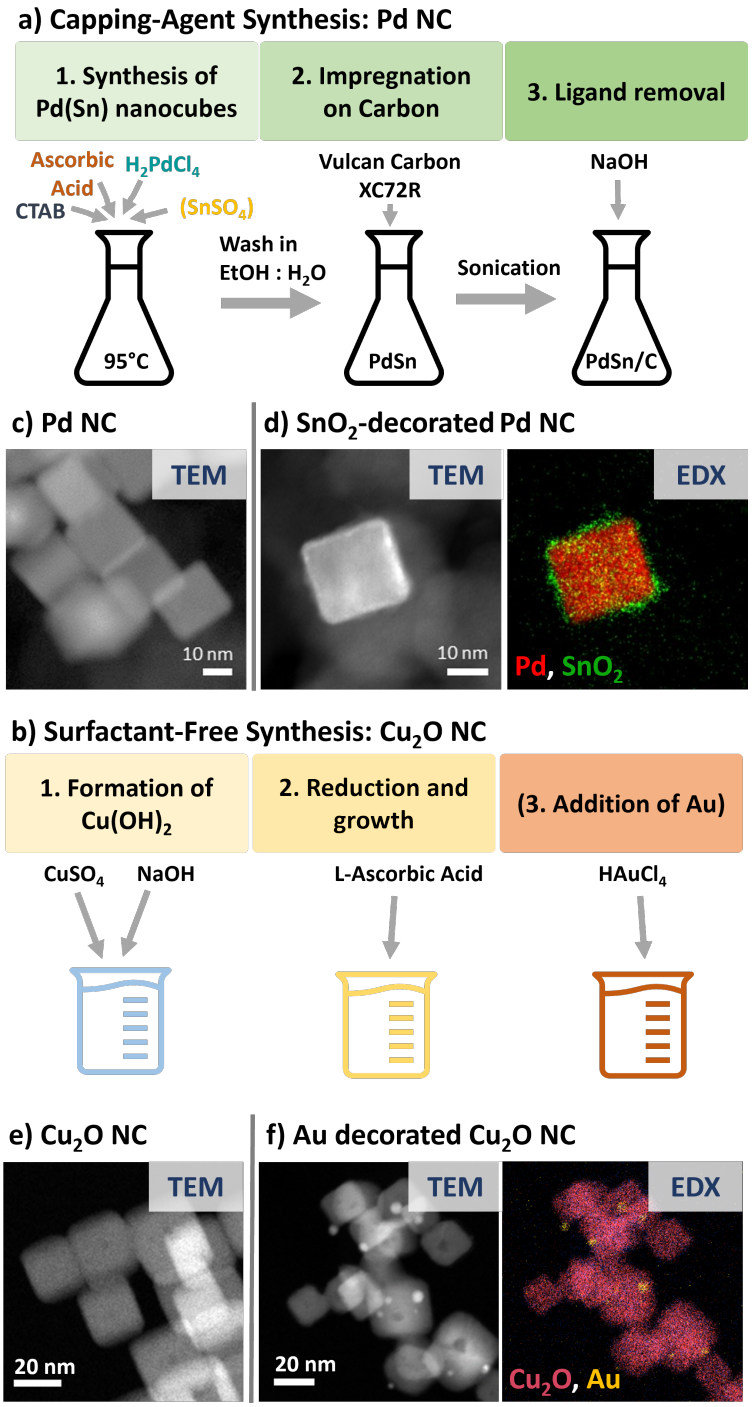

Figure 5.1: Schemes of the synthesis procedures for a) Pd NCs (with Sn) and b) Cu_2O NCs (with Au NPs). The TEM images and corresponding Energy Dispersive X-ray Spectroscopy (EDX) mapping show c) Pd NCs and d) SnO_2-decorated Pd NCs as well as the e) Cu_2O NCs and f) Au decorated Cu_2O NCs. Microscopy data are taken from [146] and chapter 8.

adapted to prepare the Pd NCs via a hydrothermal synthesis route, which is illustrated in Figure 5.1a. First, the Pd Salt H_2PdCl_4 was added to a solution with ascorbic acid and CTAB. The cubic Pd crystals grow by reducing the Pd salt with ascorbic acid and by shaping them with the cationic surfactant at 95°C.

Bimetallic catalysts were achieved by adding SnO_2 right before the end of the synthesis to ensure a shell-like formation around the Pd NCs. The pure Pd NC and the shell-like SnO_2@Pd NC were then centrifuged and washed with an ethanol:water mixture and stored in water. The catalysts were dispersed on a carbon powder support (Vulcan Carbon XC72R) to ensure the separation of each nanocrystal and to avoid agglomeration. Afterwards, the CTAB was washed off by an alkaline treatment. Particularly, the catalyst was stored in 0.25M NaOH media until precipitation and then washed with water. The catalysts were stored as powder. Examples of the resulting Pd NCs and SnO_2-decorated Pd NCs are shown as TEM images and EDX mappings in Figure 5.1c and d.

In contrast to the Pd NC, where CTAB is used as capping agent, the Cu_2O NCs were prepared by a surfactant-free wet chemical method. The particle size is tuned by the amount of inserted NaOH. After its addition to the $CuSO_4$ solution, a blue $Cu(OH)_2$ precipitate is formed.[151] The reduction is performed with ascorbic acid inducing the initial crystallization, where the growth of the crystallites can be followed by their colors from light yellow to orange in the solution. The length of the cube edges can be adjusted by increasing the volume of the NaOH solution.[151] The addition of $HAuCl_4$ at the end of the Cu_2O NCs synthesis leads to the formation of small Au NPs directly attached to the Cu_2O NCs. The catalysts were centrifuged and washed with a ethanol:water mixture and stored in ethanol or as a powder. The synthesis is illustrated in Figure 5.1b and examples of the resulting Cu_2O NCs and Au-decorated Cu_2O NCs are shown as TEM images and EDX mappings in Figure 5.1e and f.

5.2 Electrocatalysis

Electrocatalysts are a subcategory of chemical catalysts which accelerate electrochemical processes by assisting in the electron transfer from the electrode to the reactant and thus by facilitating the chemical transformation process. Specifically, electrocatalysts may permit certain redox reactions, increase the stability or lower the overpotential for certain reactions. Electrocatalytic reactions are generally performed in an electrochemical cell with a three-electrode setup. This section illustrates a few important parameters to be considered for electrocatalytic experiments, including cell design, electrochemical methods, Ohmic Drop evaluation and the analysis of the Electrochemical Surface Area (ECSA).

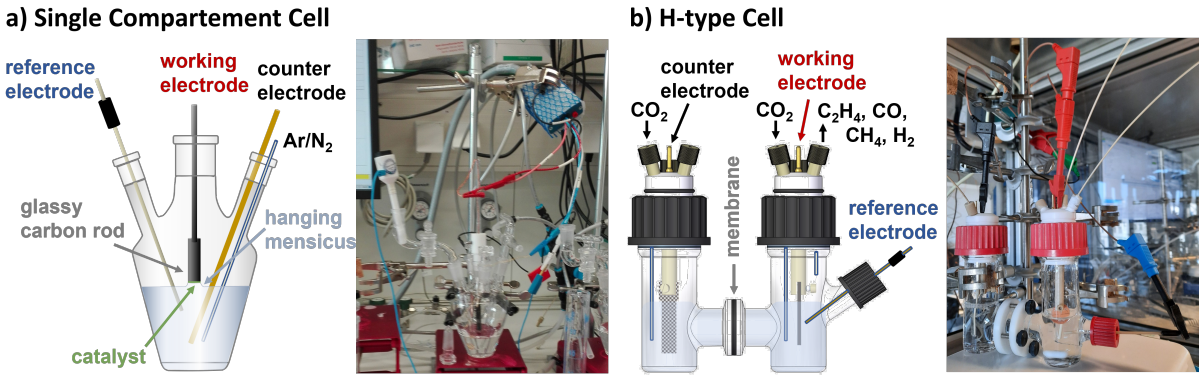

Figure 5.2: Schemes and images of a) a typical single compartment cell used for Formic Acid Oxidation Reaction (FAOR) and for electrochemical characterization and of b) an H-type cell used for the electrocatalytic CO_2 reduction reaction. Both cells include a WE, a CE and a reference electrode. However, in the H-type Cell, the compartement with the CE is separated from the comparement with other two electrodes by an ion-selective membrane.

5.2.1 Cell Designs

The design of the electrochemical cell is important as it can potentially affect the electrochemical reaction e.g. through contaminants or insufficient reaction performance. Material, shape and type of the cell and the electrodes may influence the reaction significantly. A proper design is therefore essential and each reaction requires different specifications. The single- as well as the H-type compartment cells used for the electrochemical and electrocatalytic measurements are illustrated in Figure 5.2.

The single compartment cell in Figure 5.2a contains the WE, the CE and the reference electrode in one compartment and are used for electrochemical characterization methods such as CV, characterizing the oxidation state potentials of the CO_2RR or the oxidative behavior of the formic acid during the FAOR. The single compartment cells were equipped with several inlets, as shown in Figure 5.2a. As WE, a glassy carbon rod was used for the FAOR on which the catalyst material was deposited and introduced into the cell. The CE, an Au wire, and the reference electrode (RE), a 3 M Ag/AgCl reference electrode, were immersed into the electrolyte. A gas flow system (not shown in the scheme) enabled Ar/N_2 bubbling for saturation and flow over instead of into the electrolyte during a measurement. This cell was also used for electrochemical characterization in CO_2RR. In this case, the electrodes, electrolyte and gas inlets were chosen accordingly.

To study the electrocatalysis of the CO_2RR, a gas-tight cell with two compartments is required. Figure 5.2b shows a scheme and an image of the H-type cell. This cell design was adapted from early water splitting experiments with a "Hofmann voltameter", which avoids the mixing of gaseous products.[152] For the CO_2RR, this design is typically optimized with product detection capabilities and a semipermeable membrane (Selemion, AMV, AGC Inc.) at the middle part of the cell prohibiting

poisoning ions to pass towards the investigated electrode. These membrane types usually consist of an aliphatic or aromatic polymer backbone with positive charged groups e.g. imidazolium or tertiary amines, allow crossing of the anions in the electrolyte, e.g. CO_3^{2-} and OH^- and inhibit cation crossing. The cathode compartment comprises the WE and the reference electrode, while an inlet allows CO_2 bubbling and an outlet leads the excess CO_2 and the gas products to the Gas Chromatograph (GC). The anode compartment contains a Pt gauze (MaTecK, 3600 mesh cm^{-2}) and an inlet for CO_2 bubbling. The outlet is open, as the produced oxygen is harmless. The used electrolyte was 0.1 M $KHCO_3$, purified with a cation exchange resin (Chelex 100 Resin, Bio-Rad)[153] and presaturated with CO_2.

The choice and position of the electrodes in the cell influences the performance of the reactions because it influences the Ohmic resistance through the electrolyte. The counter electrode's surface area has to be large enough to ensure a good reaction performance on the investigated WE. Certain working electrodes, e.g. single crystals, require shielding of the edges, corners and sides of the crystal. Used electrode configurations for single crystals are therefore the hanging meniscus configuration or shielding the crystal with an inert material. Nanoparticles can be immersed into the electrolyte, when they are supported on a conductive material, e.g. carbon paper, vulcan carbon powder or glassy carbon.

Different reference electrodes can be used to control the absolute potential at the working electrode.[154] In this work, two commercial reference electrodes, the reversible hydrogen electrode (RHE) (HydroFlex, Gaskatel) and the Ag/AgCl electrode (LF-1, Innovative Instruments Inc., 3.4 M KCl), were used. The RE should be placed at an optimal distance from the WE to minimize the electrolyte-induced resistance between the RE and the WE, while a distortion of the electric field formed in the vicinity of the WE should be avoided.

Electrochemical cells were also used to perform *in situ* and *operando* methods, while each spectroscopic method requires a certain type of access to the working electrode for proper investigation of the catalyst changes. Precisely, with the standard H-type cell, the incoming radiation would have to go through the electrolyte before it reaches the catalyst. However, in most of these analytic methods, the signal is damped through the electrolyte. This issue can be avoided by redesigning the cells. Spectroscopic measurements can be performed i) through a very thin electrolyte layer or ii) from the backside of the electrode (ideally with a non-absorbing support). Additionally, some methods require UHV conditions, which is incompatible with liquids and thus with electrochemical measurements. The used cells for the specific *in situ* and *operando* methods, such as XPS, X-ray Absorption Fine Structure (XAFS) or Fourier-transformed Infrared Reflection Absorption Spectroscopy (FT-IRRAS) are discussed in the respective Methods and Instrumentation sections.

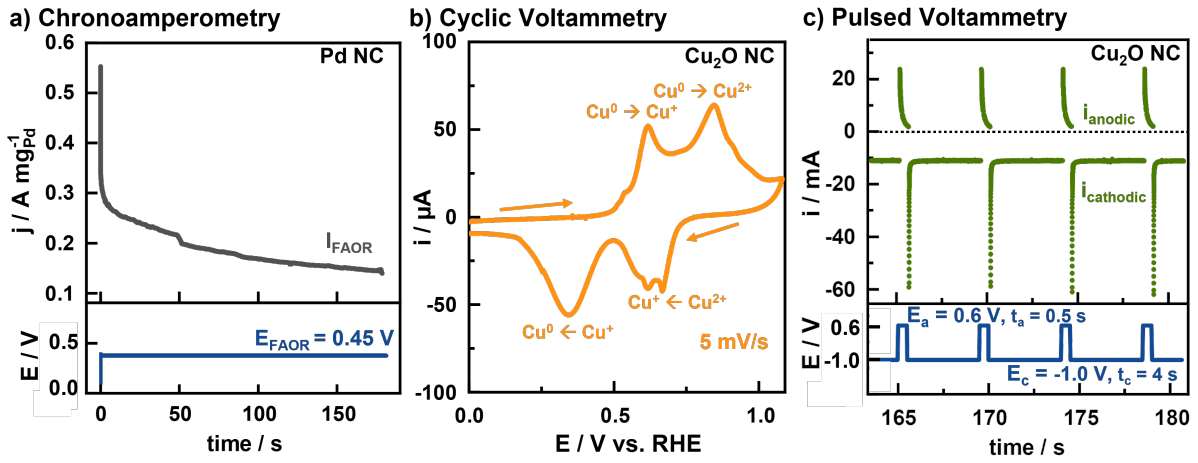

Figure 5.3: Electrochemical methods showing typical current responses on the respective applied potentials: a) Chronoamperometry of Pd NCs at 0.45 V vs. RHE for the FAOR in 0.1 M $HClO_4$ and 0.5 M HCOOH, adapted from [146]. The current decrease over time is attributed to deactivation. b) Cyclic Voltammetry (CV) of Cu_2O NC from −0.1 V to 1.08 V vs. RHE at 5 mV/s in Ar-saturated 0.1 M $KHCO_3$ and c) Pulsed Voltammetry of Cu_2O NCs pulsing between $E_a = 0.6$ V and $E_c = -1.0$ V with $t_a = 0.5$ s and $t_c = 4$ s in CO_2 saturated 0.1 M $KHCO_3$. The resulting currents go back in direction of a steady state current quickly after the application of a potential pulse. The main effects driving the currents are the CO_2RR at negative potentials and the catalyst oxidation at positive potentials.

5.2.2 Electrochemical Methods

Several electrochemical techniques were applied during this work. The most important ones are presented in the following section, showing the similarities and differences of the chronoamperometry, the Cyclic Voltammetry (CV) and the pulsed voltammetry. Further sections are dedicated to the Ohmic Drop evaluation and the determination of the Electrochemical Surface Area (ECSA).

Chronoamperometry

In this technique, the current response is measured as a function of a constantly applied potential. An example is depicted in Figure 5.3a showing the current transient of Pd NCs at an applied potential of 0.45 V vs. RHE in 0.1 M $HClO_4$ and 0.5 M HCOOH. Considering a chronoamperometry with a potential step from OCP to E_{FAOR} with diffusion limitation of the reactant towards the electrode, a superposition of two types of currents build up the total current transient i_{total}:

$$i_{total} = i_C + i_F. \tag{5.1}$$

The capacitive current i_C represents an exponential decay and resembles the charge accumulation due to a change in the polarization of the electrodes. The diffusion controlled Faradaic current i_F

reflects the continuously transferred charge to the reactants and is given by the Cottrell equation[155]

$$i_F = zFAc\sqrt{\frac{D}{\pi t}}, \tag{5.2}$$

with z being the number of the transferred electrons, c the bulk concentration of the reactant, D the diffusion current of the reacting species. F the Faraday constant, t the time and A the area of the electrode.

The equations describe the different parts of the current transient, which can be simplified by separating the first few seconds, where capacitive currents dominate the total current and the rest of the transient is controlled by the Faradaic current. In the shown example, an additional effect takes place, which is considered as the deactivation of the catalyst e.g. due to poisoning species. More detailed explanations of the deactivation mechanism on these type of catalysts can be found in chapter 3 and chapter 9.

Cyclic Voltammetry (CV)

The Cyclic Voltammetry (CV) technique serves to survey the properties of materials such as the characterization of redox potentials, the number of electrons involved, the rate of electron transfer and adsorption effects. Furthermore, catalytic reactions can be explored by analyzing the chemical processes associated with electron transfers.

Here, the current response is measured as a function of a linearly in- or decreasing potential with time.[155] An example of a cyclic voltammogram of Cu_2O NCs in 0.1 M $KHCO_3$ is shown in Figure 5.3b. First, the potential is swept towards more positive potentials (cathodic sweep), where in the shown case, two oxidation events take place. The first peak at 0.6 V is attributed to the oxidation from metallic Cu to Cu^+, while the second at 0.8 V is assigned to further oxidation to Cu^{2+}. The anodic sweep towards more negative potentials shows two peaks towards negative currents indicating electron transfers from i) the oxidized Cu^{2+} state towards Cu^+ and then ii) further reduction to metallic Cu. Additional peaks appear due to the chosen limiting potentials and the initial state of the material. A more detailed description of the CV of Cu_2O NCs can be found in chapter 7.

In this work, both, Chronoamperometry and Cyclic Voltammetry (CV) measurements were used for the FAOR in chapter 9 and for the CO_2RR in chapters 6, 7 and 8.

Pulsed Voltammetry

Pulsed Voltammetry is an electrochemical technique that was applied for CO_2RR to control the reaction and therefore the product selectivity. An example of the applied potential and response

current transients are shown Figure 5.3c. It is based on a periodic application of two sequential chronoamperometric measurements with different potentials $E_{c/a}$ and times $t_{c/a}$. Here, the negative potential refers to the cathodic potential (E_c), where the Faradaic CO_2RR occurs, while the positive potential is referred to the anodic potential (E_a).

Since the catalyst structure and its surroundings are quite sensitive to the applied potential, the responsive system allows adjustments to the reaction environment, such as a switch of the reaction, chemical state, electrode restructuring, roughening, mass transport, interfacial pH control or control of the chemical state.[156–159] Quick changes, for example pulses, can induce a non-equilibrium of all of these parameters and a different interplay between them. In this work, the application of oxidizing (anodic) pulse potentials leads to the oxidation of the catalyst surface as well as its restructuring. The oxidized surface in turn has consequences on the product distribution.

Figure 5.3c shows a square wave potential profile and its current response. Variations can be induced by changing the potentials or the pulse times. In this work (see chapter 7), the E_a and E_c were mainly kept constant, while the pulse times t_c and t_a were varied in order to study pulse time asymmetry.

The current transient of pulsed potentials contains a sequence of chronoamperometries, each including capacitive, Faradaic or non-Faradaic components. The analysis of the obtained current is however more complex compared to a simple chronoamperometry. In the latter one, a stepped potential takes place once, where non-Faradaic contributions to the current are ignored considering a much longer time period with exclusive Faradaic contributions to the current. Periodically repetitive potential steps, however, lead to i) times without Faradaic contribution at the anodic potentials and ii) an increase in the total amount of non-Faradaic contributions. In detail, currents of the total cathodic $i_{cathodic}$ and the total anodic i_{anodic} pulses can be deconvoluted into the following components:

$$\begin{aligned} i_{anodic} &= i_C + i_{ox} + i_{des} \\ i_{cathodic} &= i_C + i_{red} + i_{ads} + i_F. \end{aligned} \tag{5.3}$$

These components are categorized and described in the following:

1. **Capacitive current (i_C):** During a potential step, the ions in the electrochemical double layer reorganize as a response to the change in charge in the catalyst. The equilibration of this process is described by an exponential decay with a characteristic time, the RC time constant (in seconds). The RC time constant is the product of the resistance R and the capacitance C and is the time required to charge the catalyst electrode to $1/e$ of the maximal capacity, which itself is considered as a capacitor. It is furthermore dependent on the catalysts surface area, the applied potential difference and the ionic concentration.

2. **Redox currents ($i_{red/ox}$):** If the potentials of the pulses are chosen to pass an oxidation state of the investigated material, then the current contribution of the respective oxidation/reduction

has to be considered.

3. **Ad/Desorption currents ($i_{ads/des}$):** Intermediates that are bound to the surface during a potential step will eventually desorb and/or react further. Up to now, there is no evidence that this contribution to the current (or to the product selectivity) is significant.

4. **Faradaic currents (i_F):** Faradaic contributions can be deconvoluted by subtracting all non-Faradaic contributions from the total current.

The study in chapter 7 investigated the role of periodically regenerated oxide species on the CO_2RR. Moreover, an overview over the chemical aspects of pulses on the catalyst and its activity is given in chapter 2.

Ohmic Drop Evaluation

The Ohmic drop is an electrical potential difference between the working and the reference electrode caused by an uncompensated Ohmic resistance of transport of ions through the electrolyte. As this leads to a discrepancy between the normal and the actually applied potential,

$$E_{\text{corrected}} = E_{\text{applied}} - iR, \tag{5.4}$$

one must i) minimize R by placing the reference electrode close to the working electrode and to ii) carefully measure the residual R. Typical R values in this work were determined to be 6 Ω for NCs and 100 Ω for the single crystals.

Current-(I-)interrupt and impedance spectroscopy measurements were used to estimate the Ohmic drop before a measurement. To obtain R from the I-interrupt measurement, a potential is applied for a short time and subsequently interrupted. The immediate loss of potential is attributed to the Ohmic drop with

$$R = \frac{E_2 - E_1}{i}. \tag{5.5}$$

Electrochemical Impedance Spectroscopy on the other hand was used before and after each electrocatalytic measurement. An electrochemical system can be described well with the Randles circuit model, where the Ohmic resistance of the electrolyte is set in series to the electrodes, which are simplified described as a capacitor paralleled to a charge-transfer resistor. By applying high frequencies, the contributions of the electrodes can be eliminated and the Ohmic resistance can be read out from the first zero crossing in the Nyquist plot.[155]

Electrochemical Surface Area (ECSA) Estimation

Catalysts are materials with a complex atomic structure, where certain sites are electrochemically active while others are not. The estimation of the amount of active sites that participate in the catalytic reaction is of utmost importance in order to compare the obtained catalytic performance. However, the main challenge is the determination of the actual active sites. A rough evaluation can be done by directly calculating the mass of the catalyst or by using the geometric surface area of the catalyst and/or the support. These basic methods are upgraded with advanced methods, trying to obtain the real ECSA by "counting" the active sites through capacitive or ad- and desorption methods. Thus, aside from the two basic methods, two advanced methods were used during this work to obtain a more realistic ECSA of the catalysts. In particular, the ECSA of Cu was determined by the double layer capacitance C_{DL} method, while the ECSA of Pd was determined by the hydrogen underpotential deposition method and by CO stripping. All methods however comprise advantages and drawbacks.

- **Mass of the Catalyst:** The mass of a catalyst can be determined e.g. by ICP-MS and does technically not evaluate the surface area. The bulk material of the catalyst does not partake in the reaction and this estimation leads to an indespensable overestimation of the active surface area. But, with the high surface-to-volume ratio of nanoparticular catalysts, it can be helpful to normalize nanoparticles with similar sizes.

- **The geometric surface area** A_{geo} refers to the area of the catalyst coating the supporting material. In the case of single crystals, the catalyst is expected to be extremely flat and the active surface area is well defined. However, due to the small amount of active catalytic material, even small amounts of roughened structure can make significant differences in the actual active surface area.[80] In the case of the CO_2RR projects with Cu_2O NCs and Au-decorated Cu_2O NCs, the geometric area of the carbon paper support was used, and thus, the amount of Cu material on the support was determined as loading ($^{mass_{Cu}}/_{A_{geo}}$).[160] It normalizes the amount of catalyst material on the support. The use of A_{geo} on NPs is very fast in its evaluation, but again does not account for the actual electrochemical surface area of the NPs.

- **Double Layer Capacitance** C_{DL}**:** The Electrochemical Surface Area (ECSA) can be determined by the double layer capacitance C_{DL} (µF). The normalization by a specific capacitance of the investigated material C_S (µF cm^{-2}) leads to an estimation of the roughness R of the catalyst compared to the reference material. Thus, R_{ECSA} is described by

$$R_{ECSA} = \frac{C_{DL}}{C_S}. \tag{5.6}$$

  To obtain C_{DL} for Cu catalysts, CVs are measured in a non-Faradaic region such that the only process is capacitive charging of the double layer. The capacitive current i_C is directly

correlated to the capacitance C_{DL} and the scan rate ν (V/s) by

$$C_{DL} = \frac{i_C}{\nu}. \tag{5.7}$$

Thus, by using various scan rates, the slope of the resulting function $i_C(\nu)$ estimates the C_{DL}. This method was used for CO_2RR, where the C_{DL} was usually normalized with C_S of an electropolished Cu foil, which is 27 µF cm^{-2}.[31,161] However, this method gives only a comparison to a reference material.

- **Hydrogen Underpotential Deposition and CO Stripping:** The ECSA of Pd catalysts was determined by hydrogen underpotential deposition and CO stripping.[162] In both methods, the respective adsorbate is adsorbed by applying a specific potential. Hydrogen was adsorbed on the Pd catalysts by applying a potential right above the onset of the HER, which is characteristic for the adsorption of hydrogen on Pd. CO was adsorbed by saturating the electrolyte with CO holding a potential of 0.15 V vs. RHE in 0.1 M $HClO_4$. The desorption peaks can be observed by CVs towards higher potentials. For both methods, the areas of the respective peaks were integrated and normalized by the theoretical charges of $Q_H = 210\,\mu C\,cm^{-2}$ and $Q_{CO} = 420\,\mu C\,cm^{-2}$,[163,164] which account for a one-electron and a two-electron transfer, respectively. These methods consider the active sites that are electrochemically available, but an error of the real active area for the investigated reaction could still exist since these active sites do not need to be the same.

5.2.3 Chromatography

Gas chromatography was utilized to separate the gaseous and liquid products of the CO_2RR and to quantify them. The gas products were determined by taking an aliquot of the produced gaseous products from the gas-tight two-compartment cell every 13 min during the CO_2RR. The liquid products were measured after finishing the reaction in a liquid-gas chromatograph and with High Pressure Liquid Chromatrography (HPLC).

Several components comprise a gas chromatograph: The carrier gas supply provides continuous flow of the mobile phase. In the injector, the sample is introduced into the head of the column by a syringe. The column is a packed, or mostly a capillary column, in which the volatile analytes are separated, and which is surrounded by an oven. The increase in column temperature results in decreased retention times for all analytes and can go up to 350°C. The analysis of the separated gases is performed with a Flame Ionization Detector (FID) or a Thermal Conductivity Detector (TCD) detector.

The separation takes place in a column by distributing the analyte between the mobile phase and the stationary phase and is determined by the adsorption on the solid stationary phase and solution processes in the liquid stationary phase. The series of discontinuous equilibrium steps allows a

multiplicative distribution of the analyte in the mobile and stationary phases. In a small part of the column, an equilibrium between stationary and mobile phases is achieved, which is defined by the distribution constant K

$$K = c_s/c_m, \tag{5.8}$$

with c_s being the concentration of analyte in the solid phase, and c_m being the concentration of analyte in the mobile phase. The portion in the mobile phase is transported to the next segment with a new establishment of an equilibrium. A separation of two analytes is established, when they have different values of K.

Advantages of a FID are the low detection limits, the large dynamic linear range and the suitability for many organic compounds. A hydrogen/air flame is produced which reacts with the carbon-containing analyte through hydrogenation and C-C-bond-splitting to methane. At a higher oxidizing point in the flame, the methane reacts to CO_2. One in a million C atoms will end up in an ion, which can be then detected through a potential difference of several hundred volts between the metal tip at the base of the flame and a collector electrode. The recorded current is in the pA-nA range. The background current is low because of the low efficiency in ion production.

In principle, the TCD is sensing the difference in heat loss of an electrically heated wire between the carrier gas on the one bypass and the carrier gas with the analyte on the second bypass. A filament is heated by an electric current and cooled by the continuous carrier gas. The electrical current is then adjusted to keep the temperature of the filament constant in a thermal equilibrium. The addition of analyte in the carrier gas changes the thermal conductivity and the specific heat of the gas. The efficiency of heat transportation in the gas is therefore different. The following temperature change in the filament changes its resistance, and the current is adjusted. The current change is recorded as the signal. The thermal conductivity between the carrier gas and the analyte should be high enough. The detection limit reaches 1-10 ppm.

In the liquid GC, the injection of liquid into the GC is performed by evaporation of the compounds during injection. The products identified with an FID detector are alcohols and aldehydes.

The High Pressure Liquid Chromatrography (HPLC) is determined by a liquid mobile phase and a significantly higher operational pressures. The interaction of the liquid compounds with the mobile/stationary phase through polarity. Other differences from a GC are the smaller column dimensions, leading to a high resolving power. The here determined products for my studies are carboxylates and n-propanol.

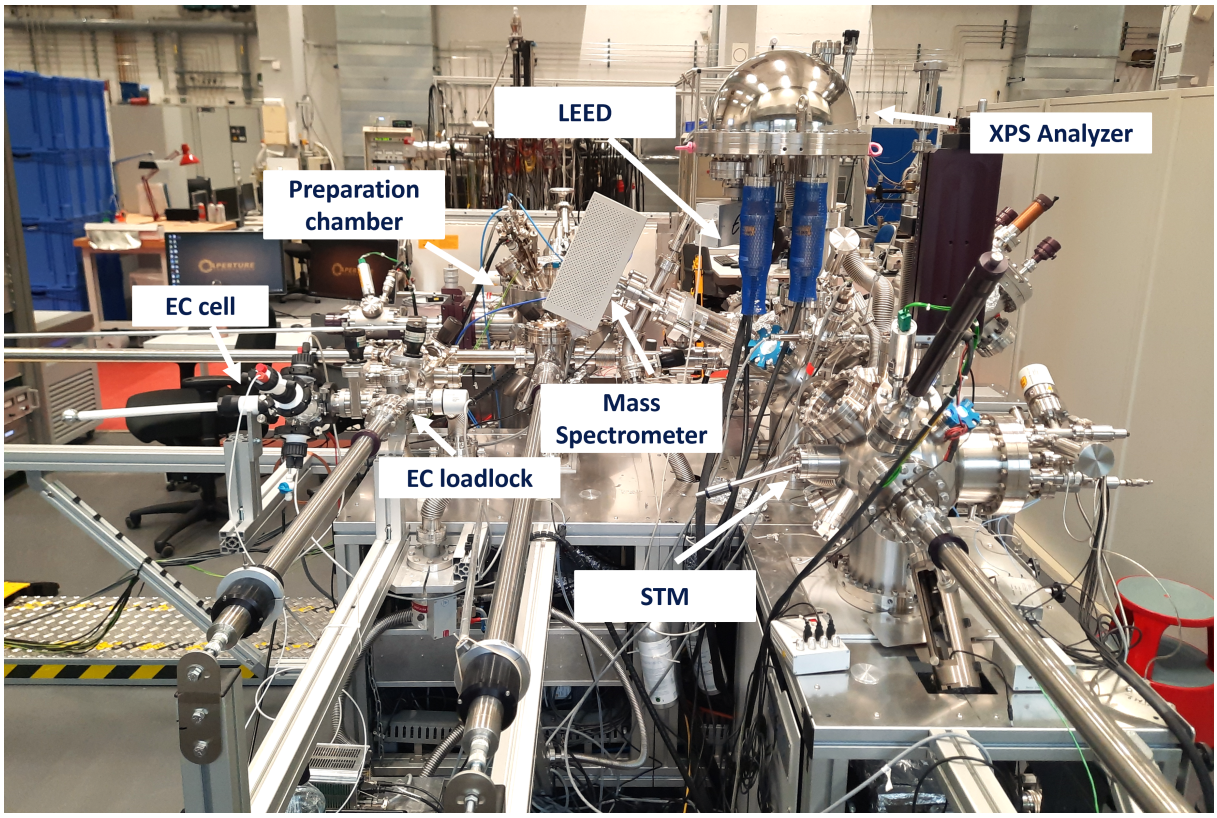

Figure 5.4: Image of the UHV system used during the work of this thesis. This system includes several analytical methods, such as LEED, XPS, TPD and an STM. Additionally it has a preparation chamber to clean single crystal samples by sputtering and annealing. An electrochemistry (EC) cell is attached to the loadlock for sample transfer under controlled ambient conditions.

5.3 Ultra high Vacuum (UHV) Methods

Vacuum is the complete absence of matter and is impossible to achieve experimentally. UHV is defined as pressure regime of 10^{-7}– 1×10^{-12} mbar, where the mean free path of a gas molecule lies between 1 km and 1×10^5 km. This implies that collisions of molecules with the walls of the system are much more frequent than between each other and the remaining gas is in molecular flow. Surface science utilizes UHV systems to study well-defined model samples. However, they are not only used to prepare and mantain clean and well controlled sample surfaces, but are also utilized for the application of surface analytical techniques, such as Scanning Tunneling Microscopy (STM), X-ray Photoelectron Spectroscopy (XPS) or Low-Energy Electron Diffraction (LEED).[165] These will be described in more detail in the next sections. Figure 5.4 shows a typical UHV system that was used during the course of this thesis. It is equipped with different chambers, which are connected by sample transfer rods. The chambers hold different analytic techniques, sample preparation tools or are used as loadlock. The electrochemical cell is attached to a loadlock. To obtain the low pressure, different pumps are used. A scroll pump is a positive displacement pump, where gas is trapped,

isolated and moved, and it reaches pressures down to 1×10^{-1} mbar. Lower pressures are achieved by a turbomolecular pump, where gas molecules are given a momentum to be directed in a certain direction. This kinetic pump reaches down to 1×10^{-9} mbar. Even lower pressures can be obtained by capture pumps, such as ion getter and titanium sublimation pumps. Here, the gas gets immobilized at the surfaces within the system, reaching down to 1×10^{-10} mbar.

5.3.1 Scanning Tunneling Microscopy (STM)

STM is a method to mimic the surface structure by mapping the topography of the electronic states near the Fermi level of a flat surface and is based on the quantum mechanical tunneling effect. A tip approaching a conductive surface will lead to a tunneling current at close proximity, when their electron wave functions overlap. The electron wave functions are non-zero outside of the surface and the tip.[166,167] A bias voltage can be then set between the tip and the surface, which leads to a closed circuit, where the electrons tunnel through the barrier. The current depends exponentially on the barrier width; thus two operation modes with constant current and variable width or constant width and variable current are applicable. A feedback loop controls the distance between the surface and the tip by comparing the actual tunneling current with the applied current. The implementation of the piezoelectric effect allows the tip to be controlled perpendicular to the surface and scan over the surface in x- and y-directions. It allows a resolution of 0.01 nm.[168] This method was used under UHV conditions to understand structure-property relations on Cu single crystal materials by providing micrographs of the surface structure with atomic resolution, e.g. in chapter 6.

5.3.2 Low-Energy Electron Diffraction (LEED)

LEED is a common technique to study crystalline surface structures. Electrons with kinetic energies between 20 eV and 200 eV hit the surface perpendicular and enter about 10 Å deep. Upon their scattering at the atoms, the diffraction follows Bragg's law as illustrated in Figure 5.5a, with λ being the wavelength of the incident beam, d the atomic spacing, θ the angle between λ and the reflected beam and n an integer. Constructive interference implies a path length difference to be an integral multiple of the wavelength:

$$n\lambda = d\sin\theta. \tag{5.9}$$

The elastically back-scattered diffraction from the low-energy electrons on the surface is then directed to a luminsecent screen resulting in highly surface sensitive structural information. Since this technique is thus sensitive to impurities, it is applied under UHV conditions to avoid surface contamination. The advantages of LEED are the simple handling of the measurements and the rapid overview over the diffraction pattern in the reciprocal space and thus the surface quality.[169,170]

By Fourier Transformation of the diffraction pattern, the size, shape and atomic structure of the

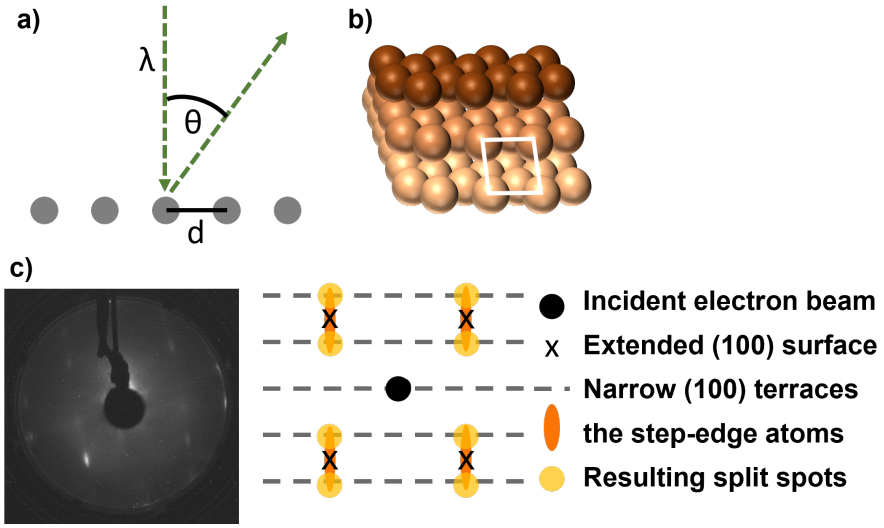

Figure 5.5: a) Illustration of the incident beam with wavelength λ diffracted on the crystallite surface with an angle θ and an atomic distance d. b) Ball model of a Cu(310) stepped single crystal and its primitive unit cell c) a LEED diffraction pattern of a Cu(310) single crystal at 111.7 eV and the construction of the diffraction pattern of a Cu(310) surface, adapted from [171].

unit cell in real space can be extracted from the diffraction pattern in the reciprocal space. It is furthermore possible to obtain information on atomic positions by analyzing spot intensities. The translational symmetry of crystallite structures can be observed in the form of the reciprocal lattice of the unit cell. This implies that information on the extended surface morphology is included in the reciprocal lattice. For instance, point defects result in a decrease in the spot intensity without modifying the spot width. Then again, size and shape of the crystalline islands can be viewed as superposition of a sharp spot and a broad component from the island with finite size. A vicinal stepped surface is made of terraces of the nearest low-index facet separated by regular steps. These terraces are observed as elongated spots in the diffraction pattern due to the finite terrace sites on the surface. The combination of these terraces widths with the periodic repeating atomic results in a superposition of these two components in the reciprocal space and thus in split spots, as shown in Figure 5.5c.[170,172]

The Cu(310) surface is shown here as example for the construction of a LEED pattern on a stepped vicinal surface, shown in Figure 5.5c. This surface comprises (100)-faceted terraces with three atomic rows per terrace, which results in a primitive rectangular unit cell, as shown in Figure 5.5b. Both components can be viewed individually, while the superposition of both results in the final pattern. A single terrace is like an extended (100) surface, illustrated as crosses in Figure 5.5c, which is finite in the direction of the steps and is assumed to be infinite in the parallel direction. The broadened diffraction spots are the effect of the narrow terraces. However, the step-edge atoms construct a row of atoms with identical sites, leading to an one-dimensional periodicity of infinite extend. Its

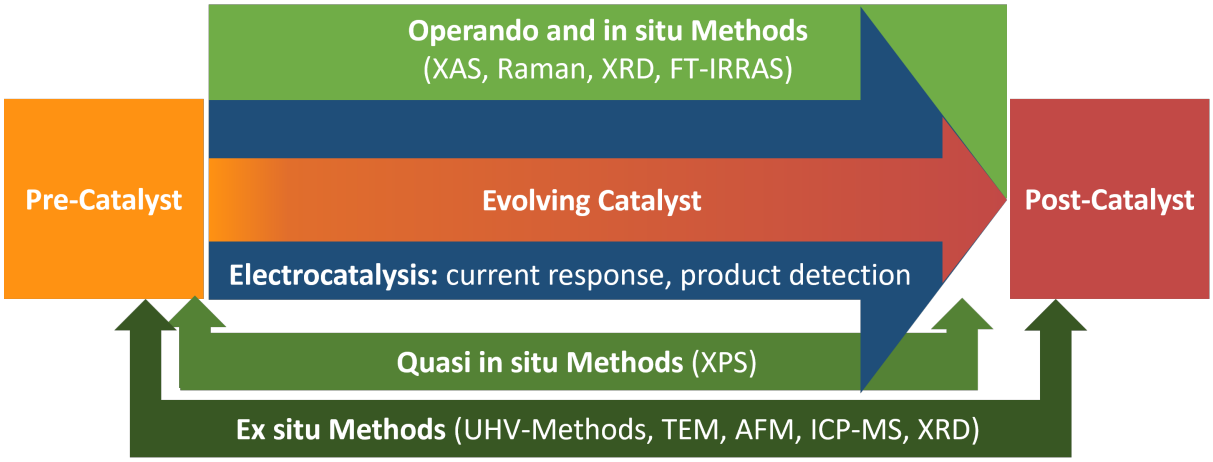

Figure 5.6: Illustration of the evolution of the catalyst from a pre-catalyst, the active catalyst during electrocatalytic reaction and the post-catalyst. *In situ* and *Operando methods* track the catalyst evolution during the reaction, while quasi *in situ* and ex situ methods characterize the catalyst at certain stages in form of a snapshot.

reciprocal pattern is observed as horizontal, perfectly sharp and infinitely long streaks, gray lines in Figure 5.5c. The product of the one-dimensional periodicity of the step-edge atoms and the elongated spots due to the finite terraces lead to split spots, which are directly correlated to the average terrace width.[171,172]

5.4 *In situ* and *Operando* Methods

Tracking the morphology, chemical composition and overall evolution of the catalyst with spectroscopic methods during an electrocatalytic reaction is essential to fundamentally understand the role of the catalyst on the reaction. However, it is very complicated to apply spectroscopic methods during electrocatalytic reaction. Figure 5.6 illustrates the different characterization types, which are described in more detail in the following.

The term *Operando Methods* appeared at first in 2002 under Miguel Bañares and is defined as the utilization of *in situ* spectroscopy during catalytic operation with simultaneous on-line activity measurements.[173] The combination of spectroscopic techniques during activity measurements facilitates the direct link between the catalyst structure and its activity and optimizes time and costs for the scientific output. In practice, this term is softened by assuming the same product formation during product measurements as well as during an *operando* measurement.

The term *in situ* differentiates from *operando* as the catalyst is spectroscopically analyzed under relevant reaction conditions but products are not detected simultaneously. This is justified as the development of electrochemical cells combined with certain spectroscopic techniques, e.g. in UHV,

is tedious and product detection adds an additional difficulty to the system.

A more modest approach is the quasi *in situ* methodology. Here, the catalyst is stabilized in an intermediate reaction state, while spectroscopy is performed *ex situ*. The stabilization implies the isolation of the catalyst from parameters that could modify the catalyst such as oxidation through air or the removal of the applied potential.

The following sections describe methods that were applied as *operando*, *in situ* or quasi *in situ* conditions on the catalysts.

5.4.1 X-ray Photoelectron Spectroscopy (XPS)

X-ray Photoelectron Spectroscopy (XPS) allows the identification of the elemental composition, the chemical state and the electronic structure of the near surface of the investigated material. The technique is surface sensitive with a few nm probing depth of the emitted photoelectrons. The kinetic energy of the emitted photoelectrons results in spectra of electron population as a function of their energy. It is based on the photoelectric effect, which was first discovered by Hertz in 1887 and explained theoretically by Einstein in 1905.[174,175] The photoelectric process is shown in a schematic in Figure 5.7a, describes the emission of photoelectrons from core shells to the vacuum level upon electromagnetic radiation. The incoming energy, X-ray photons $h\nu$, originates from an Al or Mg K_α source with 1486.3 eV and 1253.6 eV, respectively.

The resulting kinetic energy E_k of the photoelectron is determined by $h\nu$, which has overcome its binding energy E_B and the work function ϕ_sample of the material, and which correlates to the minimal required energy to eject an electron. Thus, the parameter of interest, E_B, can be calculated as

$$E_B = h\nu - E_\mathrm{k,spec} - \phi_\mathrm{sample}. \tag{5.10}$$

However, in practice, ϕ_sample and the real E_k is not known. Figure 5.7b shows, how the measured $E_\mathrm{k,spec}$ and the known work function of the spectrometer ϕ_spec compensate the uncertainties.

The formed inner shell core hole can now be filled by relaxation of the electrons. For a certain probability, the Auger effect occurs and the hole is filled with an electron of a higher shell. The excess energy is then taken by an electron of the same shell, which is then released as Auger electron, as shown in Figure 5.7c. Unlike the E_k of the photoelectron, the kinetic energy $E_\mathrm{k,Auger}$ of the emitted Auger electron is independent of the incoming X-ray radiation and its $E_\mathrm{k,Auger}$ is calculated from the energy levels of the respective shells, e.g.

$$E_\mathrm{k,Auger} = E(K) - E(L_2) - E(L_3). \tag{5.11}$$

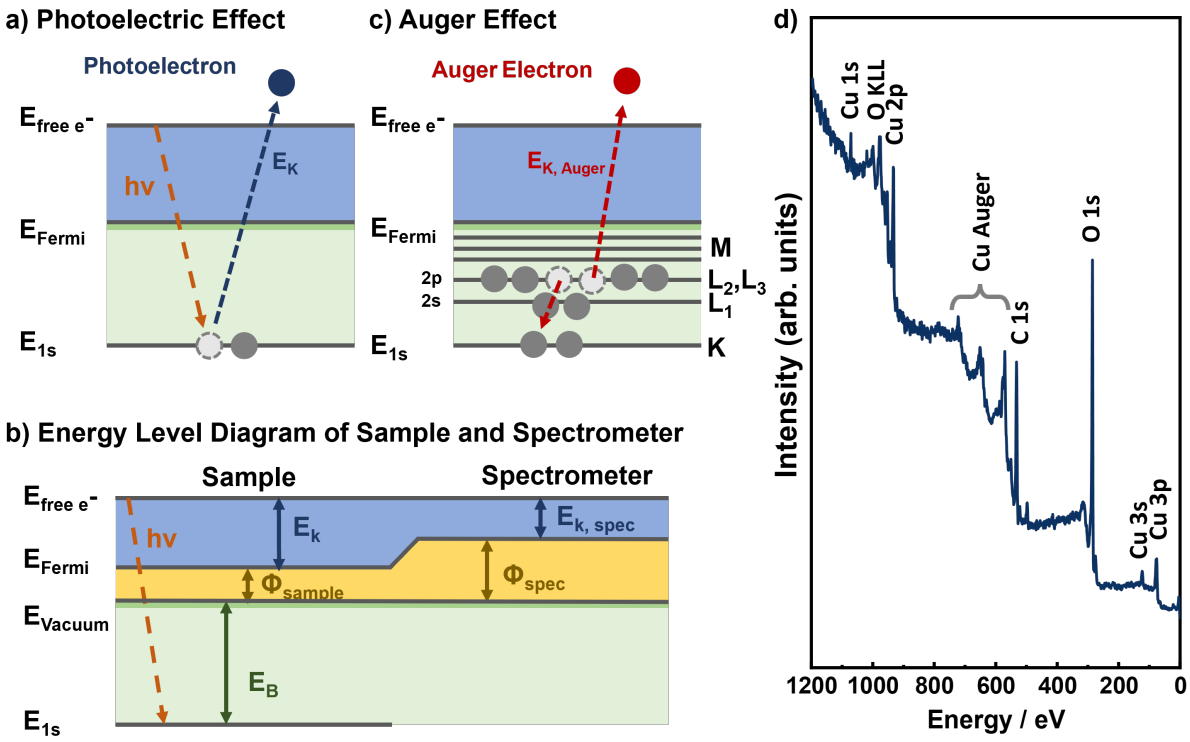

Figure 5.7: Energy level diagrams and schematics of a) the photoelectric effect, b) the Auger effect and c) the shift and compensation of the work functions of the sample and the spectrometer. d) Typical XPS spectrum of Cu_2O NCs showing the XPS and Auger peaks of copper, oxygen and carbon.

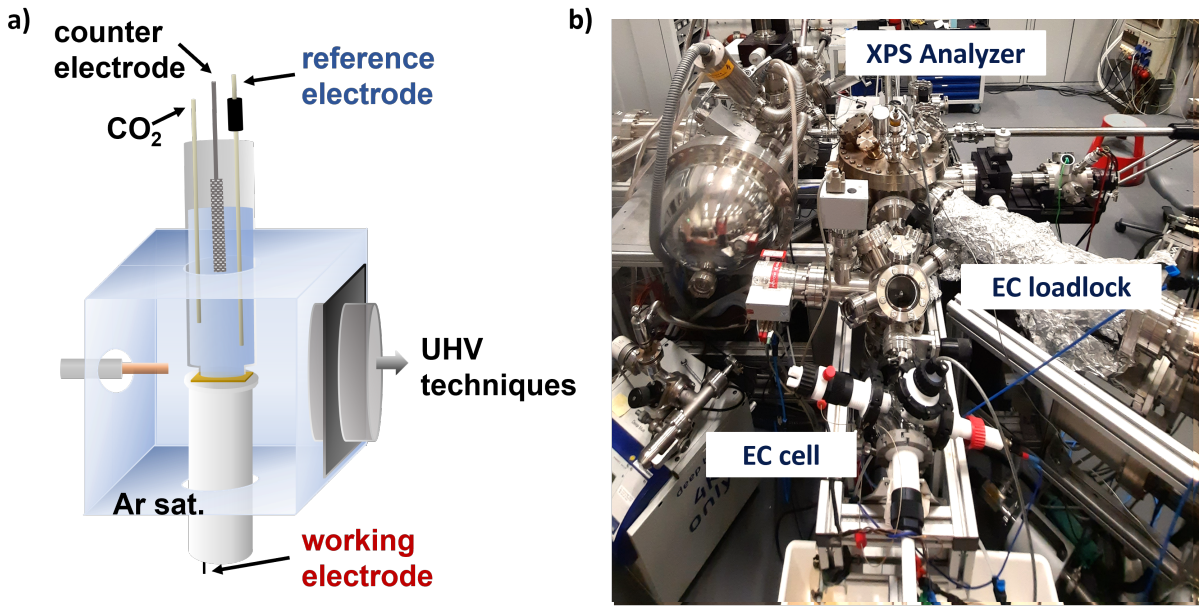

Figure 5.8: a) Scheme of the quasi *in situ* EC cell placed in a vessel, which is filled with Argon. The box is directly attached to the loadlock interconnecting the EC cell with the UHV chamber. b) Image of the used UHV chamber equipped with an XPS system, the EC cell and the loadlock.

A typical XPS spectrum from Cu_2O NCs supported on a carbon paper is shown in Figure 5.7d, presenting the XPS and Auger peaks of copper, oxygen and carbon.

The simultaneous use of an electrochemical cell with XPS is not trivial to realize as the spectroscopic detector has to be under UHV conditions, while the electrochemistry is performed in liquid. A suitable interconnection is therefore to apply quasi *in situ* technology and to set an electrochemical cell directly next to the loadlock of the UHV system. After the electrocatalytic reaction, the cell can be disassembled under Argon atmosphere, the catalyst may be washed with ultrapure H_2O and finally transferred into UHV conditions. This method benefits from the exclosure of air and possible oxidizing agents, which could change the chemical structure of the catalyst. Also, the cell was designed such that the electrochemistry can be performed on a sample holder that fits into the UHV system, which allows a fast sample transfer within seconds. However, this method does not allow to keep the applied potential until the catalyst is under UHV conditions. Thus, the potential loss could already alter the chemical structure. In summary, the quasi *in situ* XPS is a technique that makes XPS compatible with electrochemistry by removing the biggest risk factors that alter the surface structure.

Figure 5.8a shows a scheme of the electrochemical cell in Argon atmosphere, directly connected to the UHV system. The catalyst is placed on a UHV holder and can be transferred directly into the XPS chamber, which is illustrated in Figure 5.8b.

5.4.2 X-ray Absorption Spectroscopy (XAS)

X-ray Absorption Spectroscopy (XAS) enables the analysis of the local atomic and electronic structure of the investigated material. It is a complementary method to XPS to study the chemical composition and distribution of mixed materials and can, in addition, provide information about interatomic bond lengths, the neighboring atoms and sometimes also the types of ligands. XAS is bulk sensitive, however, some special geometries permit the detection of surface species. Moreover, this technique is applicable under true *operando* conditions, where the changes in morphology and structural evolution of a working catalyst can be probed while performing electrocatalysis.[160]

The main principle is the interaction of the incident X-rays with the investigated material leading to material specific absorption and fluorescence. In a classic transmission mode experiment, the transmitted intensity I_T of incident X-rays I_0 is measured as a function of the energy of the X-ray photons and described by the Beer-Lambert law

$$I_T = I_0 e^{-\mu(E)d}, \tag{5.12}$$

which includes the exponential loss of the incoming X-ray intensity I_0 dependent on the linear absorption coefficient $\mu(E)$, the energy E, and the material thickness d.[176] An absorption edge emerges when the photon energy is high enough to excite core electrons of an atom, shown in Figure 5.9a. Here, upon excitation of the core electrons to the unoccupied states of the valence band, information about the electronic structure, the chemical state of the absorbing atom, the local symmetry and the chemical bonding can be extracted from the X-ray Absorption Near Edge Structure (XANES) region.[177]

The XANES region consists of three main parts. in the pre-edge region, the electrons transition to bound states following the selection rules ($\Delta l = \pm 1, \Delta j = \pm 1,\ \Delta s = 0$). The rising edge and the white line comprise the second part representing more probable transitions to discrete unoccupied valence states. This sharp increase in the absorption is defined as the absorption jump $\Delta\mu_0(E_0)$. The post-edge, right after the white line, is dominated by multiple scattering events and is due to the electron excitations to delocalized states. The features of the XANES region due to the absorption of the X-rays are related to the unoccupied localized and delocalized states and the electron transition probability $\mu(E)$ and can be illustrated by Fermi's Golden Rule:[178]

$$\mu(E) \approx \sum_f |\langle f|\,\hat{T}\,|i\rangle|^2 \delta(\epsilon_f - \epsilon_i - E). \tag{5.13}$$

The Dirac function $\delta(\epsilon_f - \epsilon_i - E)$ depicts the conservation of energy, while the Hamiltonian-operator $\hat{T}$ describes interaction of the entire atom with the electromagnetic field. The function describes the initial state $|i\rangle$ of the absorbing atom modulated by $\hat{T}$ towards the final state $\langle f|$, where one electron was excited and the surrounding electrons rearranged to screen the generated positively charged hole.

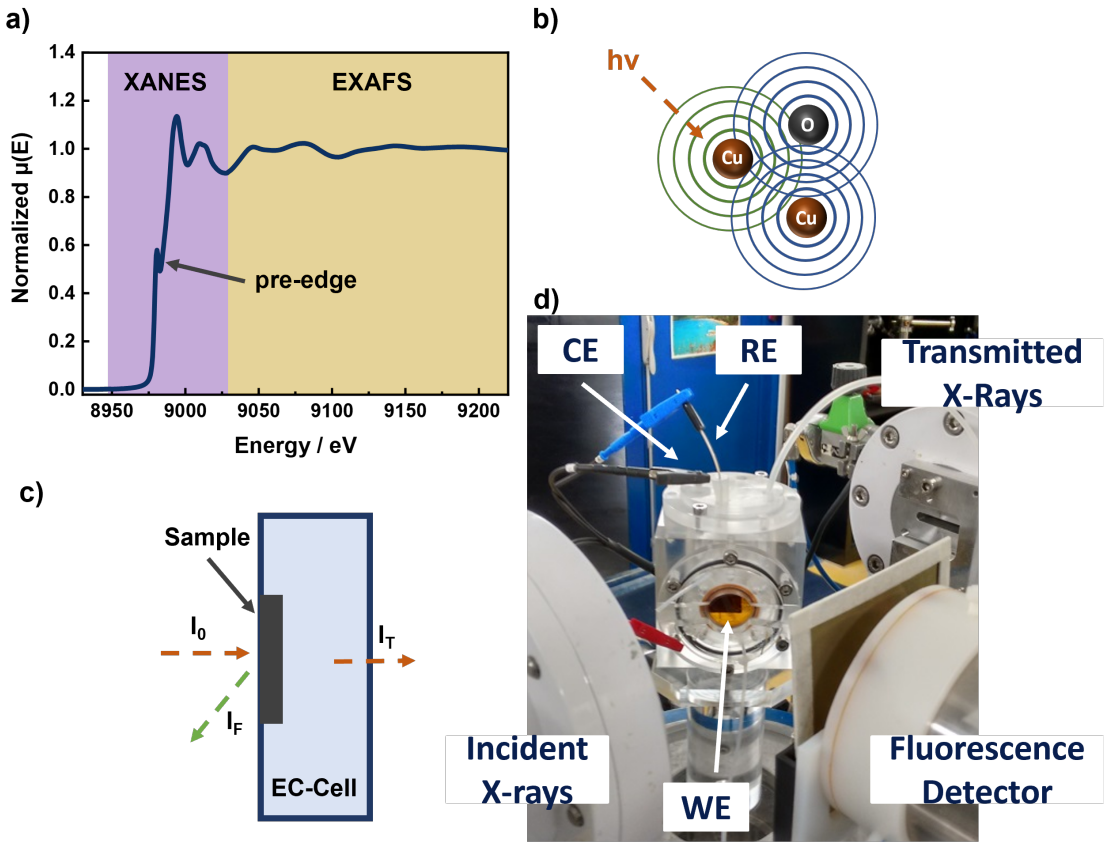

Figure 5.9: a) Copper oxide K-edge XAS data of the normalized absorption coefficient $\mu(E)$ as a function of incident X-ray energy. b) Scheme of the photoelectron scattering process. c) Illustration of the electrochemical cell, which is also shown in d) as an image during measurements at a beamline with a fluorescence detector.

The absorption edge shows a distinct feature and is described by transitions to unoccupied localized states, in particular transitions from s states to p states, and the position of the main absorption edge is sensitive to the oxidation state. However, due to orbital hybridization, the p-states of ligands (oxygen) mix with d-states of Cu, allowing pre-edge transitions. Nonetheless, symmetry considerations allow this to happen only in non-centrosymmetric symmetries of absorbing atoms, thus octahedral symmetry of the six O atoms around Cu^{2+} typically result in pre-edges of low intensity because they are distorted, also called Jahn-Teller effect. The pre-peak is shown as an example for Cu^{2+} in Figure 5.9a. The post-edge region is, similarly to the Extended X-ray Absorption Fine Structure (EXAFS) region, characterized by the interaction of the photoelectron with the neighboring atoms, but it is principally dominated by multiple scattering effects.[179]

The analysis of XANES spectra is mostly qualitative, although recent advances in XANES evaluation enabled the extraction of quantitative structural information from it.[180] Semi-quantitative evaluation may be obtained by direct comparison to reference spectra and linear combination fitting.[177]

The EXAFS region is prevailed by photons with higher energy than the absorption edge and provides information about the spatial arrangement of the nearest atomic neighbors around the absorbing atom. The EXAFS region shown in Figure 5.9a, is defined by the interaction of the excited photoelectron with the electrostatic potentials of neighboring atoms. The local atomic structure, in particular, the type of atoms closest to the absorbing atom, can be quantitatively analyzed. The absorption probability is perturbed upon the interference of the electron wave with the sample, which results in an overall oscillatory structure of the absorption coefficient $\mu(E)$, Figure 5.9b. The EXAFS component $\chi(E)$ is defined as the difference between the experimentally obtained $\mu(E)$ and the smooth background function $\mu_0(E)$ normalized by the absorption jump $\Delta\mu_0(E_0)$:

$$\chi(E) = \frac{\mu(E) - \mu_0(E)}{\Delta\mu_0(E_0)} \tag{5.14}$$

Here, E_0 is the minimal necessary energy to excite photoelectrons to the continuum.[181] The EXAFS signal can be converted from the energy space to the photoelectron wavenumber (k) space with

$$k = \sqrt{\frac{2m_e}{\hbar^2}(E - E_0)}, \tag{5.15}$$

with m_e being the mass of an electron and $\hbar$ the Planck's constant.

In order to receive geometric structure descriptors, such as the coordination number C_p, the average interatomic distance R_p and the structural disorder factor (or Debye-Waller factor) σ_p^2, the experimental signal of the contributions to the scattering paths $\chi(k)$ can be described as[179]

$$\chi(k) = \sum_p \frac{C_p S_0^2}{k R_p^2} F_p(k, R_p) e^{-2R_p/\lambda(k)} e^{-2\sigma_p^2 k^2} \sin(2kR_p + \phi_p(k, R_p)). \tag{5.16}$$

This equation contains the following material specific terms

- C_p: coordination number
- S_0^2: reduction of EXAFS amplitude due to too many electronic excitations, typically between 0.7 and 1.
- R_p: the average interatomic distance
- $F_p(k, R)$: changes in the photoelectron wave amplitude as a function of the radial distance R and wavenumber k
- $\lambda(k)$: inelastic mean-free path for the excited electron
- σ_p^2: structural disorder factor (or Debye-Waller factor)
- $\phi_p(k, R)$: phase upon scattering from a neighboring atom as a function of the radial distance R and wavenumber k

The analysis of the EXAFS data follows the above mentioned steps converting $\chi(E)$ to $\chi(k)$ and to $\chi(k)k^2$ or $\chi(k)k^3$ and least-square-fitting them with the mathematical model using the IFEFFIT code.[181] The graphical representation of the analyzed EXAFS data as the total Fourier transform EXAFS signal $\chi(k)k^2$ allows the direct observation of the interatomic distances of the neighboring atoms.

The catalysts were measured under electrochemical conditions with an one-compartement cell, Figures 5.9c and d, where the incident X-ray beam hit the catalyst from the backside of the cell and either the transmitted photons were detected and the absorption coefficient calculated as

$$\mu(E) = -\log\left(\frac{I}{I_0}\right) \tag{5.17}$$

or the energy of the emitted fluorescence electrons was detected in fluorescence mode[107,146,159] with

$$\mu(E) \propto \left(\frac{I_F}{I_0}\right). \tag{5.18}$$

The intensity of the fluorescence signal I_F is proportional to the absorption coefficient and thus represents an indirect measure of the absorption probability. Since the electrolyte in the cell also absorbs the X-ray intensity, most measurements shown in this work are in fluorescence mode, with the data acquired from the back side of the catalyst. Here, the fluorescence detector is set in a 90°C geometry to the incident X-ray beam, while the sample is positioned with 45°C to both, the detector and the X-ray beam. In this work, a PIPS (passivated implanted planar silicon) detector was usually used, counting the incoming X-rays by creating electron-hole pairs in the semiconductor

material. Measurements in the fluorescence mode are sensitive to the thickness and concentration of the sample due to the self-absorption effect. Although there exist options for correcting self-absorption after measuring, it is preferable to avoid it in general. Thus, fluorescence measurements in XAS should be performed on thin or diluted samples.

5.4.3 Fourier-transformed Infrared Reflection Absorption Spectroscopy (FT-IRRAS)

Infrared spectroscopy was used to understand adsorbed molecules, such as CO, on the catalytic surface under reaction conditions. This technique is characterized by the interaction of photons in the infrared region with matter, which may result in absorption, emission or reflection. In particular, when the radiation is absorbed by a molecule, energy is transferred to vibrational and rotational modes in the bond. The resulting vibration could be modeled by a harmonic oscillator, where the vibrational frequency ν is defined by

$$\nu = \frac{1}{2\pi}\sqrt{\frac{k}{\mu}}, \tag{5.19}$$

with the force constant k being directly correlated to the bond strength and μ the reduced mass of the atoms m_x ($\mu = {}^{m_1 m_2}/_{m_1+m_2}$).[182] In general, ν increases with the bond strength and decreases with the atom mass. The allowed transitions by an absorbed photon are explained by the change of the vibrational quantum number by $\tilde{\nu}$ ($\Delta\tilde{\nu} \pm 1$). In reality, overtones may be observed, yielding $\Delta\tilde{\nu} \geq 1$. Moreover, the selection rule allows the observation in the IR spectrum only, when a change in the dipole moment occurs perpendicular to the surface upon adsorption. The four types of vibrations, i) stretching, ii) in-plane bending, iii) out-of-plane bending and iv) torsion can appear symmetric or asymmetric and decrease in frequency in this order. Infrared spectroscopy is a differential method, where the absorbance a is calculated by the normalization of the measured spectrum I by a reference spectrum I_0 and defined as

$$a = -\log\left(\frac{I}{I_0}\right). \tag{5.20}$$

The FT-IRRAS evolved for the investigation of (sub)monolayer adsorbates on metal surfaces with low area. In particular, the signal-to-noise ratio and its sensitivity to low concentrations are improved compared to conventional infrared spectroscopy. As combined form of transmission and reflection, the incident radiation is reflected by the substrate and thus passes through the sample twice, shown in Figure 5.10a. The sensitivity is further increased by using a grazing incident angle θ of 80°. The contribution of the reflecting substrate is small, as the electric fields in both directions are almost equal with different signs and are therefore nearly canceled. However, the molecules in the vicinity of the reflecting surface experience a combination of the electric fields and are thus constructively amplified.[183]

A typical FT-IRRAS differential spectrum of Pd is shown in Figure 5.10b, showing bands of the

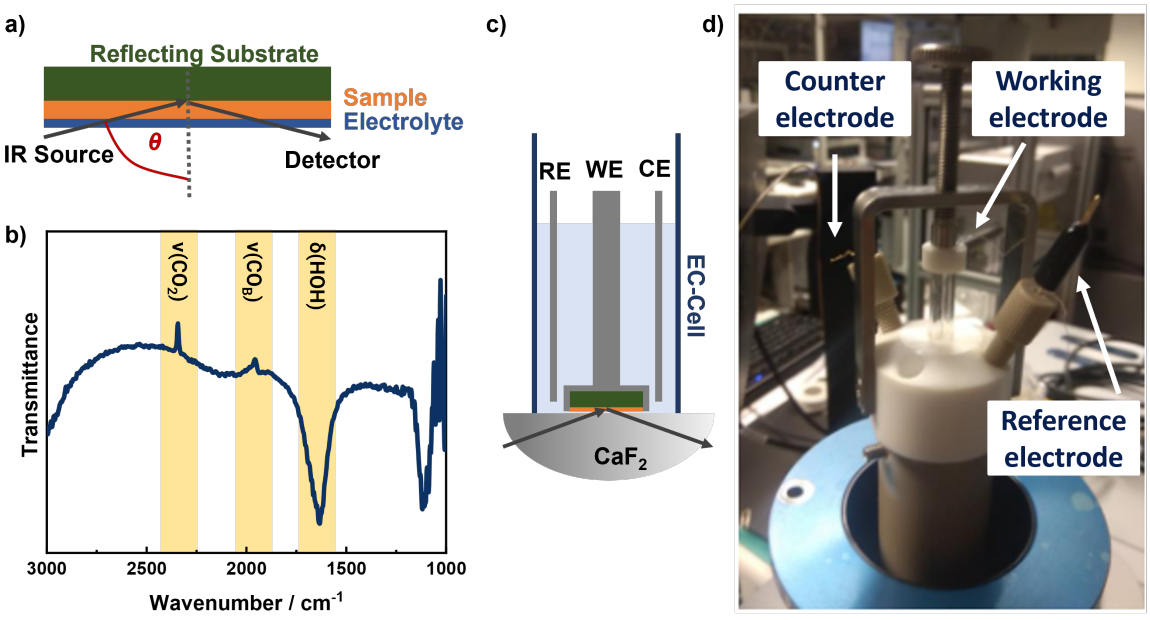

Figure 5.10: a) Geometry of the FT-IRRAS experiment considering a solid sample attached to a reflecting substrate. b) Typical FT-IRRAS differential spectrum of a CO stripping experiment adapted from [146] between 4000 cm^{-1} and 1000 cm^{-1} with a spectral resolution of 4 cm^{-1}. c) Scheme of the electrochemical cell attached to a CaF_2 window. The working electrode consists of the sample attached to a Au foil substrate or a glassy carbon and pushed towards the window. d) Image of the top of the electrochemical cell connected to the spectrometer.

asymmetric C-O band at 2345 cm^{-1} indicating CO_2 evolution, a bridge-bonded C-O stretch band around 1945 cm^{-1} and the bending mode of water around 1650 cm^{-1}.

Upon the application of a potential on the WE, an external electric field is applied on the catalytic surface and the adsorbed molecule experiences energy-level shifts of the vibrational mode and thus induces a change in the transition dipole moment. The so-called vibrational Stark effect shifts the peak intensities as a function of the intensity of the electric field.

FT-IRRAS was used as an *in situ* method for electrocatalytic measurements by building an electrochemical cell on top of an IR-transparent CaF_2 hemispherical window, shown in Figures 5.10c and d. A gold foil was used as WE and reflecting substrate, and the catalyst was attached on its surface and pushed towards the CaF_2 window. A glassy carbon was used to study the CO_2 evolution of the FAOR despite its low reflectivity to avoid a simultaneous reaction of Au. Ideally, a thin film of liquid is left between the catalyst and the window. Reference spectra were acquired in liquid in non-catalytic conditions.

5.4.4 Other *operando* Techniques

Other spectroscopic techniques functionalized with an electrochemical cell were utilized, but shown here only briefly as they were not the focus of this work.

Surface enhanced Raman Spectroscopy (SERS) was used as *operando* method by immersing the Raman objective into the electrochemical cell.[107] On rough metal surfaces, in particular on Cu, Ag or Au materials, high surface sensitiveness through an enhancement of the Raman scattering is achieved. Thus, the here investigated Cu_2O nanocubes and Au-decorated Cu_2O nanocubes constituted perfect materials for the investigation of the vibration of the adsorbed molecules on the surface. The surface enhancement originates either from the excitation of surface plasmons or from the formation of charge-transfer complexes consisting of resonance of the incoming electromagnetic radiation and the electron transition. In this technique, the scatter of the incoming electromagnetic radiation is detected, and also molecular vibrations are Raman active upon a change in the polarization of the molecule. With this *operando* technique it was possible to analyze the adsorbed intermediate species, e.g. CO or carbonates, on the catalytic active surface during the catalytic reaction.

X-ray Diffraction (XRD) is a technique to characterize the crystallographic structure and polimorphic phases and changes of a material in a non-destructive manner. The diffraction behavior is similar to LEED, but X-rays are used, making the detected reflections bulk sensitive and providing data with higher resolution. This technique was used for initial characterization of the crystalline phases in the as-prepared nanocatalysts, Cu_2O NCs and Pd NCs. Furthermore, a variant using high energy X-rays, termed High Energy X-ray Diffraction (HE-XRD), was used under *operando* conditions to further characterize the structural evolution of the CuAu-catalysts.

5.4.5 Conclusion: Overview over the used techniques

Each presented technique identifies specific properties of the catalyst. An overview over the most important results that can be obtained by each technique is depicted in Table 5.1. Note that this chapter only described some techniques, while others were omitted as they were not within the main scope of this work. Each technique was used to study the catalysts before, after or during an electrocatalytic reaction.

Table 5.1: Overview over the most important results that were obtained by each technique.

Method	Application in this work
XPS	elemental composition, chemical state and electronic structure at the surface
XAS	local atomic and electronic structure of the bulk
FT-IRRAS	adsorbates on the surface
SERS	adsorbed molecules on the surface
XRD	lattice spacing in crystals, crystalline domains
TEM, EDX	morphology of nanoparticles, atomic ordering and elemental mapping
ICP-MS	concentration of elements
LEED	crystalline surface structures
STM	topography of electronic states, morphology and structure of well-defined surfaces

Publications

This part provides the publications that were prepared to answer the objectives of this work. First, a publication under preparation tries to resolve the role of undercoordinated sites on the CO_2RR, while the second publications identifies descriptors to enhance the production of ethanol during CO_2RR. Finally Bimetallic, shaped nanoparticles were used to understand the role of Au as co-catalysts on Cu during the CO_2RR and the role of SnO_2 as co-catalyst on Pd during the FAOR.

6

The Role of undercoordinated Cu Atoms: The Electrocatalytic CO_2 Reduction Reaction on a stepped Cu(310) Single Crystal Surface

Clara Rettenmaier, Fabian Scholten, Arno Bergmann, Beatriz Roldan Cuenya

in preparation

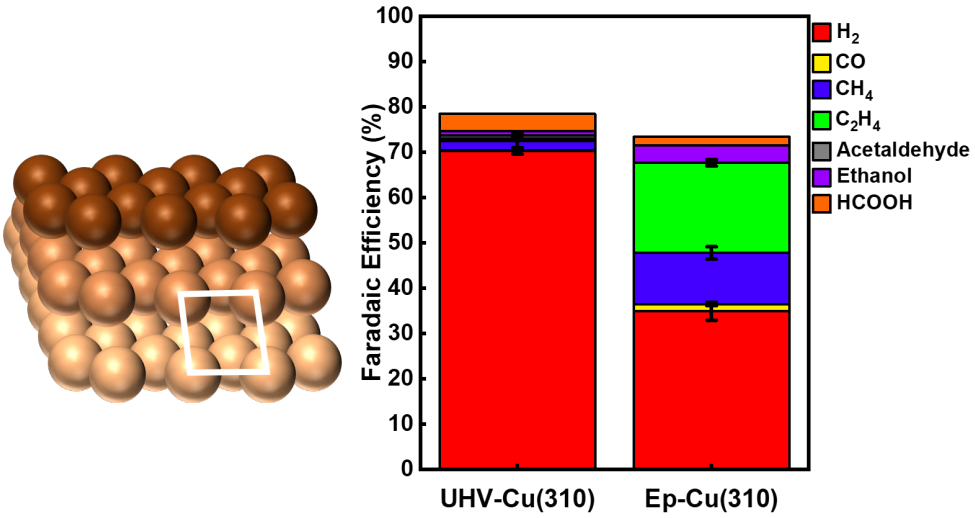

6.1 Preliminary Remarks

This chapter addresses the role of undercoordinated atoms on the selectivity of the CO_2RR. It gives in-depth understanding into well-ordered atomically flat high-index surfaces that have been barely explored. The hypothesis of this study proposes that undercoordinated atoms are significantly involved as active sites of the CO dimerization processes.

This project was designed and supervised by Arno Bergmann and Beatriz Roldan Cuenya. Experiments were performed in collaboration with Fabian Scholten.

6.2 Introduction

Cu is unique in converting CO_2 to highly valuable hydrocarbons in the CO_2RR. However, the low selectivities towards valuable products are a critical drawback for commercialization. Despite the major efforts to understand the structure pertaining the actives sites of certain product formation, clear structure-selectivity relationships have not yet been established under operation. Well-ordered atomic surfaces constitute model pre-catalyst systems, which allow the investigation of the performance as a function structure sensitivity.

The role of low-index facets on the CO_2RR has been studied recently indicating low performance to C_{2+} products, while the parasitic H_2 evolution dominates on flat Cu(100) and Cu(111).[80] These results are controversially discussed with previous results obtained with electropolished single crystals, which make significant amounts of C_{2+} products. It was shown that atomically ordered Cu(100) facets themselves are not the active sites for CO_2RR.[80] Thus, it was unveiled that the sample preparation by electropolishing can induce significant amounts of terrace disruptions through defects or step sites, leaving behind undercoordinated Cu atoms on the surface as potential catalytic active sites for CO_2RR. A good proxy for these sites could be well-defined high-index crystals comprising defined terraces as well as steps. For example, the Cu(310) terminated surface includes (100) terraces with a defined terrace width, which are interrupted by (110) steps.

Besides the studies on low-index facets, Hori et al.'s work also comprises systematic experimental studies on electropolished high-index facets, suggesting facet-specific results according to prior work on rough electropolished surfaces:[23–25]

1. Ethylene formation is highest for stepped surfaces with relatively wide (100) terraces of a width of at least 5 atoms. The steps may show a (110) or a (111) termination.

2. Ethanol formation is highest for (100) terraces with a width between 3 and 8 atoms,

featuring the Cu(310) vicinal surface structure with 30% FE for the ethanol formation.

These findings suggest that the product selectivities are dependent on the ratio of terrace sites versus the type of step sites.[27,104] Since the (100) terraces are, at present, expected to form mostly hydrogen,[80] it is suggested that either the steps or a combination of the steps with terrace atoms comprise the active site towards C_{2+} products or, in particular, ethanol.

Unfortunately, further investigations on stepped Cu single crystals have barely been resumed. Some theoretical work on Cu(711) and Cu(211) indicate improved stabilized intermediates compared to low-index facets and thus, higher probabilities of C-C coupling events resulting in C_{2+} products.[184,185] Experimental work on Cu(511) has suggested an onset of ethanol formation at −1.06 V vs. SHE without co-generation of other hydrocarbons. Furthermore, the relevance of terrace-bound CO adsorbates for the ethanol production has been proposed.[186]

The preparation of an atomically flat Cu(310) single crystal surface and its careful characterization for CO_2RR has yet not been done and presents a novelty for the investigation of well-defined high-index surface studies in this field.

In this chapter, sample preparation and characterization of the morphology, the CO binding energy and the defect sites before and after CO_2RR have been performed in order to correlate structural properties to the catalyst activity. This study aims to close the gap of understanding between atomically flat and electropolished surfaces for high-index facets. It also provides further insight on the conceptualization of roughness and defect sites e.g. undercoordinated surface atoms, and their role on the CO_2RR.

6.3 Results

The UHV-Cu(310) single crystal was prepared under UHV conditions via sputtering with Ar (10 min at $p = 2.0 \times 10^{-5}$ mbar) and annealing ($T = 850$ K) for several times. The cleanliness of the surface was verified by LEED and XPS data. The atomic structure and shape of the stepped single crystal was studied with LEED. Figure 6.1 shows the results of the LEED at different energies to visualize the differently sized unit cells of parts of the surface, e.g. the unit cell of the (100) terrace or of the (110) steps. At 95.2 eV, Figure 6.1a, a rectangular structure is observed, indicating the presence of low-index (100) facets, with (110) steps. The LEED spots are a bit elongated, indicating a narrow (100) terrace width in one direction and an infinite extension into the perpendicular orientation. A superposition of the periodically repeated step-edge atoms and the (100) spots is demonstrated in Figure 6.1b at 111.7 eV. The step-edge atoms, theoretically constructed as one-dimensional periodic and infinite lines,

are observed only within the superposition with the (100) terrace sites, leading to a peak doubling. At high energies of 139.9 eV, the rectangular unit cell from the step-edge atoms of one terrace to the next one is shown in Figure 6.1c, while the Cu(310) unit cell is presented in Figure 6.1d with a ball model of the vicinal steps of the single crystal.

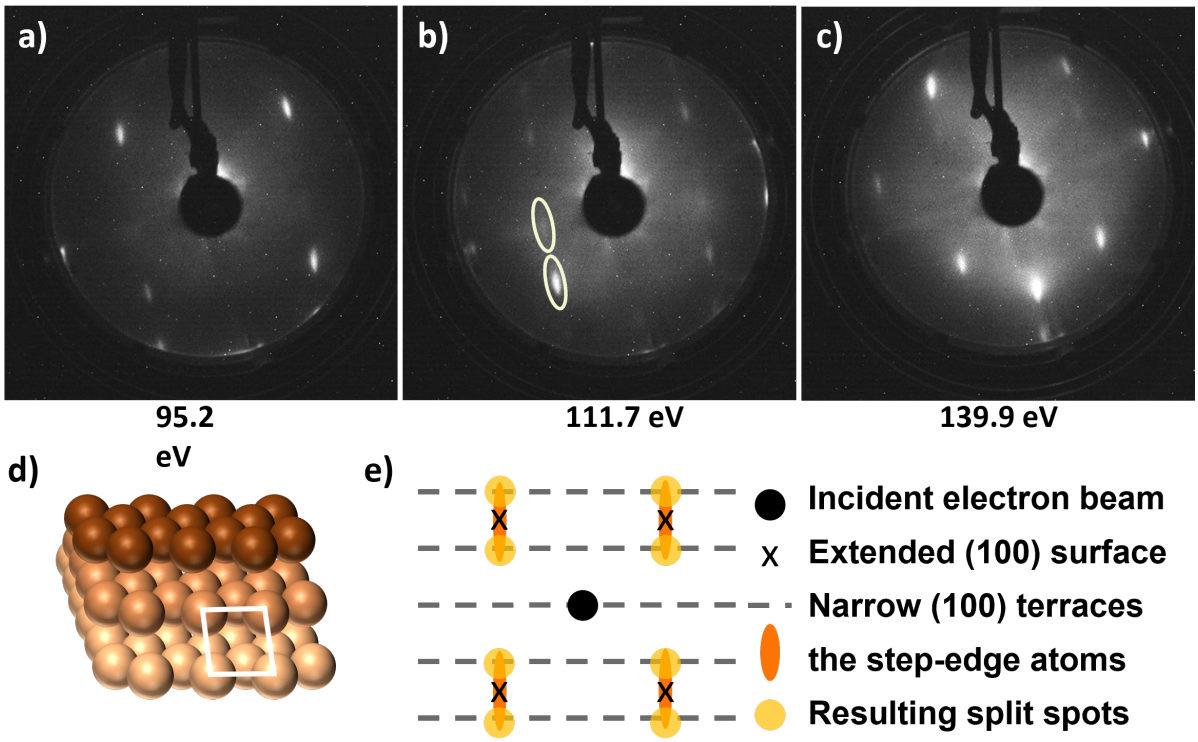

Figure 6.1: LEED patterns of the atomically cleaned UHV-Cu(310) vicinal surface at different incident electron energies a) 95.2 eV, b) 111.7 eV, and c) 139.9 eV. A ball model of the stepped Cu(310) vicinal surface is shown in d) together with the primitive unit cell of the surface.e) Scheme of the construction of the LEED pattern.

XPS was measured on the UHV prepared single crystal to confirm a clean chemical composition. It is evident from Figure 6.2a and b that the surface is metallic, without oxygen or carbon observed, as indicated in Figure 6.2c and d, respectively. Moreover, the survey spectrum in Figure 6.2e does not show any peaks, which are not coming from the Cu.

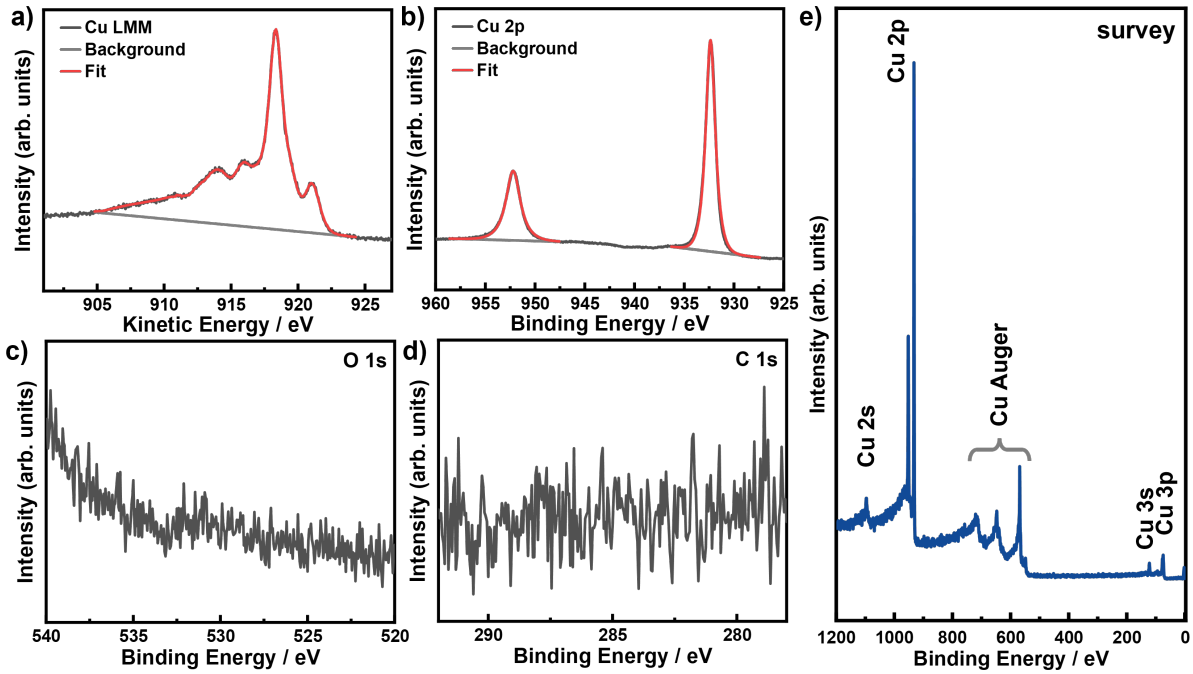

Figure 6.2: XPS data of the Cu(310) vicinal surface after UHV preparation; a) the metallic Cu LMM spectrum, b) Cu 2p XPS peaks, measurements around the expected c) O 1s and d) C 1s regions indicating the absence of oxygen and carbon and e) survey XPS spectrum.

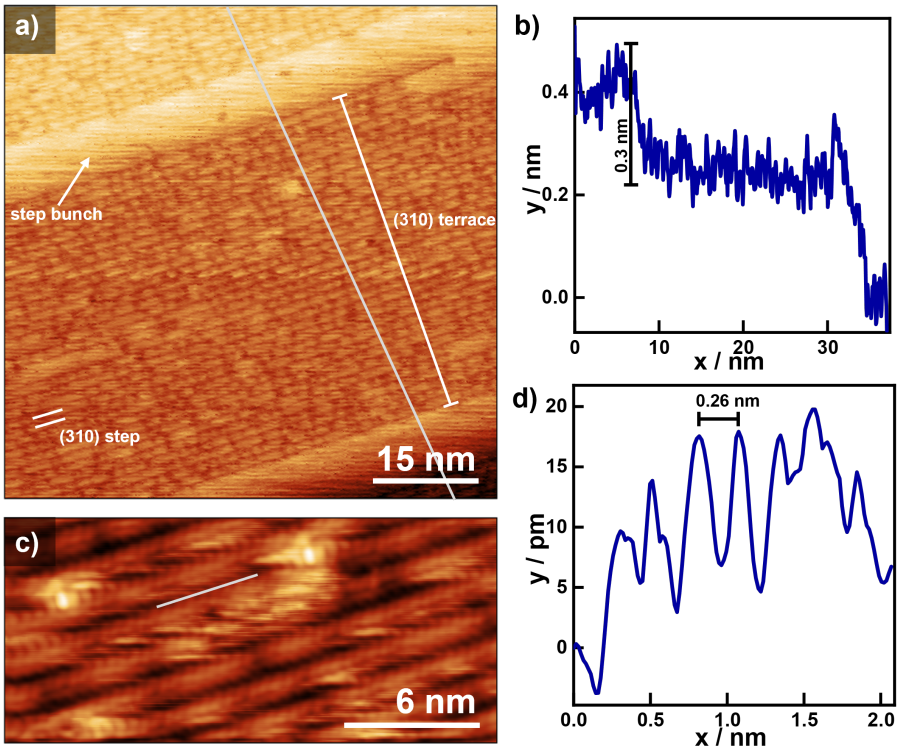

Figure 6.3: a) Room temperature UHV-STM image a) from a 50 nm wide terrace comprising 33 single-atom steps corresponding to the Cu(310) vicinal surface with b) a line profile over the whole surface. c) Atomically resolved region and d) a line profile indicating the atomic distances of Cu. The color scales range a) from 0–932 nm and b) from 0–242 pm from dark to bright.

The morphology of the UHV-prepared Cu(310) single crystal was monitored with STM under UHV conditions at room temperature. Figure 6.3a presents three terraces, on which the (310) structure was resolved, demonstrated as brighter lines on the terrace, while the step bunches are observed only in a diffuse way. The line profile in Figure 6.3b over all three terraces indicates a terrace width of about 22 nm, while the step bunches are ca. 0.3 nm high. The middle terrace comprises 33 (310) steps, indicating a unit cell length of 0.67 nm per (310) step. Note that, in the presented image, the step bunches divide the terraces in the same orientation as the (310) steps, which is not imperative for all acquired STM images. Thus, it indicates that the whole crystal might feature one orientation of the (310) steps and several orientations of the terraces. Figure 6.3c shows an atomically resolved image of the (310) terrace. The paired rows indicate the (100) surfaces within the (310) steps, which show brighter upper rows and a bit darker lower rows of atoms, followed by black rows of the steps. The line profile in Figure 6.3d shows the atomic distances of the brighter rows to be 0.26 nm, which resembles Cu-Cu atomic distances.[186] Thus, these results indicate that the single crystal is well prepared and resembles a (310) vicinal surface.

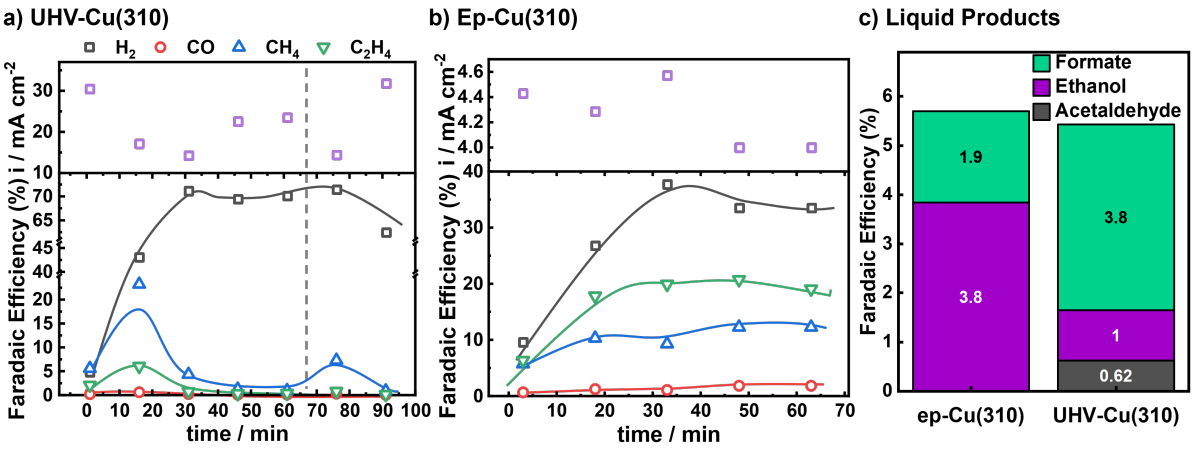

Figure 6.4: a) Gaseous product distributions of CO_2RR in CO_2 sat. 0.1 M $KHCO_3$ at −1.0 V vs. RHE and the corresponding currents normalized to the respective geometric surface area of an electropolished (Ep)-Cu(310) and a UHV-Cu(310) single crystal resolved over the reaction time. b) Accumulated liquid products acquired during the CO_2RR for both catalysts.

CO_2RR was performed by taking the single crystal out of the UHV conditions, placing it in a sample holder, which leaves solely the inner part of the vicinal surface released, and setting it up a H-type cell with CO_2 sat. 0.1 M $KHCO_3$ and measuring the product distribution at −1.0 V vs. RHE. The results are shown in Figure 6.4a and compared with an electropolished Cu(310) single crystal, Figure 6.4b. The UHV-Cu(310) produces up to 70% FE hydrogen, with small amounts below 1% FE of CO, C_2H_4 and below 5% FE for CH_4. Interestingly, the production of C_2H_4 and CH_4 was majorly increased within the first few minutes after initiating the reaction. In the presented case, the measurement was restarted after 65 min, showing a return of the increased CH_4 formation for the UHV-Cu(310). It should also be noted, that the H_2 formation lies around 42% FE in the first minutes and arranging in the area of 70% FE afterwards. The product distribution was compared with an electropolished Cu(310) single crystal. Here, the formation of H_2 is much lower than in the UHV-Cu(310) single crystal with about 35% FE, while CH_4 and C_2H_4 show more pronounced results with 12% FE and 20% FE, respectively. The CO stays at an insignificantly low level below 2% FE. These results fit into the studies made with UHV prepared and electropolished Cu(100) and Cu(111) low-index facets.[80] In this study, the electropolished catalysts show significantly less H_2 for electropolished single crystals compared to the UHV-prepared single crystals. Moreover, the production of CH_4 and C_2H_4 is significantly enhanced, while the formation of ethanol was not reported.

Figure 6.4c shows the acquired liquid products, showing 0.62% FE acetaldehyde and 1% FE of ethanol together with roughly 4% FE formate for the UHV-Cu(310) single crystal, while up to 4% FE ethanol and 2% FE formate were observed for the Ep-Cu(310) catalyst. The

CO_2RR results of an electropolished Cu(310) single crystal were only described by Hori et al. presenting the formation of 30% FE of ethanol.[25]

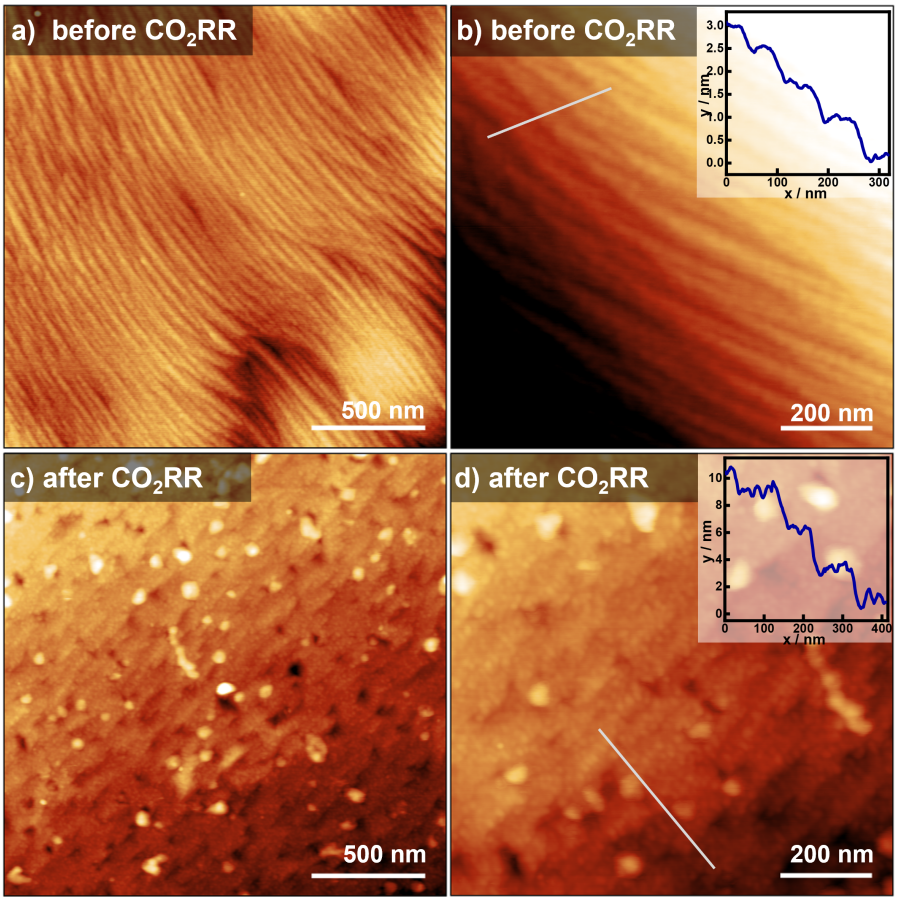

Figure 6.5: Ex situ Atomic Force Microscopy (AFM) images of the UHV prepared Cu(310) vicinal surface a) as an overview and b) as a close-up. The line profile in the inset indicates terraces of 50-80 nm width. Ex situ images of the Cu(310) single crystal after CO_2RR for 100 min in CO_2 sat. 0.1 M $KHCO_3$ c) as overview and d) as a close-up. The line profile in the inset demonstrates an increase in the terrace widths to 80-150 nm. The color scales of the images range a) from 0-7 nm, b) 0-8 nm, c) 0-38 nm and 0-30 nm from dark to bright.

The morphology of the UHV-Cu(310) was studied before and after CO_2RR with AFM. Figure 6.5a depicts an overview over the structure of periodically distributed terraces. Note here that these terraces comprise the (310) stepped surface within the terrace. Moreover, the overall impression shows a wavy terrace structure. A more detailed picture is given by Figure 6.5b. Herein, several terraces are shown, demonstrating terrace widths of 50-80 nm, with a height of 0.5-0.8 nm. Additionally, the AFM figure indicates that there are some smaller features of about 30 nm on each terrace, which all have the same orientation. It is thus suggested that these comprise the (310) terraces that have been observed in Figure 6.3. The terrace width

are quite narrow as compared to the Cu(100) and Cu(111) low index crystals show terrace widths of 150 nm and 250 nm, respectively.[80]

The morphology after CO_2RR in Figures 6.5c and d presents a quite noteworthy behavior. Next to the holes and protrusions, the terraces display widths of 80-150 nm, which are 3 nm high, which could indicate a coalescence of 2-3 of the initial terraces. Moreover, the terraces seem to show step-bunches which are more straight than before CO_2RR. Furthermore, small protrusions cover the terraces and the small terraces in the images before reaction are not visible anymore. Thus, these results indicate a major restructuring during the reaction.

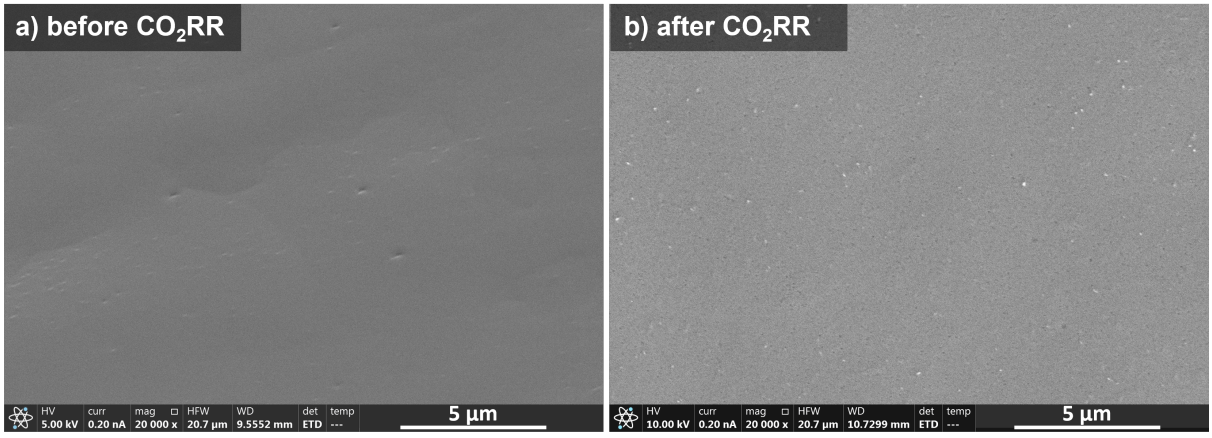

Figure 6.6: Ex situ SEM images of the Cu(310) vicinal surface a) after UHV preparation and b) after CO_2RR for 100 min in CO_2 sat. 0.1 M $KHCO_3$.

SEM images were performed to study the microscopic structure of the UHV-Cu(310) single crystal. Figure 6.6 presents the micrographs of the surface before and after CO_2RR. The low contrast indicates the flatness of the crystal, both, before and after reaction, while no major impurities, such as $KHCO_3$ crystallites, were observed. However, it can be seen in Figure 6.6b that the surface is covered with small holes and some bigger protrusions. These results may also indicate structural changes such as defect formation.

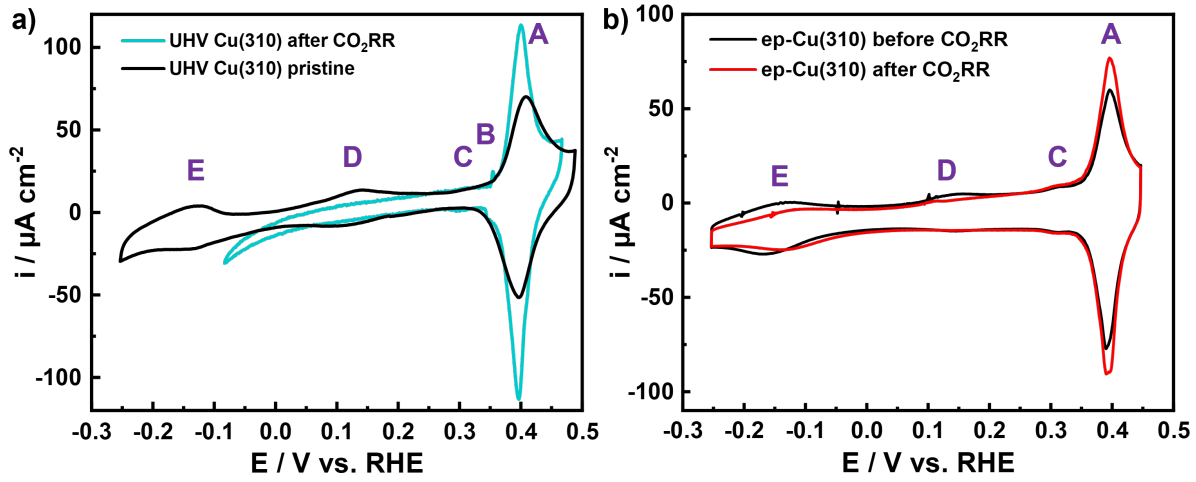

Figure 6.7: Cyclic voltammograms for a) the UHV-Cu(310) in the pristine state and after CO_2RR for 100 min in CO_2 sat. 0.1 M $KHCO_3$; b) shows the CVs for the Ep-Cu(310) before CO_2RR (black) and after CO_2RR for 65 min in CO_2 sat. 0.1 M $KHCO_3$ (red). Data were acquired in Ar sat. 0.1 M KOH at 50 mV/s.

An established method to analyze the fine-structure of the vicinal Cu surface is the OH adsorption in alkaline media. Although, low-index facets have been intensively studied, the electrochemical fingerprints of defect sites and stepped surfaces are less known. Thus, these CVs were performed for the Ep-Cu(310) and for the UHV-Cu(310) before and after CO_2RR, which is shown in Figure 6.7.

Both single crystals present the peaks **A**, which is considered specific for Cu(310) steps,,[156] **C**, for OH adsorption on unspecific defect sites,[187] and **E**, which is a broad feature around −0.13 V vs. RHE for the OH de- and adsorption on Cu(100) terrace sites. At **B**, a peak pair is shown for the UHV-Cu(310) crystal after CO_2RR and is not observed for the Ep-Cu(310) CVs, indicating OH adsorption at an atomic site that is only available in the UHV-prepared single crystal. Remarkably, this peak is also not observed for the pristine UHV-Cu(310).

Further, a broad elevation is observed for the pristine UHV-Cu(310) and the Ep-Cu(310) in the as prepared states, denoted as peak **D**. This feature disappears after CO_2RR and is sometimes observed on polycristalline Cu surfaces.

Comparing the Ep-Cu(310) before and after CO_2RR, both CVs show the same features, while the (100) terraces (peak E) are less and the (310) specific sites, peak **A**, are more pronounced after CO_2RR. These results are similar to the results in literature.[156]

6.4 Conclusion

In summary,the surface of a UHV prepared Cu(310) was characterized, then CO_2RR was conducted and compared to an electropolished Cu(310) single crystal. Unlike presented in the literature, the performances towards ethanol production was only 1% FE and 4% FE ethanol for the UHV-Cu(310) and the Ep-Cu(310), respectively. The morphology was characterized before and after CO_2RR for the UHV-Cu(310) and changes in the terrace width were observed. Particularly, two or three terraces coalesced towards a bigger terrace, which additionally show a different finestructure than in the as-prepared state. SEM analysis indicate a lack in micrometer large step bunches before and after CO_2RR.

The presented results provide first insights into this project. It is however indispensable to perform further in-depth studies to find the differences in treatment and structure to understand how such a high ethanol performance could be reached. For instance, the history of the single crystal and overall roughness, as well as the presence of minimizing subsurface species (e.g. O or C) could play a major role. Nevertheless, the here presented work already indicates that high-index facets comprise an interesting field to study structure-activity relationships.

6.5 Methods

Sample Preparation and Characterization under UHV conditions

A fresh Cu(310) single crystal (MaTecK, purity 99.9999%, orientation accuracy $< 0.4°$C has been prepared under UHV conditions by sputtering and annealing, which was repeated until the surface was free of C and O. Sputtering was performed at $p = 2.0 \times 10^{-5}$ mbar of Ar, having a base pressure $p_B = 4.3 \times 10^{-10}$ mbar for 10 min and an Ion energy of $E_{ion} = 2.5$ keV using a IQE-11 A ion source (Specs GmbH). In the last three cycles, the sample was sputtered at an Ion energy of $E_{ion} = 1.5$ keV. Annealing was performed at $T = 850$ K for 10 min and the sample was subsequently cooled down step-wise. Low-Energy Electron Diffraction (LEED) was conducted using a LEED. Scanning Tunneling Microscopy (STM) measurements were performed with a NAP-STM microscope and a Nanonis controller (SPECS GmbH). X-ray Photoelectron Spectroscopy (XPS) measurements were conducted with a monochromatic XRM X-ray source (SPECS GmbH) using a Al anode ($E = 1486.7$ eV). The pass energy was 15 eV and the X-ray source power was set to $P = 300$ W. Photoelectrons were detected with a hemispherical analyzer (Phoibos 150 and a MCD-9 Detector).

Atomic Force Microscopy (AFM)

Ex situ AFM measurements were conducted with a Bruker Multimode AFM and Conical AFM tips (Aspire CT 300R, $f_0 = 300\,\mathrm{kHz}$, $k = 40\,\mathrm{N/m}$) in tapping mode.

Electrochemical Characterization

Fingerprint CVs were performed with a polyetheretherketone (PEEK) H-type cell with an Ar sat. 0.1 M KOH solution with 50 mV/s. A Pt-mesh (MaTecK, 3600 meshcm^{-2}) served as counter electrode and a leak-free Ag/AgCl (3.4 M, LF-1, Alvatek) as a reference electrode. The electrolyte handling was conducted without contact with glass to avoid Si contamination. A Biologic SP-300 and a Gamry (Interface 1010E) were used as potentiostats.

CO_2RR was performed in H-type cells, a glass cell for the Ep-Cu(310) measurement and a PEEK cell for the UHV-Cu(310) with a three-electrode setup. A Pt mesh (MaTecK, 3600 meshcm^{-2}) and a leak-free Ag/AgCl (3.4 M, LF-1, Alvatek) were used as counter- and reference electrodes. The used electrolyte 0.1 M $KHCO_3$ was first purified with Chelex (Bio-Rad Laboratories Inc.) before it was used. The electrolyte was furthermore saturated with CO_2 (4.5 N) for at least 20 min before each measurement. CO_2RR was conducted with an Autolab (PGSTAT 302N, Metrohm) potentiostat for the Ep-Cu(310) and a Gamry (COMPANY) for the UHV-Cu(310) and prior to each reaction an evaluation of the Ohmic drop was conducted via an i-interrupt protocol. Gas products were detected on-line with a gas chromatograph (GC, Agilent Technologies 7890B), equipped with a TCD and a FID. A high-performance liquid chromatograph (HPLC, Shimadzu Prominence), equipped with a NUCLEOGEL SUGAR 810 column and a refractive index detector (RID), and a liquid GC (L-GC, Shimadzu 2010plus), equipped with a fused silica capillary column and a FID detector were used to detect liquid products. The FEs were analyzed following several published reports of our group.[31,71,80]

7

Steering the Structure and Selectivity of CO_2 Electroreduction Catalysts by Potential Pulses

Janis Timoshenko[1], *Arno Bergmann*[1], *Clara Rettenmaier*[1], *Antonia Herzog, Rosa M. Arán-Ais, Hyo Sang Jeon, Felix T. Haase, Uta Hejral, Philipp Grosse, Stefanie Kühl, Earl M. Davis, Jing Tian, Olaf Magnussen, Beatriz Roldan Cuenya*
[1]: equal contribution

Published in: Nature Catalysis (2022) 5, 259, DOI: 10.1038/s41929-022-00760-z

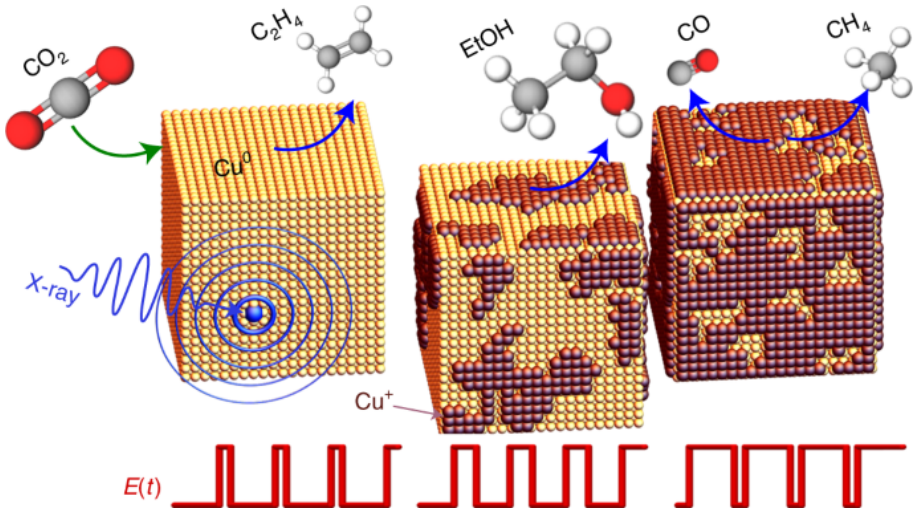

7.1 Preliminary Remarks

This chapter explores the role of oxide species on the CO_2RR by repetitive regeneration. Preliminary work on the role of Cu(I), morphological motifs and structural reconstruction on a Cu(100) single crystal and on Cu_2O NC in a gas-fed flow cell had been performed in our group.[156,159] These works have set the basis to design the presented electrocatalytic system, as well as the development and application of the *operando* XRD and quick XAS techniques. The article highlights the enormous possibilities of pulsed conditions on varying selectivities in situ and without replacing the catalyst. Furthermore, it shows how techniques, such as XAS, have evolved to be able to track the local atomic arrangement in ms-range.

Janis Timoshenko, Arno Bergmann and I contributed equally to this work. In particular, Janis Timoshenko was responsible for the *operando* quick XAS studies and Arno Bergmann guided the *operando* XRD investigations, while I led the sample synthesis, the characterization and the catalytic activity studies. The project was designed and supervised by Janis Timoshenko and Beatriz Roldan Cuenya. Other authors participated in synthesis, sample characterization and the synchrotron experiments.

This chapter is reproduced from *Janis Timoshenko[1], Arno Bergmann[1], Clara Rettenmaier[1], Antonia Herzog, Rosa M. Arán-Ais, Hyo Sang Jeon, Felix T. Haase, Uta Hejral, Philipp Grosse, Stefanie Kühl, Earl M. Davis, Jing Tian, Olaf Magnussen, Beatriz Roldan Cuenya* Steering the Structure and Selectivity of CO_2 Electroreduction Catalysts by Potential Pulses. Nature Catalysis (2022) 5, 259-267, DOI: 10.1038/s41929-022-00760-z. Open Access is given via the Creative Commons CC-BY agreement. Format, figure numbering and bibliography were adapted to fit to this thesis and possible spelling mistakes in the original article were corrected without further mentioning.

7.2 Abstract

Convoluted selectivity trends and a missing link between reaction product distribution and catalyst properties hinder practical applications of the electrochemical CO_2 reduction reaction (CO_2RR) for multicarbon product generation. Here we employ operando X-ray absorption and X-ray diffraction methods with subsecond time resolution to unveil the surprising complexity of catalysts exposed to dynamic reaction conditions. We show that by using a pulsed reaction protocol consisting of alternating working and oxidizing potential periods that dynamically perturb catalysts derived from Cu_2O nanocubes, one can decouple the effect of the ensemble of coexisting copper species on the product distribution. In particular, an optimized dynamic balance between oxidized and reduced copper surface species achieved within a narrow range

of cathodic and anodic pulse durations resulted in a twofold increase in ethanol production compared with static CO_2RR conditions. This work thus prepares the ground for steering catalyst selectivity through dynamically controlled structural and chemical transformations.

7.3 Introduction

Electrochemical energy conversion driven by renewable energy is a cost-effective, environmentally friendly route to convert undesired substances (such as CO_2) into valuable chemicals and fuels. A challenge for the practical application of complex electrochemical processes, such as the CO_2reduction reaction (CO_2RR) over copper-based catalysts, is control of selectivity.[38,49,72,188,189] One of the critical parameters affecting the catalyst's properties and function – its oxidation state[46,190] – can be conveniently manipulated in situ by choosing appropriate applied potentials. In particular, under pulsed reaction conditions the desired structural motifs and preferred oxidation state can be (re)generated.[93,97,99,156]

Previous investigations have provided conflicting explanations for the enhancement of catalytic properties under pulsed CO_2RR conditions. Studies employing polycrystalline copper electrodes,
[68,93,97,98,101,157,191–193] single crystals[156] and preoxidized copper nanocubes[99,159] revealed enhanced C_{2+} product formation, suppression of the competing Hydrogen Evolution Reaction (HER) and increased stability of catalytic activity under pulsed CO_2RR. These findings were attributed either to the formation of oxidized copper species[68,99,156] to catalyst surface morphology changes,[156,159,194] to the removal of poisoning hydrogen and carbon species from the catalyst's surface[93,101] to an enhanced adsorption of OH species and stabilization of CO_2RR intermediates[157] or to the local modulation of the electrolyte pH and CO_2 concentration.[100,101,158,159] The dominant mechanism depends on the parameters of the applied potential (for example, its value, pulse shape and duration of the working and anodic pulses).

In this article we focus on the regime in which the selected anodic potential ($E_a = +0.6\,V$ versus the reversible hydrogen electrode (RHE)) and the duration of the restoring pulse ($\Delta t_a > 0.5$ s) are sufficient for the generation of copper oxides. Thus, changes in the catalyst surface structure and composition could play a decisive role in the reaction pathway and selectivity. By controlling the type and amount of copper oxide formed during the restoring pulses we steer the CO_2RR selectivity of a Cu_2O nanocubes (NC)-derived catalyst. In particular, ethanol formation is doubled (compared with that under stationary conditions) within a narrow range of pulse durations, where a balance between metallic copper and distorted copper oxide species on the catalyst surface is achieved, as revealed by time-resolved operando X-

ray Absorption Spectroscopy (XAS) and X-ray Diffraction (XRD), and supported by quasi in situ X-ray Photoelectron Spectroscopy (XPS). Our study demonstrates the great potential of pulsed electrolysis for tailoring the catalyst performance and highlights the role of operando investigations for the mechanistic understanding of next-generation catalysts operating under dynamically changing reaction conditions.

7.4 Results

7.4.1 Selectivity under static and pulsed reaction conditions

The size-selected ($\sim 30\,\text{nm}$) and shape-selected Cu_2O NCs employed in this study (Fig. 7.1a) were shown to be catalytically active and selective for CO_2RR to C_{2+} products under potentiostatic conditions,[107,159,195] but are also well-suited for synchrotron-based operando investigations. Details of the sample preparation and characterization are given in Supplementary Note 7.6.1 and Supplementary Fig. 7.5.

Under static CO_2RR in CO_2-saturated 0.1 M $KHCO_3$ at −1.0 V, a transformation of the crystalline Cu_2O phase to metallic copper was observed by XRD, while XAS showed nearly complete copper reduction at −1.0 V (Supplementary Figs. 7.6 to 7.11).[107,195] This process is relatively slow: even after 60 min under CO_2RR, peaks of the Cu_2O phase were still present in the XRD pattern (Supplementary Fig. 7.8), and several hours were required until no further changes were visible in the XAS data (Supplementary Fig. 7.7 and Supplementary Note 7.6.2). The reduction under static CO_2RR also resulted in changes in the catalyst morphology, namely, a partial loss of the cubic shape (Fig. 7.1b and Supplementary Fig. 7.5). The selectivity of the reduced catalyst under static conditions was in line with previous reports.[45,55,195] Ethylene (C_2H_4), methane (CH_4) and ethanol (EtOH) were detected as the main CO_2RR products, with Faradaic Efficiencys (FEs) of 40%, 20% and 10%, respectively. The FE of H_2 from the competing HER was only 17% (Supplementary Note 7.6.3 and Supplementary Table 7.1).

To the pre-reduced catalyst, we applied a series of oxidizing (anodic) pulses and working (cathodic) pulses with durations Δt_a and Δt_c, respectively. Figure 7.1d-g shows the difference in the FEs of the products measured under pulsed CO_2RR with varied Δt_a and Δt_c, with respect to the FEs obtained under a static cathodic potential (−1.0 V). The potential values for cathodic and anodic pulses in all cases were $E_c = -1.0\,\text{V}$ and $E_a = +0.6\,\text{V}$, respectively. The latter is a potential that is expected to oxidize Cu(0) to Cu(I) (Supplementary Note 7.6.4 and Supplementary Fig. 7.12).[156] The striking feature in Fig. 7.1 is the distinct dependency of the ethanol FE on the pulse duration. At $\Delta t_a > 2\,\text{s}$ and $\Delta t_c < 2\,\text{s}$, the formation of ethanol is suppressed. Furthermore, an enhancement in the ethanol FE is observed for $\Delta t_a < 2\,\text{s}$ and

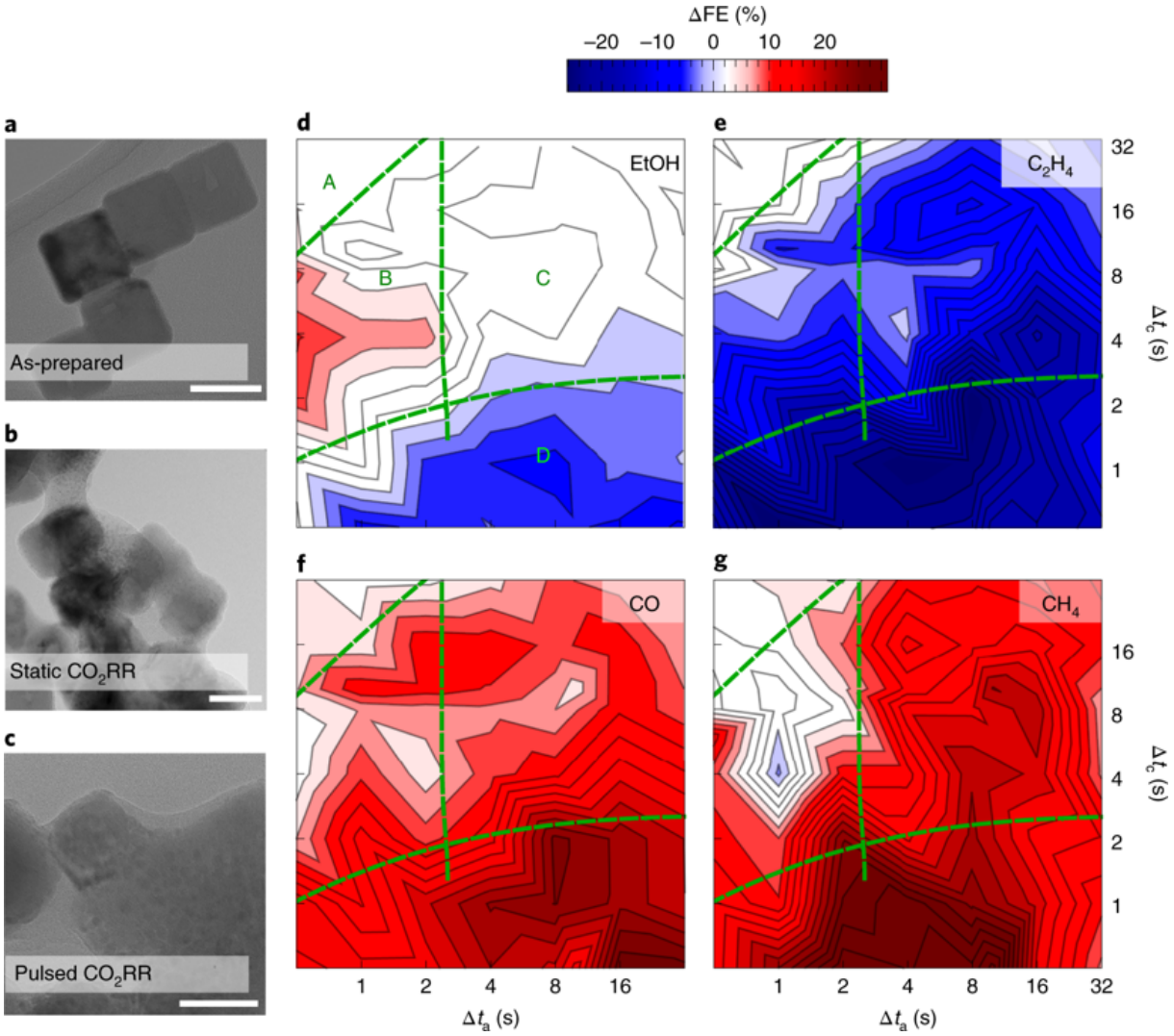

Figure 7.1: Evolution of the catalyst morphology and selectivity under static and pulsed CO2RR. a-c, Ex situ TEM images of as-prepared Cu_2O NCs (**a**), NCs after CO_2RR for 60 min under static −1.0 V (RHE) potential (**b**) and NCs after pulsed CO_2RR for 60 min ($\Delta t_c = \Delta t_a = 10$ s, $E_c = -1.0$ V and $E_a = +0.6$ V) (c). Scale bars correspond to 20 nm. **d-g**, Changes in the FE under pulsed CO_2RR with respect to that under a static −1.0 V potential: excess FE for ethanol (EtOH) (**d**), C_2H_4 (**e**), CO (**f**) and CH_4 (**g**) under pulsed CO_2RR with different lengths of anodic and cathodic pulses (Δt_a and Δt_c, respectively). Regions A-D correspond to distinct regimes with different catalyst surface composition, as explained in the text.

Δt_c values between approximately 1 s and 10 s, with a maximum at $\Delta t_a = 0.5$ s and $\Delta t_c = 4$ s, where the ethanol FE is 1.7 times higher than that under static CO_2RR (Fig. 7.1d). At the same time, the C_2H_4 formation (Fig. 7.1e) is suppressed under pulsed CO_2RR at all Δt_a and Δt_c. The latter is accompanied by a boost in the C_1 product formation (CO, Fig. 7.1f and CH_4, Fig. 7.1g), and the suppression of the H_2 (Supplementary Fig. 7.13a).

Supplementary Note 7.6.3, Supplementary Tables 7.2 and 7.3 and Supplementary Figs. 7.13-7.19 provide additional details on pulse-length dependencies of the catalyst selectivity. In particular, Supplementary Fig. 7.13a shows a remarkable independency of the H_2 selectivity on the pulse duration. This indicates that the enhanced ethanol formation observed for $\Delta t_a < 2$ s and $1\,\text{s} < \Delta t_c < 10\,\text{s}$ cannot be attributed to changes in the hydrogen coverage or local pH. These effects are considered in the prior literature[93,100,101,159] to explain the changes in CO_2RR under pulsed conditions, but should also affect the HER. While we recognize their importance for pulsed CO_2RR in general, they do not play a decisive role in the ethanol selectivity for the pulse lengths and oxidative potential values used here. We also note here that an oxidation of reaction products and intermediates by anodic pulses cannot be ruled out, but is expected to have only a minor impact (Supplementary Note 7.6.1). The FE changes observed in our system thus must stem from two different effects: periodic dynamic changes induced in the catalyst by potential pulses, and the irreversible evolution of the catalyst morphology. Indeed, the ex situ transmission electron microscopy (TEM) images in Fig. 7.1c and Supplementary Fig. 7.5 show that exposure of the catalyst to pulsed CO_2RR conditions for 1 h results in a partial loss of the cubic morphology and the formation of a peculiar granular structure, not observed under static CO_2RR. We attribute these to the dispersion/dissolution- redeposition processes that we recently revealed for cubic copper nanostructures under potentiodynamic CO_2RR-related conditions using electrochemical electron microscopy.[196–198]

To distinguish the relative contribution to the selectivity of dynamic transformations from the concomitant irreversible structural changes also induced by the pulses, the pulse sequence was interrupted after 1 h and the catalyst selectivity was subsequently measured under static CO_2RR conditions after another hour. As shown in Supplementary Figs. 7.13 and 7.14, under these conditions the high FE for CH_4 is preserved, while the FE for C_2H_4 remains low. Thus, the enhancement in CH_4 formation and suppression of C_2H_4 must stem from the irreversibly increased surface roughness and granular morphology. Nonetheless, such morphological changes cannot explain the increase in the CO FE, the suppression of HER and the pulse-length-dependent ethanol FE. In fact, when the pulses are interrupted, the FEs of CO and H_2 mostly return to the level observed for a fresh sample under static CO_2RR conditions. Moreover, the ethanol FE under pulsed CO_2RR appears to be a result of two competing mechanisms: irreversible morphological transformations and dynamic processes. The former have

a detrimental effect, similarly to the case of C_2H_4 (Supplementary Fig. 7.13e,f). The latter, within a narrow range of Δt_a and Δt_c values, results in enhanced ethanol formation, and are probably associated with changes in the copper chemical state. Their transient nature requires us to apply operando methods for their investigation.

7.4.2 Catalyst evolution under pulsed reaction conditions

Periodic reversible changes in the catalyst structure and composition under pulsed CO_2RR with Δt_a=Δt_c = 10 s and E_a = 0.6 V are evidenced by both XAS (Fig. 7.2a,b) and XRD (Fig. 7.2c). In particular, linear combination analysis (LCA) of X-ray Absorption Near Edge Structure (XANES) data (Fig. 7.2d) shows that the Cu(I) fraction increases upon applying the anodic pulse, and decreases during the cathodic pulse. An opposite trend is observed in the Cu(0) concentration, while the Cu(II) concentration varies much less (Supplementary Fig. 7.20). The variations in the fraction of the metallic copper phase and the size of the crystalline copper domains are captured also by the changes in the metallic Cu(311) Bragg peak area and width, respectively. In particular, the amount of metallic copper and the size of the copper domains are smaller under pulsed CO_2RR with respect to those during the static CO_2RR at −1.0 V. Similar variations in the catalyst composition and structure were observed for longer ($\Delta t_a = \Delta t_c = 30$ s) and shorter (Δt_a=$\Delta t_c = 1$ s) pulses (Supplementary Figs. 7.20 to 7.22).

Furthermore, for all pulse durations with Δt_a=Δt_c, the periodic variations of the Cu(I) and Cu(0) concentrations were not accompanied by accumulation of oxide: all oxide species generated during the anodic potential pulse were removed during the subsequent cathodic pulse. The removal of the electrochemically grown oxide species is quick, which contrasts with the sluggish initial reduction of the Cu_2O phase under the static CO_2RR. This implies that only the near-surface layers of the catalyst (up to 0.5 nm, as estimated from the changes in coherence length) are reoxidized during the anodic pulse, while the metallic core structure is maintained. The structure and properties of this electrochemically formed surface oxide probably differ noticeably from the properties of the bulk-like Cu_2O phase in the as-prepared NCs, making it easier to reduce. The formation of a thicker oxide layer can be achieved by increasing the anodic potential value (Supplementary Fig. 7.23e and Supplementary Note 7.6.5).[159] The catalyst properties in this regime of higher Ea values might differ strongly from those of the system exposed to $E_a = 0.6$ V pulses, and are beyond the scope of this paper.

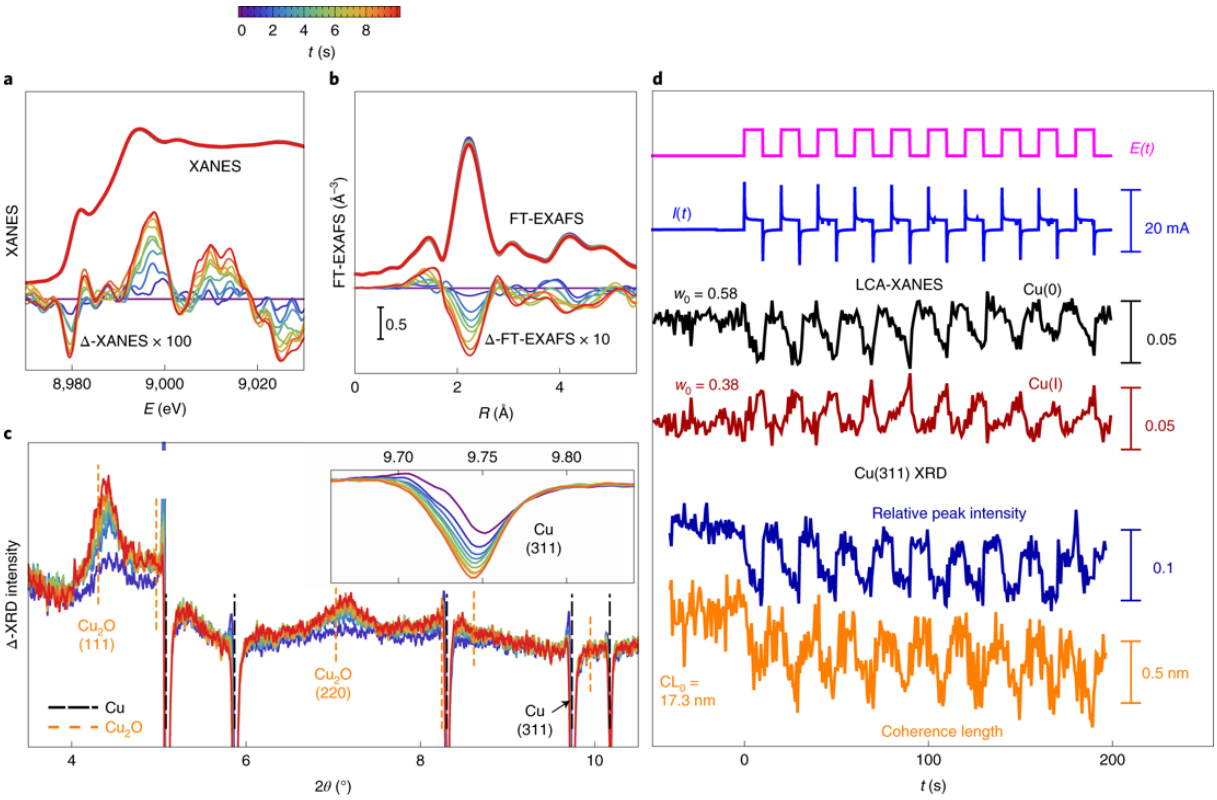

Figure 7.2: Evolution of the operando Cu K-edge XAS and XRD data under pulsed CO2RR. **a**-**c**, Changes in XANES (**a**), EXAFS (**b**) and XRD (**c**) data under an anodic pulse. Data corresponding to different times since the onset of the anodic pulse are shown (see colour bar). Panels **a** and **b** show raw spectra and the differential data, where the XANES or the magnitude of the fourier transformed (FT))-EXAFS corresponding to the onset of the anodic pulse ($t = 0$) were subtracted. Panel **c** shows differential XRD patterns, where the XRD intensities corresponding to $t = 0$ were also subtracted. Inset: zoomed-in region corresponding to the (311) Bragg peak for metallic copper. **d**, Time dependencies of the concentrations of Cu(0) and Cu(I) species from XANES analysis, and changes in the area of the Cu(311) Bragg peak as a measure of the amount of metallic copper, and in the coherence length of the metallic copper domains estimated using the Scherrer equation from the width of the Cu(311) Bragg peak. Time dependencies of the applied potential $E(t)$ and measured current $I(t)$ are also shown. w_0 and CL_0 are the concentration and coherence length, respectively, of metallic copper species at $t = 0$. Pulse parameters: $\Delta t_c = \Delta t_a = 10\,\text{s}$, $E_c = -1.0\,\text{V}$, $E_a = +0.6\,\text{V}$.

7.4.3 Characteristic time scales of catalyst transformations

To better understand the periodic changes in the catalyst structure, we averaged the XAS and XRD data points collected at the same times after the onset of each pulse cycle (Fig. 7.3 and Supplementary Figs. 7.24 to 7.28). The LCA-XANES method and Extended X-ray Absorption Fine Structure (EXAFS) data fitting for the averaged data (Supplementary Fig. 7.24) both revealed the oxidation of copper species and Cu-O bond formation during the anodic pulse, and are in excellent quantitative agreement (Fig. 7.3a and Supplementary Fig. 7.26). The periodic reoxidation of the catalyst is also observed in XRD, as evidenced by the changes in the metallic copper phase (Fig. 7.3b and Supplementary Fig. 7.27), but also by the appearance of Bragg peaks from a Cu_2O-like phase (Fig. 7.3c).

Although the spike in the current $I(t)$ detected upon changing the applied potential and mostly related to double-layer charging is relatively short ($< 1\,s$, Fig. 7.3a), the transformations of the catalyst structure and composition are much slower. Moreover, a strong asymmetry between the oxidation and reduction processes was observed, with the latter being significantly faster. Indeed, although 10–20 s of the anodic potential with $E_a = 0.6\,V$ are required for the oxidation to reach its stationary value, the complete removal of the oxide species generated is achieved within 1–2 s of the cathodic pulse. Similarly, the intensity of the XRD peaks corresponding to the metallic copper lattice decreases within 10–20 s upon application of the anodic pulse, and increases back rapidly, within 1–2 s, upon the onset of the cathodic pulse (Fig. 7.3b and Supplementary Fig. 7.27). When comparing the results for different pulse lengths, we observe that the characteristic reduction and oxidation times are independent of the pulse length (Supplementary Fig. 7.28), and thus can be used as descriptors of a particular sample under a given oxidizing potential (E_a). The XAS and XRD results are also confirmed by quasi in situ XPS measurements (Supplementary Fig. 7.29 and Supplementary Note 7.6.6). In particular, at all pulse lengths, the surface-sensitive XPS method shows much higher variations in the cationic copper concentration due to the potential pulse than the bulk-sensitive XAS, providing important evidence that catalyst oxidation is limited to its surface.

Moreover, even at $E_a = 0.6\,V$, not only Cu(I) species but also some Cu(II) is created during the anodic pulse, as evident from XANES, but also confirmed by observed variations in the Cu–O bond length in the EXAFS data (Supplementary Fig. 7.30). The presence of these Cu(II) species is attributed to the unique surface morphology adopted by the NCs under the harsh pulsed reaction conditions. Cu(II) species are likely to be unstable, as noted in cyclic voltammetry experiments where different Cu oxidation states were tracked by XAS (Supplementary Note 7.6.4) and the generation of Cu(II) coincided with the loss of copper fluorescence intensity. Indeed, Inductively Coupled Plasma - Mass Spectrometry (ICP-MS) analysis of the copper

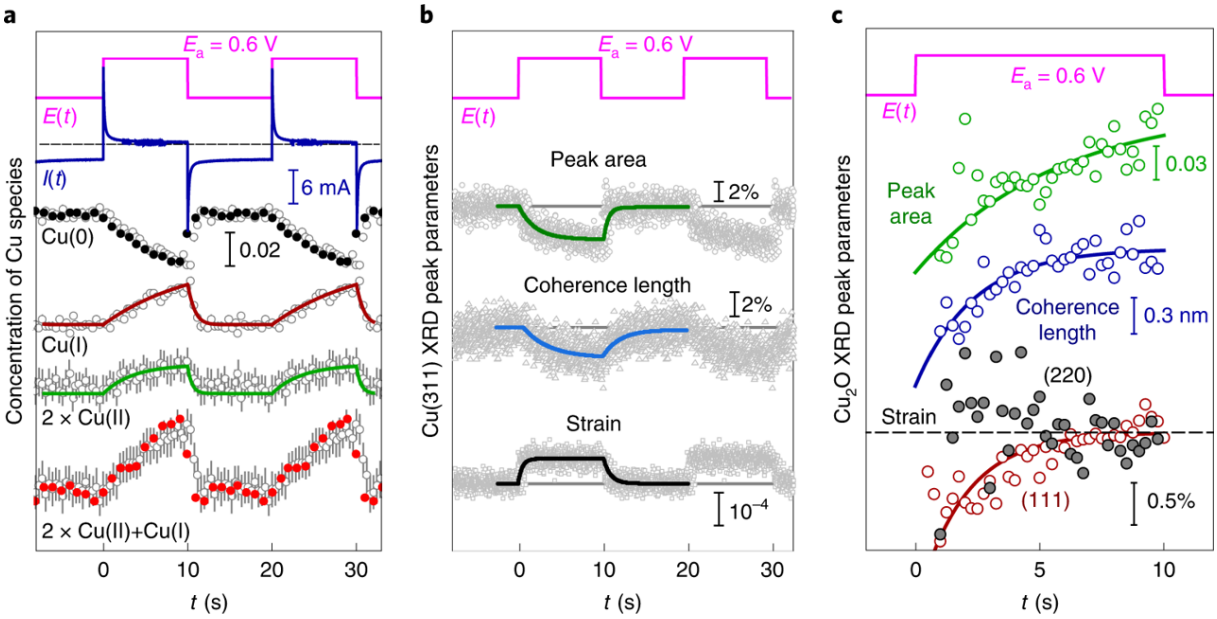

Figure 7.3: Variations in catalyst structure and composition during potential pulse. **a**, LCA-XANES analysis results (grey open circles) for averaged data for NCs under CO_2RR with pulse lengths $\Delta t_a = \Delta t_c = 10$ s, $E_c = -1.0$ V and $E_a = 0.6$ V. Results of EXAFS data fitting (filled black and red circles show the Cu(0) and total Cu(I) and Cu(II) concentrations extracted from Cu–Cu and Cu–O coordination numbers, respectively). Solid lines display the result of fitting concentration profiles for Cu(I) (red line) and Cu(II) (green line) with an analytical model. The concentration profile for Cu(II) is multiplied by 2 for clarity and to account for the twofold larger Cu–O coordination number in CuO than in the Cu_2O bulk structure. Depicted error bars reflect the standard errors of LCA-XANES fitting results. The time dependencies of the potential $E(t)$ and the current $I(t)$ are also shown (vertical bars show the scale for different datasets). **b**, Evolution of the Cu(311) Bragg peak parameters. The relative changes in the Bragg peak area, the copper coherence length and the lattice strain are depicted. **c**, Evolution of the Cu_2O-like Bragg peak parameters during the anodic pulse. The total area of the (111) and (220) Bragg peaks, average coherence length extracted from the (111) and (220) peak broadenings, and the lattice strain for the (111) and (220) lattice spacings are shown. The solid lines in **b** and **c** are guides for the eye (exponential fits).

concentration in electrolyte after CO_2RR shows partial catalyst dissolution under all pulsed regimes investigated (Supplementary Note 7.6.7 and Supplementary Table 7.4), signalling the appearance of unstable species during the anodic pulse. Due to their continuous regeneration, the importance of these species for catalytic activity cannot be excluded. We observe no delay between the formation of Cu(I) and Cu(II) species. In fact, it appears that the generation of Cu(II) species starts slightly before that of Cu(I) species. This suggests that instead of the gradual oxidation [Cu(0) $\rightarrow$ Cu(I) $\rightarrow$ Cu(II)], the generation of Cu(II) species is a separate, independent process [Cu(0) $\rightarrow$ Cu(II)]. The independence of the Cu(0) $\rightarrow$ Cu(II) and Cu(0) $\rightarrow$ Cu(I) processes is also observed in the cyclic voltammetry experiments (Supplementary Note 7.6.4). This leads to a situation that during the short anodic pulse, the concentrations of the Cu(I) and Cu(II) species are comparable, although at large Δt_a values the concentration of Cu(I) is much higher than that of Cu(II). Indeed, in the dataset corresponding to 1 s pulses (Supplementary Fig. 7.26a) the variations in Cu(II) species concentrations seem to be as pronounced as those in the Cu(I) concentration. With increasing E_a, the contribution of Cu(II) species increases strongly (Supplementary Fig. 7.26d). The generation of Cu(II) species at $E_a = 1.0\,V$ is clearly faster than that of Cu(I) species at $E_a = 0.6\,V$, resulting in a steeper drop in the Cu(0) concentration when an anodic pulse is applied (Supplementary Note 7.6.5).

We conclude that under CO_2RR pulses with $E_a = 0.6\,V$, a layer of oxide with mixed valence state (Cu(I)/Cu(II)) is formed on the surface of the copper NCs. Further insights into the structure of this oxide can be extracted from the XRD measurements. The area of the Bragg peaks attributed to Cu_2O shows similar kinetics (with opposite sign) to that of metallic copper (Fig. 7.3b,c). The coherence length of the CuOx phase increases within the entire 10 s anodic pulse, reaching $\sim 3\,nm$ at the end of the pulse. At the same time we observe a gradual expansion of the oxide lattice, as determined from the position of the Cu_2O(111)-like Bragg peak. Importantly, the Cu_2O(220)-like Bragg peak position follows a different trend: the (220) lattice expands during the first 2–3 s upon the application of the anodic pulse, and then slightly shrinks. This suggests a distortion of the Cu_2O-like phase in the early stages of the anodic pulse, which we associate with the growth of (111)-oriented Cu_2O on the metallic Cu(100) surfaces.[83,199] The lattice mismatch between Cu(100) and Cu_2O(111) induces the in-plane expansion and a relatively larger Cu_2O-like (220) lattice spacing. The reduced (111) lattice spacing in the early stages of the anodic pulse might, in turn be a consequence of a tilted growth axis which differs slightly from the surface normal and leads to anisotropic compressive strain in the oxide lattice.[83,199,200] As the oxide layer grows thicker, the distortion gradually diminishes, leading to a rather bulk-like Cu_2O after 10–20 s Changes in the lattice spacing in metallic copper under pulsed CO_2RR are also observed, but are quite different from those in the oxide phase. In particular, the copper lattice expansion upon the application of the anodic pulse is faster than the changes in the Cu_2O(111) Bragg peak position (Fig. 7.3b,c), and the

expansion magnitude practically does not depend on the anodic pulse length (Supplementary Fig. 7.28). This expansion appears to be independent from the copper oxidation process and reflects the charging of the Cu/CuOx interface.

7.4.4 Linking the catalyst's structural evolution to its selectivity

Considering that the oxidation and reduction rates do not depend on the pulse length, we estimate them from the XAS data collected during pulsed CO_2RR with the largest Δt_a and Δt_c values (30 s), and propose a simple kinetic model to predict the time dependencies of the concentrations of Cu(0), Cu(I) and Cu(II) species at arbitrary Δt_a and Δt_c (Supplementary Note 7.6.8, Supplementary Fig. 7.31 and Supplementary Table 7.5). Knowing the latter, we can now focus on: (1) the average concentration of copper oxide species present during the cathodic pulse, (2) the ratio of the Cu(II) and Cu(I) content during the cathodic pulse and (3) the concentration of oxide species remaining after the cathodic pulse is completed (Fig. 7.4a–c). Based on these results and the catalytic selectivity data in Fig. 7.1d–g, we identify four regimes (A–D, Fig. 7.4a–c) with distinct catalytic properties, which stem from distinct catalyst surface compositions. The latter are schematically depicted in Fig. 7.4d. In particular, the enhanced ethanol production at low Δt_a and intermediate Δt_c values (region B) is attributed to an optimal balancebetween oxidized and reduced copper species on the catalyst surface, and the presence of a distorted copper oxide phase.

At larger Δt_c (region A), in the absence of the effect of an irreversible morphology change, the FEs for all CO_2RR products become similar to those observed under static CO_2RR. Here the catalyst is on average completely metallic, and dynamic changes associated with the pulsed protocol take place for proportionally shorter times and cannot affect the catalyst performance noticeably. However, at shorter Δt_c, the oxide species created on the catalyst surface during the anodic pulse have a pronounced impact. Note that the formation of a complete monolayer of surface oxide on cubic nanoparticles ~ 30 nm in size is equivalent to an increase in the oxide concentration by $\sim$3%, which is in good agreement with the maximal increase in the oxide fraction observed in Fig. 7.4a for pulses with $\Delta t_a \ll \Delta t_c$, suggesting that the catalyst surface is completely oxidized during the anodic pulse in this case. During the subsequent cathodic pulse, the surface is completely (region C) or partially (region D) re-reduced, recovering the metallic copper sites active for CO_2RR. The presence of metallic islands on the catalyst surface in direct contact to copper-oxide-rich surface regions during the working pulse has a beneficial effect for CO formation. In particular, the pulse-duration dependency of the excess FE for CO (Fig. 7.1f) has a similar profile as the pulse-duration dependency of the oxide fraction present during the working pulse (Fig. 7.4a), where an increase in the oxide fraction results in

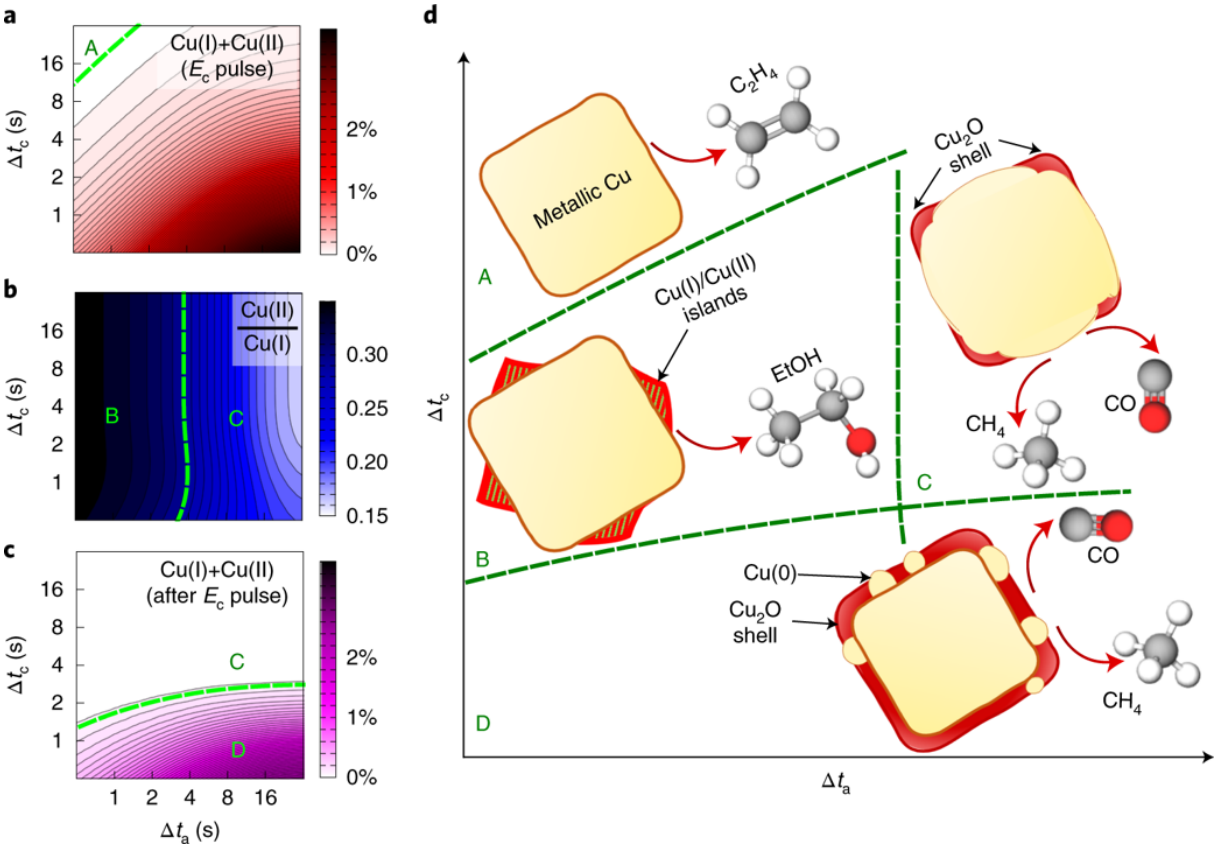

Figure 7.4: Effect of the durations of the anodic (Δt_a) and cathodic (Δt_c) pulses. a-c, Results obtained from the analysis of XAS data for copper NCs during pulses with $E_a = 0.6\,V$, showing the average concentration of the oxide species present during the cathodic pulse (**a**), the ratio of Cu(II) and Cu(I) concentrations during the cathodic pulse (**b**) and the concentration of oxide species that remains after the nth cathodic pulse is completed (**c**). **d**, Schematic depiction of the catalyst structure and composition during a cathodic pulse extracted from XAS and XRD data. The ranges of Δt_a and Δt_c values corresponding to each regime are indicated in **a-c**.

an enhanced CO formation. The latter observation is in agreement with the results obtained under pulsed CO_2RR for a copper foil, where the CO production was favoured over HER when significant accumulation of oxides was observed.[102] While the pulse parameters in ref. [102] differ from those in our work, this study provides additional evidence that strongly oxidized copper surfaces can lead to efficient CO_2 conversion to CO.

The coexistence of metallic and oxidized Cu species is also the key factor for enhanced ethanol formation. As predicted by density functional theory modelling[99,201,202] and corroborated also by recent experimental infrared spectroscopy and in situ XAS data,[203] the asymmetry between CO adsorption energies on metallic and oxidized copper sites facilitates CO dimerization and is essential for C_2 product formation.[201] Nevertheless, the more complex shape of the pulse duration dependency for ethanol production as compared with CO suggests that not only the amount but also the type of copper oxide formed during the anodic regime play a role in the increased ethanol yield. The enhancement in ethanol is observed only for the shortest anodic pulses ($\Delta t_a < 1\,s$, region B), where the distorted oxide structure (as seen from our XRD and XAS data) is formed, featuring also some contribution of Cu(II) species (oxides or hydroxides, Fig. 7.4b). We consider these distorted oxide or hydroxide species, in close contact with metallic copper, to be the crucial sites for the ethanol production. Importantly, an increase of Δt_a results in an increased thickness of the oxide layer that adopts a structure that increasingly resembles the structure of bulk Cu_2O (region C). The latter results in the loss of the enhanced ethanol production. Similarly, the reduction of Δt_c below $\sim 1\,s$ leads to an incomplete reduction of the oxide layer during the cathodic pulse (Fig. 7.4c), resulting in the gradual accumulation of the oxide and the formation of a thicker Cu_2O shell with bulk-like structure (region D). As a consequence, the enhancement in the ethanol production is not pronounced for $\Delta t_c < 1\,s$. The observed peak of the ethanol formation at $\Delta t_c \approx 4\,s$ and $\Delta t_a < 1\,s$ corresponds to the optimal ratio between distorted oxidic and metallic copper sites.

Our advanced operando X-ray studies thus revealed the complex interplay between a (reversible) oxide formation and the catalytic function of oxide-derived cubic copper nanocatalysts. We show the crucial role of the catalyst's surface repopulation with distorted multivalent copper oxide species that boost ethanol production. In contrast, extensive bulk-like copper-oxide formation prevents CO dimerization and rather facilitates CO formation. The observed dependency of the catalyst selectivity on the parameters of the applied pulsed CO_2RR protocol provides opportunities for steerig the catalyst's selectivity on demand.

7.5 Methods

Catalyst synthesis Cu_2O NCs were prepared by adapting a synthesis recipe described in a previous work.[151] Briefy, 4 ml 0.1 M $CuSO_4$ (Sigma-Aldrich, >98%) was diluted in 366 ml H_2O and stirred vigorously. Then 14 ml 1 M NaOH (Alfa Aesar, >97%) was added to start the nucleation process, while the reduction and NC growth were initialized by adding 16 ml of 0.25 M l-ascorbic acid (Sigma-Aldrich, reagent grade) after 10 s. The solution was stirred further for 13 min. The obtained sample was washed two times with an EtOH:H2O mixture (1:1) and once with EtOH. The clean sample, with a copper concentration of 1.2 mg ml^{-1}, as determined by ICP-MS, was stored in 20 ml of EtOH. The electrodes were prepared by drop-casting 42 µl of the former solution on both sides of 1 cm^2 carbon paper (Alfa Aesar, Toray Carbon Paper, GGP-H-60). The total copper loading was 50 µg.

Electrocatalytic measurements Electrocatalytic measurements were performed with an Autolab (Metrohm) potentiostat in a H-type cell equipped with an anion-exchange membrane (Selemion AMV, AGC) separating the cathodic and the anodic compartments. A leak-free Ag/AgCl reference electrode (LF-1, Alvatek) was set close to the working electrode in the cathodic compartment. A platinum gauze electrode (MaTecK, 3.600 mesh cm^{-2}) served as the counter-electrode in the anodic compartment. As electrolyte, 0.1 M $KHCO_3$ (Alfa Aesar, 99.7-100.5%) was purified with a cation-exchange resin (Chelex 100 Resin, Bio-Rad) and saturated with CO_2 (99.995%) for at least 20 min. Online products were determined for the static CO_2RR conditions by taking an aliquot of the electrolyte every 15 min. After applying a linear sweep voltammogram from the open circuit potential to −1.0 V at 20 mV s^{-1}, a potential pulse protocol was carried out with fixed cathodic potential $E_c = -1.0$ V, anodic potential $E_a = +0.6$ V and different lengths of cathodic and anodic pulses. The linear sweep step was omitted for the data points with low Δt_c and Δt_a values, since in this case it contributed non-negligibly to the final yields of reaction products. The pulse sequence was repeated for 4.000 s.

For comparison, after pulsing, another chronoamperometric measurement at constant −1.0 V was performed for 4.000 s. Gas products were detected and quantified after 1 minand every 15 min by online gas chromatography (GC, Agilent 7890B), equipped with a thermal conductivity detector and a flame ionization detector. Liquid products were analysed after each measurement with a high-performance liquid chromatograph (Shimadzu Prominence), equipped with a NUCLEOGEL SUGAR 810 column and a refractive index detector, and a liquid GC (Shimadzu 2010 plus), equipped with a fused silica capillary column and a flame ionization detector. Each presented data point was measured at least three times, and we report the

average values.

All catalytic results in this study are shown in terms of FE. The FE of the gas products was calculated as:

$$\mathrm{FE_x} = \frac{\dot{V} \cdot C_\mathrm{x} \cdot z_\mathrm{x} \cdot F}{A \cdot V_\mathrm{M} \cdot j_\mathrm{total} \cdot \frac{\Delta t_\mathrm{c}}{\Delta t_\mathrm{c} + \Delta t_\mathrm{a}}} \cdot 100\% \tag{7.1}$$

The FE for liquid products (which cannot be measured online, but only after a certain time under pulsed CO_2RR) was calculated as $\mathrm{FE}_x = \frac{V \cdot \Delta C_\mathrm{x} \cdot z_\mathrm{x} \cdot F}{\Delta Q} \cdot 100\%$. The factor $\frac{\Delta t_\mathrm{c}}{\Delta t_\mathrm{c} + \Delta t_\mathrm{a}}$ is used in the FE expression for the gas products to weight j_total according to the total time spent by the catalyst in the Faradaic (cathodic) potential regime. In contrast, for liquid products ΔQ already contains the contribution of the pulse times by integrating the cathodic charge. Here $\mathrm{FE_x}$ is the FE of product x, $\dot{V}$ is the CO_2gas flow rate ($\mathrm{l\,s^{-1}}$), C_x is the volume fraction of the product x detected by GC, z_x is the number of electrons transferred for reduction to product x, F is the Faraday constant ($\mathrm{C\,mol^{-1}}$), A is the geometric area of the electrode ($\mathrm{cm^2}$), V_M is the molar volume ($22.4\,\mathrm{l\,mol^{-1}}$), j_total is the total current density during CO_2 bulk electrolysis ($\mathrm{A\,cm^{-2}}$), $\frac{\Delta t_\mathrm{c}}{\Delta t_\mathrm{c} + \Delta t_\mathrm{a}}$ is a factor to account for the effective CO_2RR time of j_total while pulsing, ΔC_x is the accumulated concentration of product x detected by HPLC or liquid GC ($\mathrm{mol\,l^{-1}}$), ΔQ is the total charge transfer during the electrolysis at constant potential or current (C) and V is the volume of the electrolyte (l).

The electrochemical surface area after 1 h reduction at −1.0 V was obtained by double-layer capacitance with cyclic voltammetry in the non-Faradaic region with variable scan rates. The resulting capacitance of $0.23(2)\,\mathrm{mF\,cm^{-2}}$ corresponds to a 8.5-fold higher surface area compared to the copper foil (0.027 mF). Cyclic voltammetry was carried out between +0.3 and +0.45 Vversus RHE, with scan rates of 20, 40, 60, 80, 100, 120 and $140\,\mathrm{mV\,s^{-1}}$. The amount of dissolved copper in the electrolyte after CO_2RR was determined by ICP-MS (iCAP RQ, Thermo Fisher Scientific). See Supplementary Note 7.6.1 for more details on the analysis of electrocatalytic measurement data.

Characterization of catalyst morphology and composition. The morphology of the catalysts before and after CO_2RR was characterized by Transmission Electron Microscopy (TEM). TEM measurements were performed using a Thermo Fisher 300 kV Titan microscope. The catalysts after CO_2RR were sonicated in 200 µl isopropanol to detach the sample and drop-cast on a nickel lacey carbon grid.

The surface composition of the copper catalysts was determined by quasi in situ XPS in the

as-prepared state of the catalyst, after 1 h reduction under static CO_2RR and after 1 h under pulsed CO_2RR. Following the approach established in our previous work to determine the oxidation state at the cathodic and anodic pulse,[97] the catalytic procedure was interrupted at the respective potential, the sample was washed with water at open circuit potential and directly transferred into an ultra-high-vacuum system for XPS measurements without exposure to air. The ultra-high-vacuum system system was equipped with an X-ray source (XR 50, SPECS) and a hemispherical electron analyser (Phoibos 100, SPECS, $E_{\text{pass}} = 15\,\text{eV}$) and an aluminium anode (Al K_α, $h\nu = 1486.6\,\text{eV}$, 300 W)

Operando XAS measurements and data analysis To collect X-ray Absorption Fine Structure (XAFS) data, operando time-resolved XAS experiments at the Cu K-edge (8979 eV) were carried out in Quick X-ray Absorption Fine Structure (QXAFS) mode at the SuperXAS beamline at the SLS synchrotron (Switzerland). Additional experiments were carried out at the P64 beamline of the PETRA III synchrotron (Germany). In both cases the experiments were carried out in fluorescence mode using a home-made in situ cell for electrochemical measurements. A schematic of the cell is shown in ref. [160]. A platinum mesh and leak-free Ag/AgCl electrode were used as counter-electrode and reference electrode, respectively. The sample was deposited on carbon paper (Sigracet 29 BC, SGL Carbon), with the other side of the substrate covered with Kapton tape. The sample loading used in our operando XAS experiments was $500\,\mu\text{g}\,\text{cm}^{-2}$: this is the maximal loading of the sample that allows us to collect data of good quality, but is still sufficiently low to avoid self-absorption effects in fluorescence XAS data. The sample was mounted in the electrochemical cell with its Kapton-covered side acting as a window for incident and fluorescent radiation, while the side coated with the catalyst was in contact with the electrolyte. As electrolyte we used CO_2-saturated 0.1 M $KHCO_3$, which was continuously circulated through the cell using a peristaltic pump. CO_2flow ($20\,\text{ml}\,\text{min}^{-1}$) was ensured through the cell. The applied potential was controlled with a BioLogic (in the experiments at SuperXAS) or an Autolab (in experiments at DESY) potentiostat.

In the SuperXAS set-up, the super-bending magnet was used as X-ray source. A silicon-coated collimating mirror and platinum-coated toroidal refocusing mirror were used to remove higher-order harmonics, control the beam size and reduce heat load on the monochromator. A Si(111) channel-cut monochromator designed for high-speed scans was used for energy selection. The monochromator oscillated with a 5 Hz frequency, resulting in five XAFS spectra being collected every second. The beam size was 30 µm x 2.5 mm. At P64, a tapered undulator was used as the X-ray source, a Si(111) channel-cut monochromator was used for fast energy selection, and the beam size was less than 2 mm $\times$ 2 mm. The monochromator oscillation frequency was 1 Hz in this case. In both cases a PIPS detector was used for fluorescence intensity

measurements. The intensity of the incident radiation was monitored by a gas chamber filled with nitrogen.

For measurements in QXAFS mode, calibration of the acquired data is essential. For this purpose, we mounted on the surface of our cell a thin CuO pellet, the fluorescence signal from which was used as a reference. Each scan began with the pellet being in the beam, then the sample stage was moved to bring our sample into the beam. To align the spectra, the energy scale for the collected QXAFS spectra was then shifted so that the maximum of the first derivative for the first QXAFS spectrum, which corresponds to the signal from the CuO pellet, is at the same energy as the maximum of the first derivative for the standard CuO spectrum, collected independently at the same beamline. Data calibration was performed using dedicated beamline-specific software (Pro-QEXAFS at SuperXAS, and JAQ at P64).[204] Further data alignment, background subtraction, normalization, averaging and linear combination fitting of XANES spectra were performed using a set of Wolfram Mathematica scripts. EXAFS data extraction from averaged data was performed using Athena software.[181]

EXAFS data fitting for the first coordination shell was performed using the FEFFIT code.[181] Theoretical phases and amplitudes were obtained in self-consistent ab initio calculations with FEFF8.5[205] for bulk copper, Cu_2O and CuO materials. The complex exchange-correlation Hedin-Lundqvist potential and default values of muffin-tin radii as provided within the FEFF8.5 code were employed.

We started with single-shell fitting of the copper foil and Cu_2O data to obtain the values of the amplitude reduction factors S_0^2. The obtained values were used later for the fitting of the experimental EXAFS data for nanocatalysts. Fitting of spectra for reference materials was carried out in the same ranges in k- and R-spaces as the ones later used for the nanocatalysts, to partially compensate for systematic errors due to the limited signal length in k-space. Fitting of EXAFS spectra $\chi(k)k^2$ thus was carried out in R-space in the range from $R_{min} = 1.1$ Å up to $R_{max} = 2.8$ Å. Fourier transform was carried out in the k range from 2.0 $Å^{-1}$ up to 11.5 $Å^{-1}$. Fitting parameters were the coordination numbers N and interatomic distances R and disorder factors σ^2 for Cu-O and Cu-Cu bonds, and the corrections to photoelectron reference energies ΔE_0.

Operando high-energy XRD measurements and data analysis Operando time-resolved high-energy XRD experiments were conducted at the Swedish Materials Science Beamline (P21.2) at Petra III. P21.2 is an undulator beamline equipped with a cryogenically cooled double Laue Si(111) monochromator. The X-ray energy was set to 67 keV ($\lambda = 0.185\,05$ Å) and a working distance of 0.895 m was calibrated using the diffraction pattern of a CeO_2 standard. The

diffraction patterns were recorded using a Dectris Pilatus X CdTe 2M, which is a large-area detector especially suitable for time-resolved high-energy XRD experiments. The acquisition time of the individual detector images was set to 10 s under stationary conditions and to 0.127 s for the time-resolved pulse experiments. Primary data treatment (calibration, masking, detector image integration) was conducted using the software package pyFAI.[206]

A home-made electrochemical cell based on a three-electrode configuration using a leak-free miniature Ag/AgCl reference electrode (3.4 M KCl, eDAQ ET072) and a platinum counter-electrode.[207] A depiction of the operando XRD set-up can be found in Supplementary Fig. 7.6. The electrode potentials were controlled using a Biologic SP-240 potentiostat. The electrode potential and current were recorded together with XRD data to allow precise synchronization of the collected images and the electrode potential. The copper NCs were deposited on the microporous layer of the gas diffusion electrode (Sigracet 29 BC, SGL Carbon) with a loading of 0.3 $mg_{Cu}\,cm^{-2}$. For the operando high-energy XRD experiments, the sample was mounted and, subsequently, the operando X-ray cell was filled with the electrolyte. For alignment, the cell was centred and the gas diffusion electrode was aligned parallel to the X-ray beam using the beam stop diode. Subsequently, the incident X-ray angle was tuned between 0° and 1° to ensure an optimal Cu_2O to graphite Bragg peak ratio, and to ensure a sufficiently small spread of the X-rays on the sample, thus avoiding parasitic peak broadening.

After acquisition of the diffraction pattern under open-circuit conditions, a CO_2RR potential (−1 V versus RHE) was applied for at least 90 min to ensure the reduction of the catalyst. CO_2 was continuously bubbled through the electrolyte to ensure a stable pH. The electrolyte was frequently exchanged to avoid product accumulation.

The data analysis of the diffraction patterns after integration of the detector images was conducted using a set of GNU Octave scripts to perform background pattern subtraction, peak fitting using Lorentz profiles and averaging of the XRD data collected under pulsed CO_2RR. In the latter case, the averaging of the XRD data was conducted after correcting the peak profiles for low frequency variations due to, for example, bubble formation.

We limited the analysis to Cu(311), Cu_2O(111) and Cu_2O(220) Bragg peaks due to their sufficient intensity and minimal overlap with other Bragg peaks. The coherence length (size) of the crystalline domains was estimated from the individual Bragg peaks using the Scherrer equation based on the full width half maximum (FWHM) with a shape factor of 0.89. The lattice strain was calculated as $^{d\,-\,d_0}/_{d_0}$, where d_0 is the corresponding lattice spacing determined for the catalyst under the cathodic pulse from the Bragg peak position. The lattice parameter a of copper was calculated as $\sqrt{h^2 + k^2 + l^2}d$.

For comparison of pulsed CO_2RR conditions realized in different electrochemical cell set-ups, it is critical to ensure that the resistor-capacitor (RC) time constant is shorter than the duration of the studied pulses. In all our cells, we confirmed that this condition if fulfilled and does not limit the studied processes. The RC constants were determined by measuring the double-layer capacitance and the ohmic cell resistance in each cell used upon catalyst pre-reduction. In the H-type cell used for the selectivity measurements, an RC time constant of 38.7 ms (with $C = 2.87\,\text{mF}$ and $R = 13.5\Omega$) was determined for catalysts with the highest catalyst loading considered in our study ($500\,\mu\text{g/cm}^2$). This value is much shorter than the shortest pulse length applied (0.5 s). Lower catalyst loadings led to similar time constants. In our operando XAS cell, the electrode area is twice as large, and the typical resistance is $20\,\Omega$. For our XRD cell, the resistance is $40–50\,\Omega$. The latter was used with a lower catalyst loading ($300\,\mu\text{g/cm}^2$) with an electrode area of 6% of the one used for the XAS measurements.

7.6 Supporting Information

7.6.1 Supplementary Note 1. Analysis of electrocatalytic measurements data

During pulsed conditions, the real CO_2RR-related charge in the cathodic regime overlaps with a variety of additional dynamic electrochemical processes, such as electrode charging, Cu reduction and parasitic reductive reactions. The anodic current, in turn, comprises charging, Cu oxidation and the oxidation of products and intermediates. A detailed determination and quantification of each specific contribution to the current transient is challenging, in particular, due to the heterogeneity of the high-surface area electrode, and would require extensive fast timeresolved product and metal ion detection (e.g., by mass-spectrometry), which goes beyond the scope of this work. Nevertheless, Supplementary Figure 7.16 shows the I-t-profiles in a pulsed CO_2RR regime and demonstrates that the time required for the current to equilibrate during a cathodic pulse constitutes only a small fraction of the applied pulse length, even compared to the shortest pulse length used in this work (0.5 s). As a result, the total charge transferred due to these additional electrochemical processes that have not been taken into consideration here is also small with respect to the total CO_2RR-related charge. This allows us to use a simplified approach, where for the FE calculations for gaseous products we assumed the CO_2RR-related current to be equal to the current achieved upon equilibration. To determine the CO_2RR-related charge for the liquid product FE calculation, the I-t-profiles were integrated over the total reaction time, thereby assuming that the dynamic anodic and cathodic processes mostly cancel out and the CO_2RRrelated charge is approximately equal to the total transferred net charge. This is a valid approximation because currents in the Q_A and Q_B regions (see Supplementary Figure 7.16) should only reflect processes that are likely reversible, such as charging of the electrode, reduction and oxidation of the catalysts. The mathematical integration of the whole current transient, including the anodic charge ($\Delta Q = \Delta Q_{\text{cathodic}} - \Delta Q_{\text{anodic}}$) is therefore equivalent to the integration of each pulse with correction for the non-Faradaic contributions included.

Indeed, Supplementary Figure 7.16 shows that the total transferred net charge per pulse (e.g., ca. 44 mC for pulses with $\Delta t_c = 4$ s and $\Delta t_a = 0.5$ s), is significantly larger than the unbalanced anodic charge per pulse (2.6 mC). We attribute this uncompensated anodic charge to the dissolution of Cu during CuOx reduction as well as oxidation of reaction products and intermediates. Regardless of their origin, however, it is clear that for the pulse durations explored in this study, the electrochemical processes that are not related to CO_2RR can induce only a relatively minor uncertainty of the charge transferred into liquid CO_2RR product formation. The maximal resulting error in FEs, for example for the quantification of ethanol, is ca. 0.7 percentage points, which is significantly lower than the overall uncertainty of our

measurements (ca. 2 percentage points for EtOH, as estimated by repeating measurements and comparing results at each condition at least three times). We note in other regimes (different pulse durations) this systematic uncertainty could be larger, but this concerns the regimes of long anodic pulse durations and short cathodic pulses, i.e., the region with short effective CO_2RR times and, as will be shown below, where worse Faradaic efficiencies with respect to C_{2+} products were obtained. We note here that in this region we do not observe any abrupt changes in the FEs for any or the reaction products, suggesting that the possible systematic errors of our FE calculations still remain lower than random errors and do not affect significantly the accuracy of our results.

7.6.2 Supplementary Note 2. Reduction of nanocubes under static potential

Supplementary Figure 7.7 shows normalized X-ray Absorption Near Edge Structure (XANES), Supplementary Figure 7.7a) and extended X-ray absorption fine structure (EXAFS, Supplementary Figure 7.7b) data for Cu NCs in as-prepared state and under static CO_2RR conditions (in CO_2-saturated 0.1 M $KHCO_3$ electrolyte and under constant applied negative potential (−1.0 V (RHE)). Fourier-transforms of the EXAFS spectra are shown in Supplementary Figure 7.7c.By comparing the spectra with those for reference materials, we can identify the initial local structure and long-range order in Cu NCs to be very similar to that of bulk Cu_2O oxide. Significant fraction of Cu(I) oxide is present also in the Cu NP sample (due to exposure to air). High-energy X-ray diffraction (Supplementary Figure 7.8) data confirm the presence of the crystalline Cu_2O phase in the as-prepared catalyst.

Under applied potential, XAS spectra and XRD patterns experience significant transformations: XRD peaks corresponding to the Cu_2O phase decrease in the intensity, while the reflections corresponding to metallic Cu appear immediately in the X-ray diffractogram, Supplementary Figure 7.8. However, the $Cu_2O(111)$ reflection is visible up to 60 min after applying the CO_2RR potential, suggesting a rather slow transformation of the crystalline Cu_2O. Similarly, a shift of the absorption edge to lower energies and changes in the post-edge XANES 4 feature are observed in Supplementary Figure 7.7a, and suggest Cu reduction. This is confirmed also by insights from EXAFS data, where in Fourier-transformed EXAFS, Supplementary Figure 7.7c, the peak at ca. 1.5 Å (phase uncorrected) corresponding to the Cu-O bond decreases, and a new feature (corresponding to a Cu-Cu bond) appears at ca. 2.2 Å.

We note here that the fact that the features of oxide species after a few hours under CO_2RR conditions are much more obvious in the XAS data than in the XRD data, is a result of the different sensitivities of these techniques. XAS probes the composition of the sample, regardless of the degree of crystallinity, structural disorder, particle sizes, etc. On the other

hand, the XRD signal is strongly dominated by the contribution of well-ordered phases, and the particles, grains or highly disordered oxide inclusions with sizes less than a few nanometers are extremely hard to detect in XRD. The results obtained under static CO2RR conditions suggest thus that the majority of the well-ordered, crystalline Cu_2O phase is gone relatively quickly. Nonetheless, smaller inclusions (with the size of a few nanometers or less) of oxide phase and disordered oxide species are still present even after one hour under applied potential, as evidenced by the XAS data and weak features of the Cu_2O-phase also visible in the XRD data.

To track the reduction of the catalyst by XAS in a quantitative manner, we use two different approaches: linear combination analysis (LCA) of the XANES spectra, and analysis of the coordination numbers extracted from EXAFS data fitting. In the former case, the experimentally acquired Cu K-edge XANES spectra are fitted with a linear combination of reference XANES spectra of metallic Cu (Cu foil), Cu_2O and CuO. Examples of LCA fits are shown in Supplementary Figure 7.9a-b, and the full concentration profiles for Cu(0), Cu(I) and Cu(II) species are provided in Supplementary Figure 7.9c. From EXAFS data fitting (Supplementary Figures 7.10, 7.11) we extract the Cu-Cu coordination number N_{Cu-Cu}, and the fraction of metallic Cu, which is estimated as $N_{Cu-Cu}/12$, where 12 is the number of Cu neighbors in pure bulk metallic Cu with fcc structure. As shown in Supplementary Figure 7.9c and Supplementary Figure 7.11a, XANES and EXAFS provide very similar results, with minor discrepancies at higher metallic Cu concentrations attributed to disorder effects in the EXAFS data, which result in an underestimation of the coordination's numbers.[190,208–211] Note that the EXAFS and XANES results agree not only in terms of Cu-Cu, but also in terms of the Cu-O contribution. As shown in Supplementary Figure 7.9c, a small Cu(II) contribution is initially present in the Cu NCs. The expected Cu-O coordination numbers thus can be estimated as $\widetilde{N}_{Cu-O} = 4w_{CuO} + 2w_{Cu_2O}$, where 4 and 2 are the numbers of the nearest oxygen atoms in bulk CuO and Cu_2O structures, respectively, andw_{CuO} and w_{Cu_2O} are the weights of Cu(II) and Cu(I) species, respectively, as estimated from LCA-XANES. As shown in Supplementary Figure 7.11b, the $\widetilde{N}_{Cu-O}$, estimated from XANES analysis, is in an excellent agreement with the actual Cu-O coordination number obtained from EXAFS fitting. Moreover, the observed small decrease in Cu-O bond length (Supplementary Figure 7.11d) and disorder factor (Supplementary Figure 7.11e) can be attributed to the fact that the Cu-O bond length in CuO is longer than that in Cu_2O (1.937 Å and 1.836 Å, respectively). Thus, the replacement of CuO with Cu_2O results in shorter average Cu-O bond length and narrower bond length distribution. Another interesting trend that can be seen in Supplementary Figure 7.11c is an apparent increase in Cu-Cu distance upon reduction. On one hand this can be attributed to an increasing size or ordered regions of the metallic Cu phase, and the known relationship between their size and interatomic distances.15[212] However, it cannot be excluded that this result is an artifact

due to the aforementioned disorder effect and overlap of Cu-Cu contributions from metallic Cu and that of longer Cu-Cu bonds in gradually disappearing Cu_2O-like phase.

XANES, EXAFS and XRD thus provide internally consistent results and can be used with confidence to follow the evolution of the structure of Cu NCs under CO_2RR conditions. From XAS, we observe that under static CO_2RR conditions, the reduction of the catalyst is slow and takes several hours, and even after such extended time, ca. 20% of Cu remains in Cu(I) state. This sluggish reduction of the Cu NCs is in agreement with recently published data for similar systems.[45,55,107,195] We should note here, however, that the exact reduction rate for Cu NCs, can change from sample to sample due to different sample loadings and distributions over the electrode surface. The contribution of Cu(II) species in the as-prepared sample, in turn, is affected by sample ageing, and also by prolonged exposure to the X-ray beam in air. Beam damage effects for the samples immersed in the electrolyte can be considered negligible.

The trends observed here in the experimental data during a relatively well understood process - Cu_2O reduction under static potential -, and methods established and validated will be useful in interpreting the changes in the catalysts under pulsed CO_2RR conditions, as discussed in the main text.

7.6.3 Supplementary Note 3. Catalyst selectivity

Supplementary Table 7.1 shows the Faradaic Efficiency (FE) for the main CO_2RR products, as yielded by a typical chronoamperometric measurement at −1.0 V vs. RHE. At this potential, the highest selectivity for C_{2+} products is observed, as already reported for differently prepared Cu_2O derived cubes.17-19 The reported results were obtained after 4000 s under CO_2RR. The lack of further significant changes in the CO_2RR product distribution after 4000 s under static conditions is demonstrated in Supplementary Figure 7.17, where the static CO_2RR conditions were reapplied in a fresh, CO_2-saturated electrolyte. After reapplying the CO_2RR conditions, the FEs for the CO_2RR products did not change with time.

FEs observed under pulsed CO_2RR with different pulse durations are summarized in Supplementary Table 7.2. Figure 7.1d-g in the main text and Supplementary Figures 7.13-7.15 show the difference between the FEs observed under pulsed CO_2RR with different pulse lengths, and that under static potential. The excess FEs for the CO_2RR products that are most affected by changes from static to pulsed conditions are shown in Figure 7.1d-g in the main text. The results for H_2 and other significant CO_2RR products are shown Supplementary Figures 7.13-7.15. All results reported were obtained after 4000 s under the respective reaction condition. In all cases, the measured current slightly decreased (from −17 mA) with time under pulsed

CO_2RR, reaching the value between -3 and −20 mA after 4000 s, Supplementary Figure 7.18. For the selected pulse length values, we performed also additional experiments, where the pulse sequence was interrupted after 4000 s, and the catalyst exposed again to static CO_2RR conditions with −1.0 V potential applied. These additional experiments were aimed to disentangle the effect of irreversible changes in the catalyst morphology and that of dynamic changes in the surface oxidation state under pulsed CO_2RR. The FEs obtained after the static CO_2RR conditions were reapplied are summarized in Supplementary Table 7.3.

We first note that in comparison to the CO_2RR under static potential, the pulsed CO_2RR results in a suppression of hydrogen production (Supplementary Figure 7.13a). Importantly, after the pulses are interrupted and a static −1.0 V potential is applied for 4000 s, the FE of hydrogen increases again, and matches that observed under static potential for a fresh sample (Supplementary Figure 7.13d), suggesting that the observed suppression of HER is a dynamic effect that can be attributed to the changes in the adsorbed H coverage, local changes in the pH level or CO_2 concentration, as observed, for instance, in previous studies using hydrophobic polytetrafluoroethylene (PTFE) to prevent the supply of protons to the catalyst[213] and by applying high electric fields to increase the concentration of the cations, and therefore also that of CO_2.[214]

One should expect that the importance of these factors should decrease at longer cathodic pulse durations (longer Δt_c). However, our experiments suggest that HER remains suppressed event at the highest Δt_c accessible. Thus, regardless of the exact mechanism of the HER suppression, its characteristic time scale exceeds the range investigated in our study, and, thus, it cannot be unambiguously identified. One can note, however, that at the longer pulse length there are some indications of irreversible changes in HER selectivity (Supplementary Figure 7.13d), which may contribute to the HER suppression at large Δt_c.

The fact that HER selectivity practically does not depend on the pulse lengths applied, suggests that the intriguing pulse length-dependent enhancement in ethanol selectivity, as observed in Supplementary Figure 7.13c, cannot be attributed to the local changes in adsorbate and/or CO_2 concentrations, as suggested in some previous reports on pulsed CO_2RR (for low anodic potential pulses).[93,98,100,101,159,192,193] The effect of an irreversible change in the catalyst structure induced by the pulse treatments, which appears to be the main reason for the suppressed C_2H_4 formation (since the FE for C_2H_4 remains suppressed after the pulses are interrupted, compare Supplementary Figure 7.13b and Supplementary Figure 7.13e) and enhanced CH_4 formation (Supplementary Figure 7.14a,d), also cannot explain the enhancement of the EtOH selectivity. The latter is evident from the comparison of EtOH selectivity during the pulsed CO_2RR (Supplementary Figure 7.13c) and after the pulsed CO_2RR (Supplementary

Figure 7.13f): in the latter case, the EtOH selectivity is the same or lower than that under static CO_2RR conditions for all Δt_a (sic!) and Δt_c values. Similarly, the very strong enhancement in CO production (FE increases five times, from 5% to ca. 25%) observed under pulsed CO_2RR (Supplementary Figure 7.14b) at all pulse lengths, is also reversible: after the pulse sequence was interrupted, the CO FE returned to the level observed for a fresh catalyst under static CO_2RR (Supplementary Figure 7.14e).

Despite the fact that the mechanisms underlying CH_4 and CO production enhancement are thus different (irreversible changes in the catalyst morphology in the former case and the dynamic changes in catalyst structure and composition in the latter case), for both products we observe that the enhancement in the selectivity under pulsed CO_2RR is less pronounced for the region with Δt_c ca. 4 s and $\Delta t_a < 2$ s. This region corresponds also to the enhanced ethanol production. This observation thus allows us to conclude that the production of CH_4 and CO is competing with the EtOH production, thus, these reaction pathways share common intermediate species. Interestingly, unlike the case of the other major C_1 products, the formation of formate (Supplementary Figure 7.14c and Supplementary Figure 7.14f) is practically unaffected by the pulsed CO_2RR, suggesting that CO_2 conversion to formate is a separate process, decoupled from the CH_4, CO, EtOH and C_2H_4 formation.

Regarding the less significant CO_2RR products, it is interesting to note that the dependency of the FEs for more complex alcohols (propanol and allylalcohol, see Supplementary Figure 7.15) on the length of the applied pulses is qualitatively similar to that observed for ethanol, suggesting the presence of common intermediates and similar reaction pathways. In all of these cases we observe irreversible suppression of the corresponding alcohol production in the region where the Δt_a values exceed the Δt_c values, and an enhancement (at least for EtOH and PrOH) in alcohol selectivity at $\Delta t_a < 2$ s and Δt_c ca. 4 s. In the region where the Δt_a values exceed the Δt_c values, we observe also a suppression of the FE for acetaldehyde (Supplementary Figure 7.15b). However, unlike it was for alcohols, for this CO_2RR product this effect is reversible (Supplementary Figure 7.15d). As will be shown below, in this region of Δt_a and Δt_c values we expect strong reversible oxidation of our catalysts, which appears to be detrimental for acetaldehyde production. This is in line with the Δt_a and Δt_c dependence of the main C_2 products (ethanol, ethylene) as well as that of C_1 products (CH_4, CO), which show a lower and higher FE in this range of Δt_a and Δt_c values, respectively. Thus, the strong Cu oxidation observed in this regime does not facilitate C-C coupling. At the same time, at higher Δt_c values, where the oxide created during the anodic pulse is fully reduced during the cathodic pulse, the acetaldehyde production under pulsed CO_2RR is enhanced in comparison to that under static CO_2RR, which we link to the irreversible changes in the catalyst morphology and highly defective catalyst surface created.

We have tested whether the differences in the effective CO_2RR times (total time during which the catalyst is exposed to working cathodic potential) under different pulse regimes could play a direct role in determining the reaction product distribution. The effective CO_2RR time, calculated as $t_{\text{eff}} = \frac{4000\,\text{s}}{\Delta t_c + \Delta t_a} \Delta t_c$, where 4000 s is the total duration of the pulse experiment, varies in our study between 62 seconds (for $\Delta t_c = 0.5\,\text{s}$ and $\Delta t_a = 32\,\text{s}$) and 3936 s (for $\Delta t_c = 32\,\text{s}$ and $\Delta t_a = 0.5\,\text{s}$). However, Supplementary Figure 7.17 shows that that the duration of the CO_2RR experiment under static (continuous-hold) has very little impact on the distribution of the reaction products. The maximum change was observed for the Faradaic efficiency of ethylene, which in the 15 min static CO_2RR experiment was by ca. 4 percentage points lower than in 66 min experiment. For other reaction products no variations in the Faradaic efficiencies were observed when the duration of the stationary CO_2RR experiment was varied. For the main reaction products, Supplementary Figure 7.19 shows the difference between the FEs under pulsed conditions and the FEs under static reaction conditions, where the duration of the static experiment was chosen to match the effective CO_2RR time under pulsed conditions. Here, the reference values for the FEs for different reaction products were obtained by interpolating the FEs shown in Supplementary Figure 7.17. For pulsed conditions where the effective CO_2RR time was less than 15 min, we used as the reference value the FEs obtained in the static 15 min CO_2RR experiment. The latter was the shortest time for which we could carry out reliable product determination.

As one can see, Supplementary Figure 7.19a-d and Figure 7.1d-g in the main text are practically visually indistinguishable, confirming that the differences in the effective CO_2RR times under pulsed conditions themselves play a very minor role in the dependency of the CO_2RR product distribution on the duration of the applied pulses.

7.6.4 Supplementary Note 4. Identification of the oxidation potentials for Cu nanocubes

During auxiliary XAS experiment carried out at P64 beamline at PETRA-III, we collected insitu QXAFS data during cyclic voltammetry experiments for reduced Cu_2O nanocubes. The potential, applied to the sample, was changed between -1 and + 1 V (without IR correction), with the rate of 1.75 mV/s. A full Cu K-edge XAS spectrum was collected every second, and results of XANES linear combination analysis are shown in Supplementary Figure 7.12. The predominantly metallic state of the reduced catalyst was preserved until the first ca. 1120 s of experiment, where the potential reached ca. 0.56 V. After that, a significant part of Cu(0) was converted into Cu(I) species (see line A in Supplementary Figure 7.12c). In the Cyclic Voltammetry (CV), the onset of Cu(I) formation coincides with a significant increase in the

measured current (Supplementary Figure 7.12d). When the potential is further increased up to ca. 0.75 V (line B in Supplementary Figure 7.12c), the formation of Cu(I) species stops, and we observe the formation of Cu(II) species instead. Importantly, the formation of Cu(II) does not decrease the fraction of Cu(I) species, demonstrating that instead of the further oxidation of Cu(I) species, the formation of Cu(II) occurs via direct oxidation of Cu(0). However, the formation of Cu(II) blocks a further increase in the concentration of Cu(I) species. In the CV, the feature associated with the Cu oxidation to Cu(II) overlaps with that of Cu oxidation to Cu(I). The appearance of Cu(II) species is paralleled by a decrease in the Cu fluorescence signal (Supplementary Figure 7.12a), suggesting that Cu(II) is not stable under reaction conditions and is gradually leached out. When the potential is further increased to 1.0 V and then reduced to below ca. 0.72 V, Cu(II) species are reduced (line C in Supplementary Figure 7.12c) to Cu(I). The reduction of Cu(II) is paralleled by a significant increase in Cu(I) concentration, while the Cu(0) concentration continues to decrease. The latter observation highlights the asymmetry between the oxidation and reduction processes: during the oxidation at potentials larger than 0.75 V_{RHE}, Cu(0) is directly oxidized to Cu(II), with no changes in Cu(I) species concentrations. During the reduction, however, Cu(II) is first reduced to Cu(I). Only upon further reduction of the applied potential to ca. 0.59 V, the reduction of Cu(I) species to metallic Cu is observed in the LCA-XANES data, paralleled by the appearance of a small peak in the CV.

The obtained results allow us to identify the potential value of ca. 0.6 V_{RHE} as the lowest value where Cu(0) to Cu(I) oxidation is possible in our pre-reduced Cu NCs, while a potential of at least 0.8 V_{RHE} is needed to oxidize copper to the Cu(II) state. These values are in a good agreement with those reported for Cu single crystal surfaces, including Cu(100),[156] and provide important clues about relevant potentials for our pulsed experiments. They also highlight the role of time-resolved in situ XAS for the interpretation of experiments in an electrochemical environment.

7.6.5 Supplementary Note 5. Catalyst under CO_2RR pulses with $E_a = 0.0$ V and 1.0 V

As discussed in the main text and illustrated also in Supplementary Figure 7.23c-d, anodic potential pulses with an E_a value of 0.6 V result in the formation of predominantly Cu(I) species. As an important check, Supplementary Figure 7.23a-b shows that no oxidation of copper is observed at anodic pulses with lower E_a value, as, for example, at 0.0 V. Pulses with higher E_a value, in turn, result in significant fluctuations in Cu(II) species concentrations, as shown in Supplementary Figure 7.23e-f. In this regime, the amount of Cu(I) species generated

during the *anodic* pulse is low. However, rather surprisingly, we observe an increase in the Cu(I) species concentration during the *cathodic* pulse. This can be explained by the fact that the reduction of Cu(II) species is a two-step process, where at least some of the Cu(II) species are first reduced to Cu(I) upon the cathodic potential pulse, and then the latter are reduced to metallic Cu(0). For sufficiently short lengths of the cathodic pulse, this results in an accumulation of Cu(I) species, as observed in Supplementary Figure 7.23e. The accumulation of Cu(I) species also means that under the anodic potential pulse the concentration of Cu(I) species is already higher than thermodynamically favorable, leading to the lack of Cu(0) $\rightarrow$ Cu(I) oxidation during the anodic pulse in this case. In fact, closer examination shows that the concentration of Cu(I) is actually slightly decreasing during the anodic pulse. Previous reports suggest that Cu oxidized to Cu(II) state can be leached in an electrochemical environment,2[215] and this is confirmed also by our cyclic voltammetry experiment (see Supplementary Note 7.6.4). By analyzing the changes in the Cu fluorescence signal, we indeed observe some loss of the sample during the pulses with $E_a = 1.0\,V$ (ca. 14% during the 30 min of pulsed CO_2RR).

7.6.6 Supplementary Note 6. Surface composition by quasi in-situ XPS

The surface chemical composition of the as-prepared samples and of samples exposed to static and pulsed CO_2RR was probed by Cu LMM Auger electron spectroscopy (Supplementary Figure 7.28. Spectral fitting revealed that the as-prepared sample consists of 85% Cu(I), with 15% contribution of Cu(II) species, in an excellent agreement with the XAS data (Supplementary Figure 7.9c).

Next, we performed quasi in-situ XPS measurements, where the sample was reduced for 1 h under static CO_2RR conditions, with constant −1.0 V potential applied, and XPS spectra were then collected after transferring the reduced sample to the XPS UHV chamber, without exposing the sample to air. Cu LMM Auger electron spectra fitting suggests that the catalyst surface is completely reduced (the remaining concentration of Cu(I) species is 1%). A larger degree of reduction is observed in the XPS data as compared to the XAS data, confirming the formation of a core-shell like structure, where the catalyst core (probed by bulk-sensitive XAS) remains partially oxidized, while the surface (probed by surface-sensitive XPS) is metallic.

Pulsed CO_2RR was then conducted for the reduced sample, with $\Delta t_c = 4\,s/\Delta t_a = 0.5\,s$ and $\Delta t_c = 4\,s/\Delta t_a = 32\,s$. The values of the applied cathodic and anodic potentials were $E_c = -1.0\,V$ and $E_a = 0.6\,V$, respectively. Following the approach established in our previous work,[156] we compared the surface compositions for the catalysts, where after 1 h of pulsed CO_2RR the pulse sequence was interrupted at the cathodic or anodic pulse, respectively. For both sets of pulse durations, we observe a significant increase in the Cu(I) concentra-

tion, in comparison with that for the sample reduced under static CO_2RR conditions. With $\Delta t_c = 4\,s/\Delta t_a = 0.5\,s$ pulses, for the sample where the pulse sequence was interrupted at the cathodic pulse, a Cu(I) fraction of 7% was observed. If the pulse sequence was interrupted at an anodic potential, the observed oxide fraction was 12%. With $\Delta t_c = 4\,s/\Delta t_a = 32\,s$, the obtained concentrations of Cu(I) species were 24% if the pulse sequence was interrupted at the cathodic pulse, and 43% if the pulse sequence was interrupted at the anodic pulse.

The obtained results thus confirm that the Cu(I) species are regenerated during the anodic pulse, since in both cases the oxide concentration for the sample where the pulse sequence was interrupted during the anodic pulse, was noticeably higher than for the sample, where the pulse sequence was interrupted at the cathodic pulse. Moreover, we observed that the oxide species generated are not completely removed during the cathodic pulse, resulting in an accumulation of oxide, especially at long Δt_a values. We also highlight that the much higher amounts of oxide detected in the surface-sensitive XPS data in comparison to that in bulk-sensitive XAS data, confirms that the oxidation of the catalyst under the anodic pulse starts at the surface. Finally, we note that the amount of Cu(I) species, observed in the XPS data at the conditions corresponding to the enhanced ethanol formation ($\Delta t_c = 4\,s/\Delta t_a = 0.5\,s$), namely, 7%, is similar to the value reported as the optimal for ethanol production in our previous work on single crystal catalysts.[156]

7.6.7 Supplementary Note 7. Determination of Cu catalyst dissolution using ICP-MS

The dissolution of Cu was monitored via ICP-MS by analyzing the electrolytes after the electrochemical treatment. The initial loading of Cu on the carbon support was 50 µg and after 1 h of CO_2RR at constant −1.0 V, the loading reduced to 40(2) µg. The high initial sample loss can be attributed to some catalyst particles that were only in loose contact with the carbon support in the as-prepared sample.

When applying pulsed CO_2RR with $E_c = -1.0\,V$, $E_a = 0.6\,V$ and different pulse lengths, the additional dissolution of the sample was observed. The estimated remaining sample loading for different pulse durations is summarized in Supplementary Table 7.4. In all cases the additional dissolution of the sample during 1 h under pulsed CO_2RR is below 13 µg Moreover, we observe a correlation between the amount of sample dissolved and the ratio of the duration of the anodic pulse and the total cycle duration ($\Delta t_a/(\Delta t_a + \Delta t_c)$. In particular, the dissolution is the highest if $\Delta t_a \gg \Delta t_c$, and is almost negligible if $\Delta t_c \gg \Delta t_a$. This confirms that the dissolution of the catalyst takes place only during the anodic pulse.

ICP-MS measurements were performed also for electrolytes from experiments under reapplied static CO_2RR after the treatment with pulsed reaction protocols. Under a static −1.0 V potential, ICP-MS revealed only minor further Cu dissolution on the sample (below 1 µg), confirming that the dissolution of the Cu NCs (after the quick initial loss of some significant sample fraction) under cathodic potential is not pronounced.

7.6.8 Supplementary Note 8. Extrapolation of Cu(0), Cu(I) and Cu(II) species concentrations to different pulse lengths

Guided by the observations from XAS and XRD data and simple analytical considerations, we can propose a kinetic model for the changes in the Cu species concentrations. Denoting the concentrations of Cu(I) and Cu(II) species as $w_{\mathrm{I}}(t)$ and $w_{\mathrm{II}}(t)$, the rates for Cu(0) oxidation to Cu(I) and Cu(II) denoted as $1/\tau_{0\to I}$ and $1/\tau_{0\to \mathrm{II}}$, the rates for Cu(II) reduction to Cu(I) and Cu(0) given as $1/\tau_{\mathrm{II}\to \mathrm{I}}$ and $1/\tau_{\mathrm{II}\to 0}$, and the rate for Cu(I) reduction as $1/\tau_{\mathrm{I}\to 0}$, we obtain:

$$\begin{cases} \frac{dw_{\mathrm{II}}(t)}{dt} = \begin{cases} \frac{(\Delta w_{\mathrm{II}}(E_{\mathrm{a}}) - w_{\mathrm{II}}(t))}{\tau_{0\to \mathrm{II}}}, & \text{if } t < t_{\mathrm{a}} \\ -\frac{w_{\mathrm{II}}(t)}{\tau_{\mathrm{II}\to \mathrm{I}}} - \frac{w_{\mathrm{II}}(t)}{\tau_{\mathrm{II}\to 0}}, & \text{if } t_{\mathrm{c}} > t > t_{\mathrm{a}} \end{cases} \\ \frac{dw_{\mathrm{I}}(t)}{dt} = \begin{cases} \frac{\max((\Delta w_{\mathrm{I}}(E_{\mathrm{a}}) - w_{\mathrm{I}}(t)); 0)}{\tau_{0\to \mathrm{I}}}, & \text{if } t < t_{\mathrm{a}} \\ -\frac{w_{\mathrm{II}}(t)}{\tau_{\mathrm{I}\to 0}} + \frac{w_{\mathrm{II}}(t)}{\tau_{\mathrm{II}\to \mathrm{I}}}, & \text{if } t_{\mathrm{c}} > t > t_{\mathrm{a}} \end{cases} \end{cases} \tag{7.2}$$

Here we use the fact that the equilibrium concentrations of Cu(0), Cu(I) and Cu(II) depend on the applied potential. If at time $t = 0$ the system is in an equilibrium, when the potential is suddenly increased during the anodic pulse, the system finds itself in a situation with an excess of Cu(0) species, and deficiency in Cu(I) and Cu(II) species. If the difference between the equilibrium Cu(I) concentrations at $E = E_{\mathrm{c}}$ and that at $E = E_{\mathrm{a}}$ is $\Delta w_{\mathrm{I}}(E_{\mathrm{a}})$, and the corresponding value for Cu(II) is $\Delta w_{\mathrm{II}}(E_{\mathrm{a}})$, then in the simplest case of time-independent oxidation and reduction rates $1/\tau$ we end up with the differential equation system (Supplementary equation 7.2). This equation system can be solved analytically, giving rise to a simple fitting formula, which, as can be seen in Figure 7.3a in the main text and Supplementary Figure 7.25, provides very good description of the actual time-dependencies of the Cu(I) and Cu(II) concentrations. The best-fit values of the oxidation/reduction characteristic times τ, and the equilibrium concentration values $\Delta w_{\mathrm{I}}(E_{\mathrm{a}})$ and $\Delta w_{\mathrm{II}}(E_{\mathrm{a}})$ are given in Supplementary Table 7.5. Importantly, for fitting we only use the datasets obtained with 30 s pulses applied, and then apply the obtained model parameter values to describe the data collected with 10 s and 1 s pulse lengths with a good accuracy. Note also that term $max((\Delta w_{\mathrm{I}}(E_{\mathrm{a}}) - w_{\mathrm{I}}(t)); 0)$ accounts for the fact that the formation of Cu(I) will not be efficient if the concentration of Cu(I) already available is larger than the equilibrium value. We neglect here the small decrease of Cu(I) expected in

this case. The term $-\frac{w_{II}(t)}{\tau_{II}\to 0}$ describes the direct reduction of Cu(II) to Cu(0) upon cathodic pulse (in addition to a strong Cu(II) $\rightarrow$ Cu(I) transition). We found that the inclusion of this term is needed to describe the concentration profiles in the $E_a = 1.0\,V$ dataset (Supplementary Figure 7.25d). However, for simplicity we do not include it for $E_a = 0.6\,V$ data, since a good description of the concentration profiles can be obtained without it.

Equation system 7.2 is a convenient tool to describe the dependency of the catalyst composition on the applied pulse lengths: from a single experiment with pulse length 30 s, which allows us to establish the model parameters, we can determine the amounts of cationic Cu species generated at different lengths of the anodic and cathodic pulses (Δt_a and Δt_c). The predicted values are in a good agreement with direct experimental measurements (LCA-XANES analysis of XAS data, collected under CO_2RR with different pulse lengths, see Supplementary Figure 7.30).

It is convenient to summarize the results of such modeling in terms of three parameters: (i) the average amount of oxide present during the working cathodic pulse $\langle w_I + w_{II}\rangle_c = \frac{1}{\Delta t_c}\int_{t_n+\Delta t_a}^{t_{n+1}}[w_I(t) + w_{II}(t)]dt$ ii) the ratios of Cu(II) and Cu(I) species present during the cathodic pulse, $\langle w_{II}\rangle_c/\langle w_{II}\rangle_c$, and (iii) the excess of oxide species that is remaining after the *n*-th cathodic pulse is completed $w_I(t_n) + w_{II}(t_n)$. Note that $t_n = nx(\Delta t_a + \Delta t_c)$ refers to a point in time corresponding to the end of n cycles of anodic and cathodic pulses. For calculations we choose n to be sufficiently large to properly account for oxide accumulation effects ($n = 100$ is used in all cases presented). These three quantities are convenient because they describe three important aspects of the system: amount of oxide that coexists with metallic Cu during the working pulse, the nature of oxide present during the working pulse, and the accumulation of oxide species. These calculated quantities are reported in Figure 7.4a-c in the main text.

7.6.9 Supplementary Figures

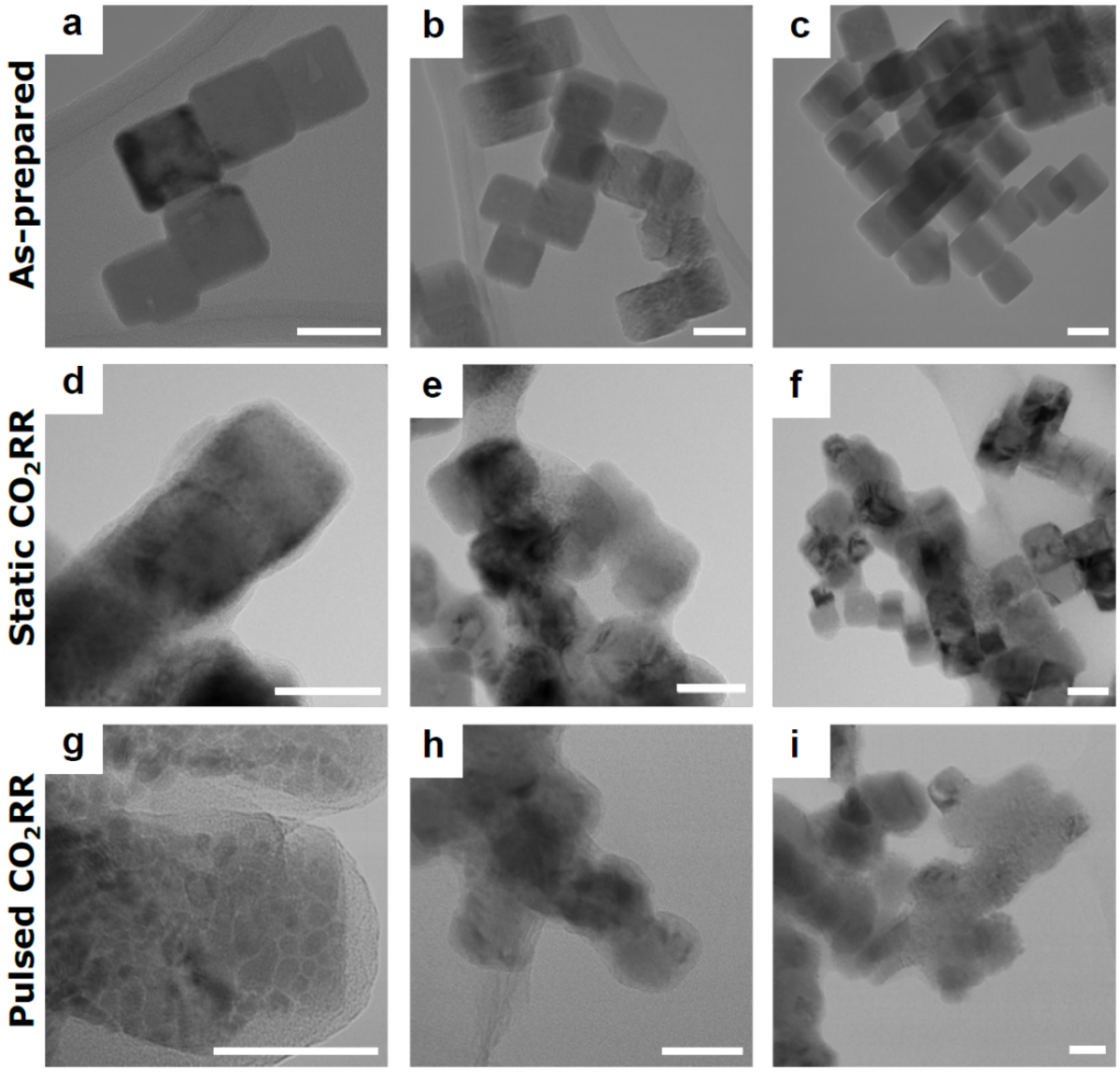

Supplementary Figure 7.5: TEM images of (a-c) as-prepared Cu NCs, (d-f) Cu NCs after CO_2RR for 60 min under static –1.0 V (RHE), and (g-i) Cu NCs after pulsed CO_2RR for 60 min ($\Delta t_c = \Delta t_a = 10$ s, $E_c = -1.0$ V and $E_a = +0.6$ V). The scale bars correspond to 40 nm.

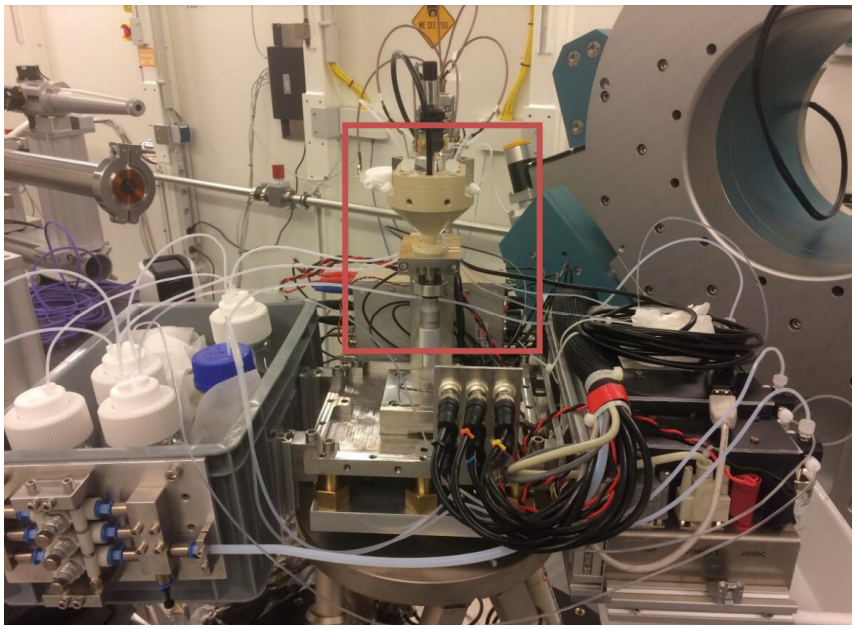

Supplementary Figure 7.6: Operando cell for surface X-ray diffraction measurements in an electrochemical environment (see Ref.[207] for more details).

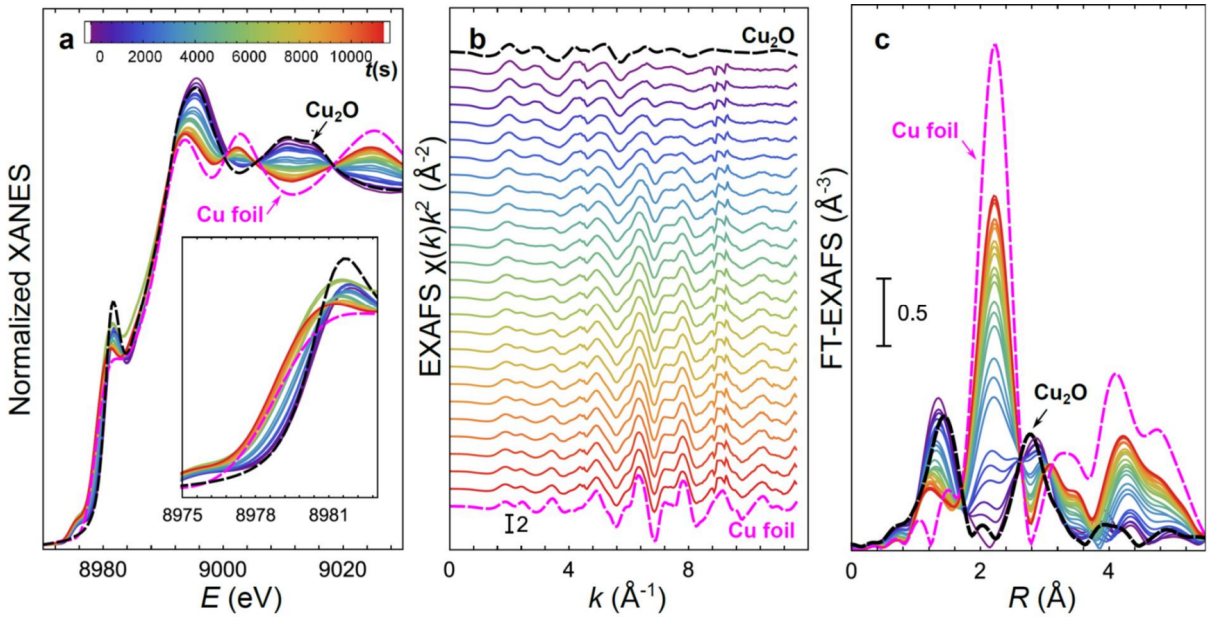

Supplementary Figure 7.7: Time-dependent Cu K-edge XAS for Cu NCs reducing under static CO_2RR conditions. (a) XANES, (b) EXAFS and fourier transformed (FT) EXAFS (c) for Cu_2O nanocubes in CO_2-saturated 0.1 M $KHCO_3$ at −1.0 V (RHE).

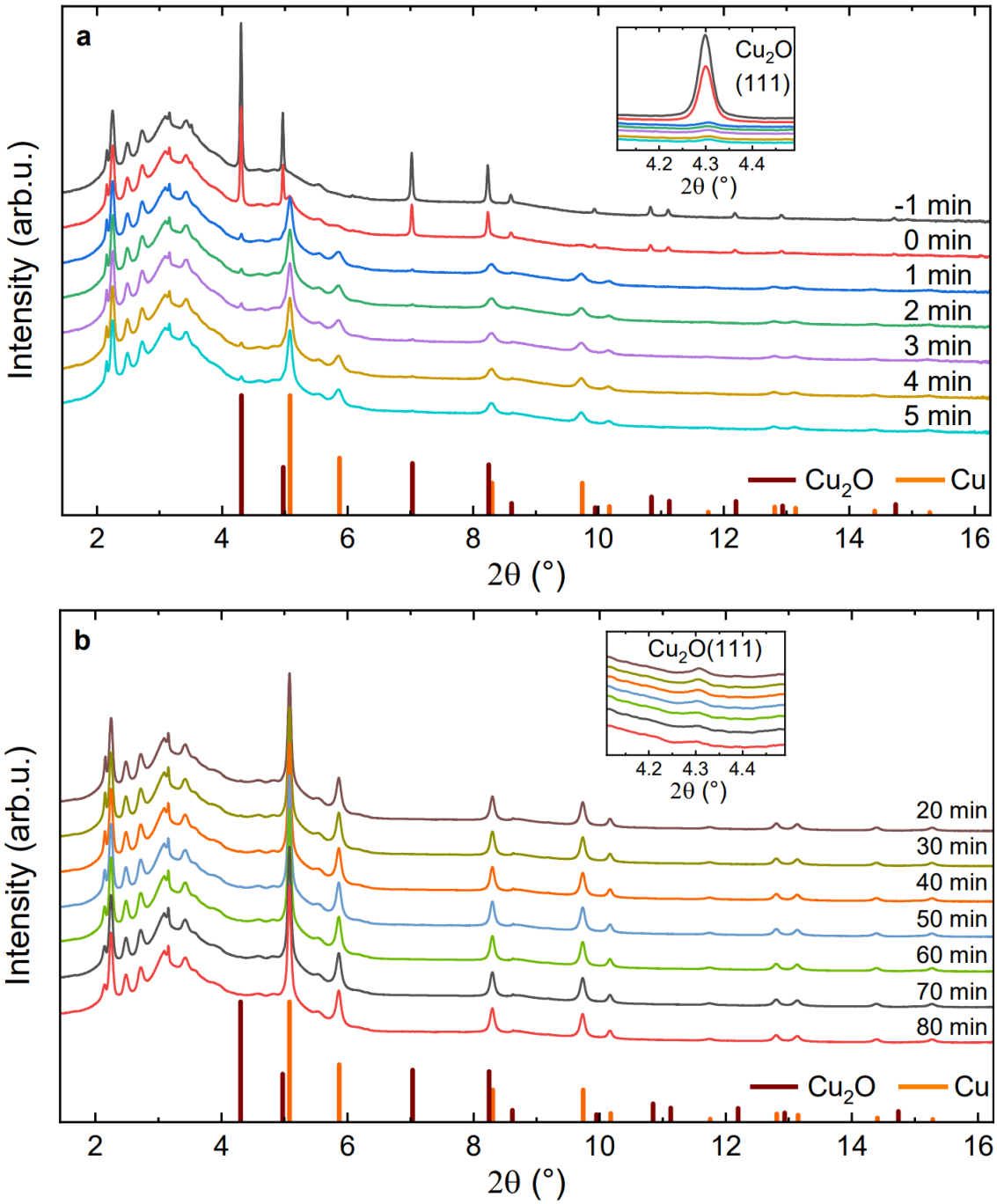

Supplementary Figure 7.8: Time-resolved XRD pattern for Cu NCs under static CO_2RR conditions. (a) XRD pattern recorded before and during the initial 5 minutes of CO_2RR in CO_2-saturated 0.1 M $KHCO_3$. (b) XRD pattern subsequently recorded during the initial 80 min of CO_2RR. The reference peak positions of Cu_2O (brown) and Cu (orange) phases are shown as bar plots. All additional diffraction peaks, especially those below 6°, are caused by the graphite of the gas diffusion electrode and the PEEK walls of the operando cell. The insets show the evolution of theCu_2O(111) Bragg peak during the initial reduction.

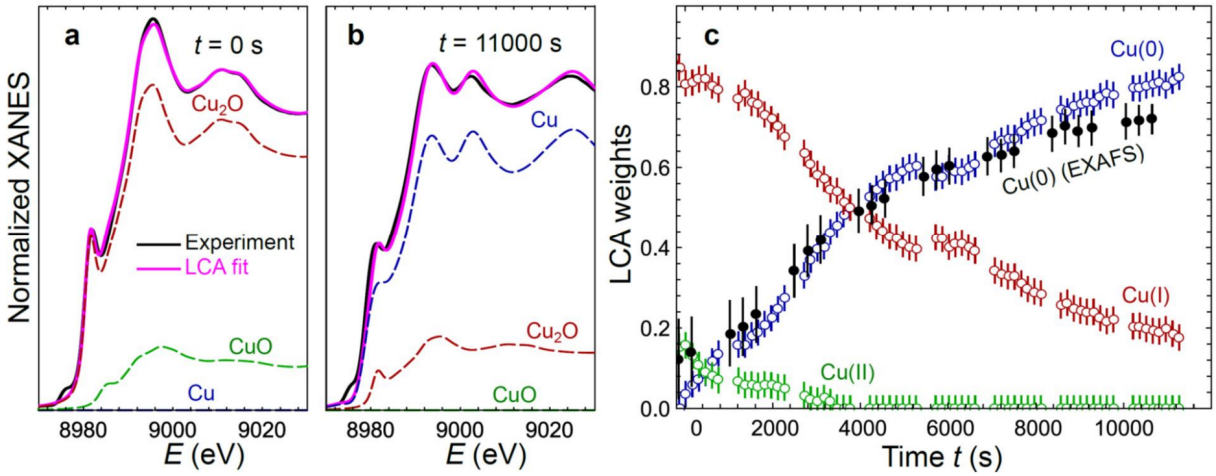

Supplementary Figure 7.9: Linear combination analysis of XANES data for Cu NCs reducing under static CO_2RR conditions. LCA fits (a,b) for a sample in as-prepared state and in the reduced state. Dashed lines show reference spectra used for fitting (Cu K-edge XANES for bulk Cu, Cu_2O and CuO), scaled by their weight in the respective linear combination. Concentration of Cu(0), Cu(I) and Cu(II) species, as obtained from LCA fits (c). Filled black circles in (c) show the concentration of metallic Cu(0), as estimated from Cu-Cu coordination numbers obtained in EXAFS data fitting. Depicted error bars reflect the standard errors of LCA XANES and EXAFS fitting results.

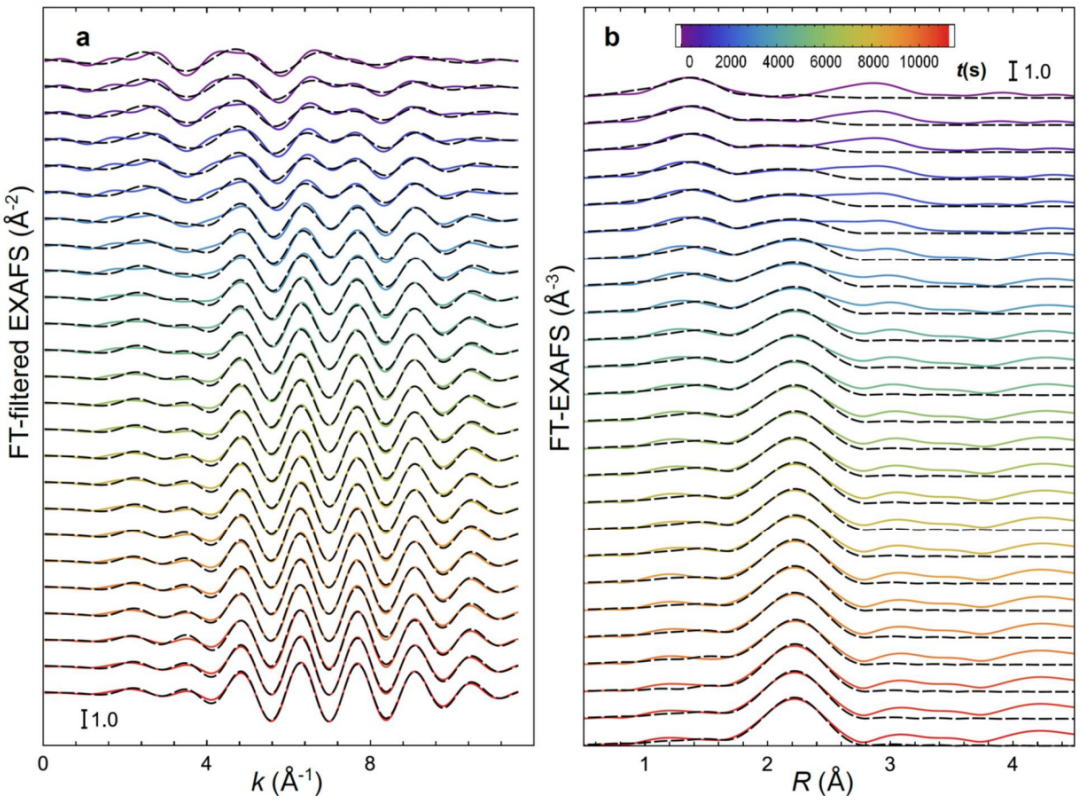

Supplementary Figure 7.10: EXAFS fitting results for Cu NCs under static CO_2RR conditions. Experimental (solid lines) and fitted (black dashed lines) Fourier-filtered EXAFS spectra (a) and fitting results in *R*-space (b). Spectra are shifted vertically for clarity.

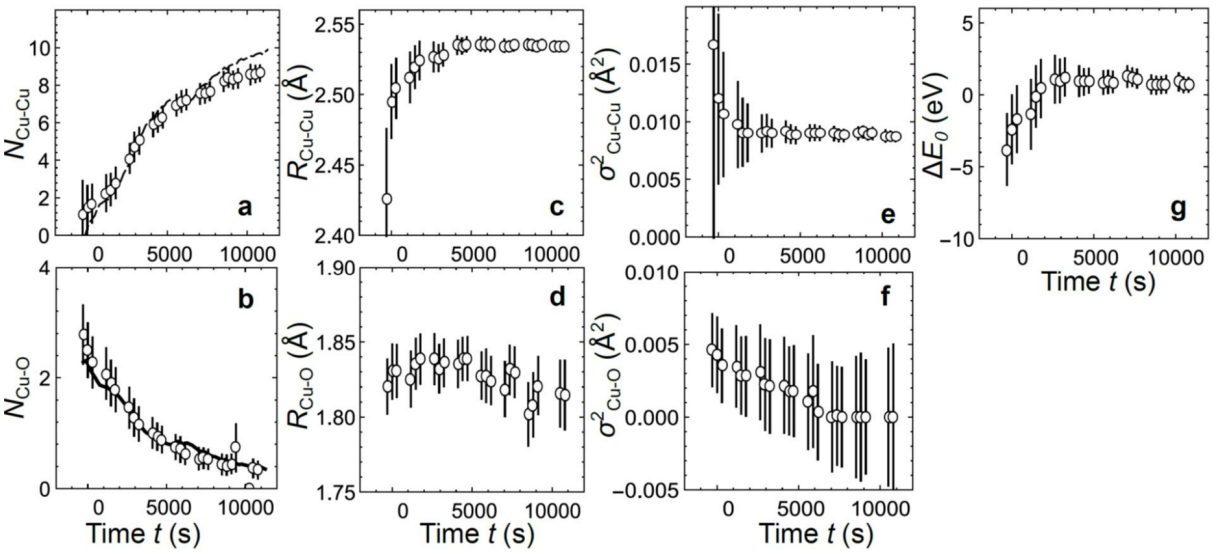

Supplementary Figure 7.11: Structure parameters extracted from EXAFS data fitting for Cu NCs under static CO_2RR. Time-dependent changes in Cu-Cu (a) and Cu-O (b) coordination numbers (N_{Cu-Cu} and N_{Cu-O}), Cu-Cu (c) and Cu-O (d) interatomic distances (R_{Cu-Cu} and R_{Cu-O}), Cu-Cu (e) and Cu-O (f) disorder factors (σ^2_{Cu-Cu} and σ^2_{Cu-O}), and the correction to the photoelectron reference energy ΔE_0 (g). Depicted error bars reflect the standard errors of EXAFS fitting results.

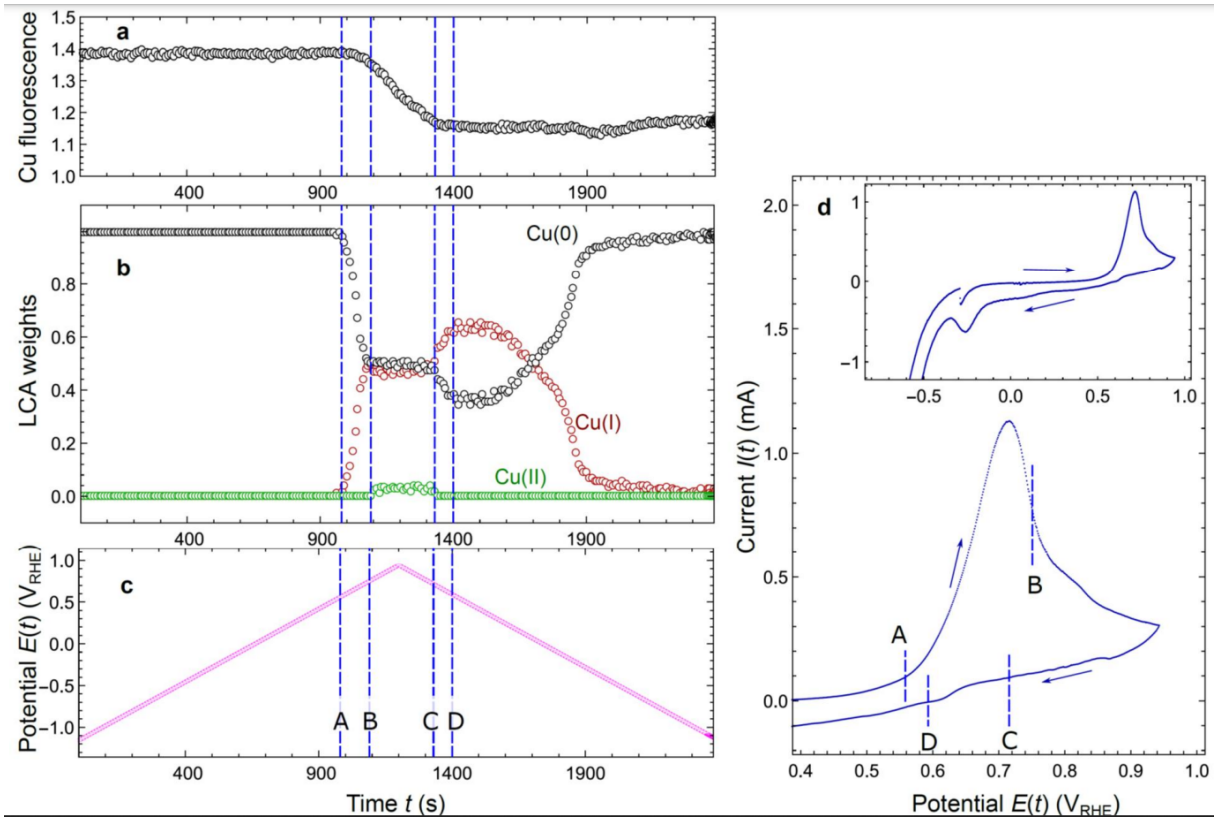

Supplementary Figure 7.12: Oxidation and reduction of Cu NCs during the cyclic voltammetry experiment. (a) Changes in Cu species fluorescence intensity during the CV scan. (b) Timedependency of Cu(0), Cu(I) and Cu(II) concentrations, as observed by LCA analysis of timeresolved XANES data. (c) Corresponding changes in the applied potential, with the potential values corresponding to the onset of Cu oxidation to Cu(I) state (A) and Cu(II) state (B), as well as to reduction of Cu(II) species (C) and Cu(I) species (D). (d) Corresponding cyclic voltammogram at 1.75 mVs^{-1} scan rate.

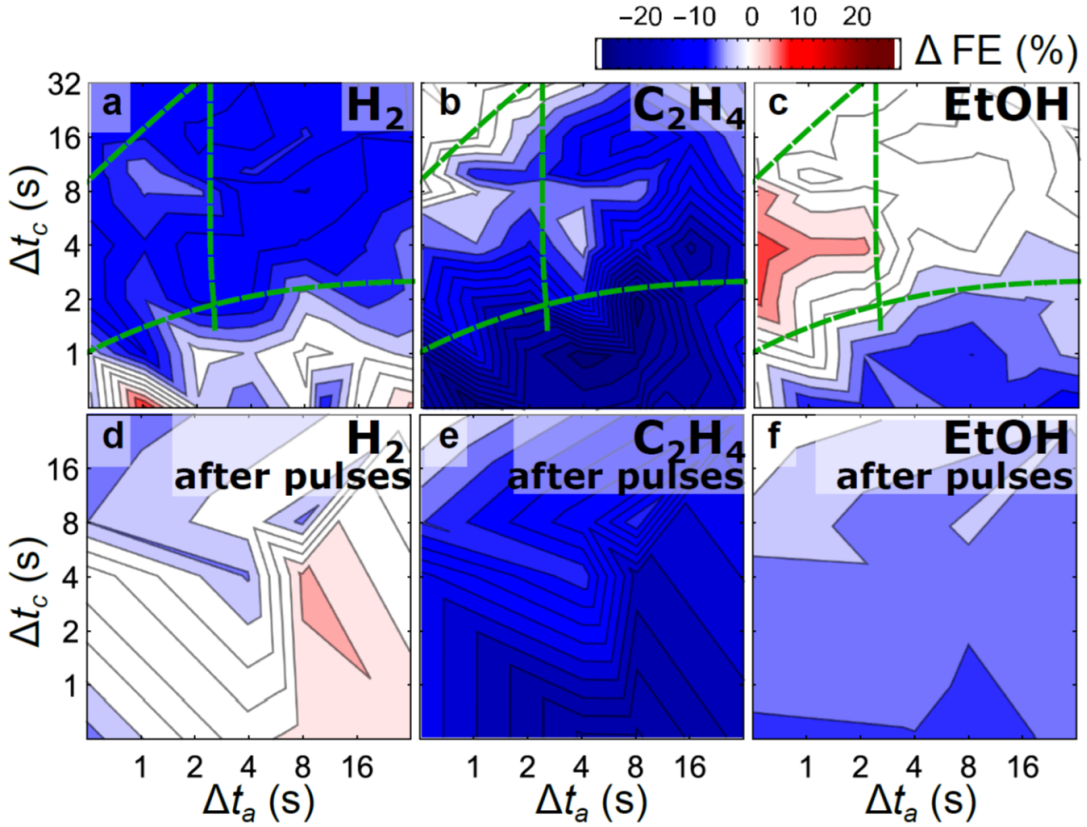

Supplementary Figure 7.13: Faradaic efficiencies for Cu NCs under pulsed CO_2RR with varied pulse lengths Δt_a and Δt_c. The values for the cathodic and anodic potentials are $E_c = -1.0\,V$ and $E_a = 0.6\,V$ vs. RHE, respectively. Depicted are changes in the FE under pulsed CO_2RR with respect to that under static −1.0 V potential. The excess FE for the H_2 (a), C_2H_4 (b) and EtOH (c), are shown. Dashed green lines indicate the boundaries of regions with distinct catalyst surface structure and composition, as discussed in the main text. (d,e,f) show the corresponding excess FEs under static CO_2RR after treatment for 1 h with pulses with different durations.

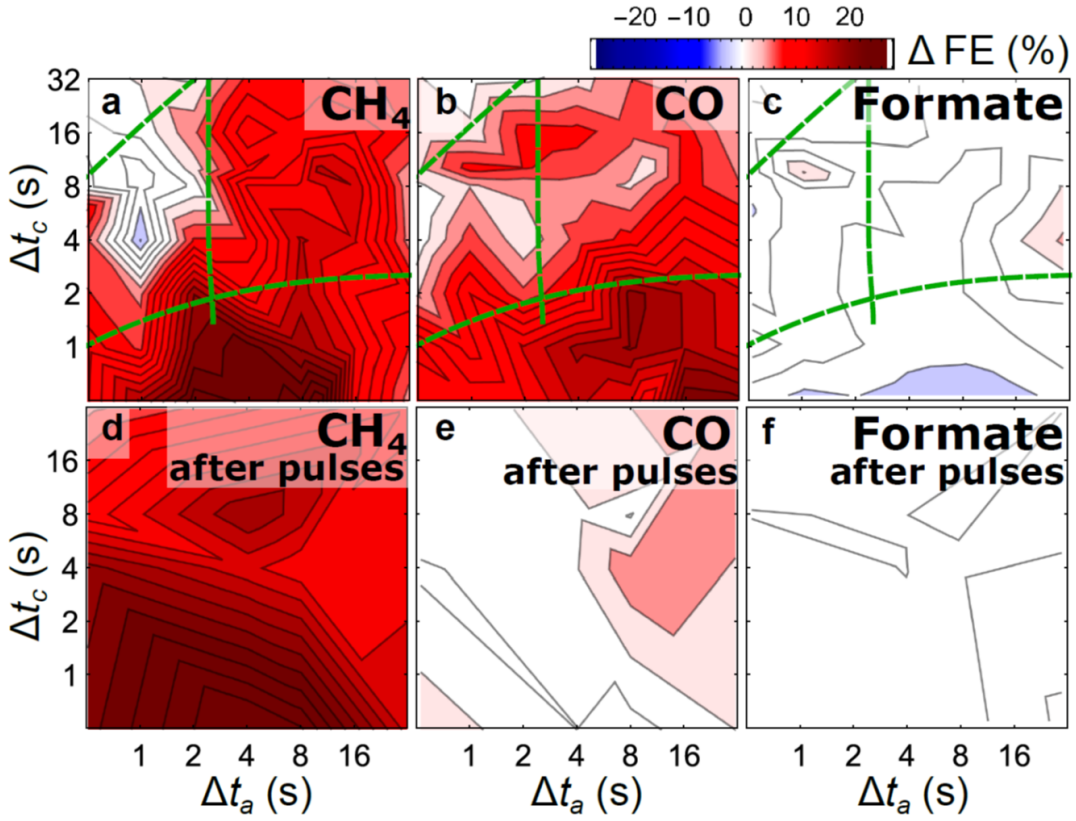

Supplementary Figure 7.14: Faradaic efficiencies for Cu NCs under pulsed CO_2RR with varied pulse lengths Δt_a and Δt_c. The values for the cathodic and anodic potentials are $E_c = -1.0\,V$ and $E_a = 0.6\,V$ vs. RHE, respectively. Depicted are changes in the FE under pulsed CO_2RR with respect to that under static −1.0 V (vs RHE) potential. The excess FE for the CH_4 (a), CO (b) and formate (c), are shown. Dashed green lines indicate the boundaries of regions with distinct catalyst surface structure and composition, as discussed in the main text. Panels (d,e,f) show the corresponding excess FEs under static CO_2RR after treatment for 1 h with pulses with different durations.

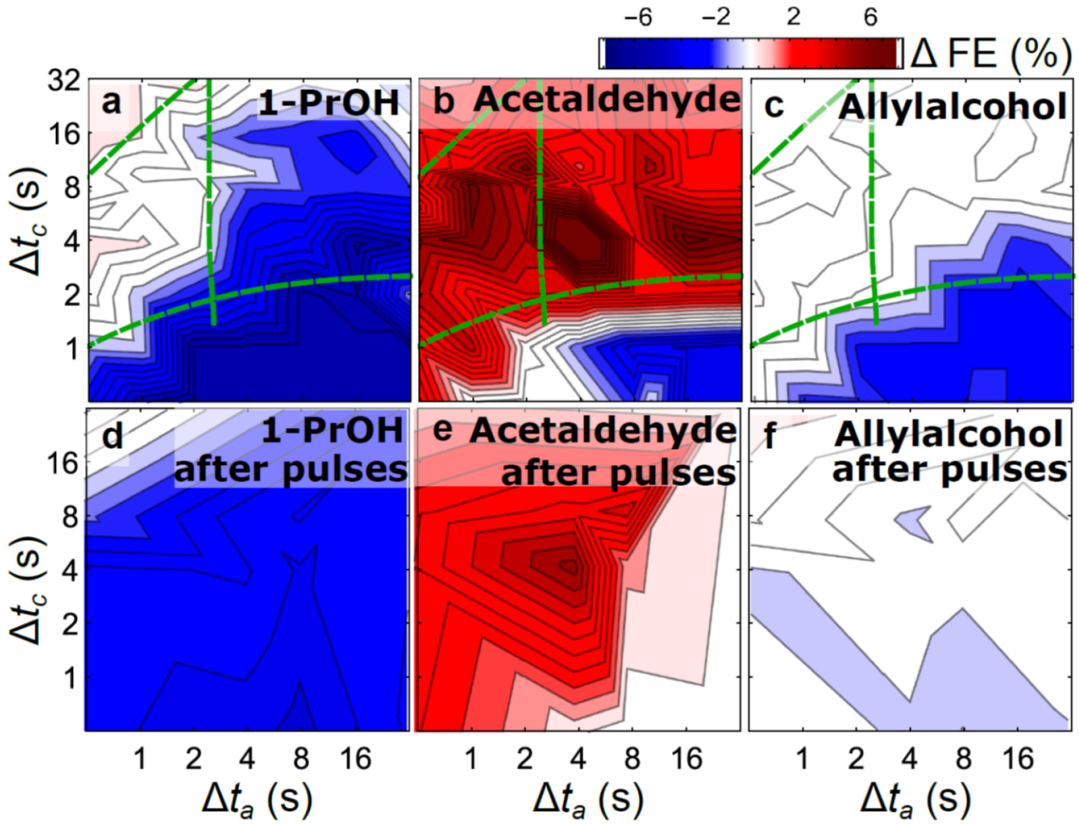

Supplementary Figure 7.15: Faradaic efficiencies for Cu NCs under pulsed CO_2RR with varied pulse lengths Δt_a and Δt_c. The values for the cathodic and anodic potentials are $E_c = -1.0\,V$ and $E_a = 0.6\,V$ vs. RHE, respectively. Depicted are changes in the FE under pulsed CO_2RR with respect to that under static −1.0 V potential. The excess FE for 1-PrOH (a), acetaldehyde (b) and allylalcohol (c), are shown. Dashed green lines indicate the boundaries of regions with distinct catalyst surface structure and composition, as discussed in the main text. Panels (d,e,f) show the corresponding excess FEs under static CO_2RR after treatment for 1 h with pulses with different durations.

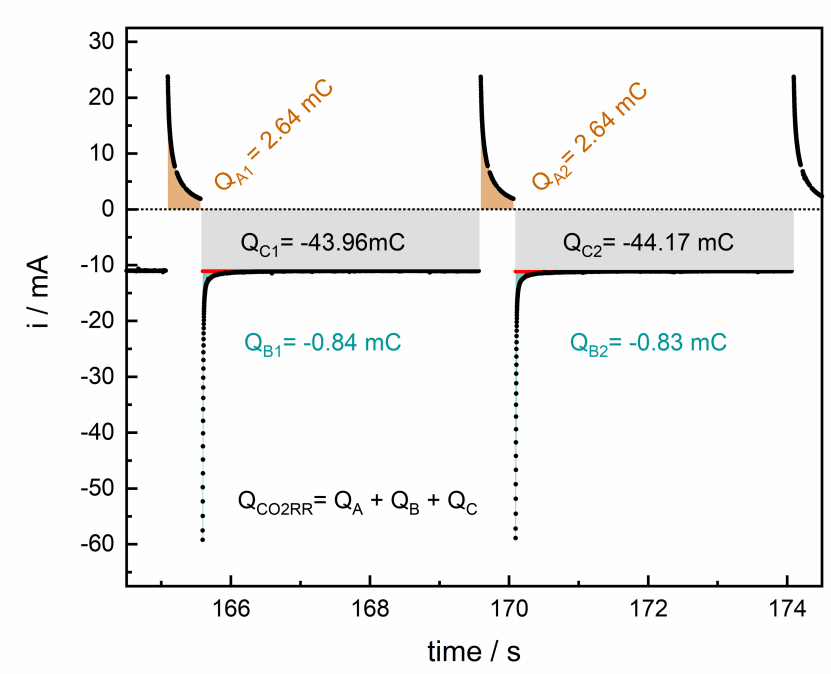

Supplementary Figure 7.16: Example of a current transient of pulsed CO_2RR at $\Delta t_c = 4\,s$ and $\Delta t_a = 0.5\,s$ with the corresponding oxidative (Q_A), reductive (Q_B) and CO_2RR charges (Q_{CO2RR}).

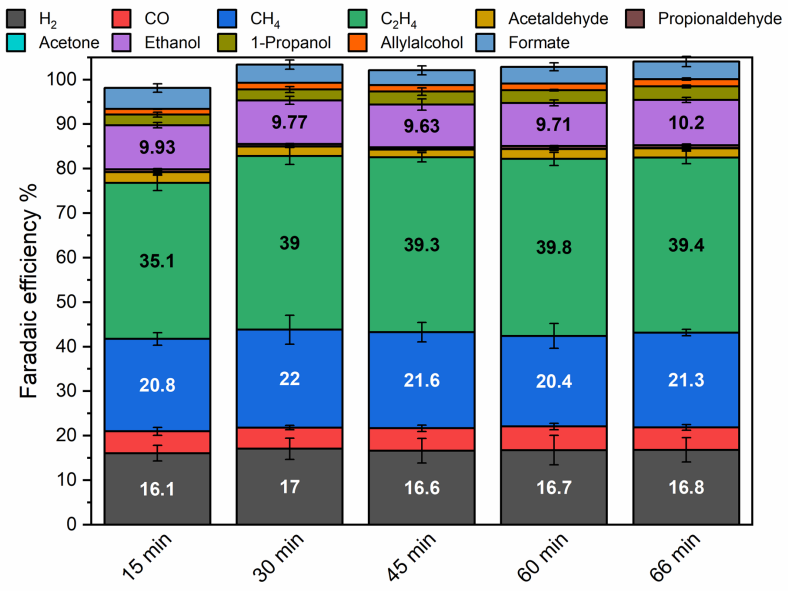

Supplementary Figure 7.17: Faradaic efficiencies of the gaseous and liquid CO_2RR products during 4000 s of reapplied stationary CO_2RR conditions (after initial exposure to static CO_2RR for 1 h) at −1.0 V vs. RHE. Depicted error bars reflect the standard deviation of the values obtained in at least three repeated measurements.

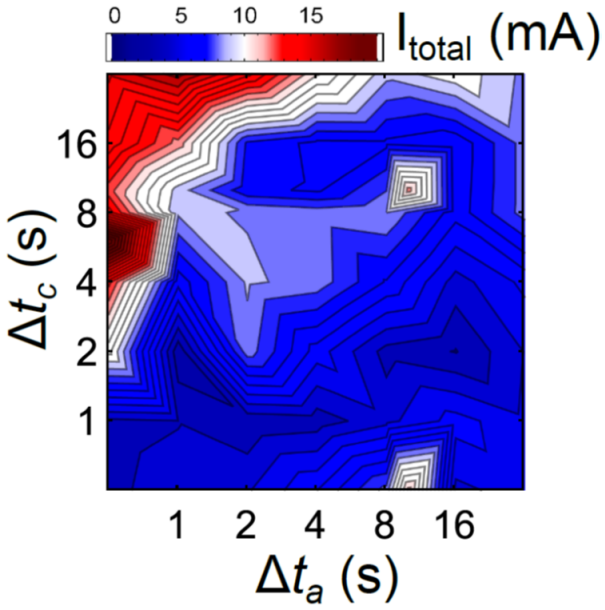

Supplementary Figure 7.18: The dependency of the total current under pulsed CO_2RR conditions on the pulse lengths Δt_a and Δt_c. The values for the cathodic and anodic potentials are $E_c = -1.0\,V$ and $E_a = 0.6\,V$ vs. RHE, respectively.

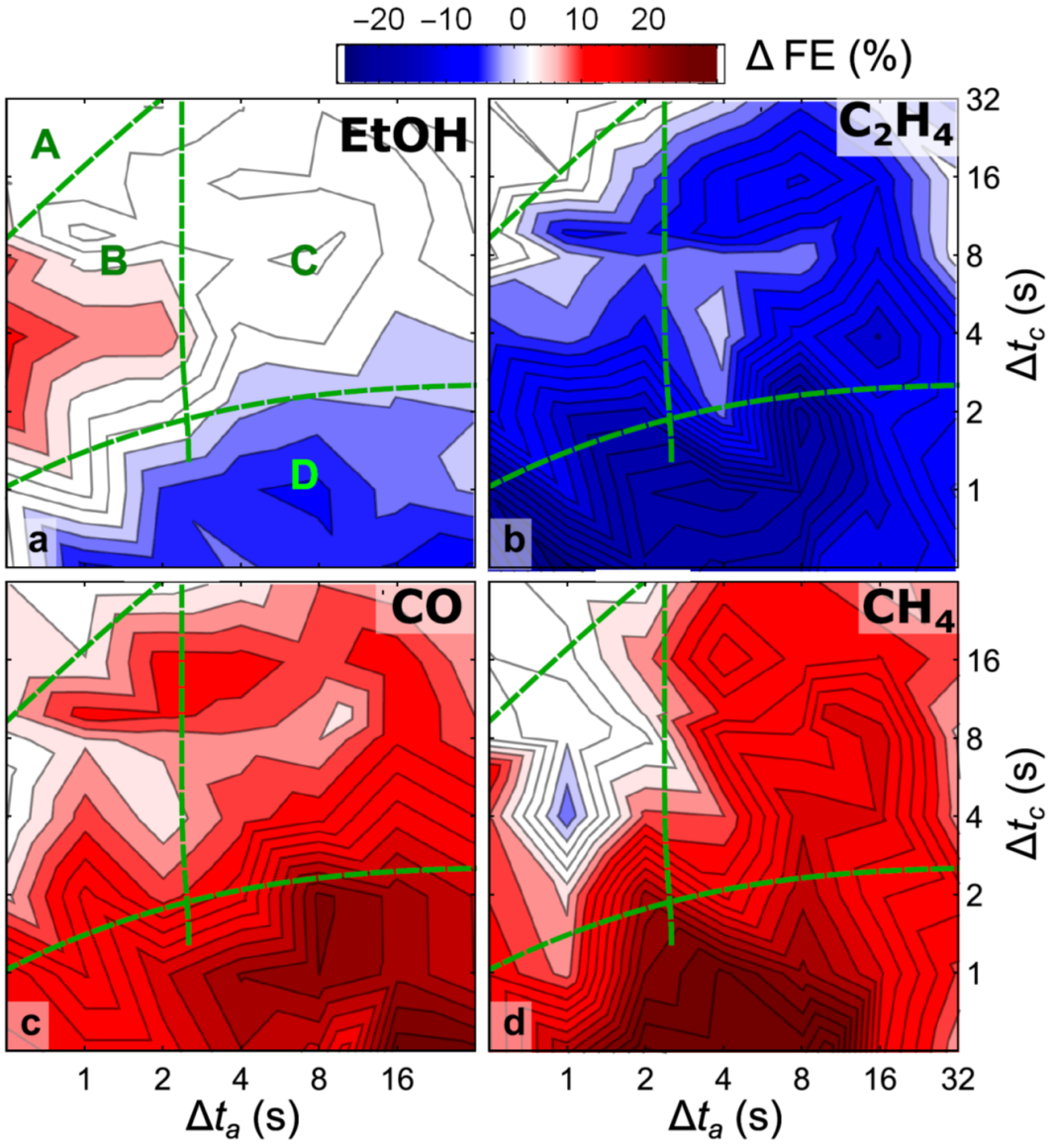

Supplementary Figure 7.19: Changes in the FEs of the main CO_2RR products under pulsed CO_2RR with respect to those observed in static CO_2RR experiments at −1.0 V with a duration matching the effective CO_2RR time in the respective pulsed regime. The excess FE for EtOH (a), C_2H_4 (b), CO (c) and CH_4 (d) under pulsed CO_2RR with different lengths of the anodic and cathodic pulses are shown. Regions A, B, C and D correspond to distinct regimes with different catalyst surface composition, as explained in the main text.

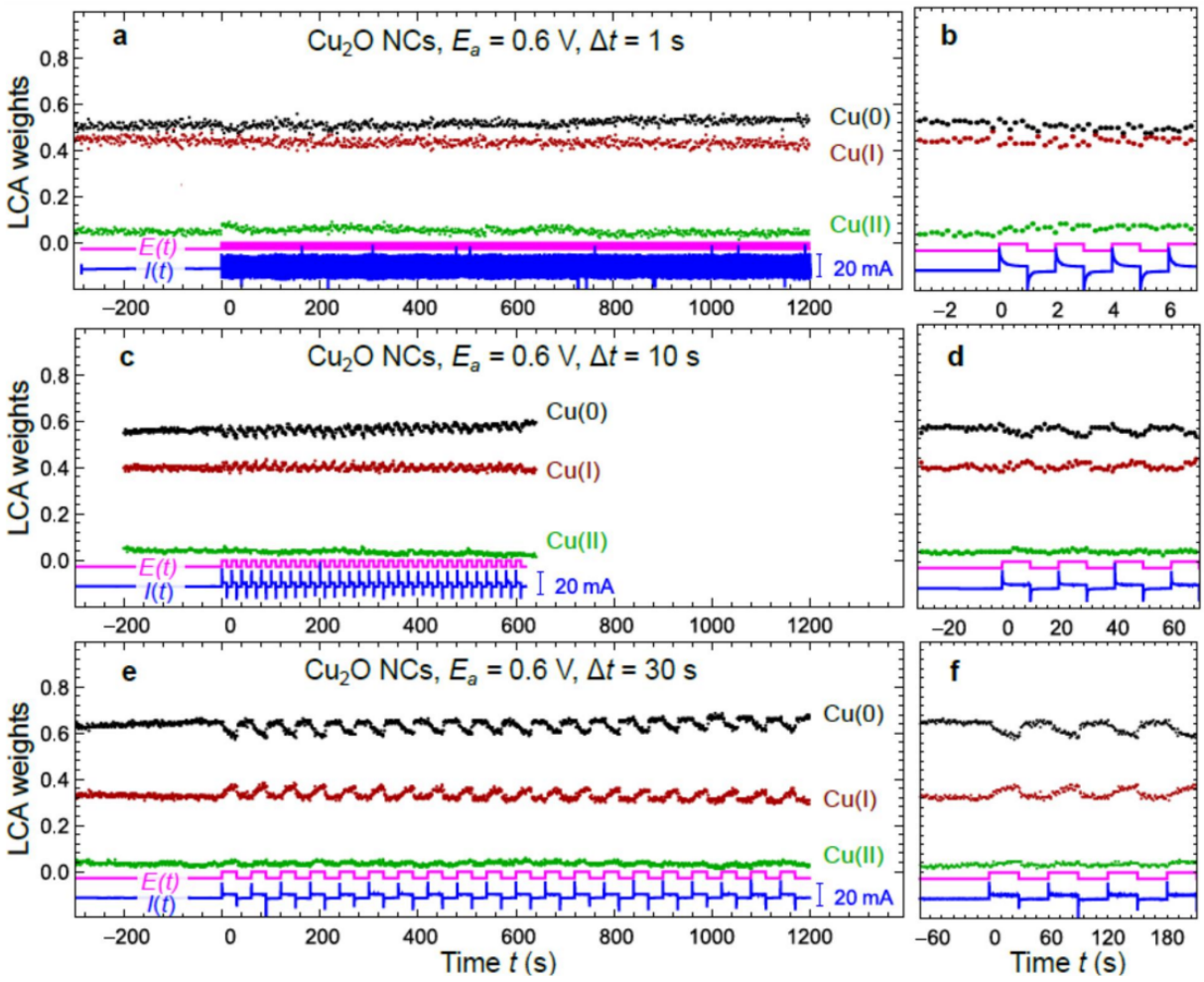

Supplementary Figure 7.20: LCA-XANES analysis results for Cu NCs under pulsed CO_2RR. The anodic potential is $E_a = 0.6$ V (RHE), the lengths of the applied cathodic and anodic potential pulses are $\Delta t_a = \Delta t_c = 1$ s (a,b), 10 s (c,d) and 30 s (e,f).

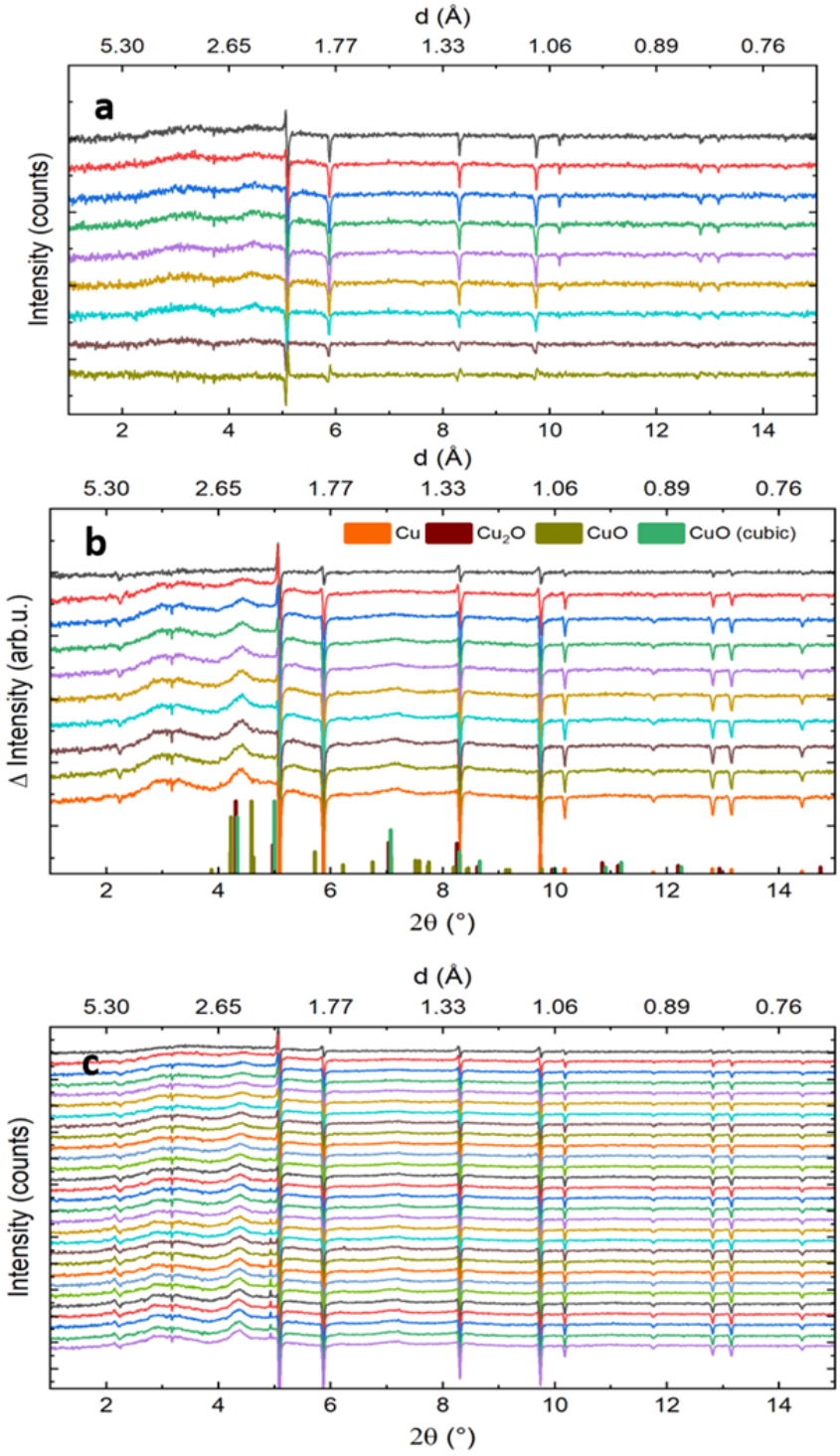

Supplementary Figure 7.21: Differential diffraction pattern during the anodic pulse. Pulse length $\Delta t_a = 1\,s$ (a), 10 s (b) and 30 s (c). Anodic potential $E_a = 0.6\,V$ (RHE). Diffraction patterns show the variations in the Cu Bragg peaks and the evolution of a Cu2O(111)-like peak at $\sim 4.35°$ as well as a peak at $\sim 7.2°$ during the anodic pulse. The broad intensity difference between 2 and $10°$ reflects the variations in the background due to the water signal.

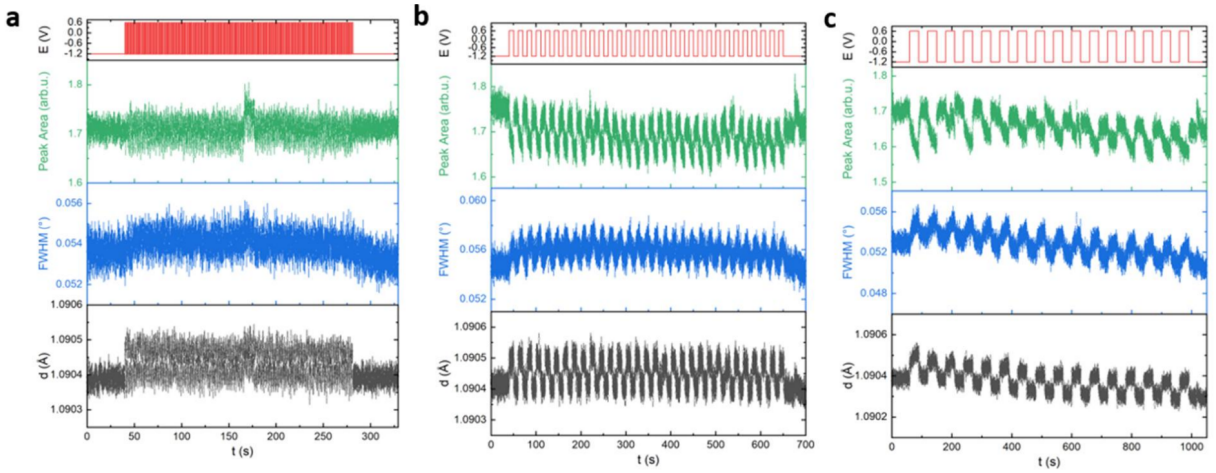

Supplementary Figure 7.22: Changes in the area, width and position of the XRD peak corresponding to Cu(311) reflection for Cu NCs under pulsed CO_2RR. Anodic potential $E_a = 0.6\,V$ (RHE), lengths of applied cathodic and anodic potential pulses are $\Delta t_a = \Delta t_c = 1\,s$ (a), 10 s (b) and 30 s (c).

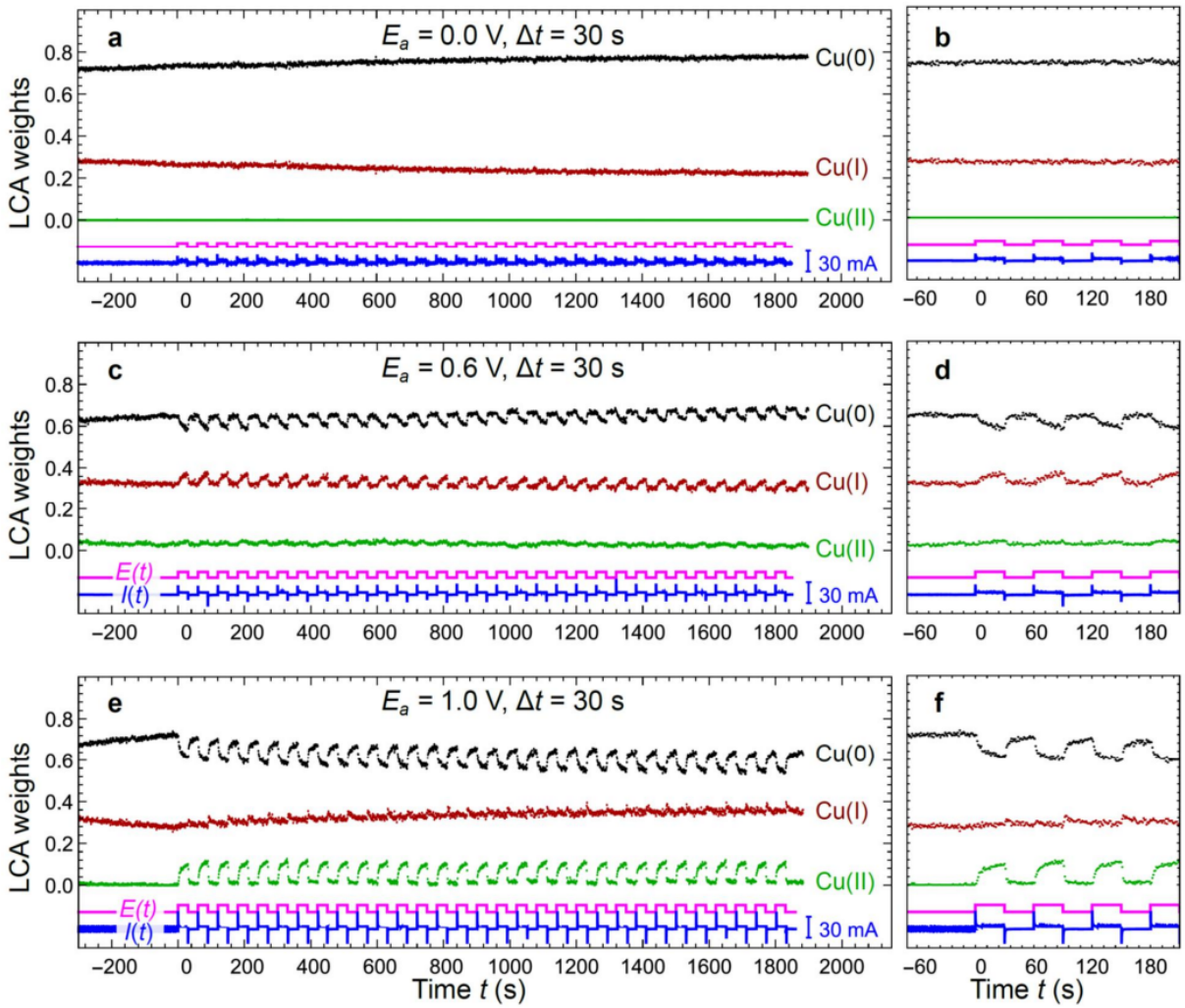

Supplementary Figure 7.23: LCA-XANES analysis results for Cu NCs under pulsed CO_2RR. Anodic potential $E_a = 0.0\,V$ (a,b), $E_a = 0.6\,V$ (c,d) and $E_a = 1.0\,V$ (e,f). In all cases the cathodic potential value was $E_c = -1.0\,V$, and the length of the applied cathodic and anodic potential pulses $\Delta t_a = \Delta t_c = 30\,s$.

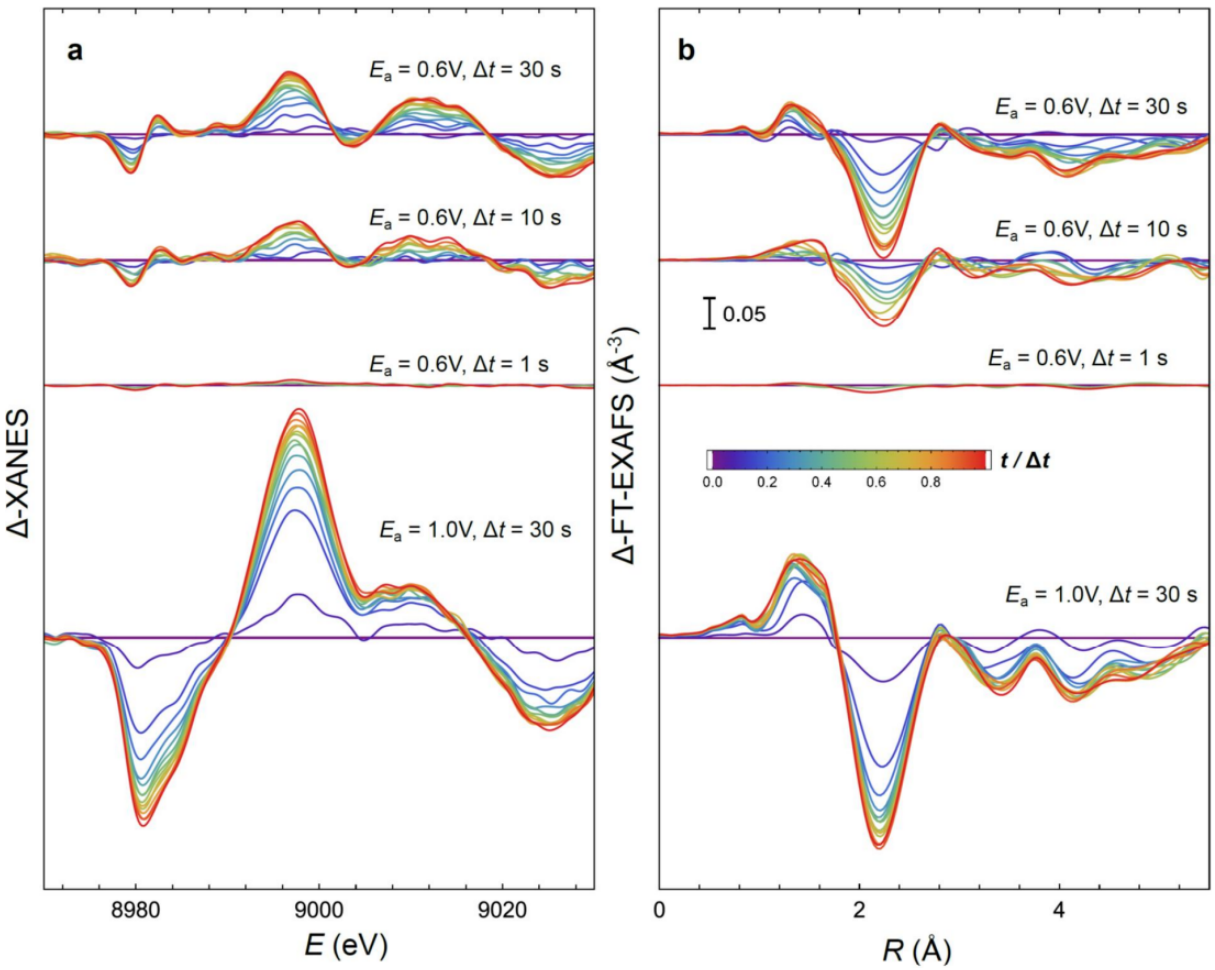

Supplementary Figure 7.24: Evolution of the differential XANES (a) and XAS-EXAFS (b) spectra for Cu NCs during the anodic pulse with different pulse lengths $\Delta t = \Delta t_a = \Delta t_c$, and different anodic potential values (E_a). The spectrum corresponding to $t = 0$ s (the onset of anodic pulse) is subtracted from averaged time-dependent XAS collected under pulsed CO_2RR conditions. In the case of XAS-EXAFS, subtraction of the magnitudes of corresponding Fourier transforms is performed.

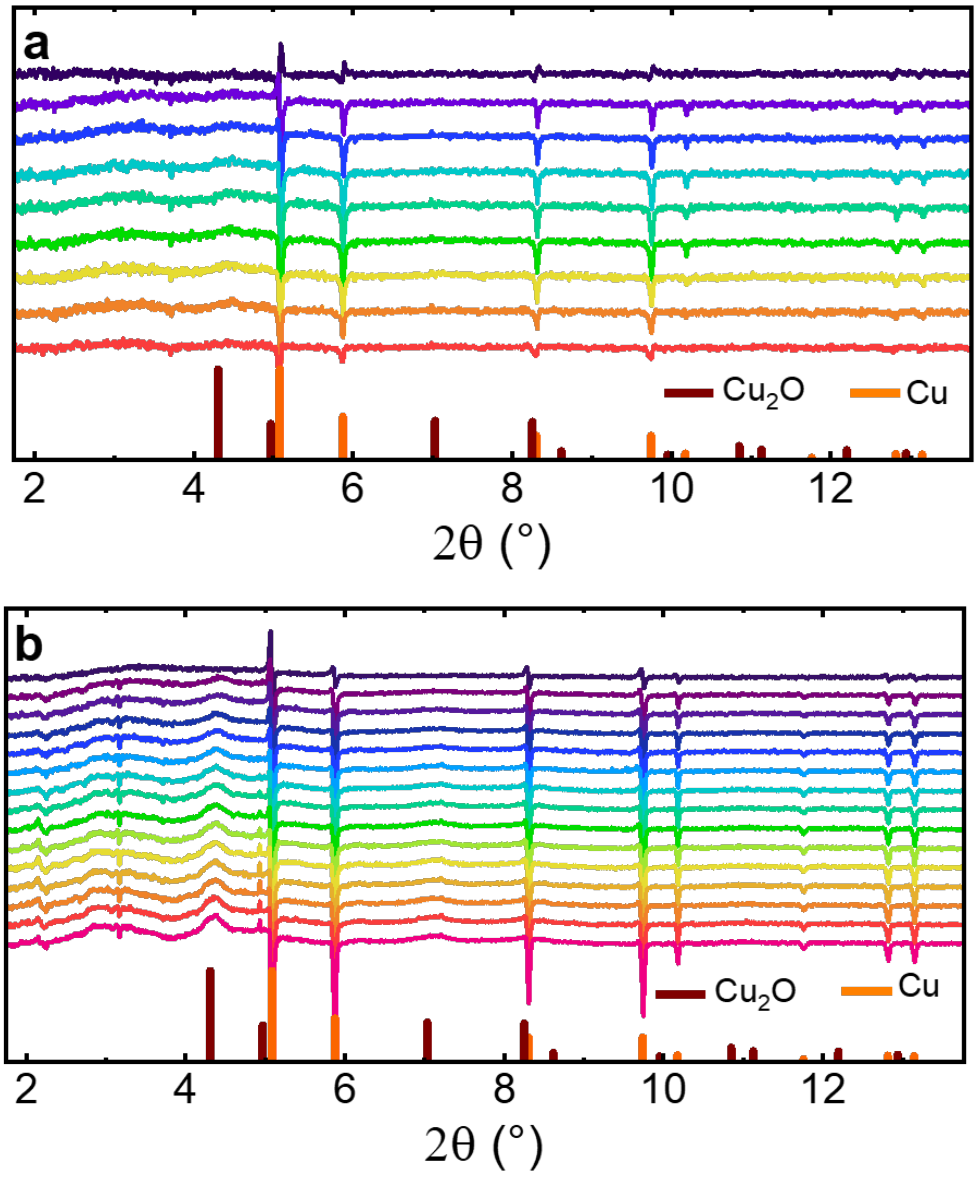

Supplementary Figure 7.25: Evolution of the differential XRD pattern of the reduced Cu NCs during the anodic pulse with an anodic potential $E_a = 0.6\,V$ and for pulse lengths of $\Delta t_a = \Delta t_c = 1\,s$ (a) and $\Delta t_a = \Delta t_c = 30\,s$ (b). The diffraction pattern corresponding to $t = 0\,s$ (the onset of anodic pulse) is subtracted from the averaged time-dependent diffraction pattern collected under pulsed CO_2RR conditions. The broad feature between 2 and 4° in both panels is induced by the variations in the water signal. Variations in line colors reflect the time passed since the onset of the anodic pulse (dark blue/purple lines correspond to $t = 0\,s$, red lines correspond to $t = \Delta t_a$).

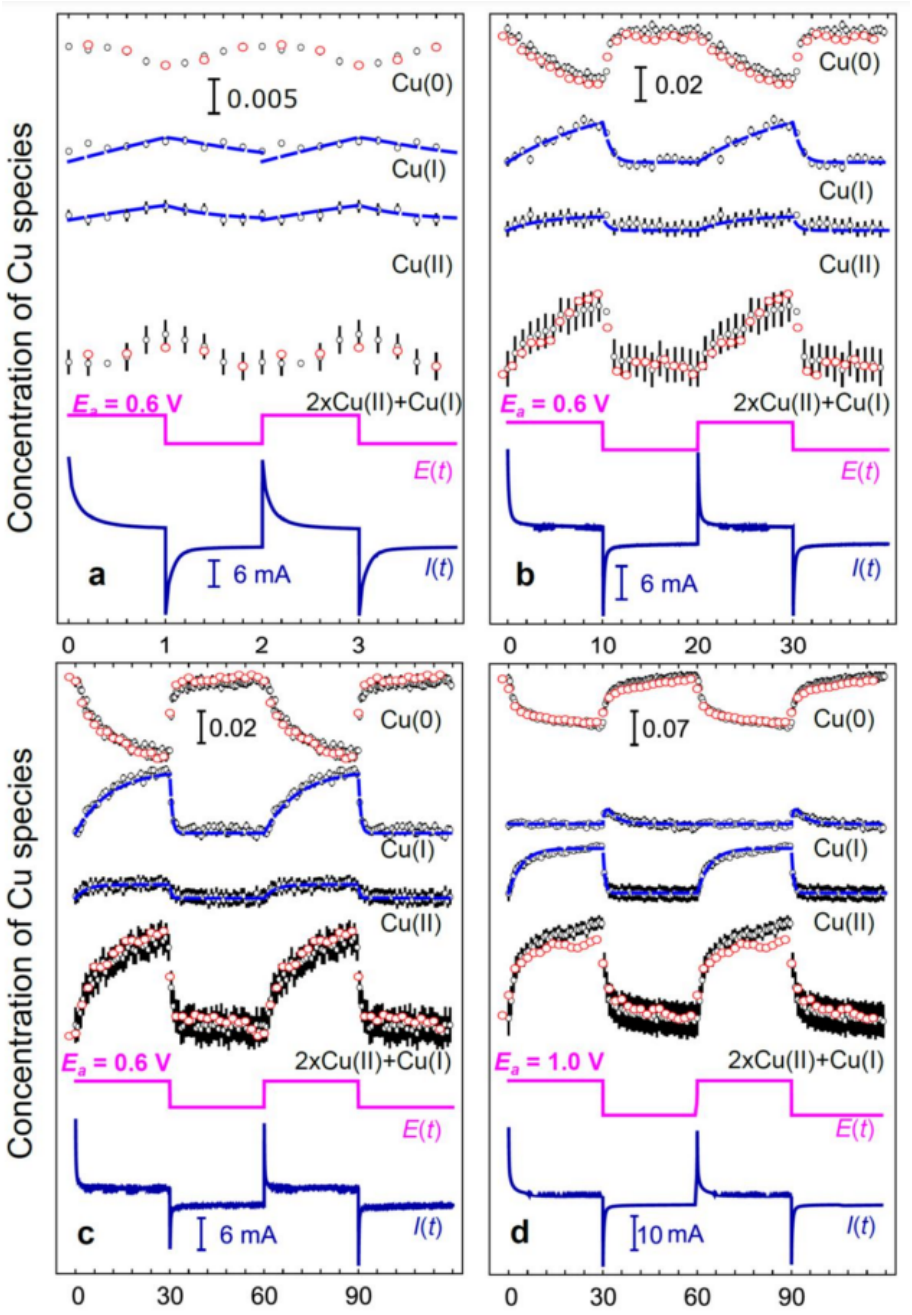

Supplementary Figure 7.26: Concentrations of Cu species in Cu NCs under pulsed CO_2RR conditions. LCA XANES analysis results (black circles) for averaged data collected under pulsed CO_2RR conditions with different pulse lengths: 1 s (a), 10 s (b) and 30 s (c, d). The anodic potential was $E_a = 0.6$ V in (a,b,c) and $E_a = 1.0$ V in (d). Results of EXAFS data fitting are shown for comparison (red circles), as well as the time-dependencies of the applied potential $E(t)$ and measured current $I(t)$. Dashed blue lines show the result of fitting concentration profiles for Cu(I) and Cu(II) species with a simple analytical model, with parameters obtained from the fit of the respective data with 30 s pulse length. Depicted error bars reflect the standard errors of LCA XANES and EXAFS fitting results.

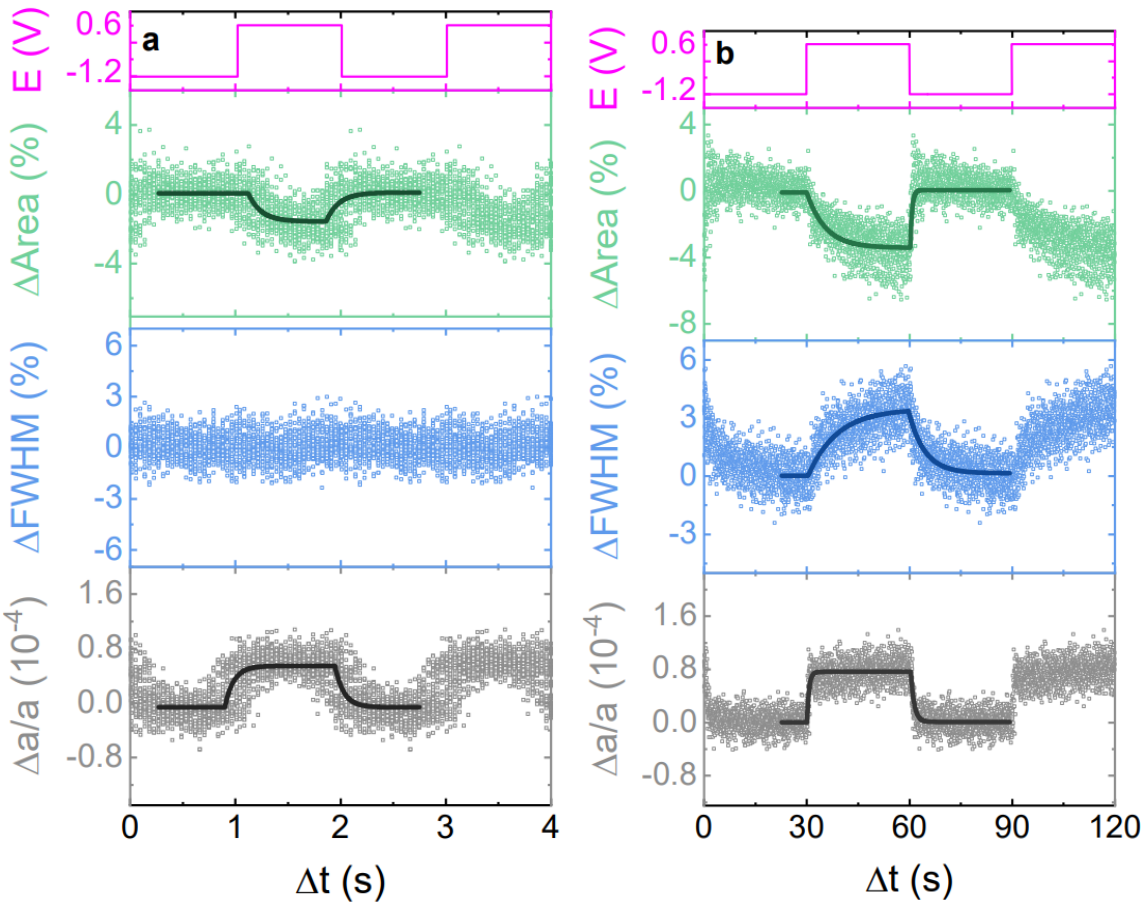

Supplementary Figure 7.27: Evolution of Cu(311) Bragg peak measures obtained from individual XRD patterns with an anodic potential $E_a = 0.6\,V$ and for pulse lengths of $\Delta t_a = \Delta t_c = 1\,s$ (a) and $\Delta t_a = \Delta t_c = 30\,s$ (b). The relative changes of the peak area (the relative amount of Cu domains, grey circles), relative peak broadening $\Delta^{FWHM}/_{FWHM}$ (the coherence length of Cu domains, grey triangles) and in the lattice spacing ($\Delta^{d}/_{d}$, grey squares) are shown. The green, blue and black solid lines the corresponding exponential fits.

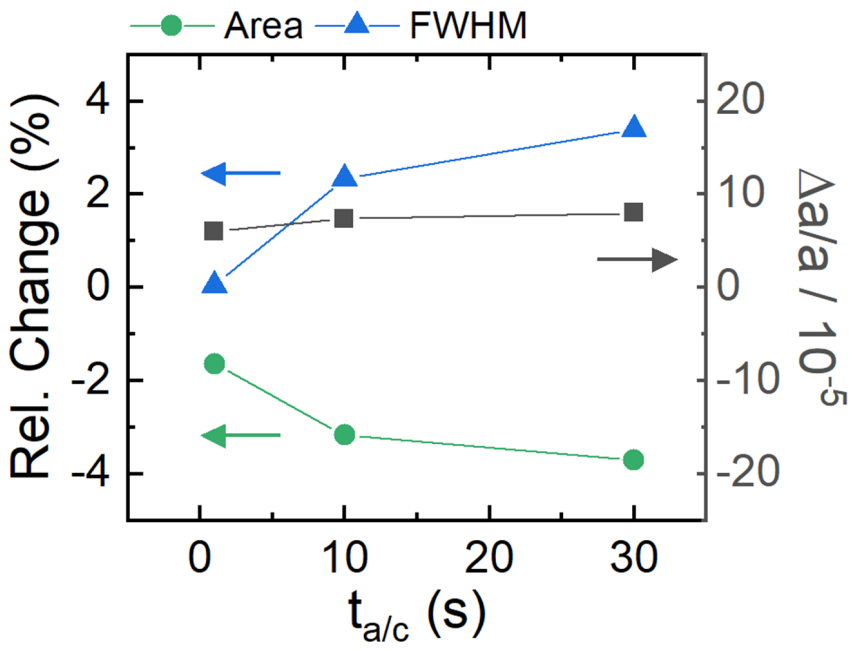

Supplementary Figure 7.28: Amplitude of the periodic variations in Cu lattice contraction, Cu restructuring and coherence length for three different pulse configurations. These results were obtained by analyzing the positions, widths and areas for XRD Cu(311) peaks for Cu NCs under pulsed CO_2RR with $\Delta t_a = \Delta t_c = 1\,s$, 10 s and 30 s. Anodic potential $E_a = 0.6\,V$.

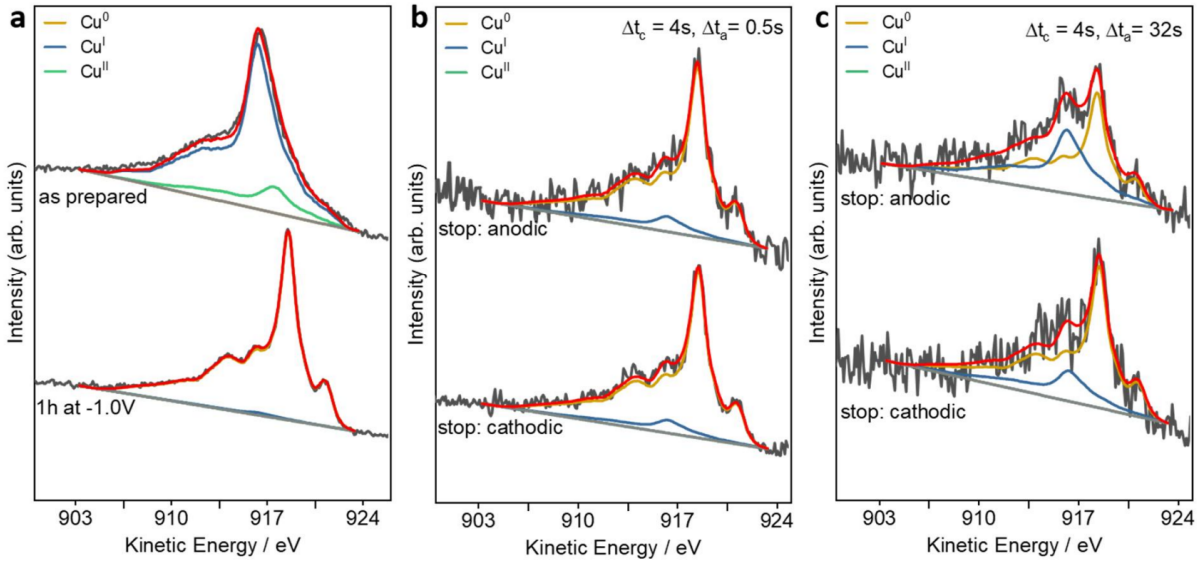

Supplementary Figure 7.29: *Quasi in situ* Cu LMM Auger spectra for Cu NCs. Spectra for as prepared catalyst and for Cu NCs after 1 h reduction under static CO_2RR conditions with constant −1.0 V potential applied (a) and for Cu NCs after 1 h of pulsed CO_2RR with pulse lengths $\Delta t_c = 4\,s$ and $\Delta t_a = 0.5\,s$ (b) and $\Delta t_c = 4\,s$ and $\Delta t_a = 32\,s$ (c). We compare spectra for samples, where the pulse sequence was interrupted at the cathodic or anodic pulse.

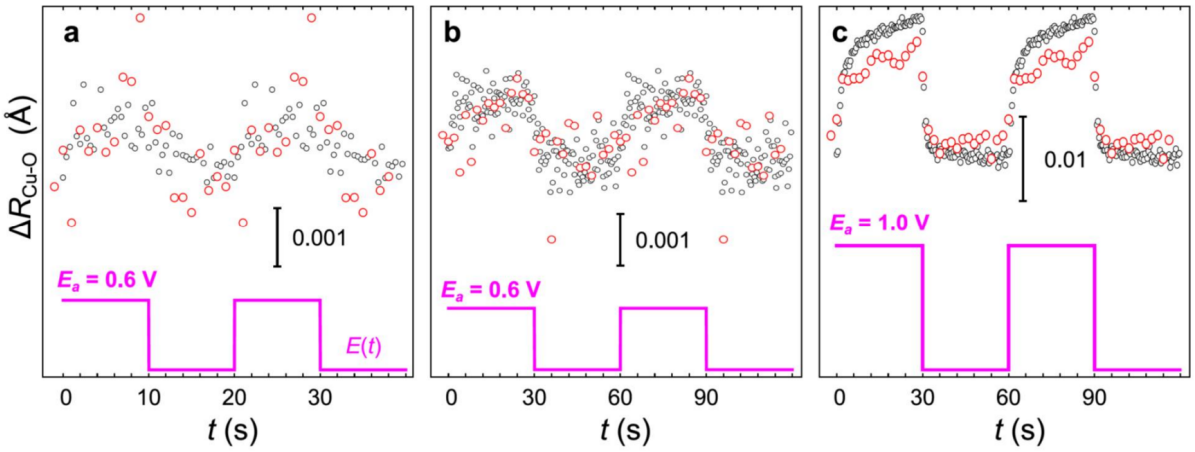

Supplementary Figure 7.30: Changes in Cu-O distance as determined from XAS data for Cu NCs under pulsed CO_2RR conditions. Red circles show the results of EXAFS data fitting for potential pulse lengths $\Delta t_a = \Delta t_c = 10$ s (a) and 30 s (b, c). Anodic potential $E_a = 0.6$ V in (a,b) and $E_a = 1.0$ V in (c). Black circles show the variation in average Cu-O bond length, as expected from LCA-XANES analysis, assuming that these changes are solely due to changes in the relative concentrations of Cu(I) and Cu(II) species, and that the local environments around these species are similar to that in their respective bulk oxides, i.e., that Cu(I) species have two Cu-O bonds with length 1.836 Å, and Cu(II) species have 4 Cu-O bonds with length 1.937 Å.

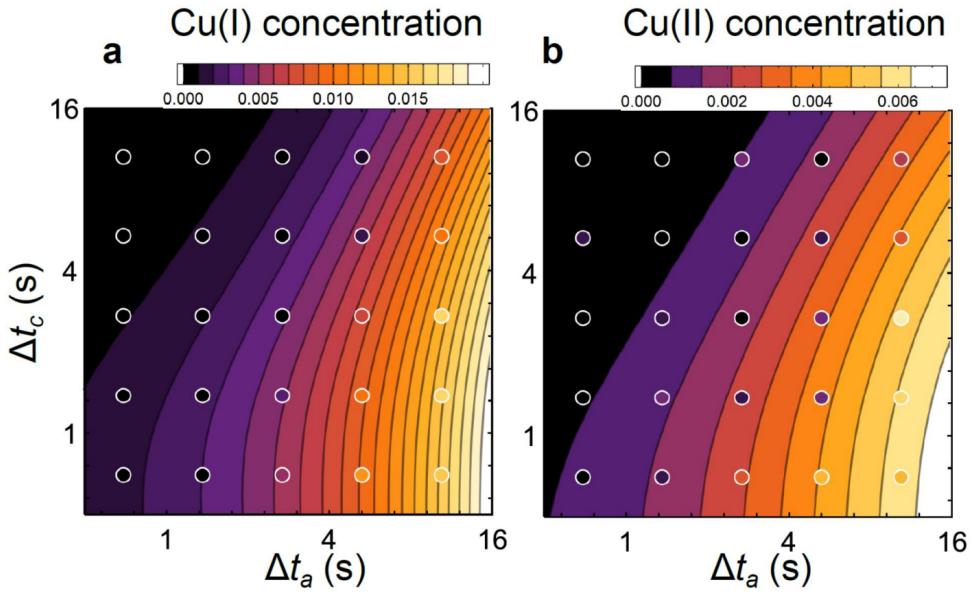

Supplementary Figure 7.31: Effect of the durations of the anodic (Δt_a) and cathodic (Δt_c) pulses on the average excess concentrations of Cu(I) (a) and Cu(II) (b) species. Contour lines show results obtained from the simple extrapolating model, as discussed in Supplementary Note 7.6.8. Circles show direct experimental results, obtained by LCA-XANES analysis of XAS data, collected in auxiliary QEXAFS experiment at DESY P64 beamline for Cu NCs under pulsed CO_2RR with different Δt_a and Δt_c values.

7.6.10 Supplementary Tables

Supplementary Table 7.1: Faradaic efficiency (FE) for Cu NCs after 4000 s of CO_2RR at static −1.0 V vs. RHE. Uncertainty (estimated as the standard deviation of the outcomes for at least three measurements) of the last digit is given in parentheses.

Product	FE (%)
H_2	17(5)
C_2H_4	40(2)
CH_4	20(3)
EtOH	10(2)
Formate	5(1)
CO	5(2)
1-PrOH	2.7(5)
Acetaldehyde	1.9(6)
Allylalcohol	1.2(2)
Propionaldehyde	0.6(3)
Acetate	0.13(2)
Acetone	0.07(3)

Supplementary Table 7.2: FE for Cu NCs under pulsed CO_2RR with different pulse lengths. Uncertainty (estimated as the standard deviation of the outcomes of at least three measurements) of the last digit is given in parentheses. The values for the cathodic and anodic potentials are $E_c = -1.0\,V$ and $E_a = 0.6\,V$ vs. RHE, respectively.

Δt_c (s)	Δt_a (s)	H_2	CO	CH_4	C_2H_4	Ethanal	Acetone	Propanal	EtOH	1-PrOH	Allylalc.	$HCOO^-$	Acetate
0.5	0.5	12(5)	15(1)	30(6)	23(3)	3.7(5)	1(1)	0.5(3)	9(1)	1.5(2)	1.3(8)	3.2(7)	0.2(1)
0.5	1	25(5)	16(6)	37(6)	12(7)	2(1)	0(0)	0.4(3)	3(1)	0.4(6)	0.2(3)	2(2)	0.1(2)
0.5	2	14(3)	16(3)	44(11)	16(4)	1.9(7)	0(0)	0.3(2)	3.5(6)	0(0)	0.3(2)	2.5(8)	0.22(2)
0.5	4	12(2)	20(6)	43(9)	17(6)	1.8(7)	0.1(1)	0.1(2)	5(3)	0(0)	0(0)	1.8(9)	0.1(1)
0.5	8	16(5)	18(4)	43(6)	18(6)	0.9(8)	0(0)	0.2(2)	4(1)	0.1(2)	0.1(2)	1(1)	0.06(8)
0.5	10	10(3)	15(3)	46(8)	23(8)	1.6(3)	0.1(1)	0.2(3)	3.2(3)	0.11(9)	0.3(3)	1.4(9)	0.03(5)
0.5	16	17(4)	26(9)	32(1)	22(1)	0(0)	0(0)	0(0)	3(1)	0(0)	0(0)	2(9)	0.2(2)
0.5	32	22(5)	25(5)	24(8)	24(6)	0(0)	0(0)	0(0)	1.3(3)	0(0)	0(0)	2.9(2)	0.1(2)
1	0.5	14(2)	17(8)	29(8)	18(2)	3(2)	0(0)	0.5(1)	8.6(2)	2.2(5)	1.2(4)	6.5(6)	0.1(1)
1	1	8(2)	13(1)	26(3)	27(3)	4.1(8)	0(0)	0(0)	11(2)	2.3(6)	1.2(2)	5(1)	0.35(8)
1	2	15(4)	19(5)	40(8)	17(6)	2(2)	0(0)	0.4(4)	4(1)	0(0)	0(0)	4.2(9)	0.1(1)
1	4	14(3)	22(5)	43(4)	13(4)	1.1(9)	0(0)	0.4(4)	3(1)	0(0)	0(0)	3.2(4)	0.16(5)
1	8	17(2)	23(6)	38(2)	15(6)	0.3(5)	0(0)	0.1(2)	2.5(9)	0(0)	0(0)	3(1)	0.2(3)
1	16	16(7)	21(3)	33(1)	21(8)	0.1(3)	0(0)	0(0)	5(1)	0(0)	0(0)	4(3)	0.2(2)
1	32	14(2)	19(3)	27(4)	28(5)	0(0)	0(0)	0(0)	6(2)	0(0)	0(0)	5.2(5)	0.88(5)
2	0.5	7(2)	8(3)	27(4)	32(2)	4.2(3)	0.1(1)	0.75(8)	16(2)	2.9(3)	1.5(2)	3(1)	0.17(1)
2	1	11(3)	15(5)	25(3)	25(7)	3.2(7)	0(0)	0.9(2)	11(1)	2.2(8)	1.2(2)	5(1)	0.22(8)
2	2	8(2)	11(2)	38(8)	24(6)	3.8(6)	0.2(4)	0.7(2)	9.5(7)	1.7(4)	1(2)	3(1)	0.2(1)
2	4	8.1(5)	14(2)	30(3)	32(2)	4(2)	0(0)	0.61(8)	6(1)	1.1(1)	0.8(2)	3.5(4)	0.31(3)
2	8	13.7(8)	24(3)	36(1)	13(2)	3.7(5)	0.1(2)	0.6(2)	5(1)	0(0)	0(0)	3.9(1)	0.03(6)
2	16	11(1)	21(4)	30(4)	23(4)	3.5(6)	0(0)	0.2(3)	5.7(5)	0.4(6)	0(0)	5.8(3)	0.2(3)
2	32	12(3)	19(5)	29(3)	26(8)	3(1)	0(0)	0.3(6)	6(2)	2(4)	0.2(4)	5.8(4)	0.2(2)
4	0.5	7(1)	6(2)	25(9)	34(3)	5(2)	0.11(7)	0.7(2)	17(2)	3.3(9)	1.4(2)	3(1)	0.3(2)
4	1	9(3)	11(3)	15(10)	35(3)	5(3)	0.1(1)	1.2(6)	14(1)	3.1(5)	1.4(1)	6(2)	0.26(5)
4	2	7(1)	7.4(9)	27(6)	32(3)	4.2(8)	0.06(1)	0.8(3)	14.4(2)	2.7(5)	1.3(2)	4(1)	0.2(1)
4	4	7.3(8)	11(3)	27(4)	36(2)	7(3)	0.02(2)	0.8(1)	8(1)	1.4(5)	0.8(2)	4(1)	0.2(1)
4	8	8(3)	12(5)	35(6)	26(5)	3.8(7)	0.1(1)	0.7(2)	9(1)	1.2(6)	0.8(4)	4(3)	0.4(4)
4	16	9.4(6)	17(2)	33(4)	20(4)	5(2)	0(0)	1(4)	7(1)	0.06(1)	0.2(4)	6.8(8)	0.3(3)
4	32	12(5)	15(4)	24(4)	25(9)	5(3)	0(0)	1.6(9)	8(2)	0.4(7)	0.5(8)	9(3)	0.6(5)
6	0.5	8(1)	5(2)	29(7)	35(6)	2.8(5)	0.11(6)	0.5(2)	14(2)	2.5(6)	1.2(4)	2(1)	0.1(1)
8	0.5	9(3)	7(3)	21(1)	41(3)	3(1)	0.12(9)	0.8(4)	16(2)	3.05(5)	1.4(2)	2.9(5)	0.19(9)
8	1	11.5(4)	9(4)	18(8)	37(4)	5(3)	0.03(3)	0.8(5)	11(3)	2.7(8)	1.2(2)	5(3)	0.1(1)
8	2	12(3)	9(3)	21(13)	34(3)	4(1)	0.19(4)	0.9(5)	11.7(8)	2.8(6)	1.3(2)	5(5)	0.05(5)
8	4	6.6(5)	9(3)	32(4)	35(5)	3.5(9)	0.2(3)	0.7(2)	10(4)	1.9(3)	1(3)	2.8(3)	0.14(8)
8	8	6.3(7)	8.3(1)	32(4)	35(2)	4(4)	0.04(6)	0.7(2)	11(1)	1.9(6)	1.1(2)	3(2)	0.13(3)
8	16	8(1)	13(1)	35(6)	27(3)	3.4(2)	0(0)	0.46(9)	8.3(6)	1.7(6)	1.2(3)	5(1)	0.2(1)
8	32	9(2)	10.4(7)	24(5)	33(2)	3.4(7)	0.02(4)	0.8(1)	10(2)	1.9(6)	1.3(5)	7(2)	0.27(7)
10	0.5	8.8(6)	8(1)	21(4)	40(4)	3.2(9)	0.08(2)	0.7(1)	12(1)	3(7)	1.3(1)	3.2(6)	0.15(9)
10	1	12(2)	13(2)	18(7)	32(1)	4(3)	0.05(4)	0.7(4)	8(1)	2.5(2)	1.2(2)	9(1)	0.1(1)
10	2	9(1)	12(1)	23(4)	33(5)	5(2)	0.12(8)	0.9(2)	10(2)	2.5(9)	1.3(2)	6(2)	0.16(4)
10	4	10(3)	11(3)	28(4)	30(6)	2.8(8)	0.03(3)	0.61(7)	9.5(8)	2.4(4)	1.17(5)	5.6(4)	0.17(8)
10	10	7(1)	8(3)	35(2)	33(2)	4(2)	0.1(2)	0.6(1)	10(2)	1.8(4)	0.94(9)	3(1)	0.09(3)
16	0.5	8.8(3)	7(1)	20(5)	41(3)	3(2)	0.13(3)	0.7(3)	12(2)	3.3(5)	1.4(2)	4(1)	0.06(1)
16	1	9(1)	7(3)	21(4)	40(3)	3(1)	0.06(4)	0.8(3)	11(2)	3(2)	1.3(2)	4(1)	0.07(7)
16	2	8(1)	13(3)	25(4)	35(3)	4(1)	0.03(3)	0.9(2)	9.3(3)	2.2(2)	1.21(8)	3.8(1)	0.14(4)
16	4	7(1)	12(1)	31(8)	30(5)	3.3(7)	0.03(3)	0.8(1)	8.3(6)	1.8(5)	1.1(1)	4(2)	0.1(5)
16	8	10(3)	11(4)	29(2)	27(7)	4(1)	0.04(6)	0.9(3)	8(2)	1.7(7)	1.1(1)	5(5)	0.11(7)
16	16	8(2)	13(3)	30(7)	31(6)	3.3(9)	0.02(3)	0.7(2)	7.6(8)	1.6(6)	0.9(2)	4.7(9)	0.3(2)
16	32	7.9(4)	9(1)	27(2)	35(4)	3.4(4)	0.05(9)	0.71(1)	11(1)	2.6(7)	1.2(4)	4.3(1)	0.16(8)
32	0.5	9(1)	7(1)	21(9)	40(5)	2.6(5)	0.08(2)	0.8(4)	11(2)	3.2(7)	1.5(2)	4(2)	0.11(9)
32	1	9(3)	6(4)	22(8)	41(4)	3(1)	0.09(2)	0.7(3)	12(2)	3(3)	1.31(5)	3.2(4)	0.07(7)
32	2	9(3)	6(3)	22(1)	40(2)	3(1)	0.13(4)	0.8(4)	12(1)	3.2(2)	1.33(9)	4(1)	0.09(2)
32	4	8(1)	8(3)	27(4)	37(3)	3(1)	0.04(2)	0.7(3)	10(2)	2.6(3)	1.24(8)	4(1)	0.09(9)
32	8	9(2)	10(2)	28(4)	33(1)	4(3)	0.02(4)	0.97(9)	8.8(6)	2.4(4)	1.21(1)	5(6)	0.09(9)
32	16	9(2)	9(8)	26(2)	36(2)	2.7(5)	0.04(7)	0.76(9)	10(1)	2.6(3)	1.1(1)	4(1)	0.1(5)
32	32	8(1)	10(1)	28(3)	33(2)	3(1)	0.2(2)	0.7(1)	9.8(9)	2.1(3)	1.1(2)	5(1)	0.1(1)

Supplementary Table 7.3: FE for Cu NCs under static CO_2RR at $E_c = -1.0\,V$ after treatment with pulses with different durations. Uncertainty (estimated as the standard deviation of the outcomes of at least three measurements) of the last digit is given in parentheses. The values for the cathodic and anodic potentials are $E_c = -1.0\,V$ and $E_a = 0.6\,V$ vs. RHE, respectively

Δt_c (s)	Δt_a (s)	H_2	CO	CH_4	C_2H_4	Ethanal	Acetone	Propanal	EtOH	1-PrOH	Allylalc.	$HCOO^-$	Acetate
0.5	0.5	12.1(8)	8(1)	41(4)	27(2)	3.1(6)	0.01(3)	0.6(3)	4(8)	1.1(3)	0.9(2)	5.1(6)	0.1(1)
0.5	4	19(4)	5(2)	49(3)	19(5)	2.3(3)	0.03(2)	0.4(2)	4.1(1)	0.9(5)	0.8(2)	4(1)	0.17(8)
0.5	8	20(4)	4.7(1)	47(3)	19(2)	2(4)	0.01(1)	0.34(1)	3.6(3)	0.7(2)	0.56(6)	5(1)	0.1(1)
0.5	32	21(6)	7(1)	34(14)	23(6)	2.1(6)	0.05(8)	0.4(2)	4(2)	1.3(1)	0.8(5)	8(4)	0.07(3)
4	0.5	19(7)	5.1(8)	39(9)	27(11)	3(2)	0.03(2)	0.4(2)	5(2)	1.2(6)	0.7(3)	4.5(6)	0.09(6)
4	4	13(3)	7(2)	34(5)	33(2)	5(2)	0.01(2)	0.7(3)	5.3(6)	1.3(3)	0.9(2)	4(1)	0.17(5)
4	8	21(4)	10(5)	32(15)	23(3)	2.5(9)	0.02(2)	0.5(1)	4.5(9)	1(6)	0.9(2)	6(3)	0.06(4)
8	0.5	13(3)	7(1)	31(5)	34(5)	3(1)	0.08(3)	1(6)	7(7)	2(7)	1.3(4)	4(1)	0.1(8)
8	4	15(8)	6.8(9)	38(4)	28(8)	4(2)	0.07(4)	0.6(3)	5(1)	1.1(7)	0.7(2)	4(1)	0.13(7)
8	8	12(4)	5.2(3)	36(5)	33(2)	3.9(4)	0.02(4)	0.7(2)	6.4(1)	1.3(3)	1.1(2)	2.7(2)	0.08(7)
32	0.5	12(3)	5.7(3)	24.6(8)	38(3)	2.4(7)	0.08(0)	0.8(3)	8.4(3)	3.1(2)	1.6(1)	4.7(4)	0.12(3)
32	32	15(2)	10(1)	31(2)	28(1)	2(1)	0(0)	0.4(3)	5.8(6)	1.2(3)	1.1(2)	4(6)	0.2(1)

Supplementary Table 7.4: Cu catalyst loading after pulsed CO_2RR. Sample dissolution, determined by ICP-MS measurements of the electrolytes, was used to determine the remaining loading of the Cu catalyst on the carbon paper support. The initial amount was 50 µg, after reducing at constant −1.0 V for 1 h the remaining sample amount was 40(2) µg. This value was used as reference to calculate the percentage of sample dissolved. The values of cathodic and anodic potentials applied during the pulses are $E_c = -1.0\,V$ and $E_a = 0.6\,V$. Uncertainty of the last digit is given in parentheses.

	Δt_c (s)	$\Delta t_a = 0.5\,s$		$\Delta t_a = 4\,s$		$\Delta t_a = 32\,s$	
		Sample loading (µg)	**Dissolved sample (%)**	**Sample loading (µg)**	**Dissolved sample (%)**	**Sample loading (µg)**	**Dissolved sample (%)**
After 1 h of pulsed CO_2RR	32	37(1)	8	31(2)	23	31(1)	23
	4	31(5)	23	30(2)	25	28(2)	30
	0.5	32(3)	20	27(7)	33	27(1)	33
After 1 h of pulsed CO_2RR, followed by 1 h of reapplied CO_2RR at constant −1.0 V	32	34(3)	15			30(3)	25
	0.5	28(3)	30			26(3)	35

Supplementary Table 7.5: Parameters of the model defined by Supplementary Equation 7.2. The parameters are obtained by best fitting the Cu(I) and Cu(II) concentration profiles for Cu NCs under pulsed CO_2RR conditions with pulse length 30 s. Uncertainty (estimated as the standard deviation of outcomes for at least three measurements) of the last digit is given in parentheses

	Δw_{I}	Δw_{II}	$\tau_{0\to\mathrm{I}}$ **(s)**	$\tau_{0\to\mathrm{II}}$ **(s)**	$\tau_{\mathrm{I}\to 0}$ **(s)**	$\tau_{\mathrm{II}\to\mathrm{I}}$ **(s)**	$\tau_{\mathrm{II}\to 0}$ **(s)**
$E_{\mathrm{a}} = \mathbf{0.6\,V}$	0.0398(9)	0.0086(2)	10.8(6)	3.5(3)	0.59(5)	0.5(1)	-
$E_{\mathrm{a}} = \mathbf{1.0\,V}$	-	0.0884(7)	-	4.1(2)	3.1(2)	1.34(9)	1.3(1)

8

Operando Insights into correlating CO Coverage and Alloying with the Selectivity of Au NP decorated Cu_2O Nanocubes during the Electrocatalytic CO_2 Reduction

Clara Rettenmaier[1], Antonia Herzog[1], Daniele Casari[2], Martina Rüscher[1], Hyo Sang Jeon, David Kordus[1], Mauricio Lopez Luna[1], Stefanie Kühl[1], See Wee Chee[1], Janis Timoshenko[1], Alexander Duncan[2], Arno Bergmann[1], Beatriz Roldan Cuenya[1]

[1]: Department of Interface Science, Fritz-Haber-Institute of the Max-Planck Society, Faradayweg 4-6, 14195 Berlin, Germany
[2]: Interdisciplinary Center for Electron Microscopy (CIME), Ecole Polytechnique Fédérale de Lausanne (EPFL), Lausanne CH-1015, Switzerland

to be submitted

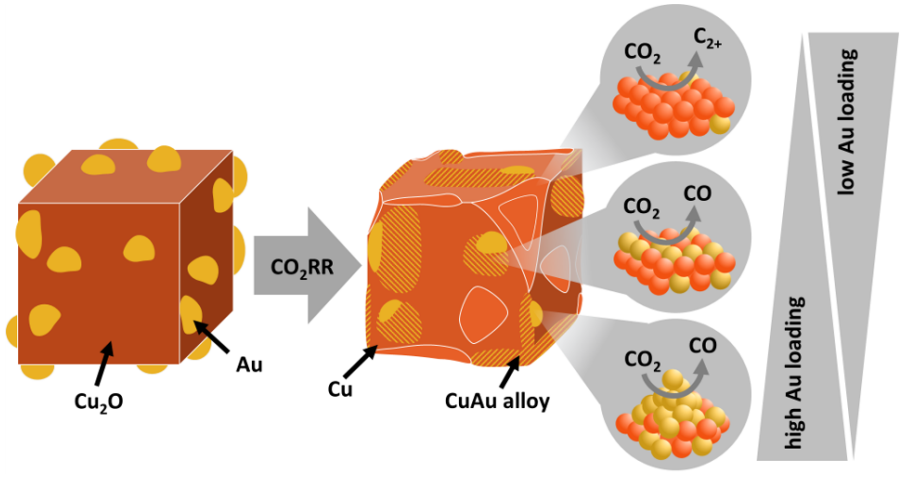

8.1 Preliminary Remarks

This chapter answers the question how bimetallic catalysts improves the selectivity towards C_{2+} products by systematically increasing the Au NP loading on the Cu_2O NCs. It is set in comparison with the SnO_2-decorated Pd NCs for the FAOR. Both catalysts are cubic shaped, each demonstrating (100) terminated facets that are beneficial for the respective reactions. Furthermore, a co-catalyst was chosen that enhances the catalytic performance.

This project was designed and supervised by Arno Bergmann and Beatriz Roldan Cuenya. I led the sample synthesis and the electrocatalytic characterization and the quasi *in situ* XPS measurements. Antonia Herzog performed the *operando* Raman measurements, Martina Rüscher and Janis Timoshenko guided the *operando* XAS measurements with contributions from Hyo Sang Jeon, Mauricio Lopez Luna and David Kordus. Stefanie Kühl performed the ICP-MS measurements and preliminary TEM measurements. See Wee Chee established the contact to the collaborators Daniele Casari and Alexander Duncan, who performed further TEM measurements and analysis.

8.2 Abstract

Electrochemical reduction of CO_2 (CO_2 reduction reaction (CO_2RR)) is an attractive technology to reintegrate the anthropogenic CO_2 back into the carbon cycle driven by renewable energy and a suitable catalyst. The combination of co-catalysts with copper boosts the selectivity towards multi-carbon (C_{2+}) products. In this study, we employ highly efficient C_{2+} producing Cu_2O NCs decorated with CO-selective Au NPs to investigate the correlation between a high CO surface concentration microenvironment and the catalytic performance.

We comprehensively studied the structure, morphology and near-surface composition upon CO_2RR and identified a complex heterogeneous tandem electrocatalysts with Au wetting the Cu surface leading to pronounced Cu-Au alloy formation. *Operando* studies showed the continuous evolution of the local structure and chemical environment of our catalysts during the first hour of the reaction, in particular, the rapid integration of the Au atoms into the Cu lattice during CO_2RR. Along with the alloy formation and with increasing Au decoration, by means of selectivity measurements and *operando* Raman spectroscopy we detect a CO-rich microenvironment as well as a weakening of the average CO binding to the catalyst surface during CO_2RR. Linking these findings to the catalytic function, we could reveal the complex compositional interplay between Au and Cu in which higher Au loadings primarily facilitate the CO formation due to the *in situ* formed Cu-Au alloys resulting in a weak CO binding. Nonetheless, we show the strongest improvement in C_{2+} formation, in particular, liquid prod-

ucts, for the lowest Au loadings, suggesting a beneficial role of the Au-Cu atomic interaction for a beneficial tandem catalytic function in CO_2RR. This study highlights the importance of site engineering and *operando* investigations to unveil the electrocatalyst's adaptations to the reaction conditions, which is a prerequisite to understand its catalytic behavior.

8.3 Introduction

The electrochemical reduction of CO_2 (CO_2RR) is an attractive technology for closing the anthropogenic carbon cycle by using renewable energy such as solar- or wind-power to convert the greenhouse gas CO_2 into energy-dense feedstock chemicals or liquid fuels.[216,217]

The ideal electrocatalysts for this reaction require low overpotentials, high stability and excellent selectivity for C_{2+} products while minimizing the parasitic Hydrogen Evolution Reaction (HER). While various materials may reduce CO_2 into C_1 products (CO, CH_4, HCOOH), copper-based materials are unique in producing C_{2+} hydrocarbons (e.g. C_2H_4), alcohols (e.g. C_2H_5OH) or carbonyls due to their ability to enable the C-C coupling reaction. Cu_2O NCs are reported as one of best catalysts for C_{2+} products.[195] The Cu-based catalysts owe their good selectivities to an optimal binding and stabilization of the CO intermediates[29] (e.g. *CO and $*CO^{2-}$);[218] yet these catalysts still suffer from low energy efficiency and low specific product selectivity.[104]

Among the multitude approaches to improve the selectivity towards C_{2+} products, sequential catalysis has been proposed to be beneficial with an optimized selectivity through combining beneficial electronic effects via alloying and an increased CO coverage or concentration.[107,108,219–221] By adjusting the local electronic structure of the catalyst though the use of bimetallic systems and alloys, the binding energies of the reaction intermediates such as *CO might be altered and thus the reaction pathways might be modified.[222–225] Furthermore, a higher local concentration and subsequently a higher coverage of adsorbed CO molecules on Cu can be induced through CO-selective co-catalysts, such as Au, Ag or Zn. This may lead to subsequent C-C coupling and thus enhanced selectivity for C_{2+} products.[105,106,226] Despite of the similar ability to efficiently reduce CO_2 to CO, Au, Ag and Zn differ from each other in particular as the onset potential for CO production, which varies from −0.25 V (vs. RHE) for Au, −0.52 V for Ag and −0.6 V for Zn. Thus, Au has the lowest overpotential and shows the highest CO partial current density, which can be explained by its weak *CO binding strength.[29,54,227] Furthermore, it has been proposed that the thus produced CO might follow a CO spillover mechanism, which has been also reported for Ag.[228,229]

Moreover, Au is an attractive co-catalyst for CO_2RR due to its particular alloying tendency

with Cu, which allows to steer the electronic structure better than the less miscible Ag-Cu catalysts.[227,230] In particular, Cu-Au can form three ordered phases with different compositions (Cu_3Au, CuAu, $CuAu_3$),[231] and CuAu superstructures[232] as well as unordered Cu-Au phases, which present a wide variety of possible active species for CO_2RR. Cu-Au alloyed systems have been reported to lead to enhanced CO_2RR performance, which was attributed to different factors including a possible protection from the formation of Cu oxide,[230,233] increased formation of CO, paralleled by the suppression of HER and CH_4 formation,[77,234,235] a shift in the onset potential for CO_2RR,[230,236] *COOH stabilization[111,223,237] and to synergistic geometric and electronic effects to boost C_{2+} production toward alcohols.[112,238–241] However, the type and the influence of the alloyed structure under CO_2RR conditions as well as the high CO coverage on Cu through CO producing co-catalysts remains an open question. Additionally, a systematic study of Cu-Au NP catalysts with a complex mixing pattern of the constituent active elements, alloy formation and the interfaces of its multiple phases under *operando* conditions has not yet been reported.

Hence, in this work we used Cu_2O NCs decorated with varying amounts of Au NPs to reveal the role of alloying and of the CO coverage on the product selectivity by analyzing the alloy formation and the influence of CO-richer micro-environments under CO_2RR conditions. The compositional restructuring was investigated with TEM and XPS, while the active phases under reaction conditions were deconvoluted with *operando* HE-XRD, *operando* XAFS spectroscopy, and quasi *in situ* XPS. The CO coverage on Cu was followed with *operando* surface-enhanced Raman. Correlations between the alloy type, amount and its evolution during CO_2RR as well as the CO coverage and the product distributions were drawn, unveiling that optimized alloyed phases and CO coverages result in increased C_{2+} product selectivity.

8.4 Results and Discussion

We have prepared Cu_2O NCs decorated with different Au NP loadings and TEM analysis confirmed the cubic shape of the as-prepared Cu_2O NCs with the lowest and the highest Au loading ($Au_{0.4}Cu_2O$ NC and $Au_{2.7}Cu_2O$ NCs), with well dispersed Au NPs primarily on the edges, Figure S8.6. We determined the bulk compositions of Cu with varying Au loadings of 0.43at%, 0.77at%, 1.08at% and 2.69at% for $Au_{0.4}Cu_2O$ NC, $Au_{0.8}Cu_2O$ NC, $Au_{1.1}Cu_2O$ NC and $Au_{2.7}Cu_2O$ NC, respectively, Table S8.6. XRD analysis of the as-prepared NCs demonstrates the presence of Cu_2O with its most intense reflections (111) at 36.4° and (200) at 42.3°, Figure 8.1a. The addition of the Au NPs induces broad and weak Au(111) reflections at 37.34°, which are present for all catalysts, with increasing intensity as a function of the Au loading. Low Au loadings resulted in a good distribution across the Cu_2O sample surface,

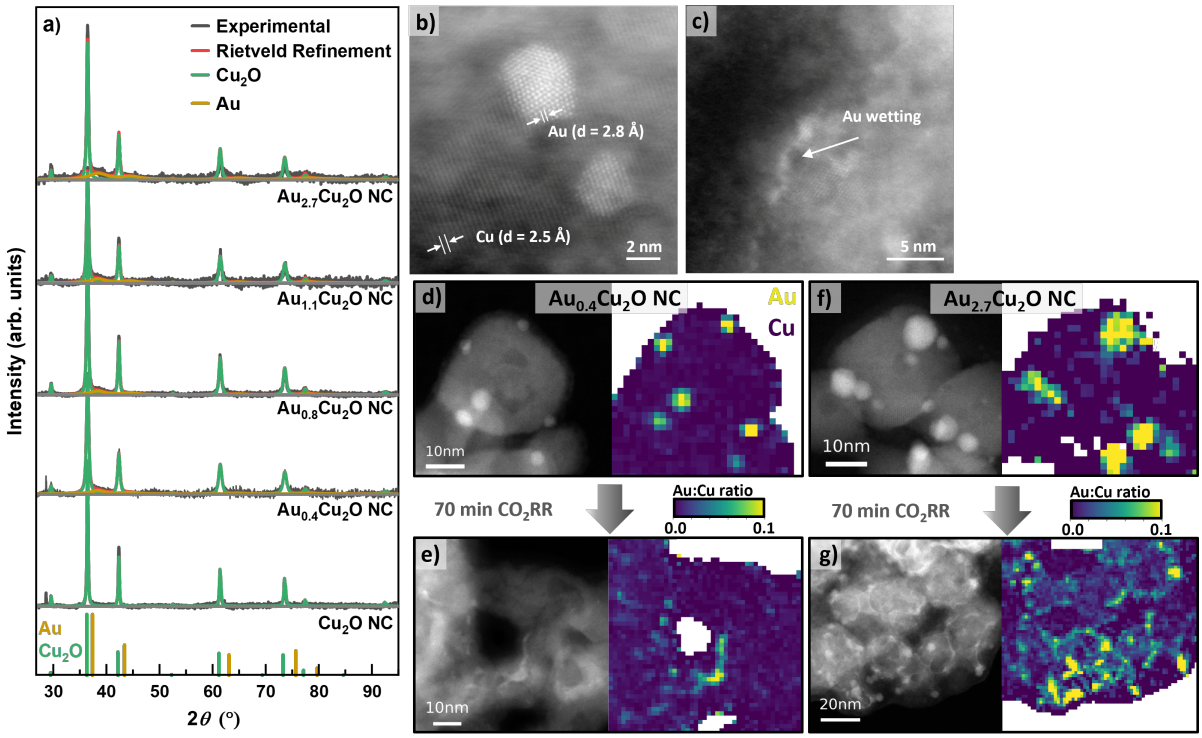

Figure 8.1: a) Ex situ XRD pattern of the as-prepared catalysts and their corresponding Rietveld refinement fits. Scanning Transmission Electron Microscopy (STEM)-High-Angle Annular Dark Field (HAADF) images of b) Au monocrystalline and polycrystalline NPs on the surface of $Au_{0.4}Cu_2O$ NC in their as-prepared state and c) an example of Au wetting on the surface of the same $Au_{0.4}Cu_2O$ NCs after 70 min CO_2RR. STEM-HAADF images with corresponding EDX mappings of (d, e) $Au_{0.4}Cu_2O$ NCs and (f,g) $Au_{2.7}Cu_2O$ NCs in as prepared state (d,f) and after 70 min CO_2RR (e,g). The reaction was carried out in CO_2-saturated 0.1 M $KHCO_3$ at −1.05 V.

which is consistent with previously reported catalysts.[242] The coherence lengths obtained by Rietveld refinement for the Cu_2O NCs of all catalysts vary between 21 and 42 nm, Table S8.2. These findings are in agreement with the Cu_2O NC edge length and Au NP size distributions displayed in Figure S8.12 andTable S8.4, revealing cube edge lengths of ca. 20 nm and Au NPs sizes of 3–4 nm. The Au NPs are evenly dispersed on the surface of the Cu_2O NCs and attach preferentially to the corners of the cubes. Interestingly, the Au NPs exhibit both, single grain and multigrain structures, Figure 8.1b.

The electrocatalytic performance of the catalysts was evaluated by chronoamperometric measurements at −1.07 V for 1 h in CO_2-saturated 0.1 M $KHCO_3$ for the different Au loadings. Figures 8.2a,b shows the selectivity trends in form of FEs as a function of the Au loading and the corresponding current densities (e). The potential dependent FEs and corresponding currents for each catalyst are given in Figure S8.8. In Figure 8.2a, the increased formation

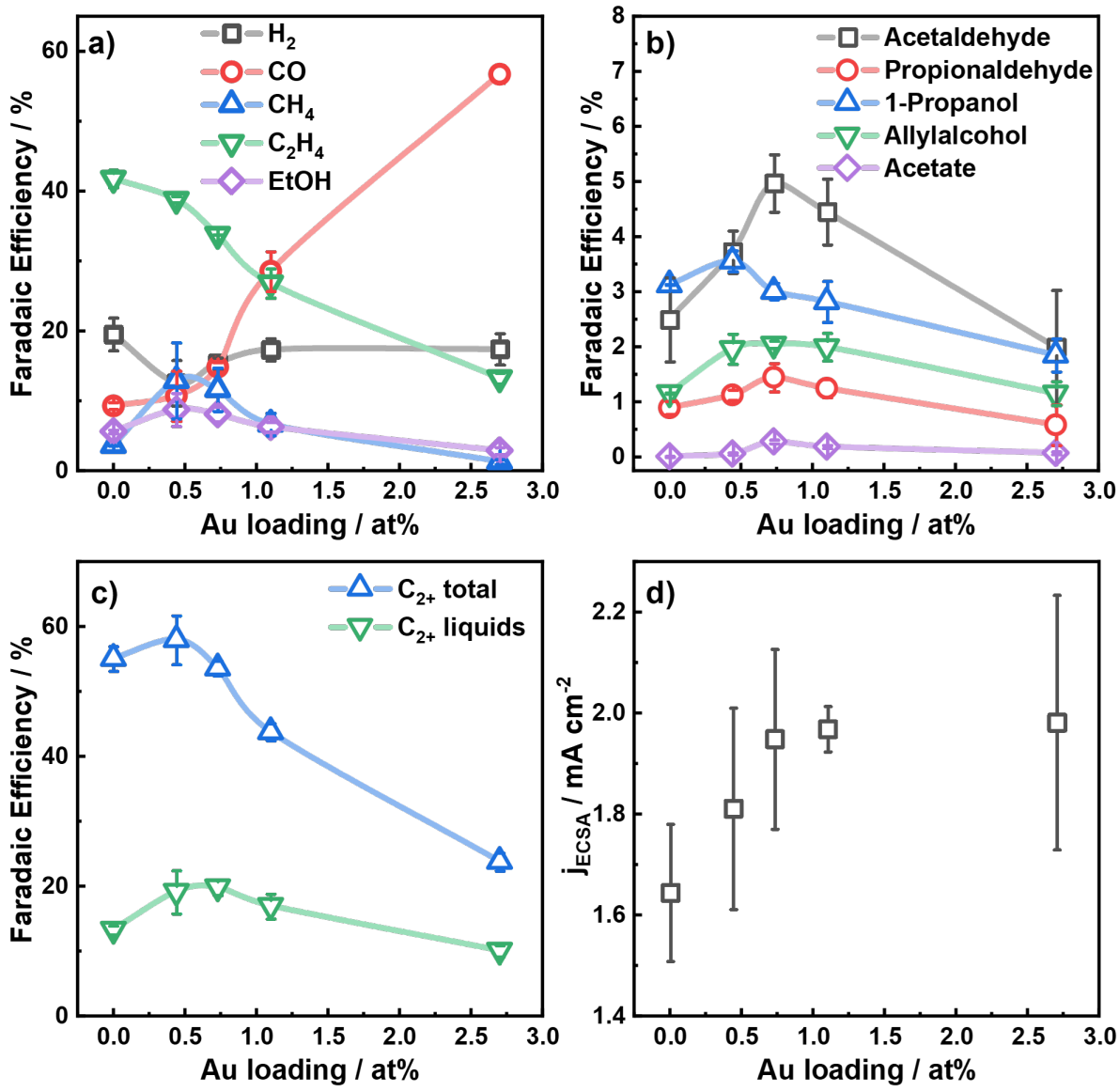

Figure 8.2: Faradaic efficiencies at -1.07 V in 0.1 M $KHCO_3$ as a function of the Au NP loading for a) H_2, CO, CH_4, C_2H_4 and ethanol; b) minor liquid products, c) C_{2+} total products, C_{2+} liquid products; d) current density, normalized by the Electrochemical Surface Area (ECSA).

of CO with increasing Au loading up to a FE of 56% for $Au_{2.7}Cu_2O$ NC is most evident. This high production of CO on Au suggests a high local CO concentration around the Au NP perimeter in the proximity of Cu. In return, the C_2H_4 production is indirectly correlated to the CO production, sacrificing the FE of C_2H_4 for CO for large Au coverages on the Cu_2O NCs. Hydrogen production decreases for the lower Au loadings ($<$1%), while a slightly higher CH_4 production is found. The FE of ethanol increases slightly by 2 percentage points for $Au_{0.4}Cu_2O$ NCs and $Au_{0.8}Cu_2O$ NCs. Remarkably, the FEs of the minor liquid products such as propionaldehyde, acetaldehyde and allylalcohol are also boosted for the lower Au loadings. Acetaldehyde, which is considered as the direct precursor of ethanol, is improved for all Au loadings investigated and is highest for $Au_{0.8}Cu_2O$ NC, with 4.8% FE, 2.6 times higher than for the pure Cu_2O NCs. For this catalyst, the highest FE is also observed for propionaldehyde, while allylalcohol has its peak FE for the three low Au loading catalysts and 1-propanol is the highest for $Au_{0.4}Cu_2O$ NC.

For the bimetallic catalysts, the increased ethanol production is typically linked to weaker binding strength of *CO intermediates and to a CO spillover mechanism, which is described well for Ag-Cu systems.[58,104,107,243] Although Au-Cu systems tend to alloy under reaction conditions, the CO spillover mechanism for these systems is not clearly understood. In our case, and in contrast to the similarly prepared Ag-Cu_2O NCs,[107] the addition of Au as co-catalyst does not improve the ethanol production significantly, despite the increased production of acetaldehyde. Ethanol is understood to be produced either directly from the *CH_2CHO intermediate through protonation, or through readsorption of acetaldehyde (CH_3CHO) with subsequent protonation.[34] We explain the preferred production of acetaldehyde and the impeded production of ethanol by the high CO-richer environment that hinders the protonation of the *CH_3CHO intermediate and the re-adsorption of acetaldehyde on the catalyst. The lowered hydrogen production, observed for our Cu-Au catalysts, is in agreement with impeded *H coverage on the surface and OH^- formation.

Figure 8.2c displays the total C_{2+} product FE, which is the highest for $Au_{0.4}Cu_2O$ NC and exceeds slightly the ones of Cu_2O NC and $Au_{0.8}Cu_2O$ NCs. With increasing Au loading, the C_{2+} product formation reduces drastically, which results mainly from the decreased FE of ethylene and ethanol. The C_{2+} liquid product formation for the two lowest Au loading exceeds that of the Cu_2O NCs by up to 5% FE. The C_{2+} carbonyl formation, however, increases for the low Au loadings and decreases drastically for the high Au loadings, demonstrating the beneficial effect of low amounts of Au on Cu_2O NCs for CO_2RR. In a similar way, the liquid C_{2+} products increases for the low Au loadings to a maximum of 21% FE and decrease for the $Au_{2.7}Cu_2O$ NCs, where the combined liquid products decrease by 4 percentage points to 17% FE. Thus, a switch in the selectivity for the gaseous products takes place, and for the

$Au_{2.7}Cu_2O$ NCs, the CO selectivity is so high that fewer liquid products are formed.

The total and partial current densities at −1.07 V vs. RHE, normalized by the geometric area of the carbon paper support and roughness factor (RF) are shown as a function of the Au loading in Figures 8.2d and S8.9 and represent the intrinsic catalytic turnover. The total catalyst current density increases slightly with increasing Au loading, indicating a higher activity of the Au compared to Cu, and consequently higher CO production rate, in accordance with literature.[111] Furthermore, the partial current densities for C_{2+} products are again highest for the low Au loadings, with decreasing activities for increasing Au loadings. Notably, the lowest Au loading of 0.4 at% leads to a 2-fold increase in C_{2+} current density and a 4-fold increase for the C_{2+} liquid product current density. Thus, the turnover of CO to C_{2+} products appears to be sensitive to the presence of small amounts of Au (low loadings), leading to a slightly CO-richer environment, while Au loadings and thus, increased CO formation, are detrimental. Stability tests over 20 h on all catalysts confirm the stable product distributions after the initial alloy formation during the first hour and are further described in Supplementary Note 8.6.2, Figure S8.10c.

Furthermore, we studied the redox behavior of the catalysts and the influence of Au decoration thereon using CV. Nonetheless, there are no major differences or trends with the Au loading as compared to the Cu foil detectable in the CO_2-saturated bicarbonate electrolyte beyond variations in the electrochemical surface area. The results, further described in Supplementary Note 8.6.2, Figure S8.7 and Table S8.3, display a lack of differences in the redox behavior comparing the CVs of our Cu-Au catalysts with the ones of pure Cu, in contradiction to hte literature,[230,233] which we assign to our generally low Au loadings.

The evolution and differences in the product distribution which we identified, suggest changes and differences in the bulk and near-surface properties of the catalysts, which have to be tackled to understand the catalyst function on the atomic level. Therefore, we carefully analyzed STEM and EDX images before and after CO_2RR to identify any irreversible morphological restructuring and Au wetting effects of the Cu surface.

Figures 8.1 and S8.11-S11 depict the TEM, HAADF-STEM images and their corresponding binned EDX mappings of the catalysts before and after CO_2RR. Two selected catalysts show well-dispersed Au NPs on the surface of the Cu_2O NC in the as-prepared state, Figures 8.1d,f, and S8.16. After 70 min of CO_2RR at −1.05 V, strong morphological changes are observed for the Cu_2O NCs, losing their cubic shape and appearing porous, Figures S8.11 and S7. Note here that the catalysts in the present TEM study have undergone exposure to air before the microscopic analysis, Figure S8.16, but these results are in line with recent *in situ* TEM studies in which the shape of the Cu_2O NCs was investigated during CO_2RR.[198] The NC edge lengths

and the Au NP sizes did not change upon CO_2RR compared to the as-prepared catalysts within the experimental uncertainty. However, the number of Au NPs decreases and the Au became incorporated into Cu as fine lines in between the retained Au NPs, Figures 8.1e,g and S8.16. This Au wetting forms a skeleton-like structure in which Cu reshapes into a new frame. A more detailed analysis on the wetting effect of the $Au_{2.7}Cu_2O$ NCs was performed via high-resolution TEM, Figure S8.11. The images clearly show separate phases in the as-prepared state and an Au-wetted Cu surface after CO_2RR framing around the nanostructures, Figure 8.1c. This Au wetting phenomenon is more pronounced for the higher Au loadings, rearranging the catalyst structure towards an Au-rich frame, Figures8.1e,g and S8.16. Indeed, significant changes in the Cu morphology were found for the low Au loading catalysts, partially with coalescence and dissolved Cu. On the other hand, when the higher Au loadings on the Cu_2O catalysts are considered, the cubic-framed shape is more easily preserved, Figures S8.11 and S8.16. in this case, the Au-wetted branch-like areas indicate an Cu-Au alloy formation, which is suggested to improve the stabilization of the Cu NCs. However, for the $Au_{2.7}Cu_2O$ NC, ever after 1 h of CO_2RR, there are still Au NPs are preserved, suggesting that the Au is not completely alloyed in this sample, which increases the compositional complexity of the catalysts with different Au and Cu-rich phases being present during catalysis.

We also followed the changes in the surface composition from the EDX maps and as expected found an increased Au:Cu ratio with increasing nominal Au loading, though with a slight offset as compared to the results obtained by ICP-MS, Table S8.5. Note that EDX is a semiquantitative method without external standards and that, due to the low-Au loadings considered, the Au ratios extracted here are all within the detection limits of this methods (1-2%). After CO_2RR we identified a relative increase of the Au:Cu ratio for the $Au_{0.4}Cu_2O$ NC, while it remains mostly stable for the other catalysts. In combination with the morphological changes, this can be explained with a stronger loss of Cu for the lowest Au loading. Supplementary Note 8.6.2, Figure S8.17 and Table S8.6. The Au:Cu ratio was also locally mapped by binning the EDX images, Figure 8.1d-g and S8.16. For the as-prepared catalysts, defined NPs are observed, while after CO_2RR, both distorted Au NPs and Au wetting of the Cu surfaces were observed. The Au wetting and skeleton-like structures observed around the cubic shapes are clearly visible.

To understand the irreversible changes of the surface composition, chemical state and alloy formation of the bimetallic catalysts upon CO_2RR, we employed quasi *in situ* X-ray Auger Electron Spectroscopy (XAS) and X-ray Photoelectron Spectroscopy (XPS). Thereby, air exposure of the catalysts after reaction was avoided to prevent surface re-oxidation and possible restructuring. Figure 8.3 shows the Cu LMM X-ray Auger Electron Spectroscopy (XAS) (a) and Au 4f and Cu 3p (b) core level XPS regions for the $Au_{2.7}Cu_2O$ NCs before and after 1 h

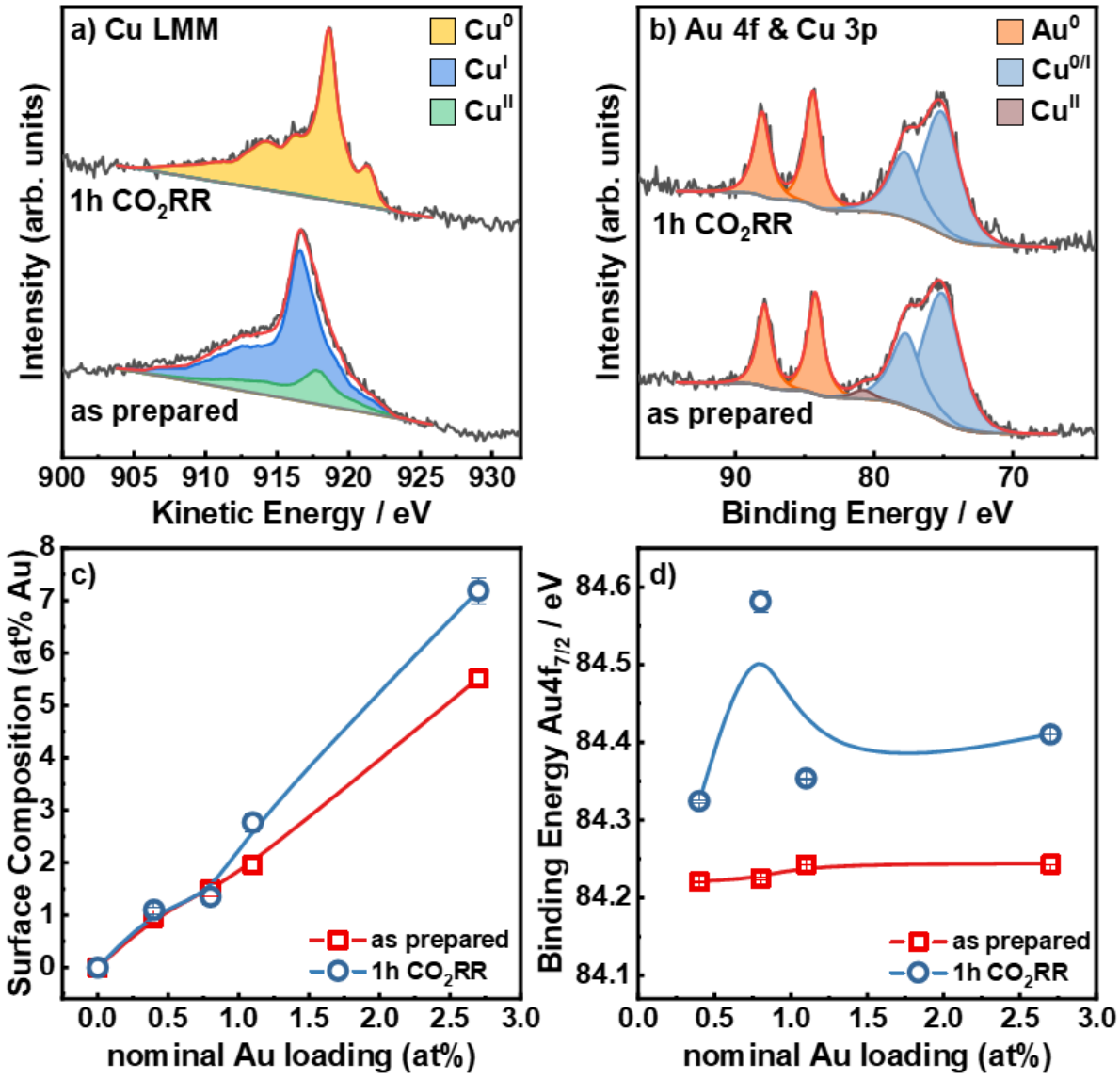

Figure 8.3: Quasi *in situ* XPS spectra for the $Au_{2.7}Cu_2O$ NCs: a) Cu LMM Auger and b) Au 4f and Cu 3p in the as-prepared state and after 1 h CO_2RR at −1.05 V vs. RHE in 0.1 M $KHCO_3$. c) Surface composition in at% Au compared to at% Cu as a function of the nominal Au loading in the as-prepared state as well as after CO_2RR. d) Binding Energies of the Au $4f_{7/2}$ core level region in the as prepared state and after 1 h CO_2RR.

CO_2RR at −1.05 V as well as the surface composition (c) and the binding energy of the Au $4f_{7/2}$ peak (d) as a function of the nominal Au loading. The Cu 2p, Au 4f, Cu 3p XPS and Cu LMM XAS for all catalysts are shown in Figures S8.18 - S8.20. The Cu LMM Auger spectra in Figure 8.3a show a combination of Cu^0, Cu^I and Cu^{II} in the as-prepared state and a reduction of Cu^{II} /Cu^I to Cu^0 after CO_2RR. In the as-prepared states, the catalysts present similar ratios of Cu_2O (80-90%) and CuO (10-20%), whereas, after 1 h under CO_2RR at −1.05 V, all catalysts appear reduced to metallic Cu within the error margins, Figures S8.18, S14, Table S8.7. The Au 4f spectra in Figure 8.3b show peaks at $E_{BE,7/2}$= 84.2 eV and $E_{BE,5/2}$= 87.9 eV, resembling metallic Au, and the increased binding energy of +0.2 eV can be assigned to a nanoparticle size effect.[54]

The surface composition of the catalysts was determined by comparing Cu 3p and Au 4f spectra, Figure 8.3b,c and Table S8.8. In the as prepared state, the Au surface loadings are with ∼1 to ∼6% significantly higher than the average bulk composition. The Au surface composition increased after 1 h CO_2RR for the higher Au loadings. This effect can be assigned to a combination of dynamic redistribution, segregation and wetting of Au on the Cu surface. These findings agree well with the STEM-EDX and ICP-MS data presented before.

Figure 8.3d demonstrates that the Au 4f binding energy does not vary strongly with Au loadings in the as-prepared state. However, the Au 4f binding energy increased upon CO_2RR by 0.2 eV, suggesting a change in the electronic structure around the Au NPs and the possible formation of an alloy formation between Au and Cu.[244] This could however also be explained as a size effect, with the higher binding energy shifts detected for the Au loadings in the as-prepared state with the smallest Au NPs. Furthermore, depending on the Au loading, the binding energy during CO_2RR varies from 84.32 eV to 84.41 eV. An increasing Cu fraction in the CuAu alloy leads to increased binding energies,[244] and thus, we conclude that the fraction of CuAu alloy regions increases with the Au loading after the CO_2RR.

Notably, this trend reflects the averaged surface chemistry of the Au atoms and shows an increasing presence of the Cu-Au alloy with increasing Au loading. Additionally, it must be considered that for the initially high Au loadings still a significant density of unalloyed Au NPs have been observed, Figure 8.1g, suggesting that the surface also comprises Cu-rich Cu-Au alloy regions. Thus, we conclude a significant decrease in the density of pristine Cu sites. Remarkably, the $Au_{0.8}Cu_2O$ NCs show relatively high binding energies of the Au $4f_{7/2}$, indicating higher alloy formation than for the other catalysts. This observation coincides with the lower CO, C_{2+} liquid products and H_2 specific activities, Figure S8.9, as compared to the $Au_{0.4}Cu_2O$ NCs, and illustrates that a large fraction of Cu-Au alloy formation is detrimental for C_{2+} production from CO_2RR.

To extract comprehensive information on the catalyst's bulk structure during CO_2RR, we employed *operando* HE-XRD to understand the formation of crystalline $Cu_{1-x}Au_x$ alloy phases during CO_2RR. Note that highly disordered metallic or cationic phases cannot be detected using XRD. We have previously shown that the bare Cu_2O NCs mostly reduce to metallic Cu using *operando* HE-XRD.[71] Figure S8.21 presents the XRD pattern of the $Au_{2.7}Cu_2O$ NC recorded at 67 keV at OCP and after 1 h at −1.05 V. At OCP, the diffraction pattern agrees well with the Cu_2O phase, in addition to the strong background caused by the electrolyte. During CO_2RR, the Cu_2O Bragg peaks disappear almost completely, and a diffraction pattern of metallic Cu developes. The broad feature at ∼4.65° could be caused by a $Cu_{1-x}Au_x$ phase(s). Compared to the as-prepared Cu_2O NCs, the Bragg peaks of the metallic Cu during CO_2RR are significantly broader, suggesting a shorter structural coherence length. Rietveld refinement reveals a coherence length of ∼7 nm of the metallic Cu domains compared to ∼17 nm for the Au-free Cu_2O at OCP. The structural properties of the potential $Cu_{1-x}Au_x$ minority phase were not reliably resolvable using Rietveld refinement. The Cu lattice parameter of ∼3.6499 Å did not show any evidence for Au incorporation into the main Cu phase during CO_2RR. Thus, *operando* HE-XRD shows the reduction of the $Au_{2.7}Cu_2O$ NCs during CO_2RR, which consists mainly of a bulk Cu phase with a potential highly disordered $Cu_{1-x}Au_x$ minority phase. Further details are given in Table S8.9.

Further insights into the chemical composition, interatomic interactions and alloy formation during CO_2RR were extracted from *operando* X-ray Absorption Spectroscopy (XAS). This technique is highly complementary to the XRD data presented above, since it unveils the disordered phases present in these samples under the different environments and reaction conditions. The analysis of the Cu K edge XANES and EXAFS data is shown in Supplementary Note 8.6.2 and Figures S8.22-S21 and Tables S8.11 and S11.

The temporal evolution of the Cu K-edge XANES profile during CO_2RR conditions was followed by QXAFS) and the chemical state components were quantified via LCA using reference spectra, Figure S8.23. The initial states in the electrolyte show varying contributions of Cu_2O and CuO, which might be attributed to an aging effect of the catalysts and/or a beam damage effect. Upon application of −1.0 V, the majority of the Cu_2O reduces within 20 s to metallic Cu and after 4 h of CO_2RR, fractions of 10% Cu_2O were observed, which indicates a robust Cu_2O phase in the core of the catalysts since quasi *in situ* XPS showed a purely metallic catalyst surface after 1 h CO_2RR. The coordination numbers during CO_2RR suggest a bulk-like metallic Cu as the dominant phase, which is in agreement with the insights from *operando* HE-XRD. These remnant Cu oxide species even after prolonged exposure to CO_2RR conditions were also observed for analogous pure Cu_2O and Ag-decorated Cu_2O NCs.[107,244] Interestingly, the CuO of the $Au_{2.7}Cu_2O$ catalysts first reduces to Cu_2O as the Cu_2O LCA weight first increases

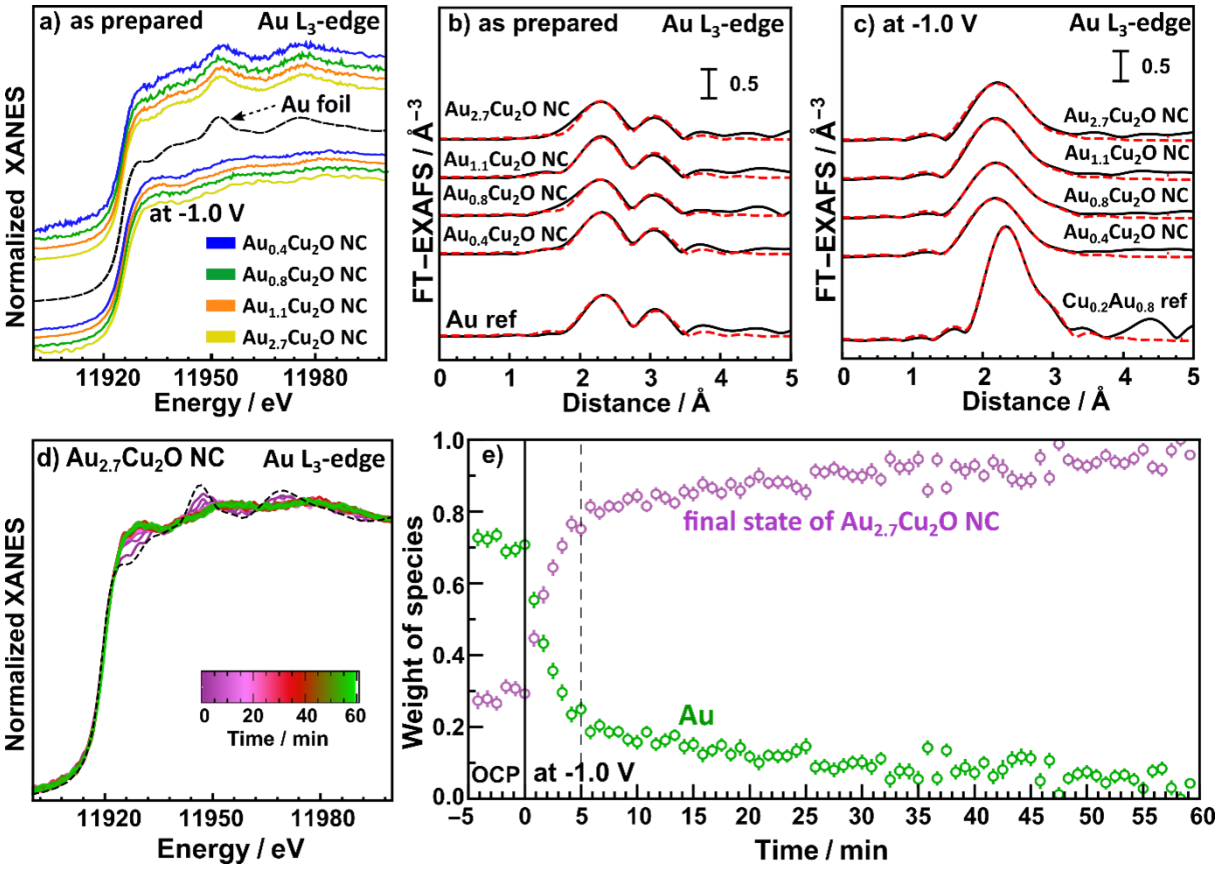

Figure 8.4: Normalized Au L_3-edge a) XANES and FT-EXAFS spectra of the Cu_2O NCs with varying Au loadings b) in the as-prepared state and c) during CO_2RR at −1.0 V. Reference spectra of Au foil and a $Cu_{0.2}Au_{0.8}$ reference alloy are shown for comparison. $Cu_{0.2}Au_{0.8}$ reference was redrawn from [245]. d) Au L_3-edge XANES spectra and e) weight of the species as a function of time during CO_2RR at −1.0 V unveiling the formation of a CuAu alloy.

by about 5-10 percentage points before the catalysts reduce further, which is also in accord with previous observations.[71]

The corresponding Au L_3 edge XANES data in Figure 8.4a demonstrate that the Au NPs in the as-prepared catalysts are in a metallic state, with a local environment similar to that in the Au foil reference material. However, during CO_2RR, a white line feature at 11 930 eV appears, reflecting a more cationic character of the Au atoms and thus, changes in the electronic structure due to alloying with Cu and an accompanying charge transfer to the Cu.[244,246] Moreover, we observe significant changes in the post-edge features, suggesting significant changes in the interatomic distances and/or changes in the types of nearest neighbors of the absorbing Au atoms as compared to bulk Au. We note that the evolution of the Au L_3-edge XANES spectra proceeds similar for all our catalysts, regardless of the Au loading.

We obtained further insights into the local atomic structure of the Au atoms from the fitting of the FT-EXAFS spectra, Figures 8.4b, c, Table S8.12. The as-prepared catalysts exhibit a prominent peak at 2.3 Å (phase uncorrected), resembling Au-Au bonds with a distance $R_{Au\text{-}Au}$ of 2.8 Å and a coordination number CN of around 12(2), matching the results obtained for the Au foil ($R_{Au\text{-}Au}$ 2.9 Å, CN = 12). This is analogous to the conclusions extracted from the XANES spectra as well as with the TEM and XPS data showing Au NPs well dispersed and attached to the Cu_2O NC surfaces. During CO_2RR, the Au-Au coordination number decreases while a Au-Cu distance evolves with coordination numbers between 8 and 10. Interestingly, we observe a significant mismatch between Au-Au and Au-Cu bond lengths, where the former remains similar to that in the Au foil (2.86 Å), while the latter is ca. 2.62 Å, which is clearly larger than the Cu-Cu bond lengths in bulk metallic Cu (2.54 Å).[247] These results suggest a heterogeneous structural evolution in which Au-rich regions coexist with regions of a Cu-rich Cu-Au alloy. The average interatomic distances for Au-Cu of 2.62 Å agrees best for a AuCu-like phase, following Vegard's rule. Furthermore, we have to note that the coordination number ratio of the Au-Au and Au-Cu distances during CO_2RR seems to decrease with increasing Au content for loadings above 0.4 at%. Thus, our *operando* analysis shows that for all Au loadings a Cu-Au alloy of low crystallinity and/or domain size forms during CO_2RR and that the extent of alloy formation increases not only irreversibly on the surface but also likely during CO_2RR.

Additionally, we investigated the evolution of the Au_xCu_y alloy formation from the Cu perspective, Figure S8.23, and the Au perspective over 60 min by collecting XAS spectra every 1 s for $Au_{2.7}Cu_2O$ NC (QXAFS) and every 12 min for $Au_{0.4}Cu_2O$ NC and $Au_{0.8}Cu_2O$ NC, Figure 8.4d and S8.26. We then evaluated the weight of the different species as a function of time with a final state of the CuAu alloy as reference, Figure8.4e. The local structure around Au evolves much slower than the reduction of Cu, and about one hour is needed to

reach a stable alloy phase. Thus, these results might explain the slow product adaptation of the Au-containing catalysts in the long-term CO_2RR measurements over 20 h. Restructuring of the catalyst during alloy formation represents significant atomic mobility and continuous altering of the active sites which in turn continuously affects the product distribution.

We furthermore studied the role of the potential-dependent CO-related adsorbates with varying Au loading by using *operando* SERS. Figures S8.27 and S23 show the SERS data recorded at potentials between OCP and −1.1 V vs. RHE for the Au-decorated Cu_2O NCs. At OCP, the Raman scattering of the Cu_2O exhibits the typical bands at 415 cm^{-1} (multiphonon process), 527 cm^{-1} (Raman active F_{2g} vibrational mode), 623 cm^{-1} (IR active F_{1u} mode) and 220 cm^{-1} (overtone $2E_u$). These bands were found to disappear at 0.2 V for all catalysts, which reflects the electrochemical reduction of surface Cu_2O to Cu.[248] Between 0.2 V and 0.1 V, bands at 360 cm^{-1} appear with corresponding bands at 706 cm^{-1}, 1050 cm^{-1} and 1074 cm^{-1}, which have been assigned to surface copper carbonate species, Figure S8.28.[31,249] Remarkably, a CO stretching band at 0.2 V around 2090 cm^{-1} was observed for the three higher Au loadings and may be linked to carbonates. The CO stretching bands around 2090 cm^{-1} are significantly stronger for the $Au_{2.7}Cu_2O$ NCs compared to the $Au_{0.8}Cu_2O$ NCs and $Au_{1.1}Cu_2O$ NCs. For the $Au_{2.7}Cu_2O$ NCs, two peaks at 2039 cm^{-1} and 2090 cm^{-1} overlap, while the former band decreases in intensity until −0.4 V.

At more cathodic potentials, new bands appear at 280 cm^{-1} and 366 cm^{-1}, which correspond to the restricted rotation of *CO on Cu (CO_{rot}) and Cu-CO stretching ($CO_{stretch}$), respectively. Following our previously established link of their intensity ratio ($CO_{stretch}/CO_{rot}$) to the formation of C_{2+} products,[31] we determined $CO_{stretch}/CO_{rot}$ ratios for the Au-decorated Cu_2O NC catalysts, which are lower those previously found for the pure Cu_2O NCs[31] as well as those for the Ag/Cu_2O NCs during CO_2RR, suggesting a lower CO coverage on the Cu surface in the case of the Cu_2O NCs decorated with Au NPs.[107] We also did not detect a potential-dependent correlation between the $CO_{stretch}$ ratios and the C_{2+} product FE for the Cu-Au samples as in the case of the bare Cu_2O NCs or Ag/Cu_2O NCs, Figures S8.29. This result suggests a lower CO coverage on Cu for the Au-decorated Cu_2O NC catalysts as compared to the pure Cu_2O NCs[31] and Ag/Cu_2O NCs[107] and indicates a more complicated mechanism. Thus, the enhanced C_{2+} (liquid) product FE identified for low Au loadings on the Cu_2O does not appear to stem from differences in the CO coverage on the Cu surface as it was the case for the Ag-decorated Cu_2O NCs. Our new findings for the Au-Cu system suggest a more complicated mechanism involving the presence of the more easily formed CuAu alloy as compared to the Cu/Ag system. Notably, bands between 500 cm^{-1} and 700 cm^{-1} develop during CO_2RR, which has not yet been unambiguously assigned and might evolve from Cu/Au-OH species.[250,251] These bands display a shift towards higher Raman frequencies with

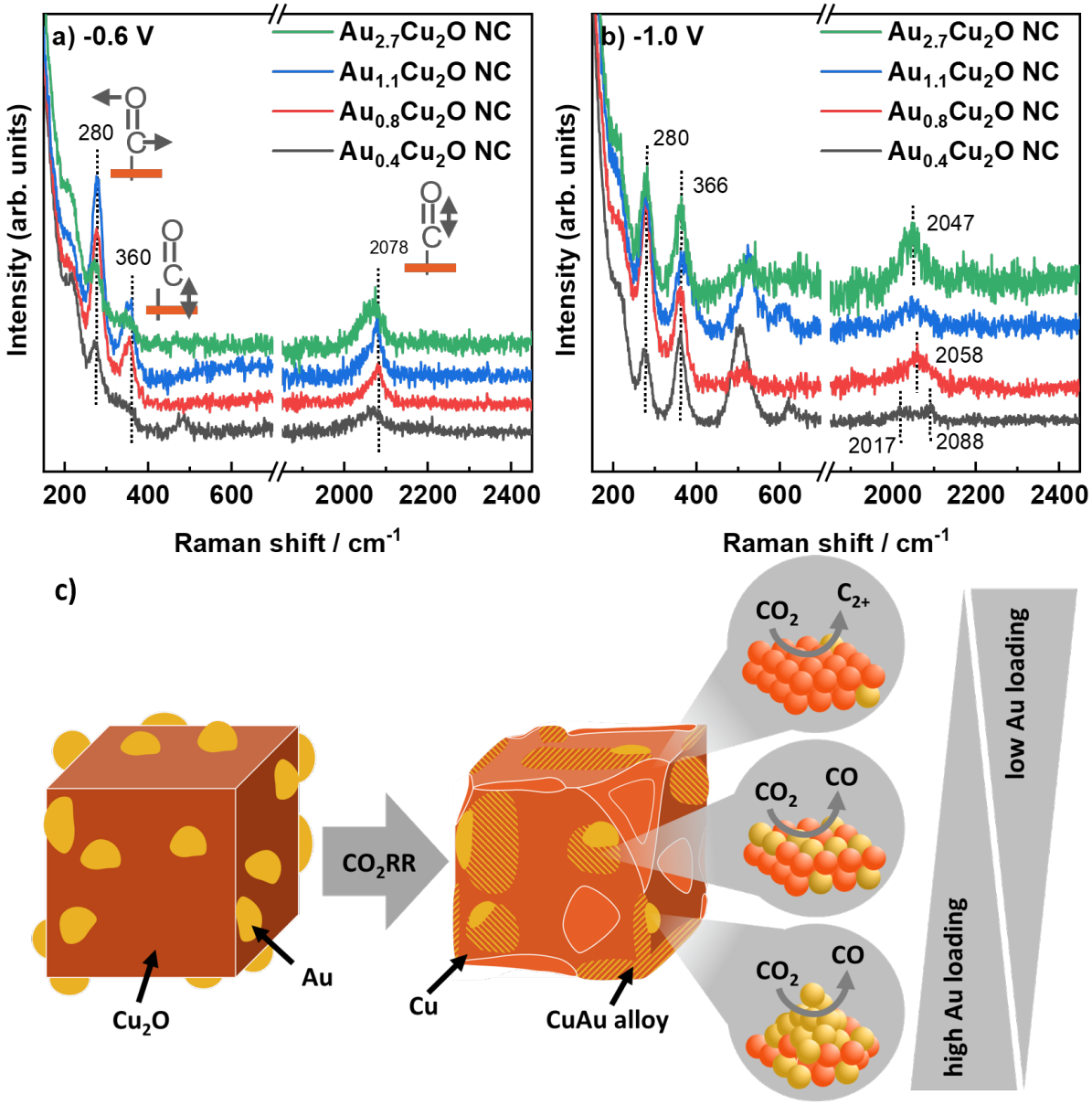

Figure 8.5: *operando* surface-enhanced Raman spectra of the Au-Cu_2O catalysts at a) −0.6 V and b) −1.1 V in CO_2-saturated 0.1 M $KHCO_3$. c) Schematic illustration of the catalyst structure in the as-prepared state and during/after the CO_2RR with their corresponding main products. The triangles indicate the amount of Au loading favoring the different Au-Cu atomic structures/redistributions.

increasing Au loading without a specific trend in the intensity and suggest a decreasing OH binding energy with increasing Au loading.

Figure 8.5a shows the Raman spectra for the different Au loadings at −0.6 V and verifies that the C-O stretching bands have similar Raman shifts at 2078 cm^{-1}. At −1.0 V, Figure S8.28, the C-O stretching bands of the $Au_{2.7}Cu_2O$ NC and the $Au_{1.1}Cu_2O$ NC blue-shift potential-dependent towards 2047 cm^{-1}. For these high Au loadings we can also identify two additional bands at ∼1900 and 2200 cm^{-1},[252] which stem from the C-O vibrations on Au sites and can be linked to the significant increase of the FE of CO. For the $Au_{0.8}Cu_2O$ NC, the C-O stretching band shifts only to 2058 cm^{-1}, while no peak shift is observed for $Au_{0.4}Cu_2O$ NC and the pure Cu_2O NC with 2088 cm^{-1}.[107,243] Interestingly, the $Au_{0.4}Cu_2O$ NC shows an additional weak Raman band at ∼2017 cm^{-1}, suggesting the presence of multiple CO adsorption sites. The position of the C-O stretching band is directly linked to the average CO binding energy to the surface[251] and thus, the observed variation in its position during CO_2RR reflects a weaker binding of the CO with increasing Au loading, which appears to stabilize for Au loadings higher than 1.1 at%. This effect agrees with the increasing fraction of Cu-Au alloy with Au loading which exhibits a weaker CO binding energy and can be explained with a downshift of the d-band center from the Fermi level with increasing Au fraction.[253,254] Furthermore, variations in the position of the C-O stretching band on pure Cu surfaces have been linked to their defect density, suggesting a lower defect density at higher overpotentials with increasing Au loading.[251] It has been discussed that adjacent OH adsorption to the CO_{ads} sites may influence the C-O stretching band, but we did not detect a link between the C-O band position and the intensity of the Cu/Au-OH band.[255] Thus, we attribute the variations in the C-O band position to variations in the CO binding primarily induced by Cu-Au alloy formation leading to a weaker bound CO on the catalyst surface for the higher Au loadings. For low Au loadings, multiple e.g. Cu- and Au-like adsorption sites with clearly different binding energies are present.

Additionally, the intensity of the C-O stretching bands at high overpotentials increases with Au loading compared to the pure Cu_2O NC, while the Cu-CO related bands do not vary strongly in intensity. This suggest that a CO-richer surface and/or micro-environment forms during CO_2RR in the presence of Au-rich regions, while any increase in CO surface coverage would be linked to Au-related sites as the Cu surface coverage does not increase following the $CO_{stretch}/CO_{rot}$ analysis.

Our comprehensive study of the active catalysts state and the catalytic function of Au-decorated Cu_2O NC suggest that there is a two-stage catalytic role of the Au decoration within the complex mixed phase between the Cu host, CuAu alloy and Au-rich NPs. Clearly,

our Au/Cu_2O catalysts easily form Cu-Au alloys *in situ* under CO_2RR conditions which, for higher Au loadings above 1at% Au, can be detected within minutes during CO_2RR and even after CO_2RR in the near-surface. A higher Au loading leads to stronger alloy formation and results in a weaker average CO binding to the catalyst surface during CO_2RR. The weaker (average) binding energy agrees with the d-band theory[253] and enhances CO production.

This interpretation is in agreement with the current state of knowledge for the formation of C_{2+} products over AuCu,[111,112,241,256] which has also been discussed in the literature for CuAg systems,[107,228,247,257,258] see also Table S8.13. Homogeneous Cu-rich Au-Cu alloys have been proven to generate only very small fraction of C_{2+} products, while Au-rich alloys produce mostly CO.[111] Thus, the Au-Cu alloy itself is not considered to improve the CO_2RR catalytic function and mixed systems with either an Au-Cu alloy or Au embedded in a Cu matrix have been a focus of further studies with more success.[112,241,256] While CO may be produced in the Au-Cu regions of our catalysts, the actual CO dimerization occurs on the Cu surface in a sequential fashion and an optimal ratio between both regions (Cu-Au interface and Cu-Cu surface) is therefore crucial. The higher fraction of near-surface AuCu alloy likely decreases the density of Cu-Cu sites which are better for C_{2+} product formation and thus, the formed CO cannot be utilized for dimerization at high Au loadings. Therefore, the beneficial effect of Au with respect to the formation of CO promotion is concurrent with the detrimental effect of the Au-Cu alloy in the subsequent C-C coupling, for which Cu-Cu sites are sacrificed.

Nevertheless, the Au-decorated Cu_2O did not improve the ethanol performance with respect to prior literature reports.[241,256] However, comparing CuAu and CuAg bimetallic systems for improved C_{2+} selectivity to pure Cu, we observe substantial differences between both systems in the onset potential of CO, the CO production rate as well as their ability to form alloyed structures. Table S8.13 displays the overall better performances towards C_{2+} products of CuAg systems, which are mainly attributed to CO spillover and/or to a good Ag/Cu miscibility without pronounced alloy formation.[107,228] In contrast, CuAu systems, with its pronounced alloy formation during reaction conditions, may benefit from synergistic effects between the electronic structure and the morphology of the catalytic system.[259]

Unlike other studies in literature, we present here an Au-loading dependent study and found optimal Au loadings <1 at% Au for improving the C_{2+} products. Only lower fractions of CuAu alloy lead to an enhanced C_{2+} FE for low Au loadings on the Cu_2O NC. Remarkably, the specific activity for C_{2+} (liquid) product formation increased by up to 400%. In this case, a significant fraction of the Cu domains remains unalloyed and the catalysts exhibit a stronger average or even weaker and stronger CO binding sites during CO_2RR. The latter ones can act as active sites for CO dimerization, while the minority CuAu alloyed regions still facilitate

CO_2 reduction to CO and the tandem catalytic function boosts the intrinsic C_{2+} formation significantly. Our findings suggest that low Au loadings, e.g. decoration on the atomic level can be a promising approach to further enhance the C_{2+} product formation. Here, we see a striking similarity to our findings on Ag-decorated Cu_2O NCs, which form disperse Ag sites on the Cu surface at even higher Ag loadings.[107] Our findings strengthen the hypothesis that i) optimal amounts of additionally formed CO are beneficial for C_{2+} formation on Cu, ii) CuAu alloys mainly contribute in CO formation but not C2 products and iii) the main species required for CO dimerization are adjacent Cu sites. We therefore conclude that the CuAu systems are worth to explore further for C_{2+} product promotion when low amounts of Au are available in the vicinity of Cu-Cu sites, such that the indispensable alloy formation during CO_2RR is low as compared to the pure Cu regions. This instance allows to display improved C_{2+} selectivity with CuAu bimetallic systems.

8.5 Conclusion

In summary, we demonstrated that the Au-decorated Cu_2O NCs yield notably enhanced C_{2+} production due to high CO coverage on copper, which results from the highly CO producing Au NPs, and due to significant restructuring towards CuAu alloy formation. Under CO_2RR relevant conditions, Cu_2O NCs with large amounts of Au NPs demonstrate significant restructuring and redistribution by forming CuAu alloyed frames with increased Au-to-Cu ratios on their surface, which appear to stabilize their initial cubic shape.

Operando XAS served to follow the alloy formation and to observe structural changes between Cu and Au within one hour, which led to a variation of the selectivity trends, in agreement to the long-term reactivity measurements. Increasing Au loadings result in a proportional increase of CO, while small Au loadings lead to a notable increase in C_{2+} liquid products such as ethanol, acetaldehyde, 1-propanol, allylalcohol and propionaldehyde. Importantly, our low Au loading catalysts show a 4-fold increase in the specific activity for liquid C_{2+} production formation and thus, an interesting starting point to design high surface area CO_2RR catalysts.

With *operando* Raman spectroscopy, we could link the catalytic function, in particular the strong CO formation to a weaker average CO binding to the catalyst surface in a CO-richer microenvironment and/or higher coverage. The preferred C_{2+} product formation is linked to minority Cu-Au alloy species being formed in close proximity with the stronger CO binding Cu regions. In contrast to our findings for pure Cu_2O NCs we did not detect a clear correlation between the Cu surface coverage with CO and the $_{2+}$ product formation. Linking to the Ag-Cu_2O system, we emphasize the importance of dispersed CO-producing sites on a Cu host in

order to facilitate the CO_2RR Faradaic efficiency, likely by interactions on the atomic level and not CO spill-over through the electrolyte. Understanding the selectivity dependencies on the restructuring of a Cu-Au system which undergoes continuous transformation under CO_2RR relevant conditions provides opportunities for a rational design of highly active and selective bimetallic catalysts.

8.6 Supporting Information

8.6.1 Methods

Synthesis of Cu_2O NC and Au_xCu_2O NCs

The synthesis of Cu_2O NC decorated with Au_xCu_2O NCs was performed following previous reports.[31,159,195,242] 14 ml of 0.1 M $CuSO_4$ (Alfa Aesar, >98%) was dispersed in 366 ml H_2O(18 MΩ) under vigorous stirring at room temperature. 14 ml of 1 M NaOH (Alfa Aesar, >97%) was added to initiate the nucleation process with $Cu(OH)_2$. After 10 s, the metal salt was reduced with 16 ml of 0.25 M L-ascorbic acid (Sigma Aldrich, reagent grade). After 12 min, a defined amount (0.8 ml, 1.6 ml, 3.2 ml, 8 ml) for the nominal loadings 0.4at%, 0.8at%, 1.1at%, 2.7at%) of 10 mM $HAuCl_4$ (Alfa Aesar, 99.99%) was added. After 13 min, the solution was centrifuged and washed two times with a EtOH:H_2O mixture and two times with ethanol. The catalysts were stored in 20ml ethanol. The resulting Cu and Au concentrations in each solution were determined by ICP-MS.

Electrode Preparation

The electrodes for H-type cell measurements were prepared on 2 cm^2 carbon paper (Alfa Aesar, Toray Carbon Paper, GGP-H-60). The stock solutions were drop-casted on each side of the carbon paper to yield a Cu loading of 50 µg on the electrode for each catalyst. The electrodes were dried over night to ensure complete evaporation of ethanol.

Electrochemical Characterization (CVs, Double Layer Capacitance (DLC))

The electrochemical characterization was performed in a H-type cell in CO_2 saturated 0.1 M $KHCO_3$ (Alfa Aesar, 99.7%-100.5%) and in a one compartment cell, equipped with a leak-free Ag/AgCl (3.4 M, LF-1, Alvatek) and an Au wire as counter electrode in Ar saturated 0.1 M NaOH. To control the potential, a Biologic SP-300 was used.

The Double Layer Capacitance (DLC) was measured after the CO_2RR measurements in CO_2 saturated 0.1 M $KHCO_3$. The potential was cycled at increasing scan rates of 10, 20, 40, 80 and 160 mV/second in the non-faradaic region between −0.4 V and −0.25 V vs. RHE.

Electrocatalytic Characterization

A H-type cell with two compartments separated by an anion exchange membrane (Selemion, AMV, AGC INC.) was equipped with a leak-free Ag/AgCl reference electrode (LF-1, Alvatek)

near the working electrode in the cathodic compartment, while a platinum gauze (MaTecK, 3600 meshcm−2) served as counter electrode. The cell was filled with a defined amount of 0.1 M $KHCO_3$ (Alfa Aesar, 99.7%) in each compartment, which was prior purified with a cation-exchange resin (Chelex 100 Resin, Bio-Rad) and pre-saturated with CO_2 (4.5 N) for at least 20 min. The CO_2 flow was held constant at 20 ml/min during CO_2RR. An Autolab (PGSTAT 302N, Metrohm) potentiostat was used for the electrocatalytic characterization. The Ohmic drop was measured with the i-interrupt method prior to the electrocatalytic protocol and with electrochemical impedance spectroscopy (EIS) afterwards. Double layer capacitance was also applied after the previously described protocol. A linear sweep voltammogram from the open circuit potential (ca. 0.5 V) to the respective reduction potential at 20 mV/s was applied followed by chronoamperometry for 4000 s. The online gas product detection was started after 60 s of chronoamperometry and repeated every 15 min with a gas chromatograph (GC, Agilent 7890B), which was geared with a TCD for H_2 detection and a FID for carbon products. After each electrocatalytic measurement, the liquid products were analyzed with high-performance liquid chromatography (HPLC, Shimadzu Prominence), which was geared with a NUCLEOGEL SUGAR 810 column and a refractive index detector, and with a liquid GC (L-GC, Shimadzu 2010plus), which was geared with a fused silica capillary column and a FID detector. All potentials are referred to the RHE with the following equation:

$$E_{RHE} = 0.059 * pH_{electrolyte} + E^{0}_{Ag/AgCl} \tag{8.1}$$

The pH of CO_2 satèlectrolyte is pH 6.4, E_0 of the used Ag/AgCl electrode was 200 mV. The Faradaic Efficiency of each gas product x (FE_x) was calculated as

$$FE_x = \frac{\dot{V} * C_x * z_x * F}{A * V_M * j_{total} * \frac{\Delta t_c}{\Delta t_c + \Delta t_a}} * 100 \tag{8.2}$$

while liquid products were calculated as

$$FE_x = \frac{V * \Delta C_x * z_x * F}{\Delta Q} * 100. \tag{8.3}$$

with A: geometric area of the electrode (cm^2), C_x: volume fraction of the product x detected by the GC, F: Faradaic constant (C mol^{-1}), j_total: total current density during CO_2RR (A cm^{-2}), ΔQ: total charge transfer (C), v: CO_2 gas flow rate (L s^{-1}), V: Volume of the electrolyte (L), V_M: molar volume.

Inductively Coupled Plasma – Mass Spectrometry (ICP-MS)

The catalyst concentration, as well as the atomic compositions of Cu and Au were determined by ICP-MS (Thermo Fisher iCAP RQ). The samples were digested by adding a mixture of acids (1:1:3 H_2SO_4:HNO_3:HCl) into a known amount of the catalyst and heated to 180°C for 30 min using the digestion Microwave Multiwave GO from Anton Paar. Samples from the electrode were digested with the carbon paper, which was discarded afterwards. The stock solutions, samples from the electrode and the electrolyte samples were diluted 3.33, 19 and 4 times in 3% HCl, respectively.

Transmission electron microscopy and energy-dispersive X-ray spectroscopy

The acquisition of Transmission Electron Microscopy (TEM)) and Energy Dispersive X-ray Spectroscopy (EDX) images were performed with a FEI Talos F200X microscope geared with a XFEG field emission gun and an acceleration voltage of 200 kV. The Scanning Transmission Electron Microscopy (STEM) was equipped with a Bright-Field (BF), two Dark-Field (DF), a High-Angle Annular Dark Field (HAADF) and a SuperX 4 SDD EDX detector. The as prepared catalysts were drop-casted directly on a Ni lacey carbon grid, while the catalyst after CO_2RR was removed from the carbon paper by sonicating it for a short time in 200 µl isopropanol. 40 µl of the obtained solution was then drop casted on a Ni lacey carbon grid.

X-ray Diffraction

A Bruker AXS D8 Advance diffractometer in Bragg-Brentano geometry was used for X-ray Diffraction (XRD) measurements with Cu Kα_{1+2} radiation and a position sensitive energy dispersive LynxEye XE-T silicon strip detector. X-ray Diffraction (XRD) patterns were measured in continuous scanning mode in the range between 20 and 100° 2θ, with an increment of 0.02° and a counting time of 1 s/step.

Operando High Energy X-ray Diffraction (HE-XRD) experiments were performed at beamline ID31 (ESRF, Grenoble). A home-made three electrode cell was based on the thin film approach with continuous electrolyte used equipped with a leak-free Ag/AgCl reference electrode and a Pt mesh counter electrode. CO_2-saturated 0.1 M $KHCO_3$ was continuously flown through the spectroelectrochemical cell. An X-ray energy of 67 keV and the working distance of the Dectris Pilatus CdTe detector was calibrated using a CeO_2 reference material. The 2D diffraction pattern were integrated using the pyFAI software package and Rietveld refinement performed using TOPAS (Bruker-AXS, v6). The sample was deposited on highly-oriented pyrolytic graphite electrodes with a loading of $\sim$0.1 mg/cm^2. The diffraction pattern

were recorded in grazing-incidence configuration with the incidence angle optimized for best sample to substrate signal ratio. Rietveld refinements using the software package TOPAS® (Bruker-AXS) were performed for analysis considering the instrumental broadening of the lab diffractometer, zero error and a sample displacement.

Quasi *in situ* X-ray photoelectron spectroscopy

Quasi *in situ* X-ray Photoelectron Spectroscopy (XPS) measurements were performed in an Ultra high Vacuum (UHV) chamber, geared with a commercial Phoibos100 analyser (SPECS GmbH, E_{pass} = 15 eV) and a XR50 (SPECS GmbH) X-ray source with an Aluminum anode ($E_{K\alpha}$=1486.7 eV). The spectra were aligned using Cu^0 (932.67 eV) as reference and fitted using a Shirley-type or a linear background subtraction for X-ray or Auger electron spectroscopy, respectively. Quasi *in situ* XPS experiments were performed in a one compartment cell, which was directly attached to the UHV chamber. After CO_2RR, the catalyst was washed with Ar-sat. H_2O to remove residual electrolyte and transferred quickly into UHV under Ar atmosphere to avoid exposure to air and the possible subsequent reoxidation. The electrochemical measurements were carried out using a potentiostat (Autolab PGSTAT 302N, Metrohm).

Operando X-ray absorption fine-structure spectroscopy

Operando X-ray Absorption Fine Structure (XAFS) measurements were performed at beamlines located at the synchrotron facilities ALBA (CLAESS beamline), SSRL (BL 2-2 beamline) and SOLEIL (SAMBA beamline) as well as the X-ray Absorption Fine Structure (XAFS) beamline (SuperXAS) at SLS synchrotron facility of the Paul Scherrer Institute, respectively. All experiments were conducted in fluorescence mode at the Cu K-edge (8978.9 eV) and Au L_3-edge (11 918.7 eV) with corresponding fluorescence detectors (SI). The *operando* measurements were performed in a three-electrode electrochemical cell (see Ref. [260] for the schematics of the cell) matching the conditions of the selectivity studies. A leak-free Ag/AgCl was used as a reference electrode, while an Pt mesh was used as a counter electrode. The samples were prepared by drop casting 0.25 mg and 10 mg of catalyst on 0.5 cm^2 area of carbon paper with a microporous layer (GDE, Sigracet 39b). Cu K-edge and Au L_3-edge data were collected separately for identical fresh samples with different loadings to optimize the absorption edge signal while avoiding self-absorption. The carbon paper with the deposited catalyst served as a working electrode. It was mounted in the electrochemical cell and fixed with Kapton tape, so that the Kapton-covered carbon paper could act as an X-ray window, while the side coated with the catalyst was in contact with the electrolyte. The measurements for both samples were performed ex-situ as well as under *operando* conditions. Energy calibration, background

subtraction and normalization of the collected X-ray Absorption Near Edge Structure (XANES) spectra were performed with a set of home-built Mathematica scripts. The Athena software was used to extract the Extended X-ray Absorption Fine Structure (EXAFS).[181] The FEFFIT code was used for EXAFS fitting.[261]

For Au L_3-edge QXAFS species were tracked every 1 s and every 100 spectra was averaged to improve the signal quality for $Au_{2.7}Cu_2O$ NC, while for $Au_{0.4}Cu_2O$ NC and $Au_{0.8}Cu_2O$ NCspectra were collected every 12 min and every two spectra were merged.

Operando surface-enhanced Raman spectroscopy

For *operando* surface enhanced Raman Spectroscopy (SERS) measurements, a Raman spectrometer (Renishaw, InVia Reflex) equipped with an optical microscope (Leica Microsystems, DM2500M), a motorized stage for sample tracking (Renishaw, MS300 encoded stage), a near-infrared laser (Renishaw, RL785, $\lambda = 785$ nm, $P_{max} = 500$ mW), a CCD detector (Renishaw, Centrus) and a water immersion objective (Leica microsystems, 63x, numerical aperture of 0.9), was used. The water immersion objective was covered with a Teflon film (DuPont, 0.013 mm film thickness) to protect it from the electrolyte. A Si(100) wafer (520.5 cm^{-1}) was used for calibration. The Raman scattering of the Rayleigh-filtered backscattered light was collected in between 100 – 3200 cm^{-1} with a grating of 1200 lines mm^{-1}. Electrochemical measurements were performed following a previous report.[107] The electrochemical cell was equipped with a Pt counter electrode and a leak-free Ag/AgCl reference electrode; the catalyst was drop-casted on a glassy carbon plate, connected from the back side to the circuit. Measurements were performed with a Biologic SP240 potentiostat. CO_2-saturated 0.1 M $KHCO_3$ was used as electrolyte. Spectrum collection was performed with 10 s exposure time. Focus optimization was done by depth scans. Steady-state conditions at the catalyst surface was ensured by waiting at least 10 min before collecting the spectra. Renishaw WiRE 5.2 software was used to baseline-subtract the data with the intelligent spline feature (8th polynomial order) and to remove cosmic rays.

8.6.2 Supplementary Notes

Supplementary Note 1: Dissolution behavior studied by ICP-MS

The catalyst loading on the electrodes and in the electrolyte was studied with ICP-MS before and after CO_2RR. Figure S8.17 and Table S8.6 demonstrate a Cu loading between 48 and 56 µg in the as prepared state. After reaction, 3-5 µg Cu was dissolved from the electrode. Interestingly, the Au metal amount increases slightly by up to 0.2 µg after reaction, involving

a compositional change towards higher Au:Cu ratios. Furthermore, only traces of Au in the ng regime were found in the electrolyte after reaction. Cu, however, was detected with amounts in between 0.2 µgand 1 µg and culminates for the catalysts with intermediate loadings. In relation to the morphological findings from TEM and EDX data, we suggest that most of the dissolved Cu in the Cu_2O NC and $Au_{0.4}Cu_2O$ NC redeposits on the surface, while the Au wetting and skeleton like structure of Au around Cu on $Au_{0.8}Cu_2O$ NC and $Au_{1.1}Cu_2O$ NC hinders the Cu redeposition. Further, total alloy framing on $Au_{2.7}Cu_2O$ NC might lead to a hindrance of Cu dissolution. Thus, these results suggest a significant influence of alloyed structure on the stability and the cuprous dissolution and redeposition mechanism.

Supplementary Note 2: Electrochemical characterization

The catalysts were characterized electrochemically by cyclic voltammetry in CO_2 sat. $KHCO_3$ and Ar sat. NaOH (Figure S8.7) after reduction of the catalyst for 1 h. All catalysts show the characteristic peaks for $Cu^0 \rightarrow Cu^I$ and $Cu^0 \rightarrow Cu^{II}$ oxidation as well as the $Cu^{II} \rightarrow Cu^I$ and Cu^I to Cu^0 reduction, respectively. Note that the untypical broad reduction peak from $Cu^{II} \rightarrow Cu^I$ overlaps with the thick oxide layer that was produced at high oxidizing potentials. The upper limit was chosen to eventually oxidize Au, which we did not observed in our CVs. In CO_2 sat. $KHCO_3$, no difference in its redox behavior was found compared to Cu foil, which is in contradiction to literature.[230,233] We assign this to the low amount of alloyed catalysts and to the unordered type of alloy formation.

In Ar sat. NaOH, OH adsorption is observed at 0.63 V vs. RHE for the catalysts and is lacking in the CV for the electropolished Cu foil. Furthermore, the shape of the oxidation peaks shows much broader shapes than the electropolished Cu foil.

Double layer capacitance was measured for the catalysts after 1 h of CO_2RR and compared to the Cu foil to retrieve a roughness factor, Table S8.3. The catalysts with Au NPs show higher capacitances and roughness factors than the Cu_2O NCs, which suggests a higher surface are due to the presence of Au. However, metallic Au species and CuAu alloys also contribute to the capacitance, which impedes a clear assignment.

Supplementary Note 3: Electrocatalytic stability tests

To gain insight over the stability of the catalysts, we performed long-term measurements over 20 h at −1.03 V and tracked the changes of the FEs, Figure S8.10. The initial product distribution resembles the previously shown data that were determined after 1 h of CO_2RR. In all cases, after the initial activation and stabilization, the product distribution remains

stable over the course of 20 h. Nevertheless, a slight decrease in CO formation is observed for $Au_{0.4}Cu_2O$ NC and $Au_{0.8}Cu_2O$ NC ,while CO production remains stable for $Au_{1.1}Cu_2O$ NC and increases for $Au_{2.7}Cu_2O$ NC , Figure S8.10c, suggesting a sluggish catalyst restructuring for low Au loadings. The total liquid products, analyzed after 20 h of CO_2RR, displays a decrease of the total amount of liquids. It is suggested to be observed due to the high volarity of the oxygenates and alcohols during the whole measurement time.

Supplementary Note 4: Cu-K edge analysis

Figure S8.23 shows the Cu K edge X-ray Absorption Near Edge Structure (XANES) for the samples in the as-prepared state and during CO_2RR in steady state at 4 h CO_2RR at −1.0 V. The XANES spectra for as prepared catalysts demonstrate the presence of oxidized Cu species, mostly in the Cu^{I} state, as suggested by the characteristic pre-edge feature. Nonetheless significant amounts of Cu are oxidized to Cu^{II}. After 4 h of CO_2RR, all catalysts are mostly reduced to Cu^0. These results are in agreement with the previously discussed XPS data.

The evolution of local atomic structure around Cu under CO_2RR was tracked by studying the Extended X-ray Absorption Fine Structure (EXAFS) spectra of the Cu K-edge, Figure S8.26 and Table S8.12. In the as prepared state, Cu K-edge FT-EXAFS exhibit prominent peaks at 1.85 Å and 2.8 Å (phase-uncorrected) corresponding to Cu-O and Cu-Cu bonds in bulk Cu_2O-like structure. EXAFS data fitting revealed that the coordination number of the Cu-O bonds are 3-3.6, which is higher than the one for Cu_2O (2), indicating significant amounts of CuO in our catalysts. Under CO_2RR, the FT-EXAFS features corresponding to Cu oxide decrease while a new peak corresponding to the Cu-Cu bonds in metallic Cu appears at 2.5 Å. EXAFS data fitting suggest that the corresponding Cu-Cu coordination number after reaching the equilibrium state after 4 h is close to 12, which fits well to the Cu reference.[247] Note here that no significant contribution of Cu-Au bonds to Cu K-edge EXAFS data are observed due to the low Au-to-Cu ratio of the catalysts.

8.6.3 Supplementary Figures

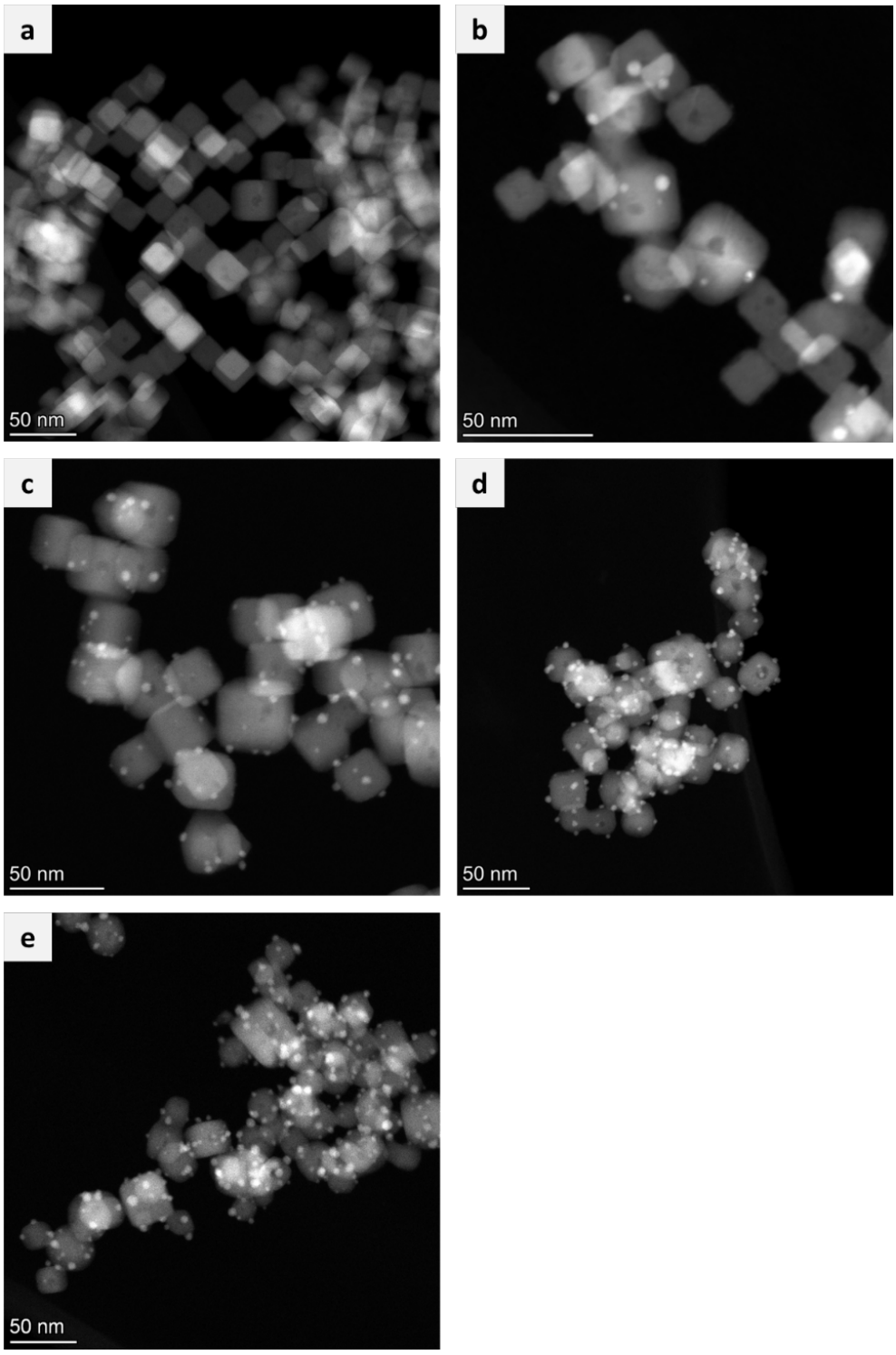

Supplementary Figure 8.6: Overview STEM-HAADF micrographs of the catalysts in the as prepared state for a) Cu_2O NC ,$Au_{0.4}Cu_2O$ NC ,c) $Au_{0.8}Cu_2O$ NC, d) $Au_{1.1}Cu_2O$ NC and e) $Au_{2.7}Cu_2O$ NC.

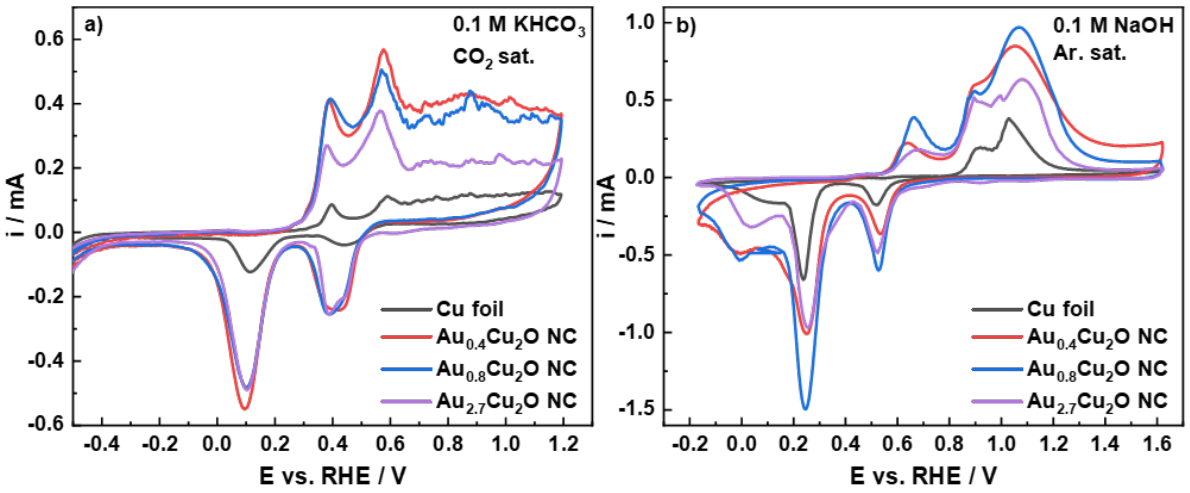

Supplementary Figure 8.7: Cyclic Voltammetrys (CVs) of the catalysts and Cu foil in CO_2 sat. 0.1 M $KHCO_3$ and in Ar sat. 0.1 M NaOH, scan rate: 20 mV/s.

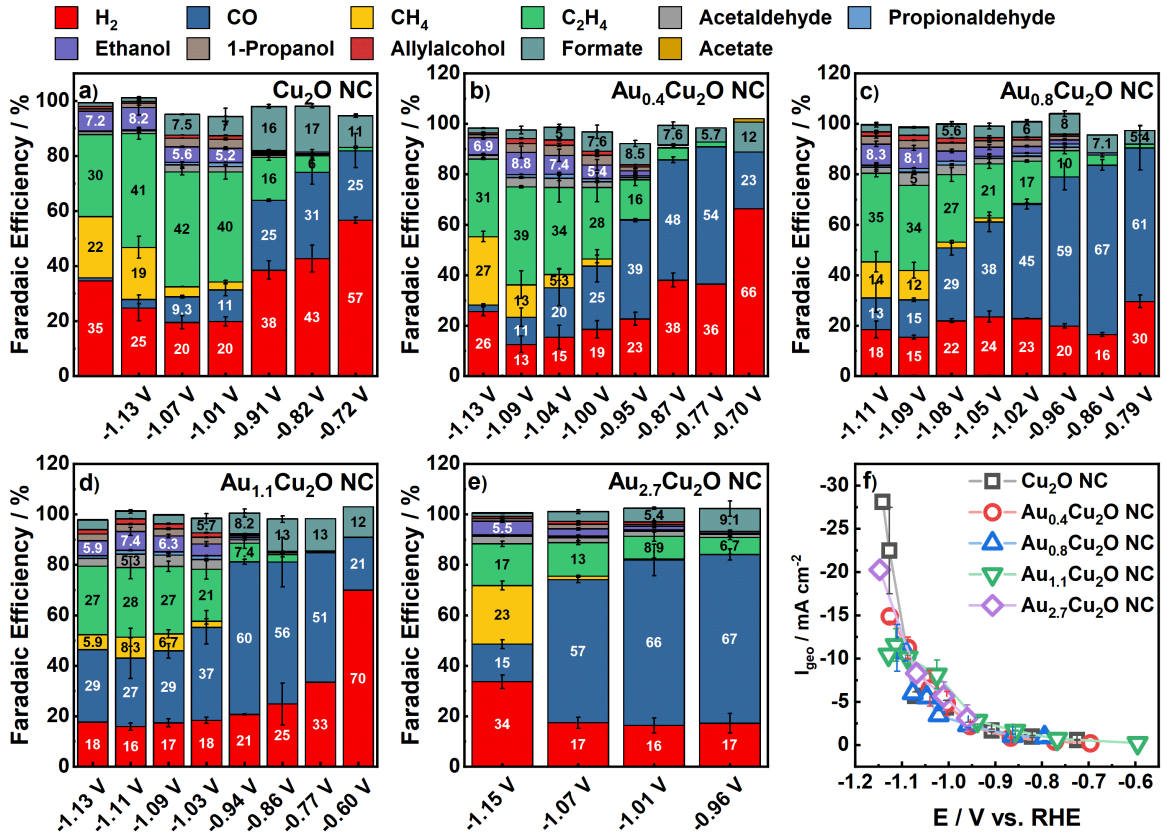

Supplementary Figure 8.8: Potential-dependent Faradaic Efficiencys (FEs) for a) Cu_2O NC ,b) $Au_{0.4}Cu_2O$ NC ,c) $Au_{0.8}Cu_2O$ NC ,d) $Au_{1.1}Cu_2O$ NC ,e) $Au_{2.7}Cu_2O$-NC with Nafion. f) Potential-dependent geometric current densities for all catalysts.

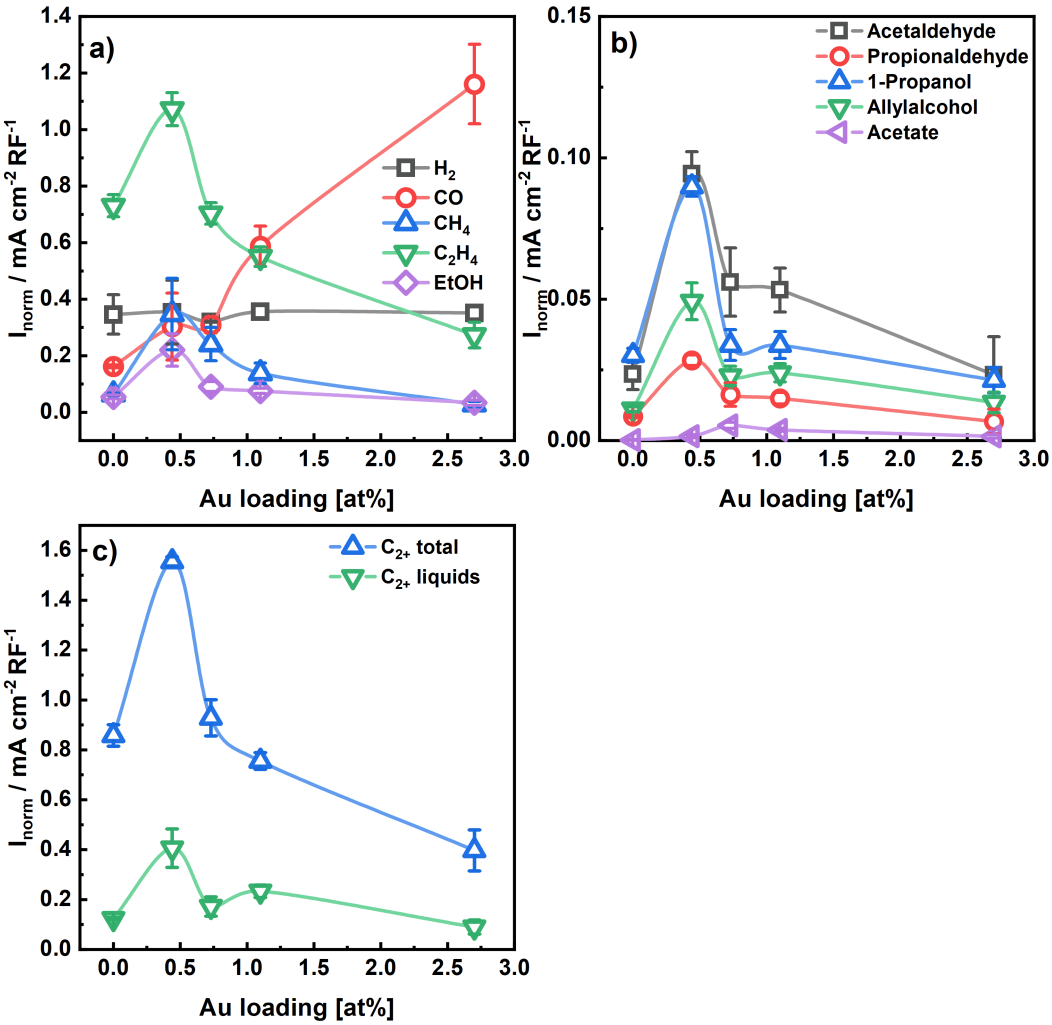

Supplementary Figure 8.9: Partial current densities, normalized by geometric area and roughness factor (RF) at −1.07 V vs. RHE in 0.1 M $KHCO_3$ as a function of Au NP loading for a) H_2, CO, CH_4, C_2H_4, b) liquids, C_{2+}, C_{2+} liquids, C_{2+} carbonyl and c) minor liquid productions.

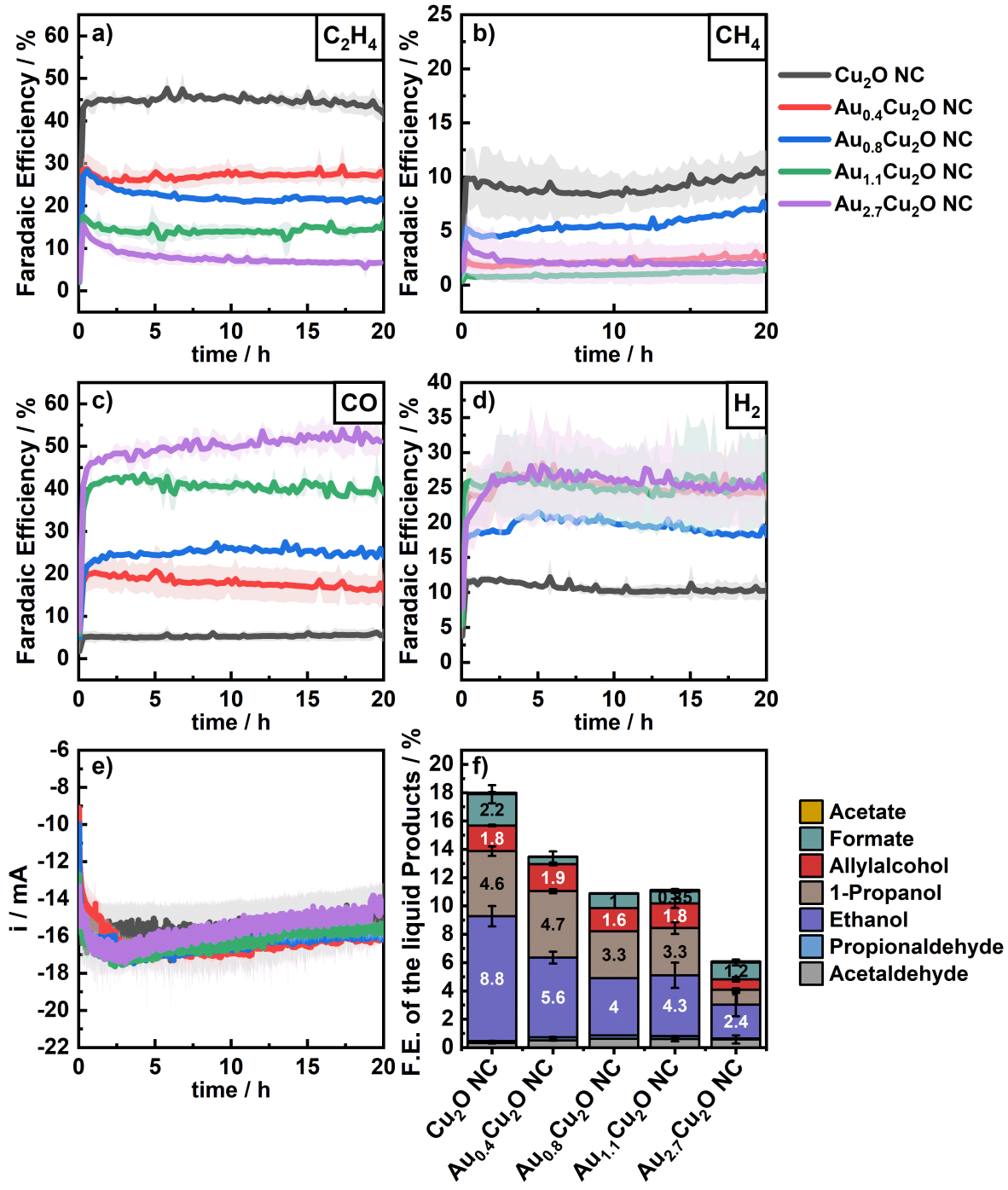

Supplementary Figure 8.10: Stability measurements over 20 h at −1.03 V. FEs of a) C_2H_4, b) CH_4, c) CO and d) H_2; e) current transients and f) liquid products of the catalysts.

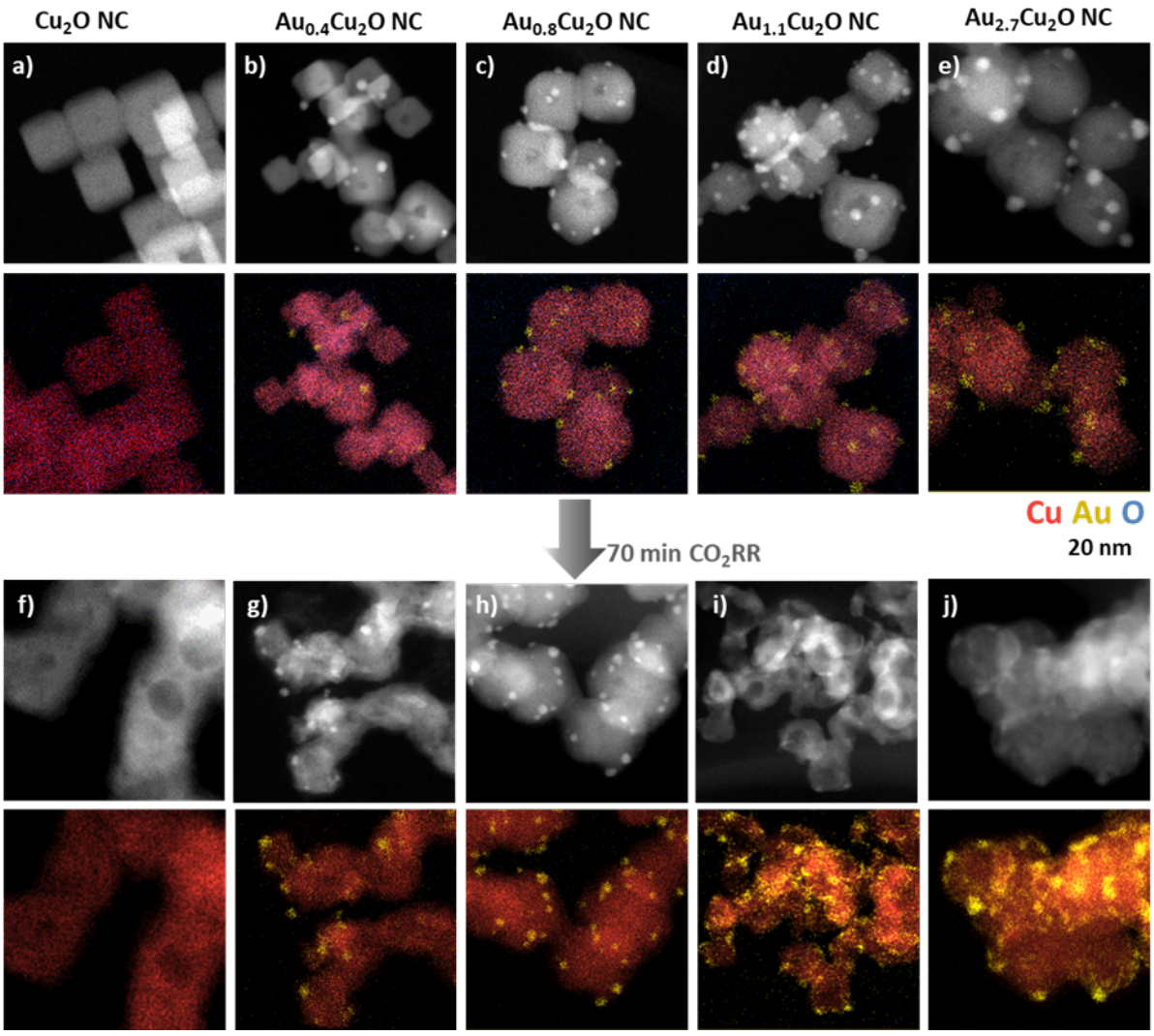

Supplementary Figure 8.11: STEM-HAADF images with corresponding EDX mappings of a) Cu_2O NC ,b) $Au_{0.4}Cu_2O$ NC ,c) $Au_{0.8}Cu_2O$ NC ,d) $Au_{1.1}Cu_2O$ NC and e) $Au_{2.7}Cu_2O$ NC in the as prepared state and the same catalysts after 70 min at −1.0 V vs. RHE (f-j).

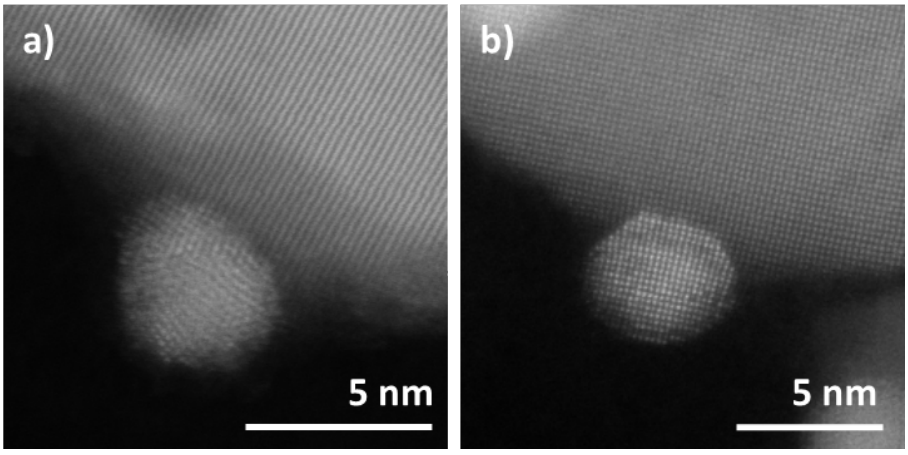

Supplementary Figure 8.13: High resolution TEM micrographs of single grain and multigrain Au NPs of $Au_{2.7}Cu_2O$ NC.

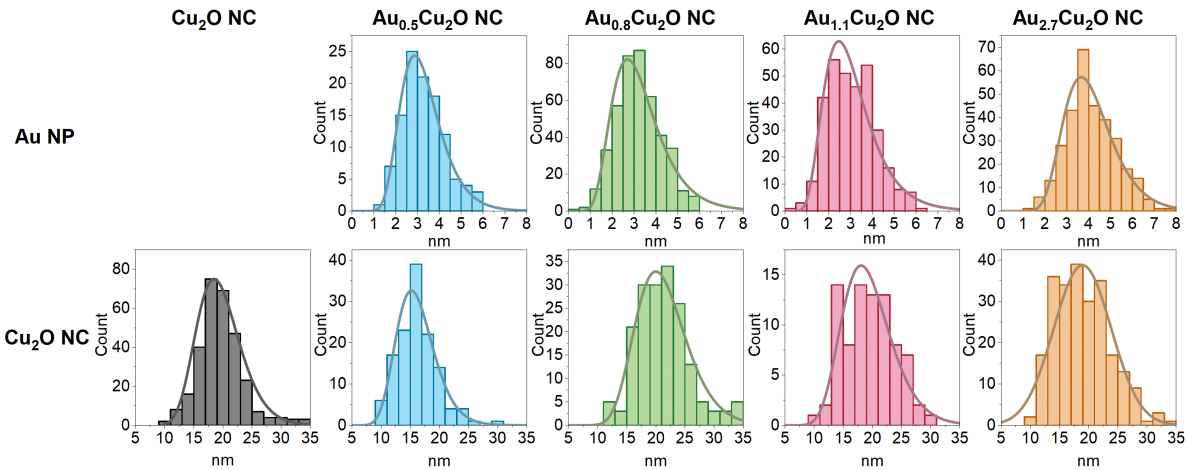

Supplementary Figure 8.12: Histograms showing the size distribution of the Cu NC edge lengths and of the Au NP diameters for the catalysts in the as prepared state. The size distributions are shown in Table S8.4.

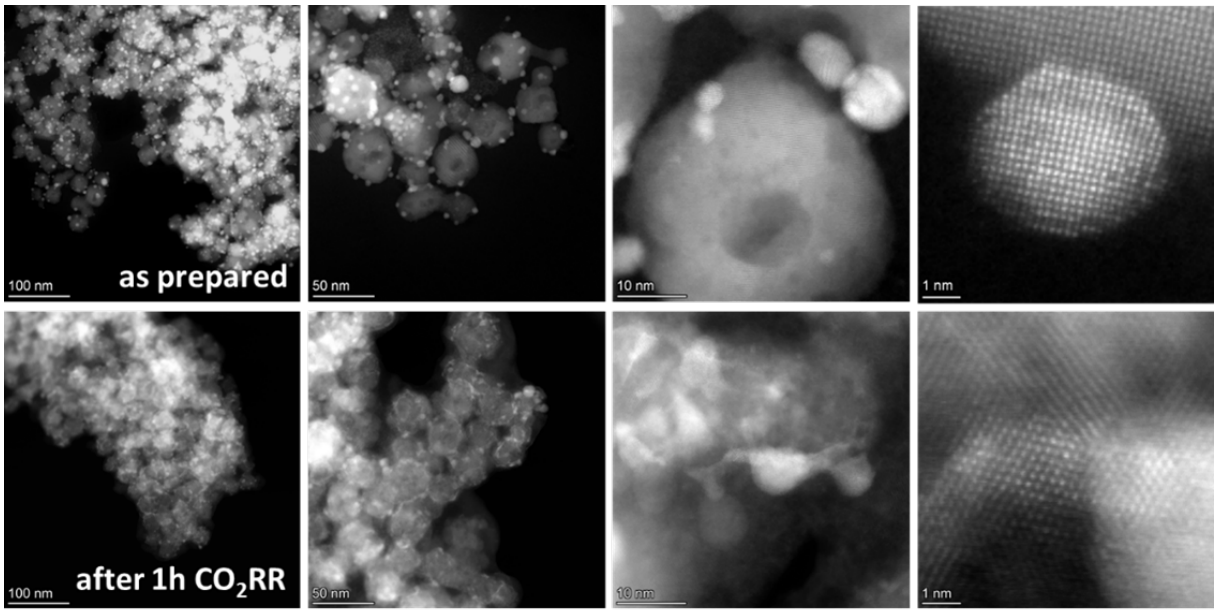

Supplementary Figure 8.14: HAADF micrographs and high resolution TEM images of $Au_{2.7}Cu_2O$ NC a) in the as prepared state and b) after 1 h CO_2RR at −1.0 V vs. RHE.

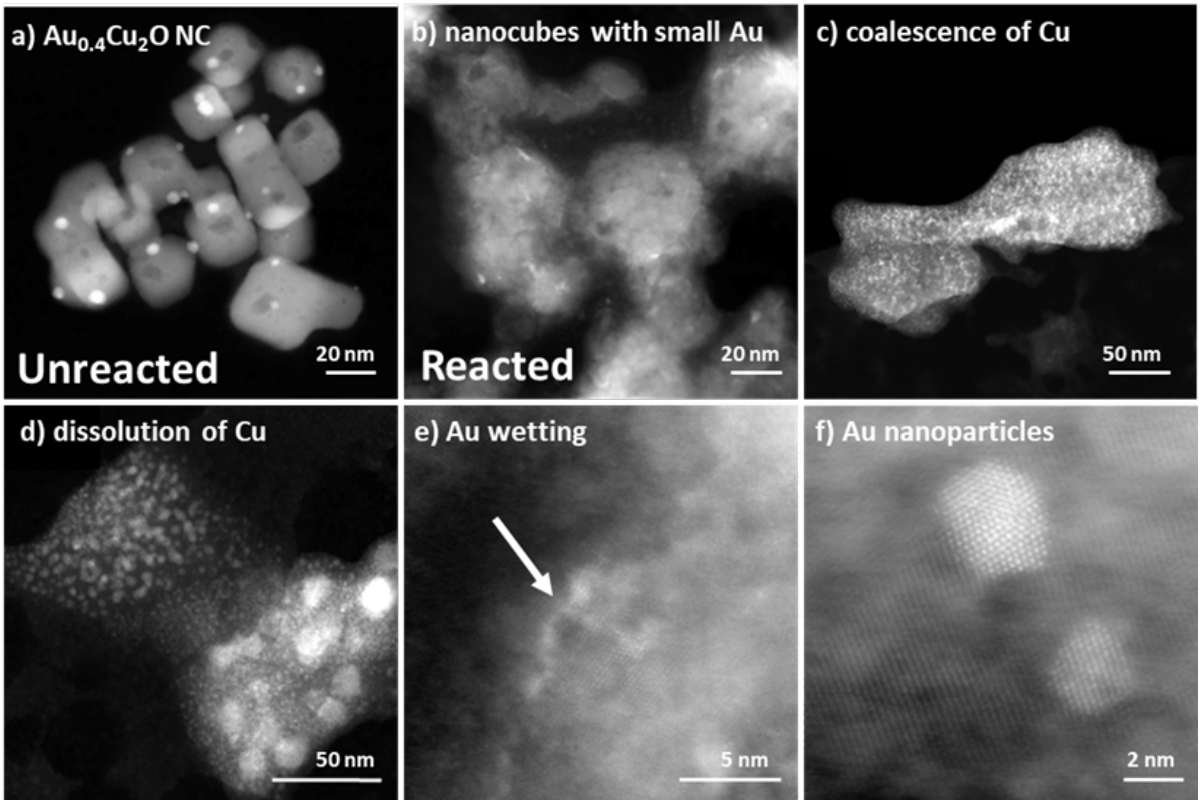

Supplementary Figure 8.15: HAADF micrographs and high resolution TEM images of $Au_{0.4}Cu_2O$ NC a) unreacted and b) reacted, c) for coalescence and d) dissolved Cu paralleled with e) Au wetting and f) unreacted stable Au nanoparticles.

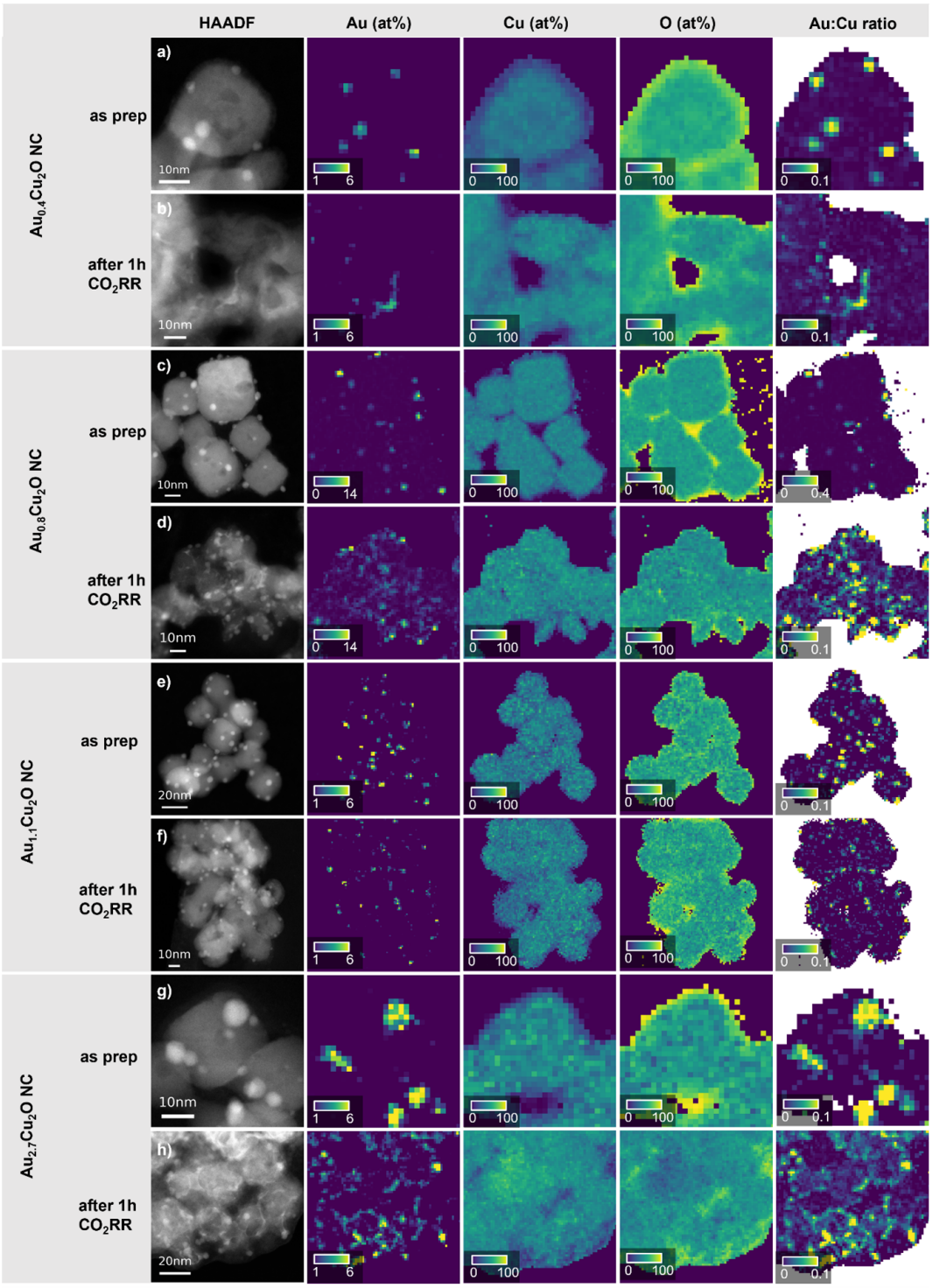

Supplementary Figure 8.16: HAADF micrographs and their corresponding binned EDX maps for Au, Cu and O as well as the Au/Cu ratio for all catalysts in the as prepared state and after CO_2RR conditions.

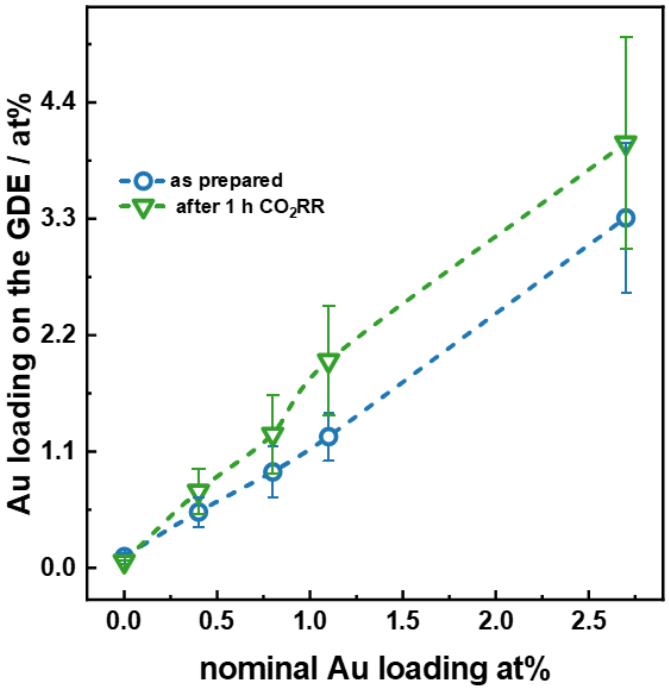

Supplementary Figure 8.17: ICP-MS study of the metal amounts of Cu an Au on the carbon paper support in the as prepared state and after 70 min of CO_2RR.

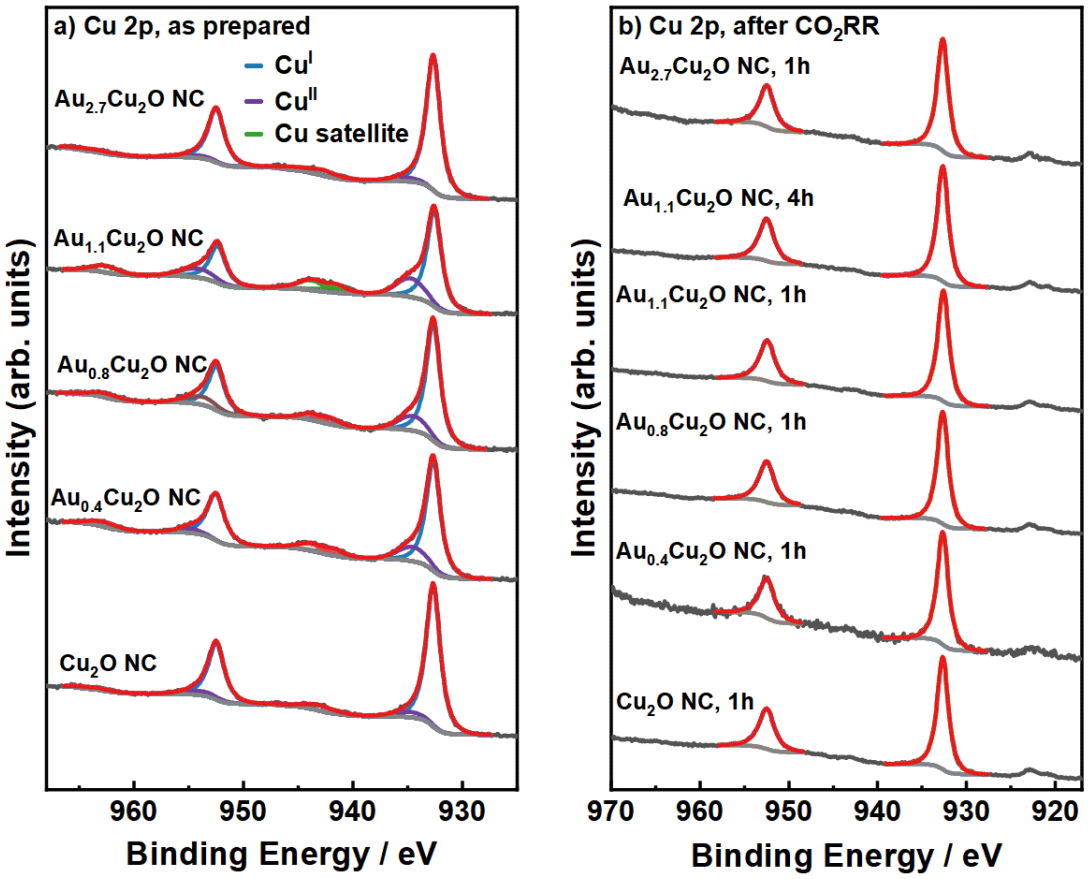

Supplementary Figure 8.19: Quasi *in situ* XPS Cu 2p core level regions of all catalysts a) as prepared state and b) after CO_2RR in 0.1 M $KHCO_3$.

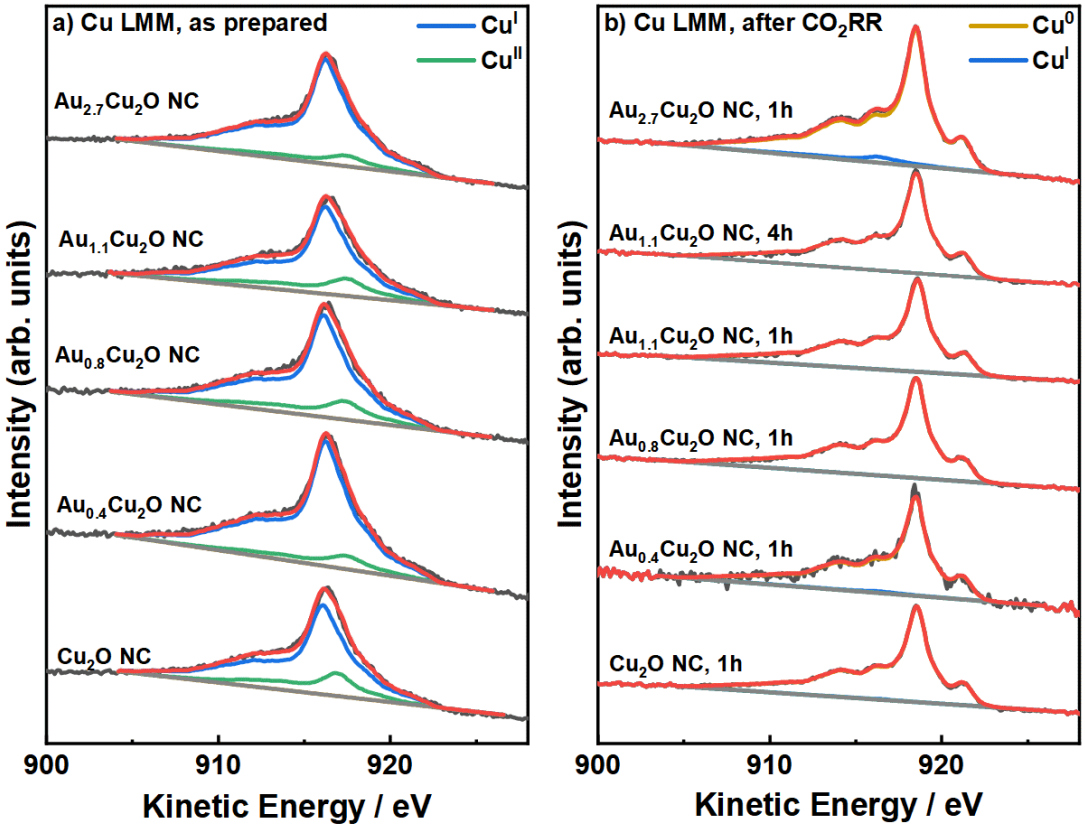

Supplementary Figure 8.18: Quasi *in situ* Cu LMM Auger spectra of all catalysts Cu LMM Auger spectra a) as prepared state and b) after CO_2RR in 0.1 M $KHCO_3$.

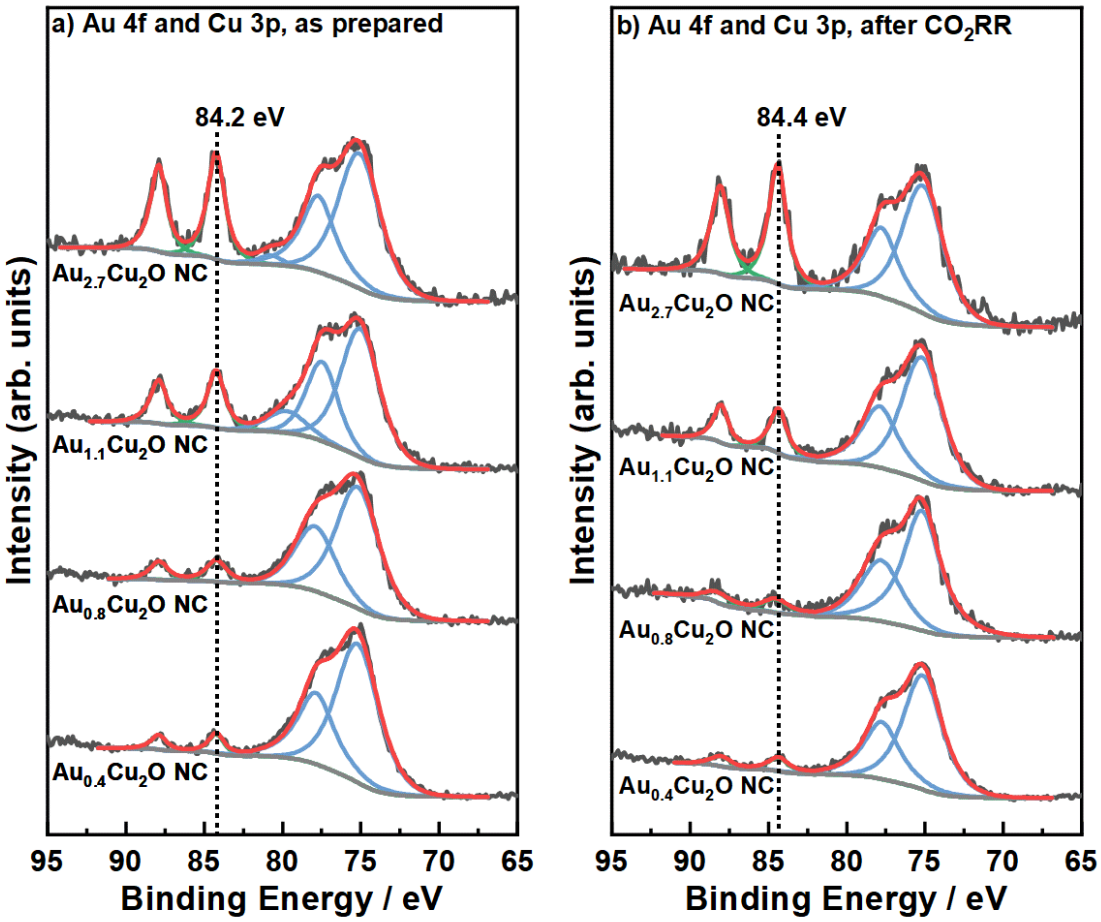

Supplementary Figure 8.20: Quasi *in situ* XPS Au 4f and Cu 3p level regions of all Au-containing catalysts a) in the as prepared state and b) after CO_2RR in 0.1 M $KHCO_3$.

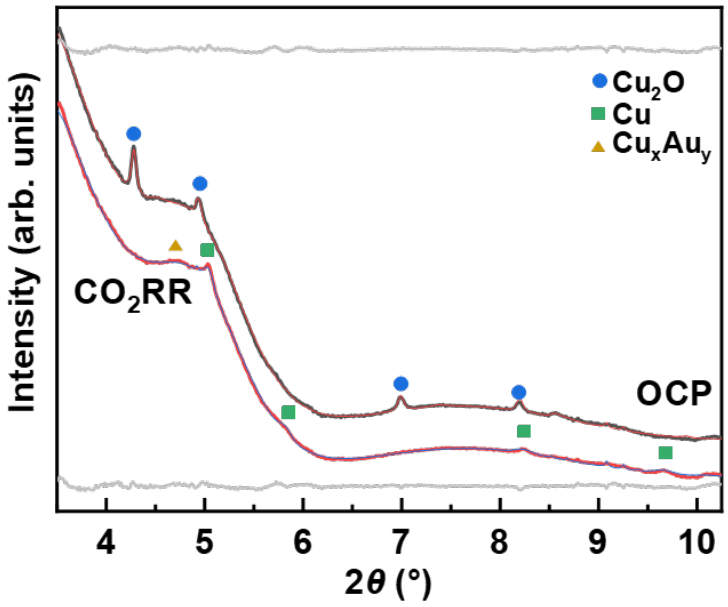

Supplementary Figure 8.21: Rietveld Refinement of XRD pattern at OCP (black) and during CO_2RR (Red) as well as the fitted profiles (thin red and blue, respectively) of the $Au_{2.7}Cu_2O$ NC. The difference between experimental data and the fitted profile are shown in grey below and above the pattern recorded at OCP and during CO_2RR, respectively. The X-ray energy was set to 67 keV.

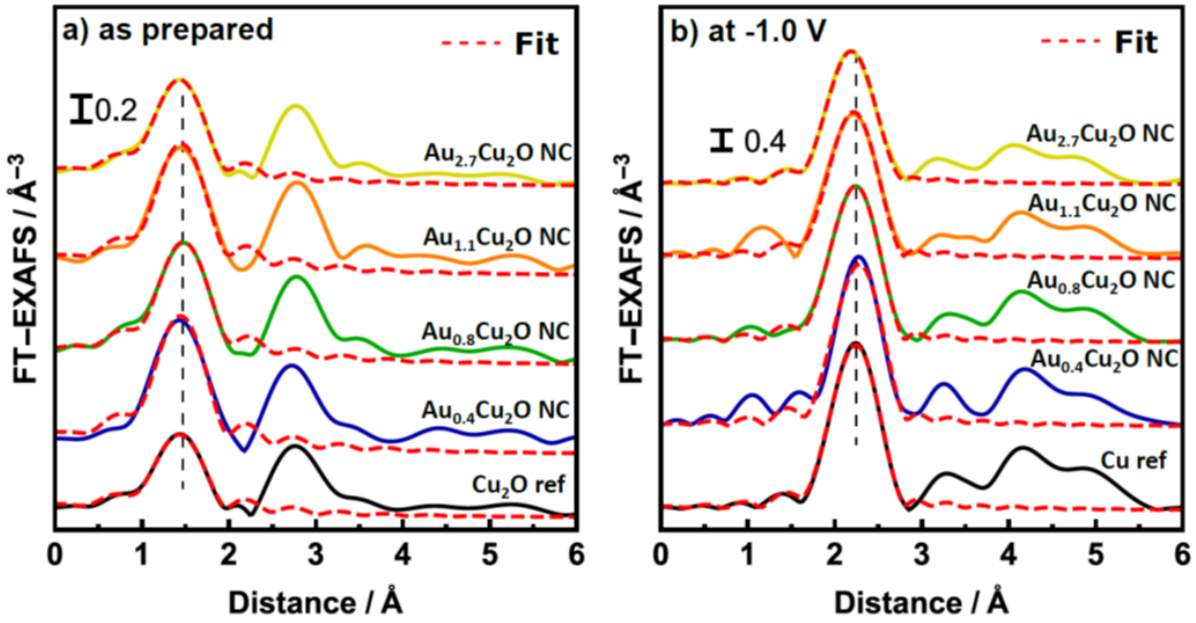

Supplementary Figure 8.24: FT EXAFS spectra of the Cu K-edge of all catalysts a) in the as prepared state and b) during CO_2RR at −1.0 V vs. RHE. Spectra are shifted vertically for clarity. Results of EXAFS data fitting are also shown.

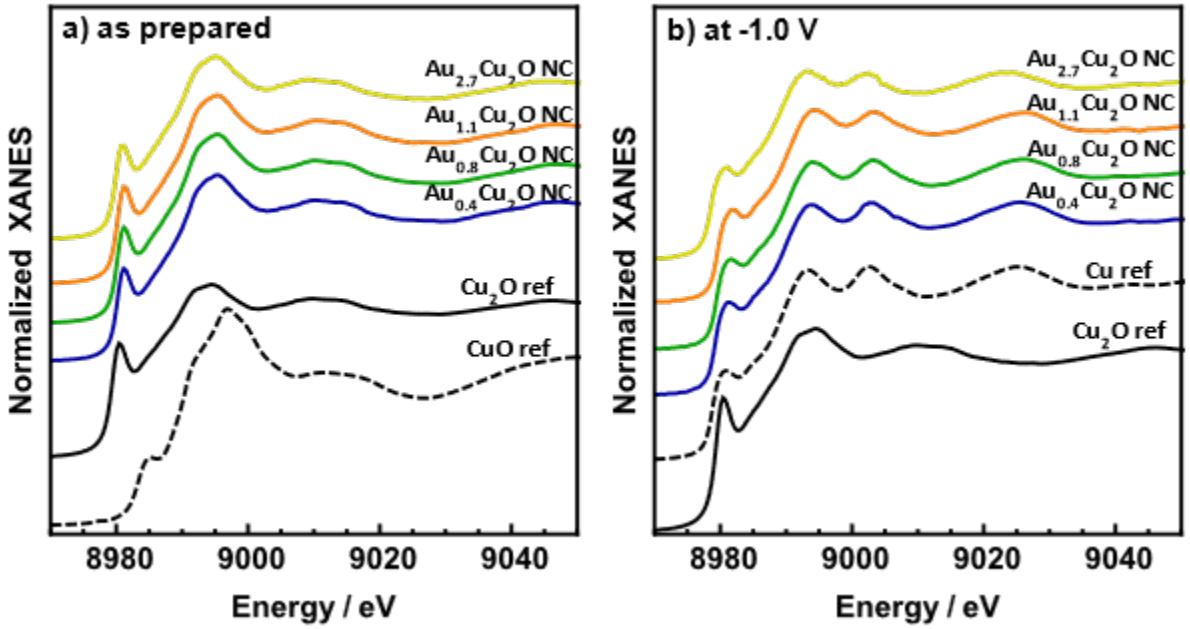

Supplementary Figure 8.22: Cu K-edge XANES spectra of all catalysts a) in the as prepared state and b) during CO_2RR at −1.0 V vs. RHE. Reference spectra for Cu foil, Cu_2O and CuO are also shown for comparison. Spectra are shifted vertically for clarity.

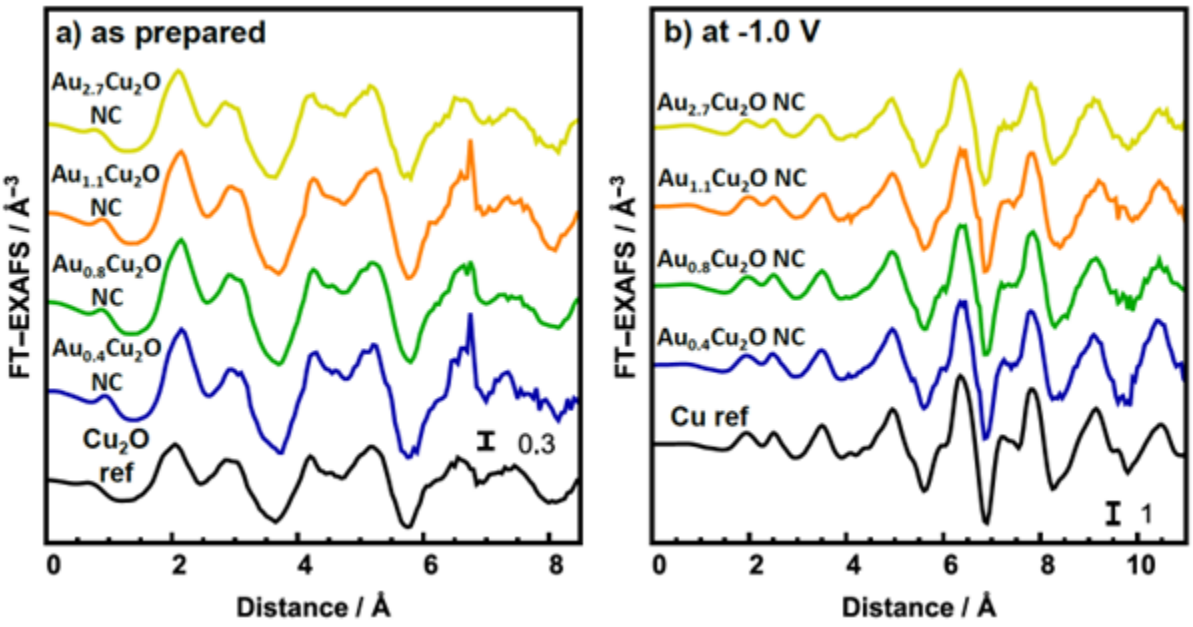

Supplementary Figure 8.25: Fourier-filtered Cu K-edge EXAFS spectra in k-space of the Au_xCu_2O NC in a) the as-prepared state and b) at −1.0 V. Reference spectra of Cu_2O and Cu are shown for comparison.

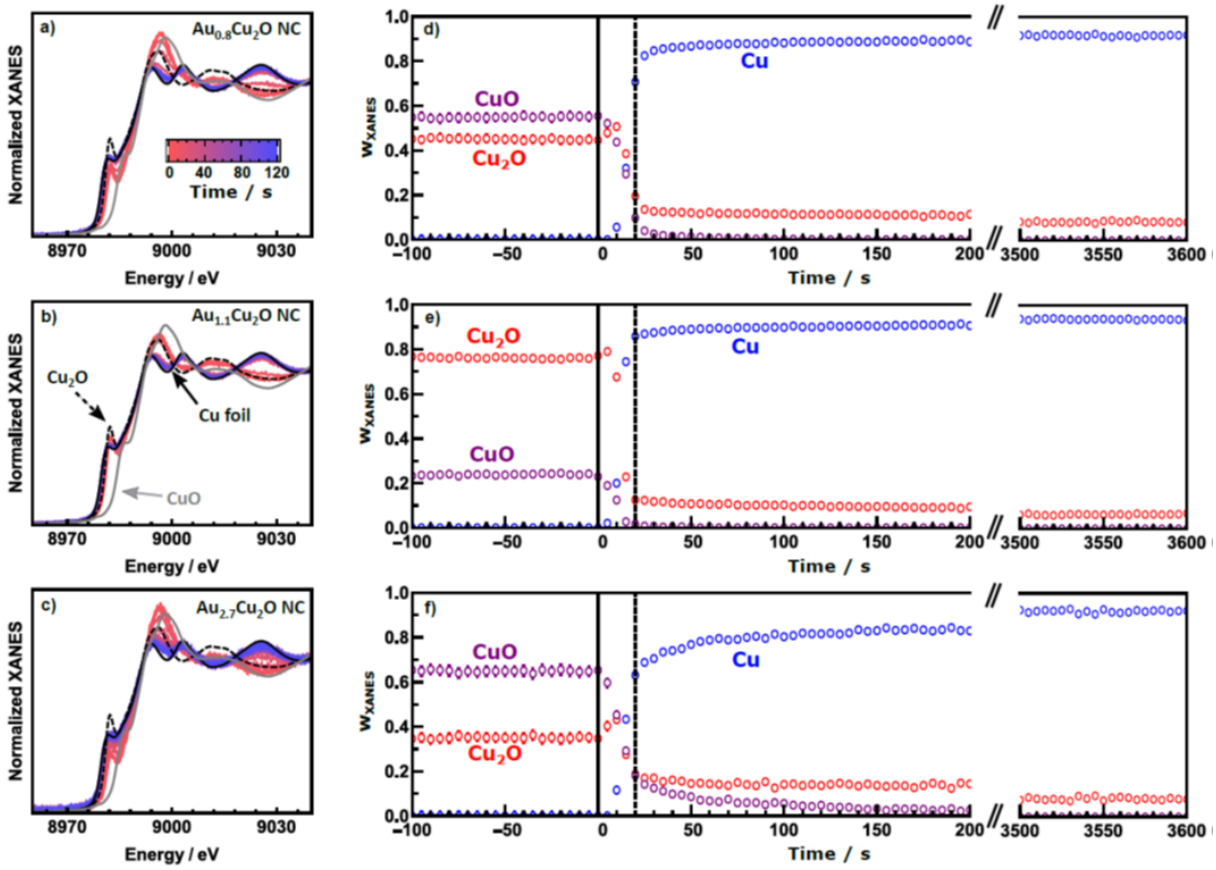

Supplementary Figure 8.23: Time dependent Cu K-edge XANES spectra of a) $Au_{0.4}Cu_2O$ NC ,b) $Au_{1.1}Cu_2O$ NC and c) $Au_{2.7}Cu_2O$ NC during CO_2RR at −1.0 V vs. RHE and their corresponding time-resolved results of linear combination fitting of the XANES spectra, using spectra for Cu foil, Cu_2O and CuO as references.

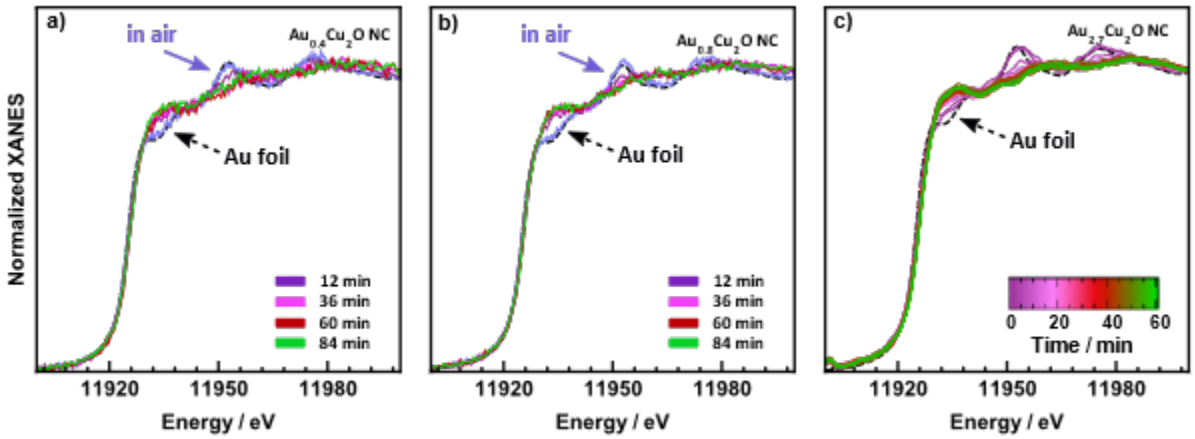

Supplementary Figure 8.26: Time dependent Au L_3-edge XANES spectra of a) $Au_{0.4}Cu_2O$ NC ,b) $Au_{0.8}Cu_2O$ NC and c) $Au_{2.7}Cu_2O$ NC during CO_2RR at −1.0 V vs. RHE.

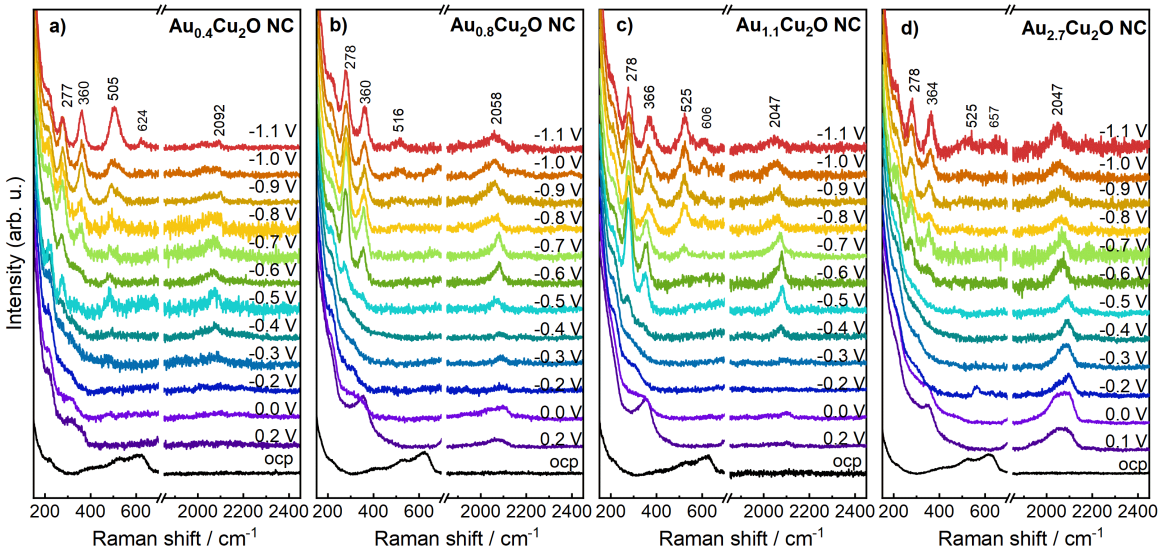

Supplementary Figure 8.27: *Operando* surface-enhanced Raman spectra of a) Cu_2O NC, b) $Au_{0.4}Cu_2O$ NC, c) $Au_{0.8}Cu_2O$ NC, d) $Au_{1.1}Cu_2O$ NC and e) $Au_{2.7}Cu_2O$ NC in CO_2 sat. 0.1 M $KHCO_3$ with stepped potentials from open circuit potential to −1.1 V vs. RHE.

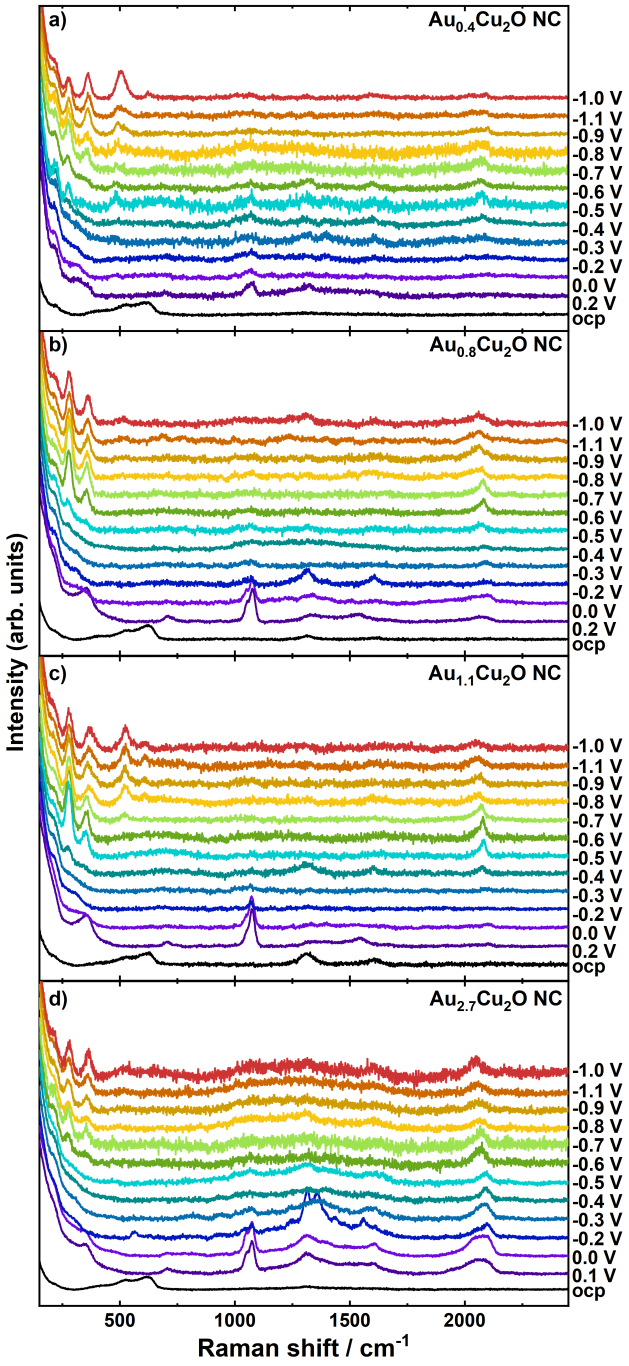

Supplementary Figure 8.28: Full Raman spectra of a) $Au_{0.4}Cu_2O$ NC, b) $Au_{0.8}Cu_2O$ NC, c) $Au_{1.1}Cu_2O$ NC ,d) $Au_{2.7}Cu_2O$ NC at increasing applied potentials vs. RHE in CO_2-sat. 0.1 M $KHCO_3$. The region between 1000 cm^{-1} and 1700 cm^{-1} holds vibration peaks of HCO^{3-} (1005 cm^{-1}) and CO_3^{2-} (1072 cm^{-1}), and from the glassy carbon support (1313 cm^{-1} and 1600 cm^{-1}).

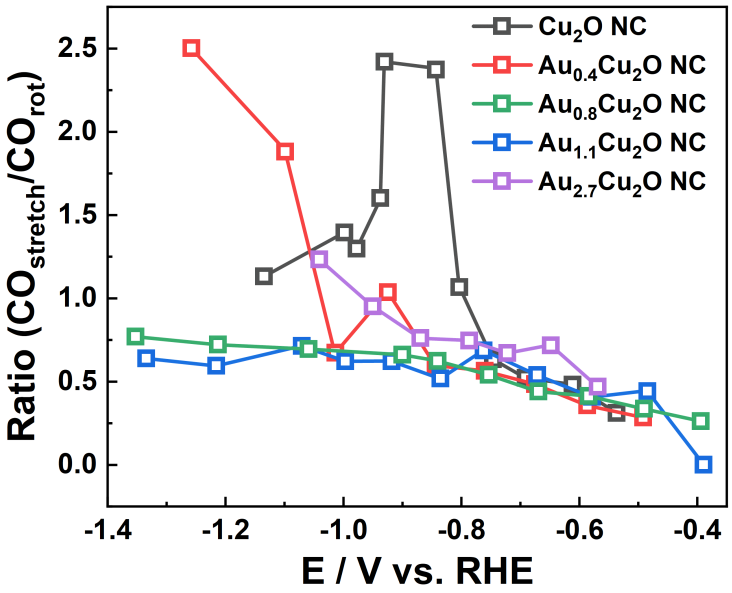

Supplementary Figure 8.29: $CO_{stretch}/CO_{rot}$ ratios of the respective bands (277 cm^{-1} and 360 cm^{-1}) as a function of applied potential (iR corrected). The results for Cu_2O were calculated from Ref [233].

8.6.4 Supplementary Tables

Supplementary Table 8.1: Composition of Cu and Au of the presented catalyst dispersions, determined by ICP-MS.

Catalyst	Cu [at%]	Au [at%]
Cu_2O NC	100.00 ± 0.01	0.00 ± 0.01
$Au_{0.4}Cu_2O$ NC	99.57 ± 0.00	0.43 ± 0.00
$Au_{0.8}Cu_2O$ NC	99.23 ± 0.01	0.77 ± 0.01
$Au_{1.1}Cu_2O$ NC	98.92 ± 0.02	1.08 ± 0.02
$Au_{2.7}Cu_2O$ NC	97.31 ± 0.04	2.69 ± 0.04

Supplementary Table 8.2: Coherence lengths, lattice parameters and atomic fractions of Cu_2O and Au extracted from Rietveld refinement of the ex situ XRD pattern of all catalysts in the as prepared state.

Catalyst	Structural coherence lengths / nm		Lattice parameters / A		Weight Fraction Weight Fraction	
	Cu_2O	Au	Cu_2O	Au	Cu_2O	Au
Cu_2O NC	120(9)		4.2668(3)		100%	
$Au_{0.4}Cu_2O$ NC	21.3(8)	1.8(2)	4.2670(5)	4.059(4)	93.5(4)%	6.5(4)%
$Au_{0.8}Cu_2O$ NC	35.0(10)	1.78(11)	4.2669(3)	4.059(4)	92.4(2)%	7.6(2)%
$Au_{1.1}Cu_2O$ NC	26.3(16)	1.8(2)	4.2668(7)	4.059(4)	90.5(5)%	9.5(5)%
$Au_{2.7}Cu_2O$ NC	42(4)	1.40(10)	4.2680(7)	4.059(4)	84.7(5)%	15.3(5)%

Supplementary Table 8.3: Double Layer Capacitances (DLCs) and corresponding roughness factors (normalized to Cu foil) of the catalysts with Nafion and of the reference Cu and Au foils measured after 1 h CO_2RR at −1.0 V vs. RHE.

Sample	Capacitance / μFcm^{-2}	Roughness factor (RF)
Cu Foil	29.3	1
Cu_2O NC	101.3	3.45
$Au_{0.4}Cu_2O$ NC	181.66	6.2
$Au_{0.8}Cu_2O$ NC	161.0 ± 3.3	5.5
$Au_{1.1}Cu_2O$ NC	150.3	5.1
$Au_{2.7}Cu_2O$ NC	122.7 ± 6.65	4.2

Supplementary Table 8.4: Edge lengths of the Cu NCs and diameters of the Au NP in the as prepared state and after 70 min CO_2RR obtained from STEM-HAADF micrographs.

Edge Length & particle sizes	as prepared		after 70 min CO_2RR	
	Cu [at%]	Au [at%]	Cu [at%]	Au [at%]
Cu_2O NC	21.8 ± 7.1	–	30.5 ± 4.4	–
$Au_{0.4}Cu_2O$ NC	16.2 ± 3.4	4.1 ± 1.2	21.4 ± 5.4	3.8 ± 1.5
$Au_{0.8}Cu_2O$ NC	21.4 ± 4.6	3.6 ± 1.0	25.4 ± 3.8	3.4 ± 1.8
$Au_{1.1}Cu_2O$ NC	19.5 ± 4.3	3.4 ± 1.0	19.6 ± 4.2	3.8 ± 1.4
$Au_{2.7}Cu_2O$ NC	18.9 ± 4.9	4.1 ± 1.4	20.2 ± 5.5	3.6 ± 1.6

Supplementary Table 8.5: EDX compositions comparing the Cu and Au ratios of the catalysts in the as prepared state and after 70 min CO_2RR. Evaluation based on L lines of the elements.

EDX Cu-Au composition	**as prepared**		**after 70 min CO2RR**	
	Cu [at%]	**Au [at%]**	**Cu [at%]**	**Au [at%]**
Cu_2O NC	100.00	0.00	100.00	0.00
$Au_{0.4}Cu_2O$ NC	99.82 ± 0.02	0.18 ± 0.02	99.55±0.14	0.45 ± 0.14
$Au_{0.8}Cu_2O$ NC	99.59 ± 0.09	0.41 ± 0.09	99.45 ± 0.11	0.55 ± 0.11
$Au_{1.1}Cu_2O$ NC	99.41 ± 0.06	0.59 ± 0.06	99.43 ± 0.06	0.57 ± 0.11
$Au_{2.7}Cu_2O$ NC	98.80 ± 0.40	1.20 ± 0.40	98.65 ± 0.51	1.35 ± 0.51

Supplementary Table 8.6: Composition and mass of Cu and Au on the catalysts on 2 cm^2 carbon paper electrode in the as-prepared state and after 1 h of CO_2RR at −1.0 V, and of the electrolyte after reaction. Results were determined by ICP-MS.

Sample	Au mass			Cu mass		
	GDE as prep. [ug]	GDE CO_2RR [ug]	Electrolyte CO_2RR [ug]	GDE as prep. [ug]	GDE CO_2RR [ug]	Electrolyte CO_2RR [ug]
Cu_2O NC	0.05 ± 0.10	0.03 ± 0.01	0.01 ± 0.46	47.33 ± 0.37	43.50 ± 0.89	0.28 ± 0.00
$Au_{0.4}Cu_2O$ NC	0.24 ± 0.01	0.30 ± 0.02	0.56 ± 0.22	45.82 ± 0.21	40.67 ± 0.21	0.55 ± 0.01
$Au_{0.8}Cu_2O$ NC	0.43 ± 0.03	0.54 ± 0.03	0.63 ± 0.06	47.14 ± 0.04	41.96 ± 0.43	0.91 ± 0.03
$Au_{1.1}Cu_2O$ NC	0.80 ± 0.04	0.97 ± 0.06	2.27 ± 0.71	53.99 ± 0.49	48.54 ± 0.68	0.90 ± 0.04
$Au_{2.7}Cu_2O$ NC	2.01 ± 0.09	2.19 ± 0.14	1.13 ± 0.30	58.62 ± 0.1	52.37 ± 0.24	0.43 ± 0.01

Sample	Au loading in at%			Au loading in at%		
	GDE as prep.	GDE CO_2RR	Electrolyte CO_2RR	GDE as prep.	GDE CO_2RR	Electrolyte CO_2RR
Cu_2O NC	0.11 ± 0.03	0.06 ± 0.02	0.36 ± 0.18	99.89 ± 0.18	99.94 ± 0.44	99.64 ± 0.00
$Au_{0.4}Cu_2O$ NC	0.53 ± 0.14	0.72 ± 0.22	0.10 ± 0.05	99.47 ± 0.10	99.28 ± 0.09	99.90 ± 0.00
$Au_{0.8}Cu_2O$ NC	0.91 ± 0.24	1.26 ± 0.37	0.07 ± 0.03	99.09 ± 0.19	98.74 ± 0.20	99.93 ± 0.02
$Au_{1.1}Cu_2O$ NC	1.24 ± 0.23	1.96 ± 0.51	0.25 ± 0.13	98.76 ± 0.22	98.04 ± 0.31	99.75 ± 0.02
$Au_{2.7}Cu_2O$ NC	3.31 ± 0.71	4.02 ± 1.00	0.26 ± 0.13	96.69 ± 0.00	95.98 ± 0.05	99.74 ± 0.00

Supplementary Table 8.7: XPS composition between Cu, Cu_2O and CuO obtained by linear combination fitting of the Cu LMM spectra in the as prepared state and after 1 h CO_2RR.

XPS composition	as prepared		after 70 min CO_2RR	
	Cu_2O [%]	CuO [%]	Cu [%]	Cu_2O [%]
Cu_2O-NC	80	20	99.5	0.5
$Au_{0.4}Cu_2O$ NC	89	11	98	2
$Au_{0.8}Cu_2O$ NC	83	17	100	0
$Au_{1.1}Cu_2O$ NC	82	18	100	0
$Au_{2.7}Cu_2O$ NC	89	11	96	4

Supplementary Table 8.8: XPS composition of Cu (all chemical states) and Au in the as prepared state and after 1 h CO_2RR.

XPS composition	as prepared		after 70 min CO_2RR	
	Cu [%]	Au [%]	Cu [%]	Au [%]
Cu_2O NC	100	–	100	–
$Au_{0.4}Cu_2O$ NC	99.07	0.93	98.25	1.75
$Au_{0.8}Cu_2O$ NC	97.65	2.35	97.34	2.66
$Au_{1.1}Cu_2O$ NC	97.27	2.73	97.12	3.88
$Au_{2.7}Cu_2O$ NC	93.71	6.29	91.46	8.54

Supplementary Table 8.9: Coherence lengths, lattice parameters and atomic fractions of Cu_2O and Au extracted from Rietveld refinement of the operando XRD pattern of all catalysts in OCP and under CO_2RR conditions.

Catalyst	Structural coherence lengths / nm		Lattice parameters / A		Weight Fraction	
OCP	Cu_2O	Au	Cu_2O	Au	Cu_2O	Au
$Au_{0.4}Cu_2O$ NC	9.2(4)	3(5)	4.2927(7)	3.98(9)	99.0(14)	1.0(14)
$Au_{1.1}Cu_2O$ NC	12.35(16)	1.42(3)	4.30880(17)	4.060(2)	96.1(6)	3.9(6)
$Au_{2.7}Cu_2O$ NC	10.7(6)	1.46(17)	4.2954(8)	4.061(11)	76.4(18)	23.6(18)

Supplementary Table 8.10: Coherence lengths, lattice parameters and atomic fractions of Cu_2O and Au extracted from Rietveld refinement of the operando HE-XRD pattern of $Au_{1.1}Cu_2O$ NC under CO_2RR conditions.

Catalyst	**Structural coherence lengths / nm**			**Lattice parameters / A**			**Weight Fraction**		
CO_2RR	**Cu_2O**	**Cu**	**Au**	**Cu_2O**	**Cu**	**Au**	**Cu_2O**	**Cu**	**Au**
$Au_{1.1}Cu_2O$ NC		12.5(15)	0.3(8)	4.2168(3)	3.6501(5)	4.0(18)	0.9(3)	96(6)	3(6)

Supplementary Table 8.11: Structural parameters (coordination number N, interatomic distances R, disorder factors σ^2) obtained from fitting the Cu K-edge EXAFS data acquired for Au-decorated Cu_2O NCs in the as prepared state and during CO_2RR at −1.0 V vs. RHE. Correction to photoelectron reference energy ΔE and the obtained R-factor that characterizes fit quality are also reported. Uncertainty of the last digit is reported in parentheses.

Sample	**Cu foil**	**Cu_2O**	**$Au_{0.4}Cu_2O$ NC**		**$Au_{0.8}Cu_2O$ NC**		**$Au_{1.1}Cu_2O$ NC**		**$Au_{2.7}Cu_2O$ NC**	
			as prep.	**during CO_2RR**	**as prep.**	**during CO_2RR**	**as prep.**	**during CO_2RR**	**as prep.**	**during CO_2RR**
N_{Cu-O}	0	2	3.6(5)	-	3.3(2)	-	3.4(4)	-	2.96(17)	-
R_{Cu-O} / Å	-	1.847(3)	1.857(13)	-	1.877(6)	-	1.859(10)	-	1.858(6)	-
σ^2_{Cu-O} / Å^2	-	0.0008(5)	-0.002(2)	-	0.002(1)	-	0.002(2)	-	0.003(1)	-
N_{Cu-Cu}	12	0	-	10(2)	-	11.9(9)	-	11(2)	-	9.8(7)
R_{Cu-Cu} / Å	2.545(4)	-	-	2.558(13)	-	2.539(5)	-	2.527(12)	-	2.539(5)
σ^2_{Cu-Cu} / Å^2	0.0093(4)	-	-	0.007(2)	-	0.0096(7)	-	0.010(2)	-	0.009(1)
ΔE / eV	3.37	1.3(4)	2.0(16)	5(2)	4.3(8)	3.3(7)	2.3(13)	2(2)	0.6(7)	-2.8(8)
R factor	0.3 %	0.02 %	6.5%	4.4%	0.1%	0.5%	0.4%	3.6%	0.1%	0.6%

Supplementary Table 8.12: Structural parameters (coordination number N, interatomic distances R, disorder factors $Å^2$) obtained from fitting the experimental Au L_3-edge EXAFS data acquired in the as prepared state and during CO_2RR at −1.0 V vs. RHE. Correction to photoelectron reference energy ΔE and the obtained R-factor that characterizes fit quality are also reported. Uncertainty of the last digit is reported in parentheses.

Sample	**Au foil**	**CuAu Alloy (from Ref [245])**	**$Au_{0.4}Cu_2O$ NC as prep.**	**$Au_{0.4}Cu_2O$ NC during CO_2RR**	**$Au_{0.8}Cu_2O$ NC as prep.**	**$Au_{0.8}Cu_2O$ NC during CO_2RR**	**$Au_{1.1}Cu_2O$ NC as prep.**	**$Au_{1.1}Cu_2O$ NC during CO_2RR**	**$Au_{2.7}Cu_2O$ NC as prep.**	**$Au_{2.7}Cu_2O$ NC during CO_2RR**
$N_{Au\text{-}Cu}$	0	6.8(6)	-	9(4)	-	8(2)	-	9(4)	-	10(6)
$R_{Au\text{-}Cu}$ / Å	0	2.700(2)	-	2.610(6)	-	2.62(1)	-	2.61(2)	-	2.63(1)
$\sigma^2_{Au\text{-}Cu}$ / $Å^2$	0	0.006(1)	-	0.011(3)	-	0.010(1)	-	0.011(4)	-	0.012(6)
$N_{Au\text{-}Au}$	12	8.6(9)	12(3)	3(4)	12(2)	4(2)	13(3)	3(4)	13(2)	2(6)
$R_{Au\text{-}Au}$ / Å	2.860(4)	2.811(7)	2.83(2)	2.72(5)	2.84(9)	2.79(4)	2.83(1)	2.74(5)	2.84(1)	2.72(7)
$\sigma^2_{Au\text{-}Au}$/ $Å^2$	0.0084(8)	0.006(1)	0.009(3)	0.01(4)	0.009(2)	0.01(1)	0.011(2)	0.01(2)	0.009(2)	0.01(5)
ΔE / eV	2.1(5)	-1.6(4)	1.82(1.7)	-0.39(1.)	1.62(1.0)	2(2)	1.49(1.4)	-0.22(2)	1.59(1.2)	2(2)
R factor	0.25	0.062	2.65	0.19	0.989	0.089	2.13	0.25	1.39	0.51

Supplementary Table 8.13: Register of the most important Au-Cu and Ag-Cu catalysts forming C_{2+} products under CO_2RR.

	Catalyst	Main C_{2+} products	explanation	Ref
CuAu catalysts				
Alloy	$AuCu_3$ alloy	<1% FE C_{2+}, <2% FE ethanol	Synergistic effects	[111]
Mixed systems	CuAu alloy NP, embedded in Cu	30% FE ethanol, 16% C_2H_4	Electronic structure effects	[240]
Au NP on Cu or Cu_2O	Au (30-50 nm) on Cu_2O NWs	23% FE ethanol, 38.7% FE C_2H_4	Synergistic effects	[241]
	Au (3-5 nm) on polyCu	12% FE ethanol, 18.3% FE C_{2+}	Synergistic effects	[112]
	Au-Cu_2O NC	60% C_{2+}, 20% FE liquids	Synergistic effects	This work
CuAg catalysts				
Mixed systems	CuAg	41% FE ethanol		[262]
	$Cu_{95}Ag_5$ thin film	9% FE ethanol, 17% C_2H_4	Miscibility between Cu an Ag	[247]
Ag NP on Cu_2O	Ag/Cu_2O_{PB}	35% FE ethanol, 10% FE C_2H_4	Miscibility of Cu and Ag	[58]
	Ag/Cu_2O	18% FE ethanol, 52% FE C_2H_4	Spillover mechanism	[228]
	5-Ag/Cu_2O NC	17% FE ethanol, 34% FE C_2H_4	Partial Cu_2O reduction, Ag redispersion, Ag/Cu miscibility	[107]

9

Enhanced Formic Acid Oxidation over SnO_2-decorated Pd Nanocubes

Clara Rettenmaier, Rosa M. Arán-Ais, Janis Timoshenko, Rubén Rizo, Hyo Sang Jeon, Stefanie Kühl, See Wee Chee, Arno Bergmann, Beatriz Roldan Cuenya

Published in: ACS Catalysis 2020, 10, 14540–14551, DOI: 10.1021/acscatal.0c03212

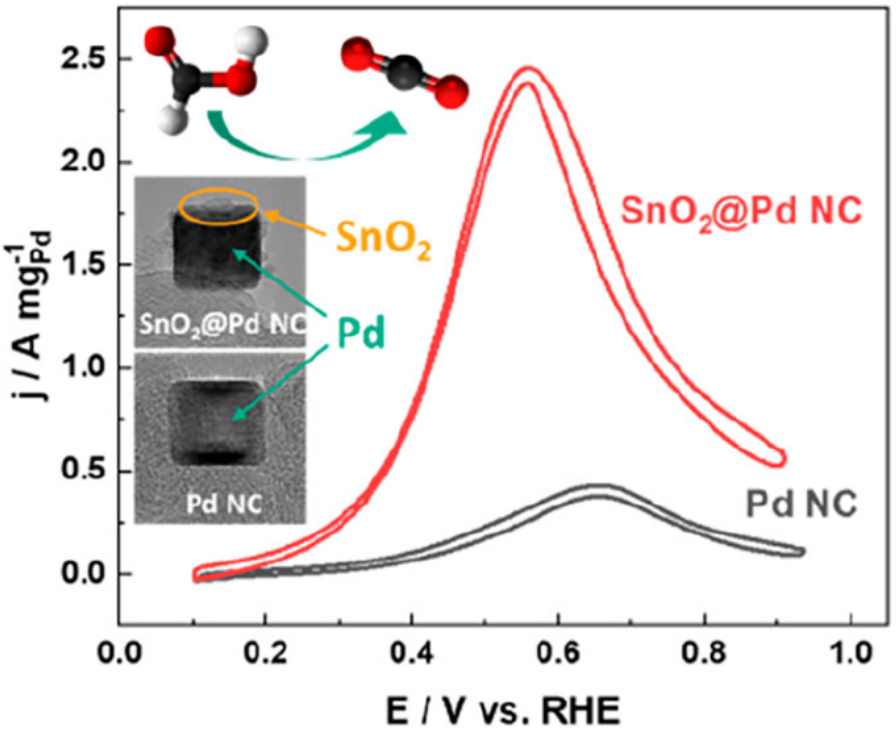

9.1 Preliminary Remarks

This chapter can be set in comparison to the Au decorated Cu_2O nanocubes (NC) with the same scientific question on how co-catalysts can enhance the activity of the shaped main catalyst. Furthermore, it was demonstrated that the already established *in situ* and *operando* setups in our lab can also be used to analyze and characterize catalysts for oxidation reactions. Here, SnO_2-decorated Pd NC are compared with Pd NC for the Formic Acid Oxidation Reaction (FAOR) and structure-activity relationships are set by *in situ* and *operando* spectrosopic methods.

The project was designed and supervised by Rosa M. Arán-Ais and Beatriz Roldan Cuenya. While I performed and analyzed the catalyst synthesis, electrocatalysis, and the spectrosopic experiments, the development of the synthesis and electrochemical system was assisted by Rosa M. Arán-Ais, while Janis Timoshenko led the *operando* X-ray Absorption Spectroscopy (XAS) experiments with support from Hyo Sang Jeon and Rubén Rizo. Stefanie Kühl and See Wee Chee performed the Transmission Electron Microscopy (TEM) measurements, while Stefanie Kühl additionally conducted the Inductively Coupled Plasma - Mass Spectrometry (ICP-MS) measurements. Arno Bergmann guided the X-ray Diffraction (XRD) experiments.

This chapter is reproduced with permission from *Clara Rettenmaier, Rosa M. Arán-Ais, Janis Timoshenko, Rubén Rizo, Hyo Sang Jeon, Stefanie Kühl, Arno Bergmann, Beatriz Roldan Cuenya* Enhanced Formic Acid Oxidation over SnO_2-decorated Pd Nanocubes. ACS Catalysis 2020, 10, 14540–14551, DOI: 10.1021/acscatal.0c03212. Copyright ACS Author Choice via the Creative Commons CC-BY agreement. Format, figure numbering and bibliography were adapted to fit to this thesis and possible spelling mistakes in the original article were corrected without further mentioning.

9.2 Abstract

The Formic Acid Oxidation Reaction (FAOR) is one of the key reactions that can be used at the anode of low-temperature liquid fuel cells. To allow the knowledge-driven development of improved catalysts, it is necessary to deeply understand the fundamental aspects of the FAOR, which can be ideally achieved by investigating highly active model catalysts. Here, we studied SnO_2-decorated Pd nanocubes (NC)s exhibiting excellent electrocatalytic performance for formic acid oxidation in acidic medium with a SnO_2 promotion that boosts the catalytic activity by a factor of 5.8, compared to pure Pd NCs, exhibiting values of $2.46\,A\,mg^{-1}{}_{Pd}$ for SnO_2@Pd NCs versus $0.42\,A\,mg^{-1}{}_{Pd}$ for the Pd NCs and a 100 mV lower peak potential. By using ex situ, quasi *in situ*, and *operando* spectroscopic and microscopic methods (namely,

transmission electron microscopy, X-ray photoelectron spectroscopy, and X-ray absorption fine-structure spectroscopy), we identified that the initially well-defined SnO_2-decorated Pd NCs maintain their structure and composition throughout FAOR. *In situ* Fourier-transformed infrared spectroscopy revealed a weaker CO adsorption site in the case of the SnO_2-decorated Pd NCs, compared to the monometallic Pd NCs, enabling a bifunctional reaction mechanism. Therein, SnO_2 provides oxygen species to the Pd surface at low overpotentials, promoting the oxidation of the poisoning CO intermediate and, thus, improving the catalytic performance of Pd. Our SnOx-decorated Pd nanocubes allowed deeper insight into the mechanism of FAOR and hold promise for possible applications in direct formic acid fuel cells.

9.3 Introduction

Fuel cells are efficient power sources that generate electric energy from chemical reactions.[263] Among the low-temperature fuel cells, the Direct Formic Acid Fuel Cell (DFAFC) has attracted significant attention since the 1960s,[120,121,264] because of the high electromotive force (1.45 V) and low fuel crossover.[265] The benefit of formic acid as a fuel source is based on its safety, low toxicity, and its straightforward synthesis from abundant natural biomass.[263] Moreover, the Formic Acid Oxidation Reaction (FAOR) serves as a model system for a structure-sensitive, two-electron-transfer electrochemical reaction,[266] of which fundamental understanding can serve to elucidate more-complex processes.

FAOR proceeds through a widely accepted dual-path mechanism. In the direct pathway, CO_2 is produced through an active intermediate of unclear nature, while in the indirect pathway, the formation of the poisoning intermediate $HCOO_{ads}/CO_{ads}$ occurs through dehydration.[120,121,267,268] Extensive studies have shown that the direct pathway is more favorable on Pd than on Pt.[130,269,270] The less favorable poisoning by CO and lower FAOR onset potential for Pd, compared to Pt, leads to an enhanced initial catalytic performance of Pd-containing systems.[121,130,271] However, it is also widely accepted that Pd still suffers from slow deactivation through the adsorption of poisoning CO_{ads}.[270,272]

The structure sensitivity of FAOR has been systematically explored using Pd single crystals,[133,273] as well as shape-controlled (and thus facet-oriented) Pd nanoparticles (NPs).[274,275] Particularly, the {100} orientation exhibits the highest FAOR performance of all basal planes, which was explained by its capacity to stabilize two bridge formate species as compared to other facet.[134,150,273–275] In this respect, cubic NPs are enclosed by six {100} facets in bulk face centered cubic (fcc) structures, making these nanostructures perfect model systems for studying FAOR. However, a limitation of the shaped NPs is their morphological instabil-

ity.[276,277] It has been reported that monometallic Pd catalysts deactivate and degrade by dissolution of Pd under acidic operation conditions,[272,278,279] and, thus, the preservation and optimization of the activity and stability of the catalyst is of crucial interest. Therefore, the addition of a second metal, such as Au,[278,279] Pt,[280] Ag,[281] Ti,[282] Pb,[283] Fe,[284] or Sn,[127,263,265,285–290] provides a common strategy for enhancing the activity and stability of Pd-based catalysts. Most known Pd-M catalysts form alloys, which not only lead to a variation of the reaction mechanism, but also generally improve the stability.[291]

A few examples of the use of Pd–Sn systems for FAOR applications have been previously reported, all demonstrating that CO oxidizes more easily on the Sn-containing samples, leading to an improved catalytic activity for FAOR.[127,285–289] The particular interest in Sn arises from its ability to oxidize potentially poisoning intermediates such as CO on Pd or Pt at low overpotentials, through an electronic effect,[127,285,292] a bifunctional mechanism,[287,293] or a third-body effect.[130,138,294] Regarding the electronic effect, alloying Sn with Pd modifies the electronic structure of the catalyst, lowering the adsorption energy of the intermediates. In fact, the increased catalytic performance of alloyed PdSn/C NPs, prepared via a microwave-assisted polyol method, was assigned to an expansion of the lattice parameter of Pd and, thus, to a modified electronic structure.[127,285] Regarding the bifunctional mechanism, the presence of oxidized Sn species was found to facilitate the CO oxidation and, hence, increase the FAOR activity,[287,293] while it also improved its stability.[265] In particular, PdSn–SnO_2 catalysts with different degrees of interfacial contact have demonstrated substantially lower CO poisoning and higher catalytic activity, compared to alloyed PdSn catalysts.[286] The third-body effect, in turn, is defined by the inhibition of possible COads adsorption sites through adatoms or steric hindrance, thereby facilitating the adsorption of formic acid.[130,138,294]

Therefore, SnOx decoration is a promising approach to increase the catalytic activity, but it is not yet clear how SnOx interacts with the most active Pd$\{100\}$ surface, particularly under FAOR conditions, and whether the reaction pathway is modified. Furthermore, FAOR on Pd electrocatalysts has rarely been studied with spectroscopic methods under reaction conditions, although the few existing *in situ* Fourier-transformed Infrared Spectroscopy (FTIR) studies reveal interesting mechanistic aspects. For example, the dependence of the CO_{ad} coverage on the CO_2 concentration at the surface was observed, leading to the conclusion that the origin of CO_{ad} could be the reduction of the product CO_2 over the Pd surface.[130,131,295,296]

In the present study, we report a comparison of SnO_2-decorated Pd (SnO_2@Pd) NCs and monometallic Pd NCs with a preferential Pd100 surface structure, prepared via a hydrothermal synthesis route and supported on carbon. Spectroscopic and microscopic characterization of the SnO_2@Pd catalysts revealed a cubic Pd core with an incomplete SnO_2 outer shell, which

remains in close contact with Pd during the reaction. Quasi *in situ* X-ray Photoelectron Spectroscopy (XPS) and *operando* X-ray Absorption Spectroscopy (XAS) data revealed that the Sn^{4+} oxidation state is preserved under reaction conditions, while *in situ* Fourier-transformed Infrared Spectroscopy (FTIR) spectroscopy suggested the presence of a weaker CO adsorption site on Pd. We found that the addition of SnO_2 improves the catalytic activity of Pd NCs toward FAOR in acidic media, because it leads to a decrease in the oxidizing potential of CO intermediates, keeping the active Pd sites free of poisoning intermediates.

9.4 Experimental Section

Synthesis of Pd and SnO_2@Pd Nanocubes

Pd nanocubes were prepared through a hydrothermal synthesis route by modifying a previously reported method.[150] Dihydrogen tetrachloropalladate (H_2PdCl_4, 10 mM) was prepared from 10 mM $PdCl_2$ (99.9%, Sigma–Aldrich) and 20 mM HCl (ACS reagent, 37%, Sigma– Aldrich) and reduced by l-ascorbic acid (99%, Alfa Aesar) under the presence of hexacetyltrimethylammonium bromide (CTAB, >99%, Sigma–Aldrich) at 95 °C. After 25 min, the solution was centrifuged, washed two times with 1:1 ethanol/water, and dispersed in ultrapure water (resistance = 18.2 MΩ). The SnO_2@Pd NCs were prepared by following the same method and with further addition of 5 at.% $SnSO_4$ (>95%, Sigma–Aldrich) 15 min after the start of the reaction. The NCs were supported on carbon by adding carbon Vulcan XC72R powder to the nanocubes' aqueous dispersion and sonicating the suspension thoroughly. The ligands were removed by adding 0.25 M NaOH. After complete precipitation, the samples were washed thoroughly with ultrapure water and dried at 105 °C overnight. The catalyst inks with a concentration of 4 mg/mL were prepared by sonicating the carbon-supported NCs in isopropanol for 5 min. From this, a 10 µL aliquot, corresponding to 40 µg of catalyst, was pipetted onto a glassy carbon substrate and dried in air.

Electrochemical Measurements

Electrochemical characterization was performed in Ar-saturated 0.5 M H_2SO_4 (95%, VWR). FAOR was studied in an Ar-saturated 0.1 M $HClO_4$ (70%, 99.999% trace metal basis, Sigma–Aldrich) containing 0.5 M HCOOH (96%, Sigma–Aldrich) in a three-electrode electrochemical cell at 50 mVs^{-1} using a Biologic SP300 potentiostat. A reversible hydrogen electrode (RHE) (HydroFlex, Gaskatel) and a leak-free Ag/AgCl (LF-1, Innovative Instruments Inc., 3.4 M KCl) were used as reference electrodes. Au wire served as a counter electrode. The catalyst-covered glassy carbon electrode was immersed into the solution with a hanging meniscus configuration.

Before each experiment, the catalysts were activated by cycling 10 times in 0.1 M $HClO_4$ between 0.1 and 0.7 V at 50 mVs^{-1}. The collected electrochemical data were IR-corrected, and the ohmic drop was obtained based on i-interrupt or impedance measurements. In addition, the data were normalized by the Pd mass of each catalyst obtained by Inductively Coupled Plasma - Mass Spectrometry (ICP-MS). All potential scales were converted to RHE.

CO-stripping experiments were performed by dosing CO (Westfalen, 3.7) into the electrolyte while holding the potential of the working electrode at 0.15 V until total surface inhibition, which was monitored by cyclic voltammetry between 0.1 V and 0.4 V through the disappearance of the $H_{Ads/Des}$ peaks. The residual CO in the electrolyte was removed by purging with Ar for 15 min. The adsorbed CO was completely stripped off the surface through a cyclic voltammogram up to 1.0 V at 20 mVs^{-1}. The second cycle shows the reappearance of the H_{upd} adsorption and desorption peaks, which disappeared during the CO_{ads} blockage. Chronoamperometric measurements were performed by holding the working potential at 0.1 V for 10 s, where no reaction occurs, and at 0.45 V for 180 min. Tafel slopes were calculated in a quasi-steady state from forward linear sweep voltammograms at 1 mVs^{-1}.

The Electrochemical Surface Area (ECSA) electrochemical surface area (ECSA) was evaluated from the H_{des} peak after CO-stripping experiments and by the area of the CO oxidation features. For H_{des}, the values were calculated by integrating the CVs between 0.11 V and 0.42 V and normalizing by the theoretical charge ($QH = 210\,\mu Ccm^{-2}$ for a one-electron transfer per Pd atom.[163] The surface area through CO oxidation was obtained by integrating the CVs between 0.75 V and 1.0 V with the blank CV as a baseline and normalizing by $Q_{CO} = 420\,\mu Ccm^{-2}$ for a two-electron transfer per Pd atom.[164]

Inductively Coupled Plasma - Mass Spectrometry (ICP-MS)

The compositions of the catalysts, based on atomic percentage and weight percentage, were determined by Inductively Coupled Plasma - Mass Spectrometry (ICP-MS) (Thermo Fisher iCAP RQ). The digestion of the samples was performed by adding a mixture of acids (1:1:3 H_2SO_4:HNO_3:HCl) into a known amount of the catalyst and heating to 180 °C for 30 min, using the digestion Microwave Multiwave GO from Anton Paar. The solution was then filtered to remove any remaining carbon residues and then diluted 100 times in 3% HCl. The electrolyte was diluted 3.33 times in 3% HCl.

Transmission Electron Microscopy (TEM) and Energy Dispersive X-ray Spectroscopy (EDX)

Transmission Electron Microscopy (TEM) and Energy Dispersive X-ray Spectroscopy (EDX) have been employed to investigate the morphology, size distribution, and local elemental composition of the catalysts. The measurements were performed with a FEI Talos F200X microscope equipped with a XFEG field-emission gun with an acceleration voltage of 200 kV, a Scanning Transmission Electron Microscopy (STEM) unit with a bright-field (BF) detector, two Dark-Field (DF) detectors, and a High-Angle Annular Dark Field (HAADF) detector, as well as SuperX 4 SDD EDX detector. The samples were prepared by placing a drop of a 4 mg/mL suspension in isopropanol on a Ni or Cu lacey carbon grid and allowing it to dry in air. For each sample, more than 200 nanocubes located on different parts of the grid were analysed to estimate the average size distribution. The composition of the NCs was analyzed via EDX, where maps were collected to analyze the elemental distribution. A schematic visualization of the obtained structure was made with VESTA.[297]

X-ray Diffraction (XRD)

X-ray Diffraction (XRD) measurements were collected on a Bruker AXS D8 Advance diffractometer in Bragg–Brentano geometry. The setup employs Ni-filtered Cu $K\alpha_{1+2}$ radiation and a position-sensitive energy-dispersive LynxEye silicon strip detector. XRD patterns were measured in the range of 20°–100° 2θ in continuous scanning mode, with an increment of 0.02° and a counting time of 1 s/step, which resulted in 185 s of total accumulation time per data point. The analysis of the diffraction patterns was performed with Rietveld refinements considering the instrumental broadening and sample displacement, using the software package TOPAS (Bruker-AXS).

Quasi *In Situ* X-ray Photoelectron Spectroscopy (XPS)

XPS measurements were performed with a commercial Phoibos100 analyzer (SPECS GmbH, $E_{pass} = 15$ eV) and a XR50 (SPECS GmbH) X-ray source with an Al anode ($E_{K\alpha} = 1486.7$ eV). All spectra were aligned using Pd^0 (335.2 eV) as reference and fitted using a Shirley-type or a linear background subtraction for X-ray or Auger electron spectroscopy, respectively. Quasi *in situ* XPS experiments were performed while avoiding the exposure of the sample to air after the electrochemical treatment. In this setup, an electrochemical cell is directly attached to the Ultra high Vacuum (UHV) system where the XPS chamber is located to allow the sample transfer without air exposure. The samples were first cycled between 0.1 V and 0.7 V in 0.1 M $HClO_4$, then the reaction was performed after adding 0.5 M HCOOH to the electrolyte.

Afterward, the samples were rinsed with deaerated ultrapure water and transferred to an Ultra high Vacuum (UHV) system in an Ar atmosphere. The electrochemical measurements were performed using a potentiostat (Autolab PGSTAT 302N).

Operando X-ray Absorption Fine-Structure Spectroscopy (*Operando* XAFS)

XAFS measurements were performed at the undulator beamlines P64 and P65 of the PETRA III storage ring. A Si(311) double-crystal monochromator was used for energy selection, and an Rh-coated collimating mirror was used for the removal of higher harmonics and the reduction of the power load density on the monochromator. All experiments were conducted in fluorescence mode, using a passivated implanted planar silicon (PIPS) detector at the Pd K-edge (24 350 eV) and Sn K-edge (29 200 eV). The *operando* measurements were performed in a three-electrode electrochemical cell (see ref [260] for the schematics of the cell). A leak-free Ag/AgCl component was used as a reference electrode, while an Au wire was used as a counter electrode. The samples were prepared by drop casting 10 mg of catalyst on a 0.5 cm^2 area of carbon paper. Pd K-edge and Sn K-edge data were collected separately for identical fresh samples, to optimize the signal absorption edge and to avoid self-absorption. Carbon paper with the deposited catalyst served as a working electrode. It was mounted in the electrochemical cell and fixed with Kapton tape, so that the Kapton-covered carbon paper could act as X-ray window, while the side coated with the catalyst was in contact with the electrolyte. Measurements for both samples were performed in air as well as under *operando* conditions, in Ar-saturated 0.1 M $HClO_4$ + 0.5 M HCOOH solution. Energy calibration, background subtraction and normalization of the collected XAFS spectra were performed with the software Athena.[181] Details regarding the Extended X-ray Absorption Fine Structure (EXAFS) fitting are summarized in Supplementary Note 9.7 in the Supporting Information.

In situ Fourier-transformed Infrared Reflection Absorption Spectroscopy (FT-IRRAS) Spectroscopy

In situ FT-IRRAS data were acquired with a Vertex 80v spectrometer (Bruker) that was equipped with a MCT detector, using a thin layer configuration in the external reflection mode. An electrochemical cell was home-built around a CaF_2 IR window with a Au counter electrode and a leak-free Ag/AgCl reference electrode. A Au foil was chosen as the substrate for CO-stripping experiments to enhance the reflectivity (no CO adsorption was observed on the gold support in the potential range used). The electrode was transferred to the cell filled with an Ar-saturated 0.1 M $HClO_4$ electrolyte, CO was adsorbed under potential control, the remaining CO in the electrolyte was removed with Ar, and then the electrode was pressed

against the CaF_2 window for the *in situ* FTIR measurements. For FAOR experiments, glassy carbon was used as a support; the amount of formic acid was reduced to 25 mM for better sensitivity of the onset potentials and to decrease the CO_2 bubble formation, which could displace the electrolyte in the thin-layer configuration. IR spectra were collected between 4000 cm^{-1} and 1000 cm^{-1} with 100 interferograms per spectrum and a spectral resolution of 4 cm^{-1}. Background spectra were acquired at 0.06 V for CO stripping and -0.04 V for the FAOR experiments. The spectra are represented as absorbance, $A = -\log \frac{R}{R_0}$, where R and R_0 are the sample and reference reflectances, respectively. For CO-stripping and FAOR experiments, the background spectra were obtained after CO adsorption and after the addition of HCOOH, respectively. Thus, oxidation of CO is indicated by negative peaks for CO-stripping experiments, while CO_2 formation is indicated by a positive peak for both experiments.

9.5 Results and Discussion

9.5.1 Catalyst Morphology and Structure Characterization

The crystalline structure, morphology, chemical composition, and distribution of the carbon-supported SnO_2@Pd NCs and Pd NCs have been characterized by XRD (see Figure 9.1a, as well as Figure S9.7 in the Supporting Information), high-resolution TEM (Figures 9.1b and 9.1c), and STEM (see Figure 9.2, as well as Figures S9.8 and S9.9 in the Supporting Information). Moreover, the shape and the elemental distribution of both catalysts were tracked by High-Angle Annular Dark Field (HAADF)-STEM and Energy Dispersive X-ray Spectroscopy (EDX) mapping in the as-prepared state, after cycling 20 times in the presence of formic acid and after 3 h of reaction at a constant working potential (see Figure 9.2, as well as Figure S9.9). Cycling under oxidizing conditions was performed for testing the stability of the NCs in terms of morphology and chemical changes in the working potential range, while potentiostatic measurements were done to gain insight into the nanocubes' activity, stability, and resistance against CO poisoning. Figure 9.1a shows XRD patterns of the as-prepared catalysts. Besides the broad (002) reflection of the hexagonal graphite structure of the carbon support, all other diffraction peaks can be assigned to the typical fcc Pd bulk structure. In the SnO_2@Pd catalyst, the presence of crystalline Sn or a SnOx phase is not observed, which indicates the absence of significant Sn agglomeration. Note here that the presence of small amounts of Sn species on Pd cannot be ruled out by XRD. Rietveld refinement of the XRD pattern revealed very similar Pd lattice parameters for both samples with 3.889 59(12) Å for SnO_2@Pd NCs and 3.889 78(8) Å for the Pd NCs, suggesting the absence of an alloyed PdSn phase (see Figure S9.7). The volume-averaged coherence lengths of the Pd NCs and the SnO_2@Pd NCs were determined to be 21.26(17) nm and 20.0(2) nm, respectively.

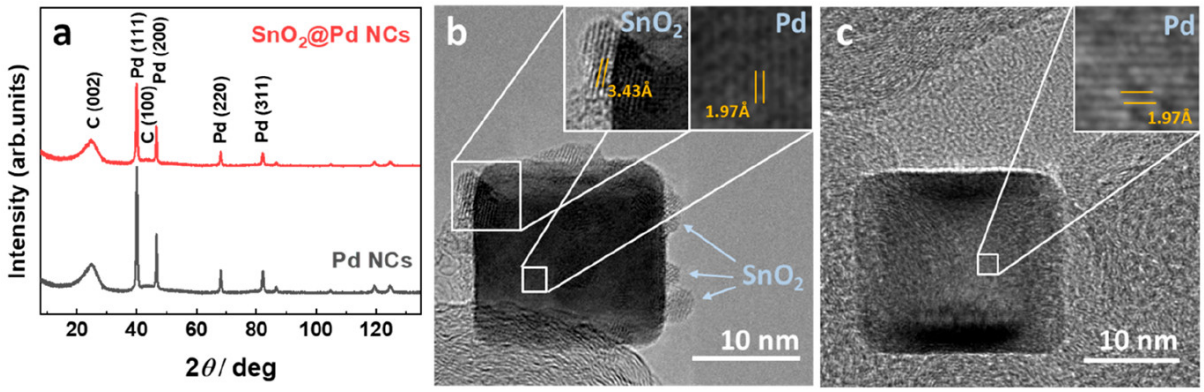

Figure 9.1: (a) XRD pattern of the as-prepared SnO_2@Pd NC and Pd NC catalysts. High-resolution TEM images of (b) SnO_2@Pd NCs and (c) Pd NCs supported on carbon powder.

Figures S9.1b and S9.1c display high-resolution TEM images of a SnO_2@Pd NC and a Pd NC supported on carbon, respectively, showing a structural periodicity of 1.97 Å for both catalysts, which is in good agreement with the (200) of fcc Pd. The SnO_2@Pd NC additionally shows crystalline structures on top of the Pd NCs with 3.43 Å periodicity, corresponding to the (110) spacings of the rutile SnO_2 structure. The SnO_2 structures have a size of ∼2 nm. Figures 9.2a and 9.2b show HAADF-STEM images of uniformly shaped NCs in both samples, suggesting a high density of {100} facets in the as-prepared state. The EDX elemental mapping of the SnO_2@Pd NCs in Figure 9.2c demonstrates that Sn covers the Pd NCs, forming an incomplete shell. The average particle sizes (estimated edge length of the cubes) are 22(4) nm for the Pd NCs and 21(7) nm for the SnO_2@Pd NCs, and these values indicate a symmetric size and shape distribution. The reported error is the standard deviation. The latter sample has a SnO_2 shell ∼2 nm thick, which contributes to the overall cube size. The distributions of the as-prepared NCs on the carbon support for both samples are shown in Figure S9.8. The Pd loading on carbon determined by ICP-MS was 7.2 wt% for the Pd NCs and 5.2 wt% for the SnO_2@Pd NCs, with 0.3 wt% Sn. After 3 h FAOR, neither Pd nor Sn from the catalysts were detectable in the electrolyte, which indicates a stable ratio between Pd and Sn for the SnO_2@Pd NCs. The overall atomic ratio determined by EDX is 96:4 for Pd:Sn, which is comparable to the Pd:Sn ratio of 94:6 determined by ICP-MS.

Prior to the electrocatalytic investigation, the catalysts were electrochemically activated by running 10 cycles between 0.1 V and 0.7 V in 0.1 M $HClO_4$. The STEM images and EDX mapping of the SnO_2@Pd NCs after the activation process, shown in Figure S9.9, reveal that the cubic structure is maintained, with a slightly smaller average size of 19(4) nm, and only a negligible fraction of Sn lost (1%). Interestingly, the cubic morphology of Pd was also mostly preserved after cycling in formic acid up to 0.95 V for 20 cycles (see Figures 9.2d–f), as well as after 3 h of chronoamperometry at 0.45 V (see Figures 9.2g–i). However, constant

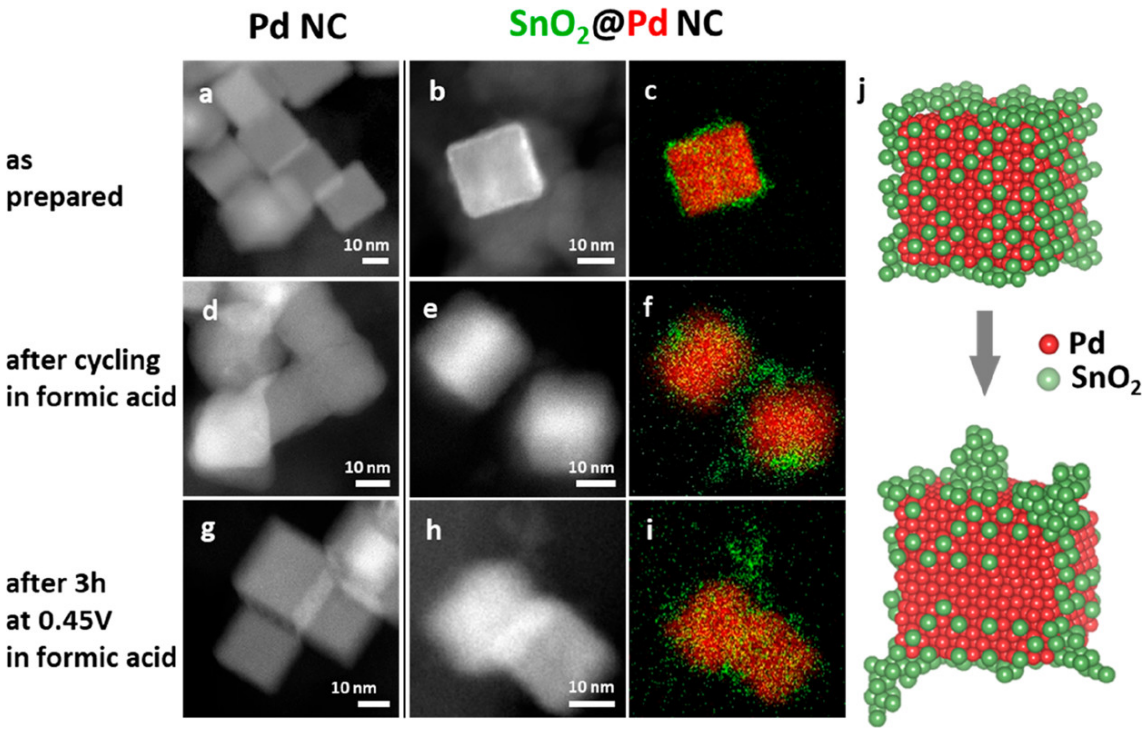

Figure 9.2: HAADF-STEM of Pd NCs (panels (a), (d), (g)) and SnO_2@Pd NCs (panels (b), (e), (h)) with EDX mapping of SnO_2@Pd NCs (panels (c), (f), (i)). TEM data of the as-prepared state of the samples are included in panels (a)–(c), those after cycling 10 times in formic acid (FA) are shown in panels (d)–(f), and those obtained after 3 h at 0.45 V in FA are shown in panels (g)–(i). The EDX maps of the SnO_2@Pd NCs correspond to the same regions of the HAADF-STEM images shown. An model depicting the evolution of the structure and surface composition of the SnO_2@Pd NC catalyst during FAOR is shown in panel (j). Sn atoms appear in green and Pd in red. The model representation is only for visual purposes, and it does not reflect the actual crystallographic size or atomic positions.

reaction conditions for3 h seem to be less harmful (Figures 9.2g–i), while cycling the catalysts in formic acid leads to a deterioration of the NC shape for both catalysts (Figures 9.2d–f). The upper potential limit of 0.95 V during cycling induced Pd oxide formation, leading to the dissolution of Pd which can explain the morphological changes.[298–300] Remarkably, the EDX maps show the growth of the uniformly distributed SnO_2 particles from ∼2 nm in size to SnOx agglomerations of up to 8 nm after FAOR. The STEM/EDX data also indicate that SnO_2 may dissolve, to some extent, from the Pd NC surface during the reaction. After 3 h of reaction at 0.45 V, the EDX ratio for Pd:Sn is 98:2, which is similar to that obtained after cycling in formic acid (99:1). A scheme in Figure 9.2j illustrates the evolution of the SnO_2@Pd nanocubes from a homogeneously distributed SnO_2 shell around the Pd NC to the formation of SnO_2 agglomerates on Pd after reaction.

9.5.2 Quasi *In Situ* X-ray Photoelectron Spectroscopy (XPS) and *Operando* X-ray Absorption Fine Structure (XAFS) Characterization

To further understand the role of the surface composition and chemical state of Pd and Sn, quasi *in situ* XPS and *operando* XAFS measurements have been conducted. Figure 9.3a displays the XPS spectra of the Pd 3d core level of both catalysts in the as-prepared state and after 1 h of FAOR at 0.45 V with a direct transfer from the electrochemical cell into UHV without exposure to air. Note that our XPS data were not acquired *in situ*, but quasi *in situ*, which is a terminology employed to signify that the samples were never exposed to air during the transfer from the electrochemical cell to the UHV-XPS analysis system. Nevertheless, a major limitation of this method must be considered, which is the fact that the XPS data are not acquired under potential control. The spectra are deconvoluted in three doublets with $3d_{5/2}$ peaks at E_B = 335.2 eV, E_B = 336.3 eV, and E_B = 338.1 eV, corresponding to Pd, PdO, and PdO_2, respectively.[301] Both catalysts show, besides the main Pd metal peak, small amounts of PdO and PdO_2 in the as-prepared state.[302,303] Residues of the ligands and the ligand-removing agent were not observed in our as-prepared samples, as demonstrated by the absence of the Cl 2p, Br 3d, and Na 1s peaks in the XPS spectra (see Figure S9.10 in the Supporting Information). After reaction, and without sample exposure to air, it is observed that the Pd component of both catalysts, SnO_2@Pd NCs and Pd NCs, remains partially oxidized. Our XPS results do not indicate the intermixing of Pd and SnO_2 and the formation of an interfacial PdSn alloy.

The Sn 3d spectra (see Figure 9.3b) were fitted with a spin-orbit doublet ($3d_{5/2}$ and $3d_{3/2}$), corresponding to SnOx at E_B = 487.0 eV ($3d_{5/2}$).[304] Furthermore, the analysis of the Sn MNN Auger spectra was used to verify the Sn^{4+} oxidation state. Figure 9.3c depicts the

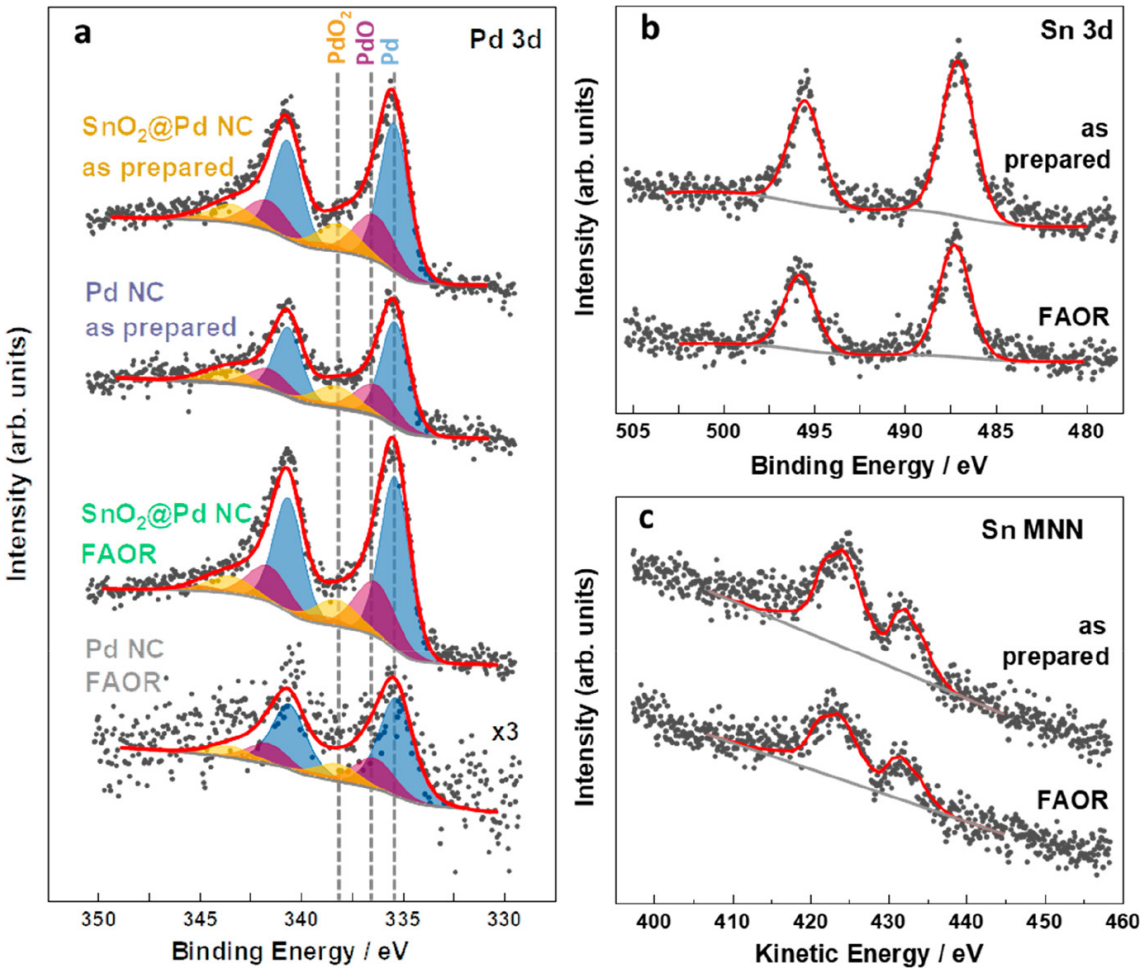

Figure 9.3: Quasi *in situ* XPS spectra for (a) Pd 3d core level of the Pd NCs and SnO_2@Pd NCs in the as-prepared state and after 1 h FAOR at 0.45 V in 0.1 M $HClO_4$. (b) Sn 3d XPS peaks and (c) Sn MNN AES peaks for the SnO_2@Pd NCs in the as-prepared state and after FAOR.

Auger spectra of the SnO_2@Pd NCs in the as-prepared state and after FAOR at 0.45 V. Both spectra were fitted with a SnO_2 reference spectrum. The data reveal a 4+ oxidation state of Sn in the as-prepared state, as well as after the activation process and after FAOR. The surface Pd/Sn atomic ratio was quantified from the spectral area of the Pd and Sn 3d XPS peaks. The estimated Pd:Sn atomic ratio for the SnO_2@Pd catalyst is 75:25 (XPS). A comparison of the Pd and Sn contents extracted from EDX and XPS data after the different sample treatments is shown in Table S9.1 in the Supporting Information. After reaction, the Pd:Sn surface ratio changes to 83:17, indicating an 8% loss of Sn at the surface. Thus, the distribution of SnO_2 on the Pd NC surface changes significantly toward a lower surface area of Sn, which indicates the formation of larger SnO_2 NP-like structures during the electrochemical reaction. Furthermore, when comparing the Pd-3d signal intensity of the bimetallic and monometallic samples, it is clear that the Pd NCs suffer from drastic material loss during the reaction, which was not observed for the SnO_2@Pd NCs that appear to be stabilized by the presence of SnO_2. Complementary to the surface-sensitive XPS data, *operando* XAFS measurements were employed to probe the chemical state and structure in the bulk of the catalysts. The Pd K-edge data shown in Figure 9.4b, as well as Figure S9.10 in the Supporting Information, demonstrate that the Pd species are in a reduced state and with a local environment similar to that in metallic fcc-Pd, both in the Pd NCs and in the SnO_2@Pd NCs as-prepared catalysts. The Pd oxidation state and local structure also do not change under the reaction conditions. X-ray Absorption Near Edge Structure (XANES) analysis at the Sn K-edge (Figure 9.4a) confirms that the oxidation state and local structure around Sn in the SnO_2@Pd NC catalyst is similar to that observed in the SnO_2 reference material, and does not change significantly during the reaction.

Figure 9.4c depicts the Fourier-transform extended X-ray absorption fine structure (fourier transformed (FT)-EXAFS) spectra for the Pd K-edge. In agreement with the XANES data analysis, the EXAFS analysis shows that the as-prepared catalyst, as well as the catalyst during reaction, are in the reduced state, with a local structure similar to that of pure metallic Pd. The fitted EXAFS spectra and the structural parameters are shown in Figure S9.11 andTable S9.2 in the Supporting Information.

9.5.3 Electrochemical Analysis

For the electrochemical characterization of the catalysts, a sulfuric acid containing electrolyte was chosen since the specific adsorption of sulfates leads to a defined profile of the hydrogen adsorption/desorption region.[26,305] The voltammetric profiles of the catalysts after 10 cycles in Figure S9.12a in the Supporting Information show peaks at 0.22 and 0.29 V for Pd NCs,

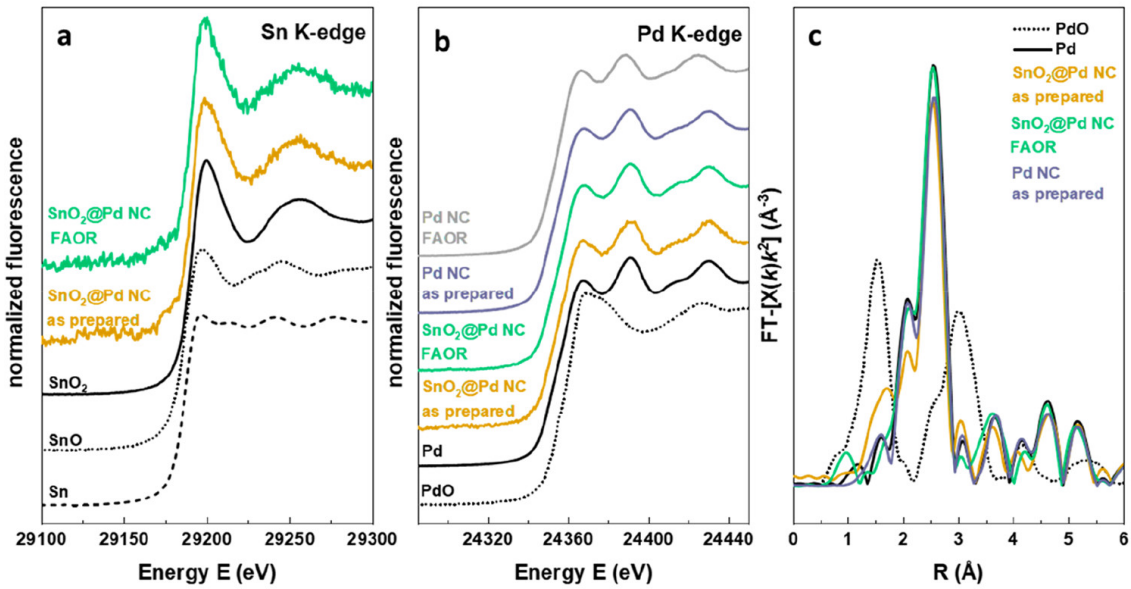

Figure 9.4: XANES spectra at the (a) Sn K-edge of SnO_2@Pd NCs and (b) Pd K-edge for the Pd NCs, as well as SnO_2@Pd NCs in the as-prepared state and *operando* spectra collected during 3 h of the FAOR in 0.1 M $HClO_4$ + 0.5 M HCOOH at 0.45 V vs. RHE. (c) fourier transformed (FT) k2-weighted Pd K-edge EXAFS spectra for both catalysts in the as-prepared state and during reaction. Reference spectra for bulk Sn, SnO, SnO_2, Pd, and PdO are shown for comparison.

which are associated with hydrogen adsorption/desorption on long {100} domains,[306] confirming the cubic shape. The SnO_2@Pd NC catalyst features a shifted hydrogen desorption peak at 0.27 V, indicating a distorted catalyst surface that is due to the presence of the second metal. Prior to every FAOR reaction, an electrochemical pre-treatment was performed by cycling the catalysts 10 times in the 0.1 M $HClO_4$ electrolyte. The FAOR measurements, as well as the CO-stripping experiments, were performed in 0.1 M $HClO_4$ because higher current densities are obtained, compared to the often-used 0.5 M H_2SO_4.[26,150,306,307] The specific adsorption of bisulfate at oxidative potentials blocks the active sites on Pd, which, hence, are not active for FAOR.[271,308,309] CO-stripping experiments were used to evaluate the CO tolerance of the catalysts. Under potential control, with the electrode at 0.1 V, CO was adsorbed on Pd such that the characteristic $H_{Ads/Des}$ peaks were suppressed as shown in Figure 9.5a. The adsorbed CO was completely oxidized through a single cycle up to 1.0 V and the $H_{Ads/Des}$ peaks reappeared subsequently in the second cycle. The similar peak potentials of both catalysts (0.86 V) indicate a mainly constant CO binding strength for both catalysts and, hence, no strain effect of the SnO_2 on the Pd lattice. However, the onset potential for CO oxidation was found to be reduced from 0.73 V for Pd NCs to 0.61 V for SnO_2@Pd NCs, as indicated by the gray dashed line. This result is in accordance with reports for non-shape-selected Pd and PdSn samples, where Sn-containing samples exhibited a 50-100 mV lower onset potential,

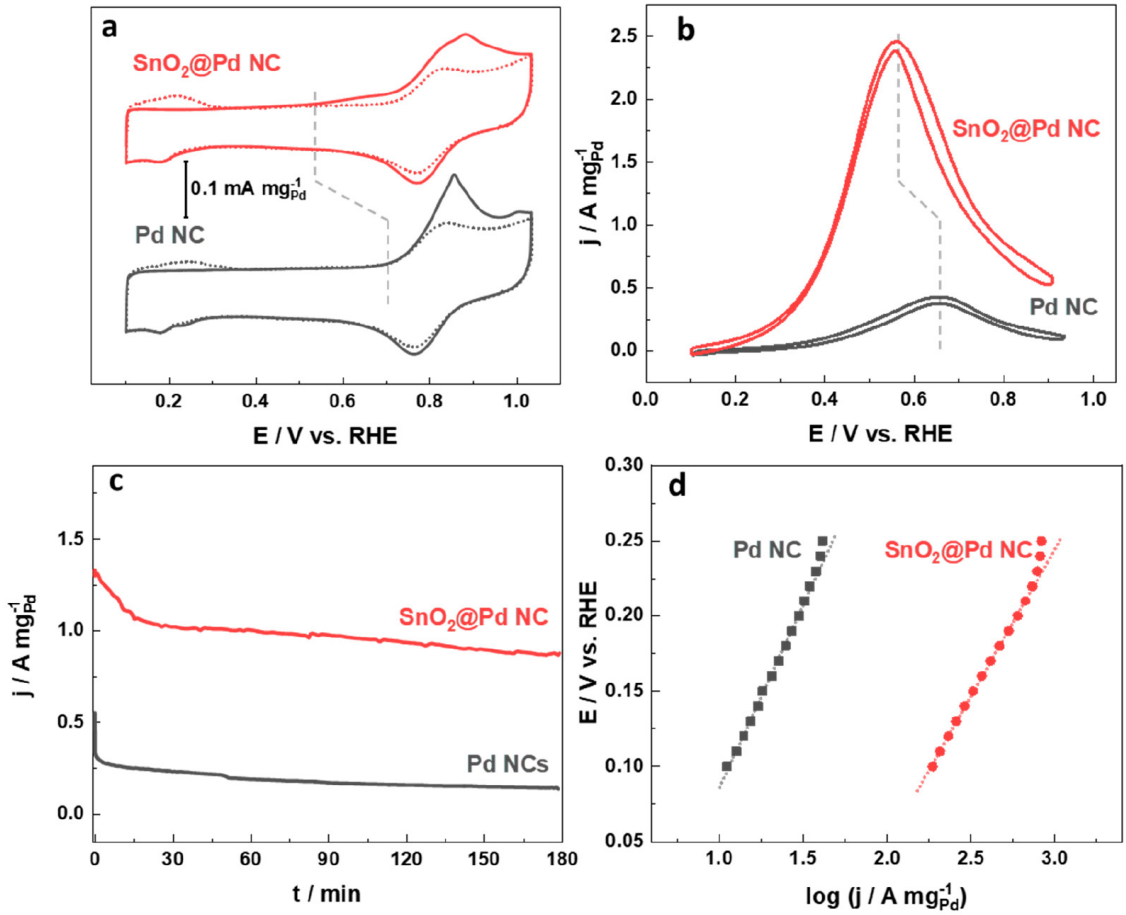

Figure 9.5: (a) CO-stripping voltammograms (solid lines) and subsequent cyclic voltammetry (dotted lines) of SnO_2@Pd catalysts (red) and Pd catalysts (gray) in 0.1 M $HClO_4$ at 20 mVs^{-1}. (b) Voltammetric profiles of the SnO_2@Pd NC (red) and Pd NC (gray) in 0.1 M $HClO_4$ + 0.5 M HCOOH at 50 mVs^{-1}. (c) Chronoamperometric curves of the SnO_2@Pd NC (red) and Pd NC (gray) at 0.45 V. (d) Tafel plots for SnO_2@Pd NCs (red) and Pd NCs (gray).

because of the oxophilic sites providing oxygen at lower Sn oxidation potentials.[127,285–289] The lower onset potential is accompanied by a slightly elevated oxidative current in a broad potential range, suggesting a more facile CO oxidation on Pd during this potential span. The broader CO oxidation peak of the SnO_2@Pd NCs suggests surface heterogeneity and a slower CO surface diffusion toward the reactive Pd sites in the presence of Sn. Thus, the presence of Sn atoms appears to facilitate the oxidative removal of CO.

The electrocatalytic activities of Pd NCs and SnO_2@Pd NCs for FAOR were characterized by cyclic voltammetry in 0.1 M $HClO_4$ + 0.5 M HCOOH between 0.1 V and 0.95 V at 50 mVs^{-1} (Figure 9.5b). The currents were normalized to the amount of Pd obtained by ICP-MS, thus reporting mass activities. The specific activities, where voltammetric profiles are normalized

by the electrochemical surface area calculated by CO stripping, are reported in Table S9.3 and Figures S9.12b and S9.12c in the Supporting Information. A comparison of the ECSA calculated from CO oxidation and the $H_{Ads/Des}$ is displayed in Table S9.3, with larger CO-stripping normalization, compared to the $H_{Ads/Des}$.[162] The FAOR peak potential for our Pd NCs occurs at 0.65 V, which agrees well with the finding of Vidal-Iglesias et al. for unsupported Pd NCs under similar reaction conditions.[150] Remarkably, the peak potential for SnO_2@Pd NCs shifts by 100 mV to a lower potential of 0.55 V, and they show a 5.8-fold increase of the current density at this potential, compared to the Pd NCs. A comparison of our catalysts with PdSn systems from the literature is shown in Table S9.4 in the Supporting Information, demonstrating the excellent performance of our catalysts. The higher FAOR current and the lower onset potential of our SnO_2@Pd NCs highlight the beneficial effect of SnO_2 for the enhancement of the catalytic activity. Chronoamperometric curves for FAOR at different potentials were performed to test the CO poisoning rate and stability of the samples under reaction conditions (see Figure 9.5c, as well as Figure S9.12c in the Supporting Information). At 0.45 V, the current densities decrease slowly for both catalysts over a period of 3 h. However, the stationary currents for SnO_2@Pd NCs are 5.8 times higher, compared to Pd NCs. Thus, high catalytic activity and stability of our materials is obtained for the SnO_2@Pd NCs at 0.45 V. Figure 9.5d displays the Tafel plots for FAOR, which were obtained from linear sweep voltammograms measured in quasi-steady state at $1\,mVs^{-1}$. The lower overpotential region between 0.1 V and 0.2 V displays a linear Tafel relationship indicating a kinetically controlled regime of the reaction. A lower Tafel slope was obtained for SnO_2@Pd NCs ($196(6)\,mVdec^{-1}$), compared to Pd NCs ($247(15)\,mVdec^{-1}$), suggesting faster electrokinetics of the SnO_2-containing catalyst. The high Tafel slopes indicate that mass-transfer kinetics must be involved in the reaction process. Similar Tafel slopes have been reported for Pd catalysts for FAOR.[310] A second Tafel slope at higher potentials, as shown in Figure S9.12d in the Supporting Information, suggests strong mass-transfer limitations. The exchange current densities (j_0) were further calculated to demonstrate the particular portion of the electrode kinetics and the intrinsic catalytic activity. As the standard potential for FAOR, an E^0 ($HCOOH/CO_2$, H^+) value of -0.19 V vs. RHE -(0.25 V vs. SHE) at 298 K was used.[311] Promoting Pd cubes with Sn appears to be very effective for boosting the catalytic activity, since SnO_2@Pd NCs resulted in a j_0 value of $0.96\,mAcm^{-2}$, compared to Pd NCs with $0.44\,mAcm^{-2}$. The order of magnitude is in a similar range to values for Pd reported in the literature.[144,312,313] Thus, this result confirms the improved catalytic activity of SnO_2@Pd NCs, mainly because of its enhanced electrokinetics.

9.5.4 Spectro-electrochemical Measurements

The effect of the SnO_2 on the CO adsorption on SnO_2@Pd NCs was studied *in situ* via CO stripping by applying FTIR. For these experiments, the carbon-supported NCs were deposited on an Au foil to enhance the reflectance of the IR light, while being inert for CO adsorption at room temperature. Hence, the electrode was pressed on the CaF_2 window after CO adsorption under potential control. The background spectrum was recorded at 0.06 V, then the potential was swept to positive values and held at the acquisition potential. With this configuration, negative bands indicate a disappearance of adsorbed species, while the species being formed appear as positive bands.[314] CO_{ads} features on Pd and Pt are usually influenced by an electrochemical Stark effect, leading to a potential-dependent wavenumber shift of the adsorbates.[314–316] The position of the center of the CO band increases in wavenumber with applied potential, because of the perturbation of the vibrational frequency in the static electric field of the double layer. Potential-dependent peaks are shown at 1945 cm^{-1} (see Figures 9.6a and 9.6b and 2345 cm^{-1} (see Figures S9.13a and S9.13b). The first one can be assigned to the bridge-bonded CO (C–O stretch; $\nu(CO_B) = 1900–1955\,cm^{-1}$), and the latter one can be assigned to dissolved CO_2 (asymmetric C–O stretch; $\nu(CO_2) = 2345\,cm^{-1}$).[267] The acquired spectra show relatively weak CO bands, which can be attributed to the low catalyst loading on the carbon support. For the Pd NCs (Figure 9.6a), a CO_B band appears at 1945 cm^{-1}, which shifts from 1951 cm^{-1} (0.16 V) to 1958 cm^{-1} (0.71 V) and decreases starting from 0.71 V. Similar bands for SnO_2@Pd NCs start to shift in the same manner at 0.16 V from 1951 cm^{-1}, but the peak intensity decreases already at 0.66 V. A negative band remains at 1945 cm^{-1} at higher potentials. These results are similar to the onset potentials observed in the electrochemical CO-stripping experiments and support the earlier CO oxidation of the SnO_2@Pd NCs.

Figure S9.13 in the Supporting Information depicts the CO_2 evolution from the CO-stripping experiments for Pd NC and SnO_2@Pd NC at 2345 cm^{-1}, respectively. The potential dependence of the integrated band intensities of the CO_2 formation are displayed in Figure 9.6c. While the onset potential for Pd NCs is observed at 0.71 V, CO_2 evolution starts 100 mV lower, at 0.66 V, for the SnO_2@Pd NCs. The results from the *in situ* FTIR measurements are in good agreement with the CO_2 evolution of the CO-stripping experiments (0.73 V for Pd NCs and 0.61 V for SnO_2@Pd NCs). Thus, we could show a weaker bond of CO to Pd when SnO_2 is present. Furthermore, FAOR was followed using *in situ* FTIR by monitoring the CO_2 evolution. Figures 9.6d and 9.6e show the respective potential-dependent CO_2 evolution for Pd NCs and SnO_2@Pd NCs, respectively. Glassy carbon was chosen as a substrate for the catalysts in these measurements, for better comparison with the catalytic investigation. No CO adsorption was observed in this experiment, which can be assigned to the low intrin-

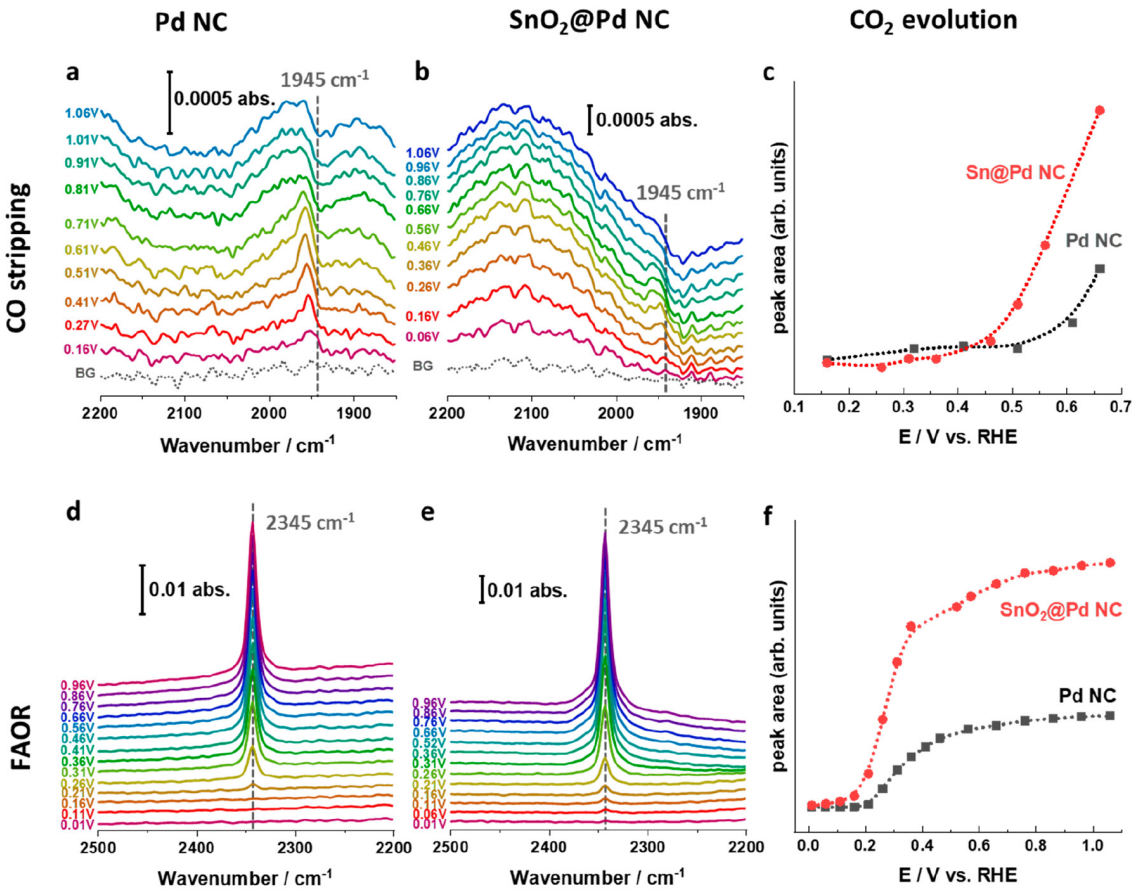

Figure 9.6: *In situ* FTIR of the CO-stripping experiments in the CO regime of (a) Pd NCs and (b) SnO_2@Pd NCs; (c) depicts the integrated intensities of the corresponding CO_2 bands. Reference spectra taken at 0.06 V vs. RHE, spectra taken on Au foil in 0.1 M $HClO_4$. *In situ* FTIR of FAOR show CO_2 bands during FAOR for (d) Pd NCs and (e) SnO_2@Pd NCs, while panel (f) depicts the integrated band intensities of the CO_2 bands during FAOR. Reference spectra taken at -0.04 V vs. RHE. Spectra taken on glassy carbon in 0.1 M $HClO_4$ and 25 mM HCOOH.

sic adsorption of CO on Pd while sweeping the potential up. It is expected that significant amounts of adsorbed CO and formate only form after exposure to the oxidizing potentials for an extended period of time. The background was taken at -0.04 V after the immersion of the electrode into the 0.1 M $HClO_4$ + 25 mM HCOOH solution to avoid the spontaneous FAOR and ensure that we have a metallic Pd surface. The low formic acid concentration was chosen to reduce massive CO_2 bubble formation and to increase the sensitivity for the onset potential of CO_2 formation. For Pd NCs, CO_2 generation by formic acid decomposition starts to evolve at 0.21 V, while for the SnO_2@Pd NCs, small amounts of CO_2 are already seen at 0.01 V, Figure 9.6f. The onset potentials for the catalytic activities measured by CV are 0.35 V (Pd NC) and 0.15 V (SnO_2@Pd NC), which are both 140 mV higher than the onset potentials observed by FTIR, which again could be assigned to the higher sensitivity of the latter technique and to the intrinsic decomposition of formic acid. These results demonstrate a significant enhancement of the catalytic activity of SnO_2@Pd NC already at low potentials. The high catalytic performance of SnO_2@Pd NCs, which exceeds that of the current catalysts in the literature (Table S9.4 in the Supporting Information), originates from the presence of SnO_2 close to the $\{100\}$ facets of Pd NCs. CO-stripping experiments and their corresponding *in situ* FTIR revealed a decreased oxidizing potential of adsorbed CO, because of the presence of SnO_2. The role of SnO_2 on the removal of poisoning CO is demonstrated. In this study, the enhanced FAOR performance is linked to the exclusive presence of SnO_2 on Pd in a segregated way, without the formation of a PdSn alloy. However, the role of the third-body effect and the diminution of unfavorable COads formation through adatoms or steric hindrance cannot be excluded. The calculation of the electrochemical surface areas revealed a lower amount of active sites for SnO_2@Pd NCs (see Table S9.3), which indicates a possible blockage of sites on which CO could bound. The presence of SnO_2 results in weaker bound CO_{ads}, which, in turn, can be oxidized at milder overpotentials, making Pd active sites available for catalytic activity already at low overpotentials.

9.6 Conclusion

In the present "synthesis-by-design" approach, SnO_2@Pd nanocubes and Pd nanocubes were prepared via a hydrothermal chemical synthesis, supported on carbon powder, and studied for the electrochemical oxidation of formic acid in an acidic medium. The system was chosen, because Pd NCs are expected to exhibit high catalytic performance due to the presence of $\{100\}$ facets, while the existence of a second metal such as Sn is known to further enhance the activity through a bifunctional mechanism. The SnO_2@Pd NCs presented here are the first non-alloyed Pd–Sn nanocube FAOR catalysts with an incomplete SnO_2 shell. The presence

of SnO_2-like species on Pd was found to promote FAOR, which is linked to the oxidation of adsorbed CO at lower potentials as compared to Pd NCs. Since slow CO poisoning of the Pd surface leads to deactivation during FAOR, the presence of SnO_2 results in enhanced catalytic performance of SnO_2@Pd NCs compared to bare Pd NCs. In particular, the SnO_2@Pd NCs outperformed the Pd NCs, in terms of activity, with a 5.8-fold increase of current density with 2.5 $AmgPd^{-1}$ and a 100 mV lower peak potential. The catalytic properties also exceeded those of the known PdSn catalysts in the literature. However, the proposed catalyst is still prone to deactivation, to some extent. STEM and EDX, as well as quasi *in situ* XPS and *operando* XAS revealed that the shape, as well as the oxidation state, of the catalysts remained stable during and after reaction at 0.45 V. *In situ* FTIR studies confirmed the lower CO desorption potentials and lower overpotentials, as well as higher FAOR catalytic activities for SnO_2@Pd NCs. In summary, our electrochemical and spectroscopic data suggest a bifunctional reaction mechanism in which SnO_2 promotes the oxidation of CO residues close to the Pd surface, improving the catalytic performance of Pd toward formic acid oxidation. Consequently, the SnO_2@Pd NCs proposed here are promising candidates in order to achieve an optimum performance of formic acid fuel cells.

9.7 Supporting Information

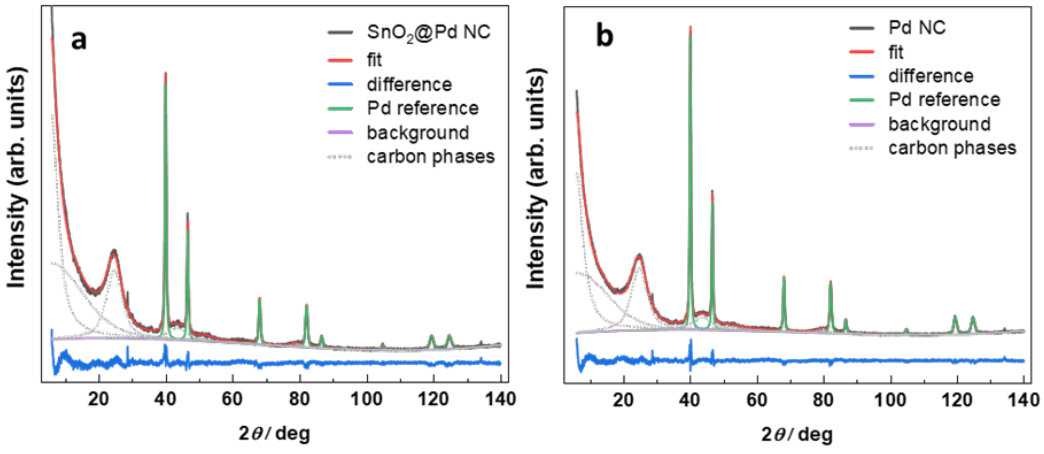

Supplementary Figure 9.7: XRD data refinements of (a) SnO_2@Pd NCs and (b) Pd NC.

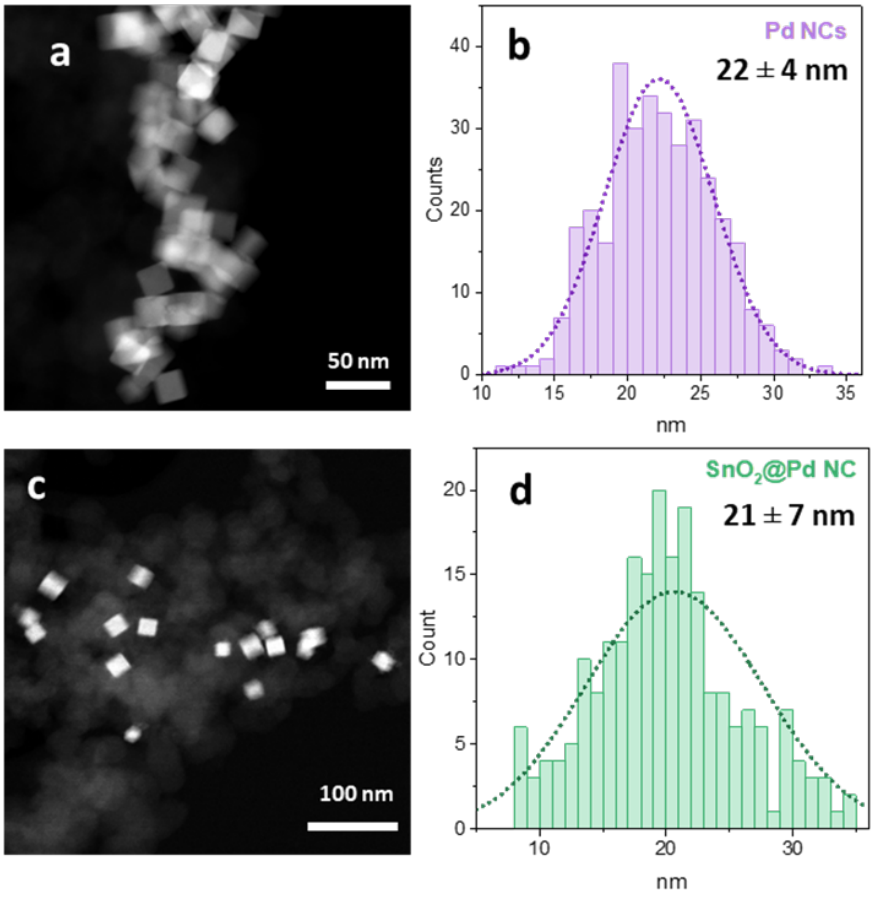

Supplementary Figure 9.8: STEM images (a,c) and corresponding histograms (b,d) of Pd NCs as prepared (a,b), and SnO_2@Pd NC as prepared (c, d).

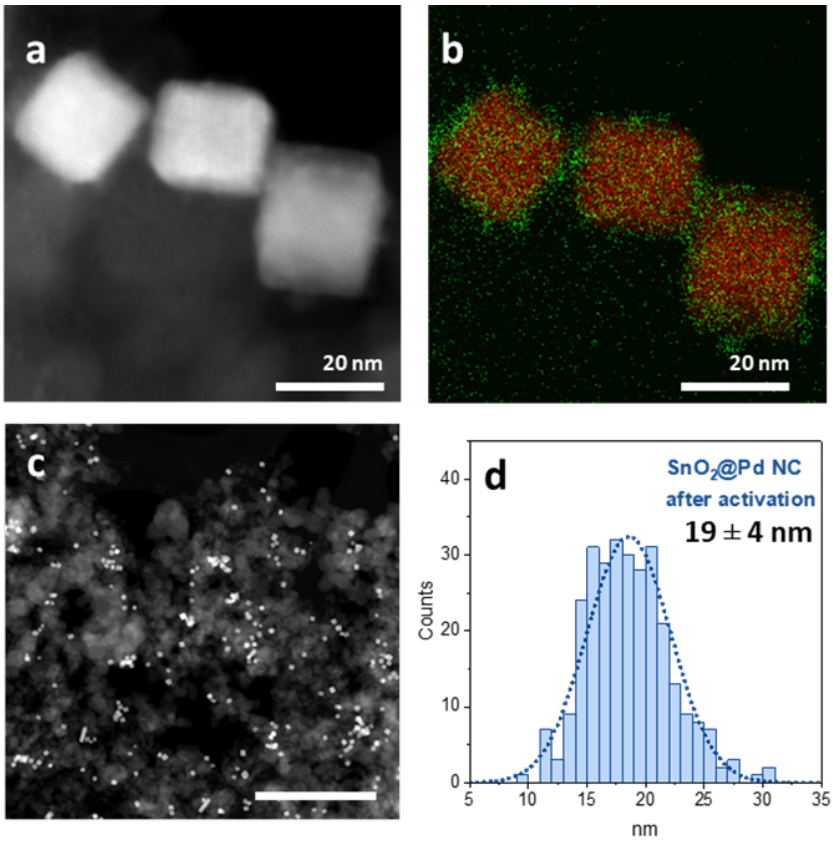

Supplementary Figure 9.9: (a) STEM image, (b) EDX map, (c) low magnification STEM image showing the particle distribution and the corresponding histogram (d) for SnO_2@Pd NCs after activation in 0.5 M $HClO_4$.

Supplementary Table 9.1: Pd and Sn content (%) in the SnO_2@Pd NCs extracted from TEM-EDX and XPS measurements of the as prepared NCs the same sample after activation in 0.5 M $HClO_4$, after cycling in 0.5 M $HClO_4$ + 0.5 M HCOOH and after chronoamperometric FAOR reaction for 3 h.

Content ratios (%)	**EDX**		**XPS**	
	Pd	**Sn**	**Pd**	**Sn**
SnO_2@Pd NC as prepared	96	4	75	25
SnO_2@Pd NC after activation	97	3	72	28
SnO_2@Pd NC after FAOR (cycling)	99	1	75	25
SnO_2@Pd NC after FAOR (chrono)	98	2	84	16

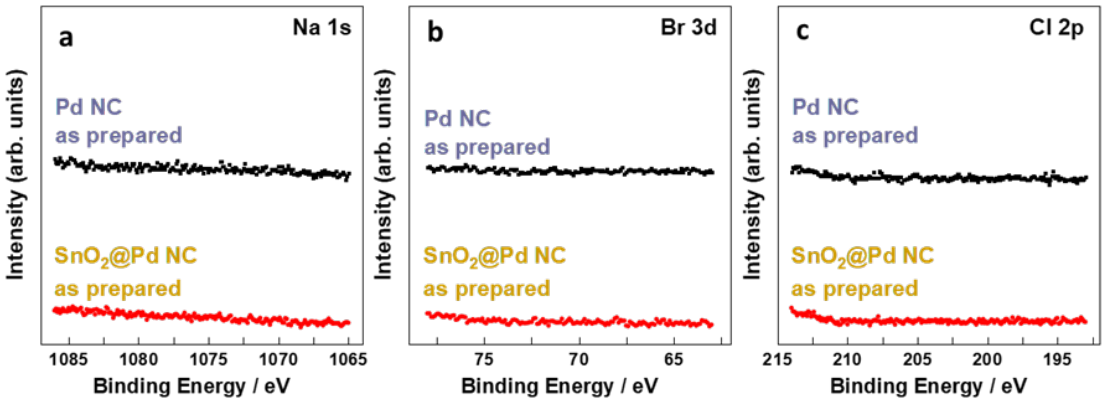

Supplementary Figure 9.10: XPS spectra of the (a) Na 1s, (b) Br 3d and (c) Cl 2p core levels of as-prepared SnO_2@Pd NCs (bottom) and Pd NCs (top).

Supplementary Note 9.7: EXAFS fitting details The Pd K-edge EXAFS data were aligned and normalized using the Athena software.[181] Conventional least-square fitting was performed using the FEFFIT code (Figure S5).[317] We have found that the 1st shell contribution to the experimental EXAFS data in all samples can be modeled with a single Pd-Pd contribution. Theoretical phases and amplitudes were obtained in self-consistent ab-initio calculations with the FEFF8.5 code for the bulk fcc-type Pd structure.[205] The complex exchange-correlation Hedin-Lundqvist potential and default values of muffin-tin radii as provided within the FEFF8.5 code were employed.

The amplitude reduction factor $S_0^2 = 0.77$ was obtained from the fit of the Pd K-edge EXAFS for the Pd foil. Fitting of the EXAFS spectra $[\chi(k)k^2]$ was carried out in R-space in the range from $R_{\text{min}} = 1.2$ Å up to $R_{\text{max}} = 3.0$ Å. The Fourier transform was carried out in the k range from 2.4 Å^{-1} up to 12.0 Å^{-1}. Fitting parameters were the Pd-Pd coordination numbers $N_{\text{Pd-Pd}}$, Pd-Pd interatomic distance $R_{\text{Pd-Pd}}$, disorder factor $\sigma^2_{\text{Pd-Pd}}$, as well as a correction to the photoelectron energy origin ΔE_0. The values of the parameters obtained in the fit are summarized in Table S2.

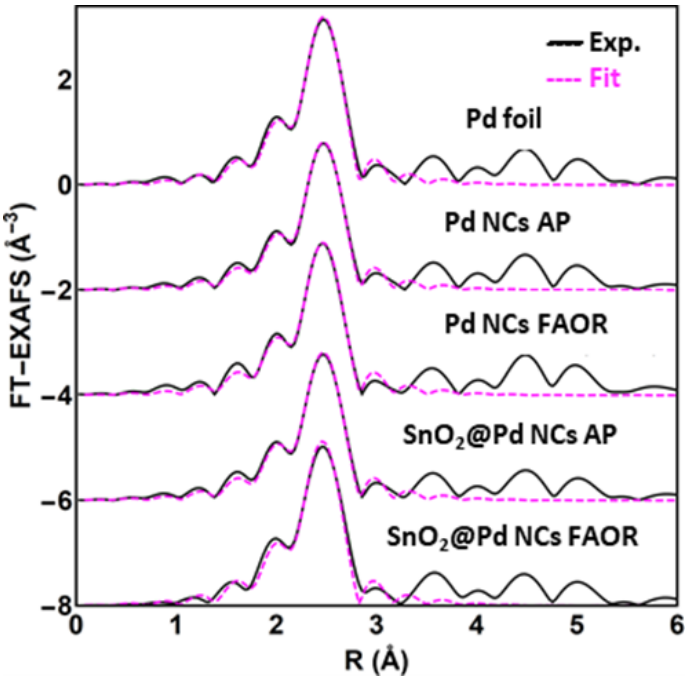

Supplementary Figure 9.11: EXAFS fitting results for Pd foil, Pd NCs and Sn@Pd NCs in the as prepared state and during FAOR.

Supplementary Table 9.2: Structure parameters (1st nearest neighbour Pd-Pd coordination number N, Pd-Pd interatomic distance $\langle r \rangle$, disorder factor σ^2, energy shifts ΔE_0, and goodness of fit parameters ("R-factor")), obtained from the fit of experimental EXAFS data of the Pd K-edge. Uncertainties of the last digit are given in parentheses. The data were measured during FAOR.

Sample	$\mathbf{N_{Pd\text{-}Pd}}$	$\langle r \rangle_{\mathbf{Pd\text{-}Pd}}$	$\sigma^2_{\mathrm{Pd-Pd}}$	ΔE_0 **(eV)**	R-factor
Pd foil	12	2.734(2)	0.0052(4)	-9.3(5)	0.5%
Pd NC (air)	10.7 (8)	2.734(3)	0.0053(4)	-9.4(5)	0.8%
Pd NC (FAOR)	11.2 (7)	2.738(2)	0.0054(4)	-9.8(4)	0.5%
SnO_2@Pd NC (air)	11.0 (6)	2.736(2)	0.0055(3)	-9.5(4)	0.4%
SnO_2@Pd NC (FAOR)	12(1)	2.731(5)	0.0052(4)	-9.8(8)	1.8%

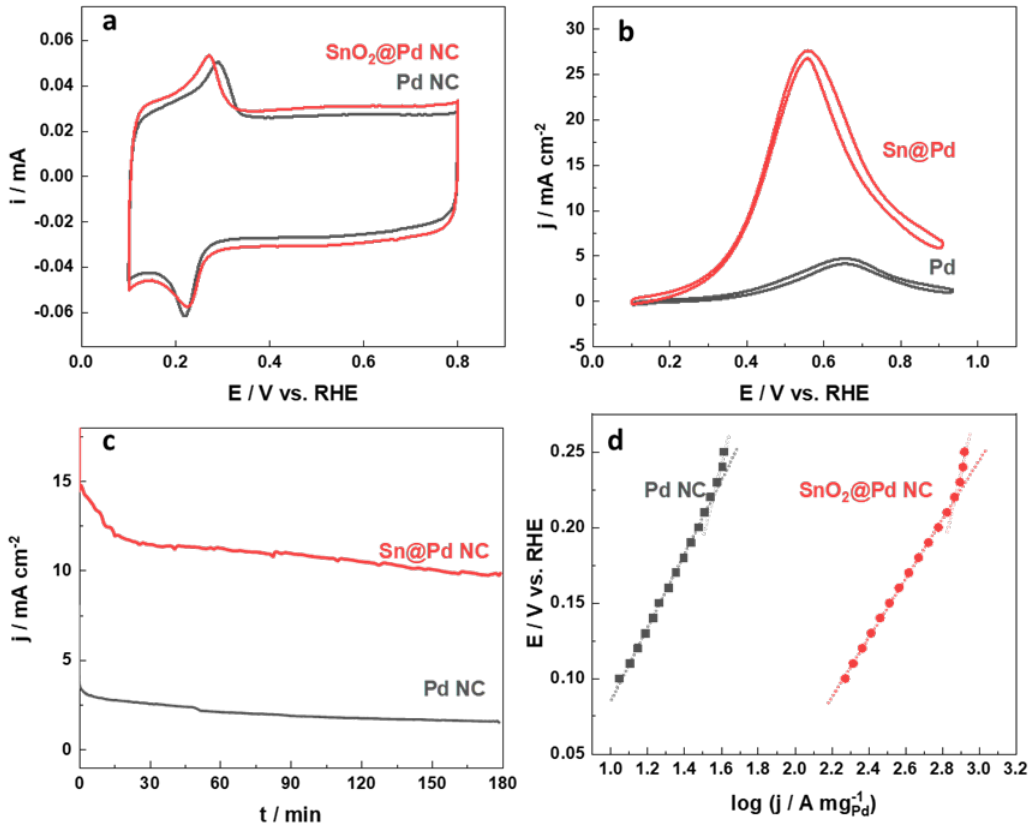

Supplementary Figure 9.12: (a) Cyclic voltammograms of SnO_2@Pd NCs and Pd NCs in 0.5 M H_2SO_4 at 50 mVs^{-1}. (b) Voltammetric profiles reported as specific activity of the SnO_2@Pd NC (red) and Pd NC (grey) in 0.5 M $HClO_4$ + 0.5 M HCOOH and at 50 mVs^{-1}. (c) Chronoamperometric curves of the SnO_2@Pd NC (red) and Pd NC (grey) at 0.45 V (line), reported as specific activities. (d) Tafel plots for SnO_2@Pd NC (red) and Pd (grey), with 196 $mVdec^{-1}$ and 470 $mVdec^{-1}$ for Pd NCs, and 274 $mVdec^{-1}$ and 524 $mVdec^{-1}$ for SnO_2@Pd NCs.

Supplementary Table 9.3: Electrochemical surface areas of the catalysts by CO stripping and the hydrogen desorption (H_{des}) in 0.5 M $HClO_4$.

ECSA	**CO stripping**	**H_{des}**
Pd NCs	0.263 cm^2	0.207 cm^2
SnO_2@Pd NCs	0.185 cm^2	0.173 cm^2

Supplementary Table 9.4: Electrocatalytic activities of FAOR on PdSn systems and their corresponding Pd electrocatalysts, including the peak current densities normalized by the mass, the corresponding peak potential, which were converted to RHE, and the ratio of the current densities reported for PdSn bimetallic systems versus pure Pd.

PdSn catalyst	PdSn catalyst Peak current density of PdSn (j/Amg^{-1})	Peak potential of PdSn vs. RHE	Pd catalyst reference	Pd catalyst Peak current density of (j/Amg^{-1})	Peak potential of Pd vs. RHE	PdSn:Pd ratio of peak current densities	Reaction conditions	Ref
Pd NC	–	–	–	0.42	0.65 V	–	0.5 M HCOOH, 0.1 M $HClO_4$	This work
SnO_2@Pd NC	2.46	0.55 V	Pd NC	0.42	0.65 V	5.8	0.5 M HCOOH, 0.1 M $HClO_4$	This work
Pd-Sn INN	0.55	0.39 V	Pd/C	0.1	0.40 V	5.6	0.5 M HCOOH, 0.5 M H_2SO_4	[265]
Pd_4Sn	0.85	0.40 V	Pd/C	0.21	0.40 V	4	0.5 M HCOOH, 0.5 M H_2SO_4	[263]
NCNs PdSn/	3	0.40 V	Pd/C	0.92	0.42 V	3.27	1 M HCOOH, 0.5 M H_2SO_4	[290]
MWCNT PdSn-	0.9	0.37 V	Pd/C	0.33	0.53 V	2.70	0.5 M HCOOH, 0.5 M H_2SO_4	[286]
SnO_2- islands/C	1.35	0.51 V	Pd/C	0.58	0.52 V	2.30	0.5 M HCOOH, 0.5 M H_2SO_4	[291]
Pd_2Sn_1	0.34	0.39 V	Pd/C	0.18	0.39 V	1.80	1 M HCOOH, 0.5 M H_2SO_4	[318]
Pd_2Sn_1/C								

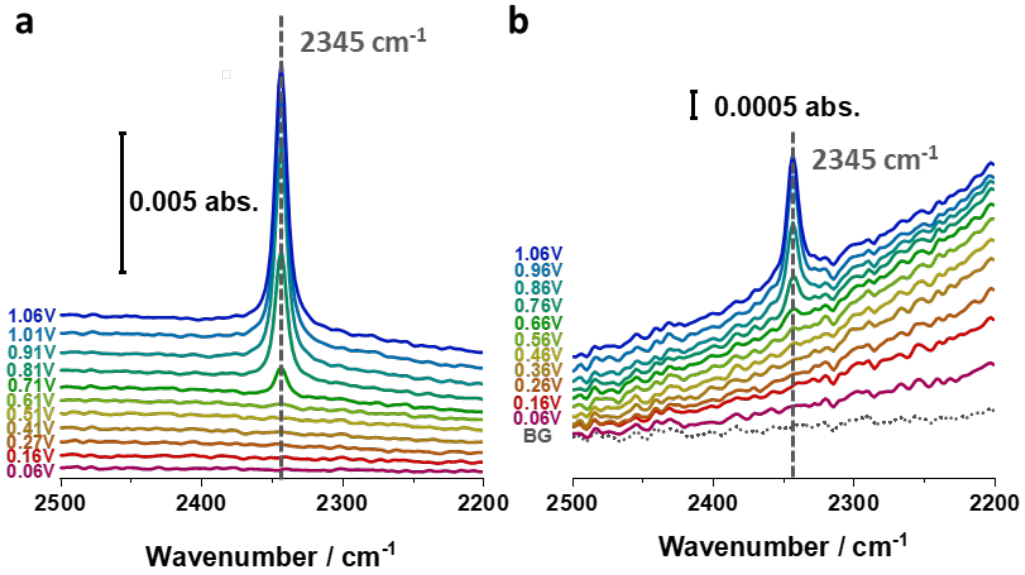

Supplementary Figure 9.13: (a) Cyclic voltammograms of SnO_2@Pd NCs and Pd NCs in 0.5 M H_2SO_4 at 50 mVs^{-1}. (b) Voltammetric profiles reported as specific activity of the SnO_2@Pd NC (red) and Pd NC (grey) in 0.5 M $HClO_4$ + 0.5 M HCOOH and at 50 mVs^{-1}. (c) Chronoamperometric curves of the SnO_2@Pd NC (red) and Pd NC (grey) at 0.45 V (line), reported as specific activities. (d) Tafel plots for SnO_2@Pd NC (red) and Pd (grey), with 196 $mVdec^{-1}$ and 470 $mVdec^{-1}$ for Pd NCs, and 274 $mVdec^{-1}$ and 524 $mVdec^{-1}$ for SnO_2@Pd NCs.

Summary and Outlook

10

Summary

This work addresses the relation of catalyst design and potential variations with pulses to its electrocatalytic performance. Primarily, shaped nanoparticles and their exposed facets were studied as catalysts for the Formic Acid Oxidation Reaction (FAOR) and the CO_2 reduction reaction (CO_2RR). The fundamental understanding of the role of specifically designed catalysts for these reactions are motivated by their huge potential of creating a closed carbon cycle. In particular, the CO_2RR has the capability to produce synthetic fuels and valuable chemicals out of CO_2 and renewable energy. Moreover, the FAOR can be used in fuel cells as alternative to proton exchange membrane fuel cells with the main advantage of avoiding storage and transportation problems that comes hand in hand using hydrogen has as direct fuel.

Although catalysts are not consumed during a catalytic reaction, they behave dynamically and adapt to the electrocatalytic reaction conditions. Thus, general questions arise on how these catalysts alter during an electrocatalytic reaction and how this changes affect the catalyst performance. This work focuses on studying the catalyst evolution during both reactions with *in situ* and *operando* spectroscopic methods. In doing so, structure-composition-activity correlations have been established. These correlations involve not only the preparation of the catalysts and their catalytic performance, but also the study of structural and compositional properties during the catalytic reaction both at static potentials as well as under pulsed conditions.

One scientific objective, objective **A**, questioning the role of undercoordinated Cu atoms has been addressed by studying the behavior of a Cu(310) surface with well defined (100) terraces and (110) steps. Upon the measurements performed, comparing a UHV-prepared sample with an electropolished one, we have found that the ethanol production is increased by electropolishing the sample, while only 1% ethanol was found for the pristine crystal. Thus, these results suggest that this type of step edges alone, combined with finite (100) terraces are not the main driver for ethanol formation as it has been suggested in prior literature from studies comparing rough electropolished single crystals with different orientations.

In objective **B**, the question was raised whether and how surface oxide species influence the catalytic selectivity. This challenge has been addressed by repetitive regeneration of oxide species on a Cu surface by the application of potential pulses with different pulse duration. Precisely, the catalytic activity depending on the potential pulse lengths was systematically studied and correlated to the results of *operando* Quick X-ray Absorption Fine Structure (QXAFS) and *operando* XRD measurements. Remarkably, a complex interplay between the reversible oxide formation and the catalytic function has been found. In particular, the product formation is partially improved when a highly disordered mix of Cu oxides is created on the surface. For instance, ethanol formation doubled with small amounts of disordered oxides are created and coexist with metallic Cu, while CO and CH_4 products are facilitated by extended bulk-like oxide phases. Further, the creation of Cu(II) species parallel to the formation of Cu(I), was demonstrated, revealing that non-equilibrium phases can be produced by the alternating potential pulses. The formation of both oxide types leads to high ratios of Cu(II)/Cu(I) species for short anodic pulses and this resulted in a boost of ethanol production. Complementary, *operando* XRD revealed the population of a distorted multivalent Cu oxide phase for the short anodic pulse lengths, which also plays a crucial role in the ethanol production.

This project highlights that, in addition to conventional methods, the catalytic activity of Cu catalysts for CO_2RR can be steered simply by the application of pulsed potential profiles. Furthermore, in order to understand the structure-activity relationships, the investigation of the observed catalytic changes by *operando* spectroscopic methods is essential. It is expected, that potential pulsing the CO_2RR will provide further understanding on the underlying structural dependencies on the catalytic activity.

Objectives **C** and **D** query how shaped NP pre-catalysts combined with a secondary metal enhance the catalysis. To answer this question, studies on cubic shaped Cu_2O NC decorated with Au NPs for the CO_2RR and cubic shaped Pd NCs decorated with a SnO_2 shell for the FAOR have been performed.

The catalytic improvement, in particular the selectivity trends towards C_{2+} products for the former catalytic system, was studied as a function of Au loading. The role of Cu-Au alloying and the CO coverage on the catalytic surface was investigated and their synergistic effects on the product selectivity were investigated. The compositional changes were studied under reaction conditions with *operando* high-energy XRD, *operando* XAFS and quasi *in situ* XPS, while CO coverages were assessed by *operando* surface enhanced Raman Spectroscopy (SERS). We have determined that increasing amounts of Au NPs on the Cu_2O NC leads to significant surface restructuring and the formation of CuAu alloys. Additionally, the *CO coverage on the surface is guided in a positive trend with increasing Au loading. These results of alloy type

and amount, the temporal changes under reaction conditions and the CO coverages were then correlated to the product selectivities. The CO formation is enhanced significantly with Au loading, but we observed that only small amounts of CO producing Au on a Cu surface are needed to boost the C_{2+} products. We attribute the low Cu-Au alloy formation due to small Au loadings to the formation of CO, while the formation of C_{2+} products is mainly performed on the pure Cu phase.

To study Objectives **C** and **D** for the FAOR, SnO_2@Pd NC were synthesized to enhance the catalytic performance of Pd(100), which is considered the best Pd facet to promote this reaction. The additional improvement was done by adding SnO_2-like species, which reactivate the catalytic active Pd species through the removal of poisoning CO from the surface. Combining electrocatalytic methods with microscopic characterization and *in situ* as well as *operando* spectroscopy reveals the beneficial effect of the secondary metal with a stable catalyst structure during the reaction. The lower CO desorption potentials are correlated to the lower overpotentials and the 5.8-fold higher catalytic activity compared to bare Pd NCs. We attribute these results to a bifunctional mechanism, where SnO_2 in the vicinity of the catalytically active Pd species promotes the oxidation of the poisoning CO intermediates.

All addressed objectives highlight the requirement of *in situ* and *operando* spectroscopic methods to understand structure-composition-activity correlations during reaction conditions. We observe structural and compositional changes, as well as alterations of the intermediates at the catalytic surface that are affecting the catalytic properties during the reactions. Furthermore, the careful selection of the type and amount of a co-catalyst is crucial to improve catalytic reactions through a "synthesis-by-design" approach. Both catalysts are examples for a deeper comprehension of combining several well-known effects together, such as shaping the catalyst, adding a co-catalyst or performing *in situ* and *operando* studies.

11

Future Challenges and Objectives

Research goals in CO_2RR

Research and development in CO_2RR has attracted great attention due to its high potential to innovate the synthesis of CO_2 neutral fuels and valuable chemicals. It is as well considered as storage solution for renewable electricity. Despite the huge efforts in advancing the overall mechanistic comprehension of this reaction, many challenges remain:

- **Fundamental Research:** Full understanding of the fundamental mechanism(s) underlying this reaction is indispensable to design catalysts, which generate the desired products. Here, significant progress can be made by studying well defined model catalysts, e.g. single crystals. Although, studies on copper single crystals have been performed from early on,[23] different preparation methods have led to varying starting surfaces and thus varying results. Thus, it is a current research question to study the CO_2RR with close-to-perfect facetted Cu surfaces. Not only low-index surfaces, but also high-index surfaces should be considered, the latter to understand the role of specific step edge structures. The goal is to create a picture on the role of each unique surface structure and extract mechanistic insight of the possible pathways to the wanted products.

  Furthermore, new fundamental research questions arise from the needs of lab-scale reactions or industrial scale up. Among the mentioned challenges below, this involves fundamental studies on well-defined bimetallic systems or the effect of variations in the reaction conditions, e.g. potential pulses on well-defined surfaces.

  It is further necessary to investigate the micro-environment around the catalyst, involving the electrolyte, and thus the local pH or the local concentrations of ions, as well as potential variatios.

- **Lab-scale Reactions:** The found fundamental insights have to be transferred to the

device level with more applicability. Moreover, several structural effects can only be found by preparing catalysts with higher surface areas and higher surface-to-volume ratios and thus with increased currents and optimized material utilization. Here, a focus is set on screening nanoparticular catalysts, applying currents $>100\,\mathrm{mA\,cm^{-2}}$ and deducing structure-activity correlations. In order to really understand structural effects and parameters, experimental techniques that can be applied under realistic *operando* conditions, are needed.

Cu_2O NCs have been studied in this thesis towards understanding the role of oxides on the product distribution by applying pulsed potentials. Although, this work sets a fundamental basis, the parameter range is not yet exhausted. It is expected that different chosen cathodic and anodic potentials, galvanostatic pulses, different catalysts or a variation in the catalyst loading may lead to other interesting product distributions with different mechanisms. Current research questions involve the role of adsorbed hydroxide through potential pulses and the influence on particle dissolution and readsorption on the product distribution.

Further research questions for Au-Cu_2O NCs include the minimization of the Au-loading towards a more beneficial effect of the CO-producing Au at the vicinity of pure Cu sites to increase the C_{2+} product yield. Moreover, pulsed potentials and bimetallic catalytic systems could be combined to study the reversibility of the alloyed structure during potential pulses and investigate this effect through the a wide parameter range (potentials, time lengths, Au loading).

- **Industrial Scale-Up:** The development of reactor systems and catalysts for industrial scale-up and commercialization is yet in its early stage. Key parameters comprise the operation time, stability, product selectivity and scalability of the chosen catalysts. Moreover, the energy efficiency including product separation and single pass consumption of CO_2 has to be established from a techno-economic perspective. Many challenges will still arise during the development of industrially-scaled systems, such as the tolerance to realistic gas feeds as well as the variation or interruption of the power inputs.[319] Finally, the integration of the CO_2RR into the processes of chemical industry, will probably lead to new and unforeseen challenges.

Research goals in the FAOR

Formic acid (FA) is considered as power source in fuel cells for portable devices due to its superior properties than other fuels (methanol or hydrogen), which are, amongst others, its

relatively easy handling in storage and transportation.[114] However, commercialization has not been achieved inter alia due to its fast catalyst deactivation, the high overpotentials required, the high catalyst costs and high production costs of the fuel FA:[115]

- **Fundamental Research:** The knowledge about the catalytic mechanism has come far in the past years, however, several issues remain regarding the degradation and deactivation mechanism of the catalysts. In particular, SnO_2@Pd NCs is a promising catalyst system, which circumvents the rapid deactivation. However, it is still prone to deactivation, which raises the question, whether structural or compositional rearrangements, such as a more homogeneous distribution of Sn^{4+} on the Pd(100) surface, other chemical states of Sn or even (partial) alloy formation, would further improve the performance. Furthermore, it is necessary to continue the studies of the structural evolution of the catalysts during reaction conditions. Moreover, a step towards commercially applicable devices is to investigate the catalyst response on varying reaction conditions, such as turning the device on or off, a decreasing input of the fuel or decreasing cell voltage. Thus, further *in situ* and *operando* studies to understand structural changes as well as dissolution or particle agglomeration with different high-performance catalytic systems and under different reaction conditions are needed.

- **Industrial Scale-Up:** The development of commercially available DFAFCs has been pursued since about 15 years, but so far without official statement on the results.[320] Not only the above mentioned challenges, but also the realistic dynamic power demands of portable devices might have challenged the development. However, the potential benefits of DFAFCs and the recent research and development in catalysts and fuel cells should motivate to achieve commercialization.

Bibliography

[1] N. O. (NOAA), A. Administration, Global Monitoring Laboratory - Carbon Cycle Greenhouse Gases.
[2] C. P. Morice, J. J. Kennedy, N. A. Rayner, P. D. Jones, *Journal of Geophysical Research Atmospheres* **2012**, *117*, DOI 10.1029/2011JD017187.
[3] A. A. Lacis, G. A. Schmidt, D. Rind, R. A. Ruedy, *Science* **2010**, *330*, 356–359.
[4] Arias, P.A., N. Bellouin, E. Coppola, G. R.G. Jones, J. Krinner, V. Marotzke, M. Naik, G.-K. Palmer, J. Plattner, M. Rogelj, J. Rojas, T. Sillmann, P. Storelvmo, B. Thorne, K. Trewin, B. Achuta Rao, R. Adhikary, K. Allan, G. Armour, R. Bala, S. Barimalala, J. Berger, C. Canadell, A. Cassou, W. Cherchi, W. Collins, S. Collins, S. Connors, F. Corti, F. Cruz, C. Dentener, A. Dereczynski, A. Di Luca, Niang, D. F.J., A. Doblas-Reyes, H. Dosio, F. Douville, V. Engelbrecht, E. Eyring, P. Fischer, B. Forster, J. Fox-Kemper, J.S. Fuglestvedt, N. Fyfe, L. Gillett, I. Goldfarb, R. Gorodetskaya, J.M. Gutierrez, E. Hamdi, H. Hawkins, P. Hewitt, A. Hope, C. Islam, D. Jones, R. Kaufman, Y. Kopp, J. Kosaka, S. Kossin, J.-Y. Krakovska, J. Lee, T. Li, T. Mauritsen, M. Maycock, S.-K. Meinshausen, P. Min, T. Monteiro, F. Ngo-Duc, I. Otto, A. Pinto, K. Pirani, R. Raghavan, Ranasinghe, A. Ruane, J.-B. L. Ruiz, B. Sallée, S. Samset, S. Sathyendranath, S. Seneviratne, A.A. Sörensson, I. Szopa, A.-M. Takayabu, B. Tréguier, R. van den Hurk, K. Vautard, V. Schuckmann, S. Zaehle, X. Zhang, K. Zickfeld in *Climate Change 2021: The Physical Science Basis. Contribution of Working Group I to the Sixth Assessment Report of the Intergovernmental Panel on Climate Change*, Cambridge University Press, Cambridge, United Kingdom and New York, NY, USA, **2021**, pp. 33–144.
[5] Smil Vaclav, *Energy Transitions: Global and National Perspectives, 2nd Edition*, **2017**, p. 296.
[6] BPstats, BP Statistical Review of World Energy 2022, tech. rep. June, **2022**.
[7] European Union, Energy roadmap 2050 Energy, tech. rep., **2012**, pp. 1–20.
[8] International Renewable Energy Agency, *Renewable Power Generation Costs in 2019*, **2020**, p. 160.
[9] Report of the Basic Energy Sciences Roundtable on Liquid Solar Fuels, tech. rep., Rockville, Maryland, **2019**.
[10] S. Fawzy, A. I. Osman, J. Doran, D. W. Rooney, *Environmental Chemistry Letters* **2020**, *18*, 2069–2094.
[11] J. Eppinger, K.-W. Huang, *ACS Energy Lett* **2017**, *2*, 188–195.
[12] J. Song, Z. Hao, K. Zhang, Z. Yan, J. Chen, *Angewandte Chemie* **2021**, *133*, 20795–20816.
[13] E. W. Lees, B. A. Mowbray, F. G. Parlane, C. P. Berlinguette, *Nature Reviews Materials* **2022**, *7*, 55–64.
[14] Y. Hori, K. Kikuchi, S. Suzuki, *Laboratory Techniques in Biochemistry and Molecular Biology* **1985**, *20*, 5–51.
[15] Y. Hori, K. Kikuchi, A. Murata, S. Suzuki, *Chemistry Letters* **1986**, *15*, 897–898.
[16] J. C. S O C, C. Commun, **1988**.
[17] Y. Hori, A. Murata, R. Takahashi, S. Suzuki, *Journal of the American Chemical Society* **1987**, *109*, 5022–5023.
[18] Y. Hori, A. Murata, R. Takahashi, *Journal of the Chemical Society Faraday Transactions 1: Physical Chemistry in Condensed Phases* **1989**, *85*, 2309–2326.
[19] Y. Hori, H. Wakebe, T. Tsukamoto, O. Koga, *Electrochimica Acta* **1994**, *39*, 1833–1839.
[20] Y. Hori, A. Murata, T. Tsukamoto, H. Wakebe, O. Koga, H. Yamazaki, *Electrochimica Acta* **1994**, *39*, 2495–2500.
[21] Y. Hori, O. Koga, H. Yamazaki, T. Matsuo, *Electrochimica Acta* **1995**, *40*, 2617–2622.
[22] Y. Hori, H. Wakebe, T. Tsukamoto, O. Koga, *Surface Science* **1995**, *335*, 258–263.
[23] Y. Hori, I. Takahashi, O. Koga, N. Hoshi, *Journal of Physical Chemistry B* **2002**, *106*, 15–17.
[24] I. Takahashi, O. Koga, N. Hoshi, Y. Hori, *Journal of Electroanalytical Chemistry* **2002**, *533*, 135–143.
[25] Y. Hori, I. Takahashi, O. Koga, N. Hoshi, *Journal of Molecular Catalysis A: Chemical* **2003**, *199*, 39–47.
[26] N. Hoshi, M. Kuroda, Y. Hori, *Journal of Electroanalytical Chemistry* **2002**, *521*, 155–160.
[27] S. Nitopi, E. Bertheussen, S. B. Scott, X. Liu, A. K. Engstfeld, S. Horch, B. Seger, I. E. Stephens, K. Chan, C. Hahn, J. K. Nørskov, T. F. Jaramillo, I. Chorkendorff, *Chemical Reviews* **2019**, *119*, 7610–7672.
[28] A. Bagger, W. Ju, A. S. Varela, P. Strasser, J. Rossmeisl, *ChemPhysChem* **2017**, *18*, 3266–3273.

[29] K. P. Kuhl, T. Hatsukade, E. R. Cave, D. N. Abram, J. Kibsgaard, T. F. Jaramillo, *Journal of the American Chemical Society* **2014**, *136*, 14107–14113.
[30] K. P. Kuhl, E. R. Cave, D. N. Abram, T. F. Jaramillo, *Energy and Environmental Science* **2012**, *5*, 7050–7059.
[31] C. Zhan, F. Dattila, C. Rettenmaier, A. Bergmann, S. Kühl, R. García-Muelas, N. López, B. Roldan Cuenya, *ACS Catalysis* **2021**, *11*, 7694–7701.
[32] J. Kim, J. T. Song, J. Oh, *Journal of Chemical Physics* **2020**, *153*, 0–6.
[33] Z. Wang, Y. Li, J. Boes, Y. Wang, E. Sargent, **2020**, DOI 10.21203/rs.3.rs-66715/v1.
[34] X. Chang, A. Malkani, X. Yang, B. Xu, *Journal of the American Chemical Society* **2020**, *142*, 2975–2983.
[35] E. L. Clark, A. T. Bell, *Journal of the American Chemical Society* **2018**, *140*, 7012–7020.
[36] Y. Zheng, A. Vasileff, X. Zhou, Y. Jiao, M. Jaroniec, S. Z. Qiao, *Journal of the American Chemical Society* **2019**, *141*, 7646–7659.
[37] S. Wang, T. Kou, S. E. Baker, E. B. Duoss, Y. Li, *Advanced Energy and Sustainability Research* **2022**, *3*, 2100131.
[38] L. Fan, C. Xia, F. Yang, J. Wang, H. Wang, Y. Lu, *Science Advances* **2020**, *6*, DOI 10.1126/SCIADV.AAY3111/ASSET/66053D8E-1B71-4E90-920B-41E8C3EF29AD/ASSETS/GRAPHIC/AAY3111-F8.JPEG.
[39] D. Ren, J. Fong, B. S. Yeo, *Nature Communications* **2018**, *9*, 1–8.
[40] Y. Hori, R. Takahashi, Y. Yoshinami, A. Murata, *Journal of Physical Chemistry B* **1997**, *101*, 7075–7081.
[41] R. Reske, H. Mistry, F. Behafarid, B. Roldan Cuenya, P. Strasser, *Journal of the American Chemical Society* **2014**, *136*, 6978–6986.
[42] A. Loiudice, P. Lobaccaro, E. A. Kamali, T. Thao, B. H. Huang, J. W. Ager, R. Buonsanti, *Angewandte Chemie* **2016**, *128*, 5883–5886.
[43] C. Hahn, T. Hatsukade, Y. G. Kim, A. Vailionis, J. H. Baricuatro, D. C. Higgins, S. A. Nitopi, M. P. Soriaga, T. F. Jaramillo, *Proceedings of the National Academy of Sciences of the United States of America* **2017**, *114*, 5918–5923.
[44] F. S. Roberts, K. P. Kuhl, A. Nilsson, *Angewandte Chemie* **2015**, *127*, 5268–5271.
[45] D. Gao, I. Zegkinoglou, N. J. Divins, F. Scholten, I. Sinev, P. Grosse, B. Roldan Cuenya, *ACS Nano* **2017**, *11*, 4825–4831.
[46] H. Mistry, A. S. Varela, C. S. Bonifacio, I. Zegkinoglou, I. Sinev, Y. W. Choi, K. Kisslinger, E. A. Stach, J. C. Yang, P. Strasser, B. R. Cuenya, *Nature Communications* **2016**, *7*, 1–8.
[47] H. S. Jeon, S. Kunze, F. Scholten, B. Roldan Cuenya, *ACS Catalysis* **2018**, *8*, 531–535.
[48] R. G. Mariano, K. McKelvey, H. S. White, M. W. Kanan, *Science* **2017**, *358*, 1187–1192.
[49] H. Mistry, A. S. Varela, S. Kühl, P. Strasser, B. R. Cuenya, *Nature Reviews Materials* **2016**, *1*, 16609.
[50] X. Wang, A. S. Varela, A. Bergmann, S. Kühl, P. Strasser, *ChemSusChem* **2017**, *10*, 4642–4649.
[51] D. Kim, C. S. Kley, Y. Li, P. Yang, *Proceedings of the National Academy of Sciences of the United States of America* **2017**, *114*, 10560–10565.
[52] K. Manthiram, B. J. Beberwyck, A. P. Alivisatos, *Journal of the American Chemical Society* **2014**, *136*, 13319–13325.
[53] D. Kim, C. Xie, N. Becknell, Y. Yu, M. Karamad, K. Chan, E. J. Crumlin, J. K. Nørskov, P. Yang, *Journal of the American Chemical Society* **2017**, *139*, 8329–8336.
[54] H. Mistry, R. Reske, P. Strasser, B. Roldan Cuenya, *Catalysis Today* **2017**, *288*, 30–36.
[55] P. Grosse, D. Gao, F. Scholten, I. Sinev, H. Mistry, B. Roldan Cuenya, *Angewandte Chemie* **2018**, *130*, 6300–6305.
[56] O. Baturina, Q. Lu, F. Xu, F. Xu, B. Dyatkin, X. Sang, R. Unocic, T. Brintlinger, Y. Gogotsi, *Catalysis Today* **2017**, *288*, 2–10.
[57] D. Ren, B. S. H. Ang, B. S. Yeo, *ACS Catalysis* **2016**, *6*, 8239–8247.
[58] S. Lee, G. Park, J. Lee, *ACS Catalysis* **2017**, *7*, 8594–8604.
[59] Y. Lum, J. W. Ager, *Energy and Environmental Science* **2018**, *11*, 2935–2944.
[60] M. Dunwell, Q. Lu, J. M. Heyes, J. Rosen, J. G. Chen, Y. Yan, F. Jiao, B. Xu, *Journal of the American Chemical Society* **2017**, *139*, 3774–3783.
[61] S. Zhu, B. Jiang, W. B. Cai, M. Shao, *Journal of the American Chemical Society* **2017**, *139*, 15664–15667.
[62] D. Gao, F. Scholten, B. Roldan Cuenya, *ACS Catalysis* **2017**, *7*, 5112–5120.

[63] A. S. Varela, W. Ju, T. Reier, P. Strasser, *ACS Catalysis* **2016**, *6*, 2136–2144.
[64] M. R. Singh, Y. Kwon, Y. Lum, J. W. Ager, A. T. Bell, *Journal of the American Chemical Society* **2016**, *138*, 13006–13012.
[65] K. J. P. Schouten, E. Pérez Gallent, M. T. Koper, *Journal of Electroanalytical Chemistry* **2014**, *716*, 53–57.
[66] M. Todoroki, K. Hara, A. Kudo, T. Sakata, *Journal of Electroanalytical Chemistry* **1995**, *394*, 199–203.
[67] O. Melchaeva, P. Voyame, V. C. Bassetto, M. Prokein, M. Renner, E. Weidner, M. Petermann, A. Battistel, *ChemSusChem* **2017**, *10*, 3660–3670.
[68] Z. Tang, E. Nishiwaki, K. E. Fritz, T. Hanrath, J. Suntivich, *ACS Applied Materials and Interfaces* **2021**, *13*, 14050–14055.
[69] M. Ramdin, A. R. Morrison, M. De Groen, R. Van Haperen, R. De Kler, L. J. Van Den Broeke, J. P. Martin Trusler, W. De Jong, T. J. Vlugt, *Industrial and Engineering Chemistry Research* **2019**, *58*, 1834–1847.
[70] S. C. Perry, P. ki Leung, L. Wang, C. Ponce de León, Developments on carbon dioxide reduction: Their promise, achievements, and challenges, **2020**.
[71] J. Timoshenko, A. Bergmann, C. Rettenmaier, A. Herzog, R. M. Arán-Ais, H. S. Jeon, F. T. Haase, U. Hejral, P. Grosse, S. Kühl, E. M. Davis, J. Tian, O. Magnussen, B. Roldan Cuenya, *Nature Catalysis* **2022**, *5*, 259–267.
[72] D. Gao, R. M. Arán-Ais, H. S. Jeon, B. Roldan Cuenya, *Nature Catalysis* **2019**, *2*, 198–210.
[73] R. M. Arán-Ais, D. Gao, B. Roldan Cuenya, *Accounts of Chemical Research* **2018**, *51*, 2906–2917.
[74] J. Du, P. Zhang, H. Liu, *Chemistry – An Asian Journal* **2021**, *16*, 588–603.
[75] Y. Pei, H. Zhong, F. Jin, *Energy Science and Engineering* **2021**, *9*, 1012–1032.
[76] K. W. J. FRESE, *ChemInform* **2010**, *24*, no–no.
[77] J. Christophe, T. Doneux, C. Buess-Herman, *Electrocatalysis* **2012**, *3*, 139–146.
[78] Y. Huang, A. D. Handoko, P. Hirunsit, B. S. Yeo, *ACS Catalysis* **2017**, *7*, 1749–1756.
[79] K. Jiang, R. B. Sandberg, A. J. Akey, X. Liu, D. C. Bell, J. K. Nørskov, K. Chan, H. Wang, *Nature Catalysis* **2018**, *1*, 111–119.
[80] F. Scholten, K. L. C. Nguyen, J. P. Bruce, M. Heyde, B. Roldan Cuenya, *Angewandte Chemie - International Edition* **2021**, *60*, 19169–19175.
[81] K. J. P. Schouten, E. Pérez Gallent, M. T. Koper, *ACS Catalysis* **2013**, *3*, 1292–1295.
[82] A. Verdaguer-Casadevall, C. W. Li, T. P. Johansson, S. B. Scott, J. T. McKeown, M. Kumar, I. E. Stephens, M. W. Kanan, I. Chorkendorff, *Journal of the American Chemical Society* **2015**, *137*, 9808–9811.
[83] G. H. Simon, C. S. Kley, B. Roldan Cuenya, *Angewandte Chemie International Edition* **2021**, *60*, 2561–2568.
[84] G. L. De Gregorio, T. Burdyny, A. Loiudice, P. Iyengar, W. A. Smith, R. Buonsanti, *ACS Catalysis* **2020**, *10*, 4854–4862.
[85] J. Wang, C. Liu, A. Lushington, N. Cheng, M. N. Banis, A. Riese, X. Sun, *Electrochimica Acta* **2016**, *210*, 285–292.
[86] P. Iyengar, J. Huang, G. L. De Gregorio, C. Gadiyar, R. Buonsanti, *Chemical Communications* **2019**, *55*, 8796–8799.
[87] J. E. Pander, D. Ren, Y. Huang, N. Wei Xian Loo, S. Hui Lee Hong, B. Siang Yeo, N. W. X. Loo, S. H. L. Hong, B. S. Yeo, *ChemElectroChem* **2018**, *5*, 219–237.
[88] M. Favaro, H. Xiao, T. Cheng, W. A. G. Iii, J. Yano, E. J. Crumlin, **2017**, *114*, 6706–6711.
[89] C. S. Le Duff, M. J. Lawrence, P. Rodriguez, *Angewandte Chemie* **2017**, *129*, 13099–13104.
[90] A. J. Garza, A. T. Bell, M. Head-Gordon, *Journal of Physical Chemistry Letters* **2018**, *9*, 601–606.
[91] D. Kim, C. S. Kley, Y. Li, P. Yang, *Proceedings of the National Academy of Sciences of the United States of America* **2017**, *114*, 10560–10565.
[92] R. Casebolt, K. Levine, J. Suntivich, T. Hanrath, *Joule* **2021**, *5*, 1987–2026.
[93] R. Shiratsuchi, Y. Aikoh, G. Nogami, *Journal of The Electrochemical Society* **1993**, *140*, 3479–3482.
[94] D. W. DeWulf, T. Jin, A. J. Bard, *Journal of The Electrochemical Society* **1989**, *136*, 1686–1691.
[95] B. Jermann, J. Augustynski, *Electrochimica Acta* **1994**, *39*, 1891–1896.
[96] J Yano, A. S. Yamasaki, *Journal of Applied Electrochemistry* **2008**, *38*, 1721–1726.

[97] A. Engelbrecht, C. Uhlig, O. Stark, M. Hämmerle, G. Schmid, E. Magori, K. Wiesner-Fleischer, M. Fleischer, R. Moos, *Journal of The Electrochemical Society* **2018**, *165*, J3059–J3068.
[98] K. W. Kimura, K. E. Fritz, J. Kim, J. Suntivich, H. D. Abruña, T. Hanrath, *ChemSusChem* **2018**, *11*, 1781–1786.
[99] S. C. Lin, C. C. Chang, S. Y. Chiu, H. T. Pai, T. Y. Liao, C. S. Hsu, W. H. Chiang, M. K. Tsai, H. M. Chen, *Nature Communications* **2020**, *11*, 3525.
[100] N. Gupta, M. Gattrell, B. Macdougall, Calculation for the cathode surface concentrations in the electrochemical reduction of CO2 in KHCO3 solutions, **2006**.
[101] C. Kim, L. C. Weng, A. T. Bell, *ACS Catalysis* **2020**, *10*, 12403–12413.
[102] B. Kumar, J. P. Brian, V. Atla, S. Kumari, K. A. Bertram, R. T. White, J. M. Spurgeon, *ACS Catalysis* **2016**, *6*, 4739–4745.
[103] J. M. Strain, S. Gulati, S. Pishgar, J. M. Spurgeon, *ChemSusChem* **2020**, *13*, 3028–3033.
[104] Y. Hori, *Modern Aspects of Electrochemistry* **2008**, 89–189.
[105] J. H. Montoya, C. Shi, K. Chan, J. K. Nørskov, *Journal of Physical Chemistry Letters* **2015**, *6*, 2032–2037.
[106] J. H. Montoya, A. A. Peterson, J. K. Nørskov, *ChemCatChem* **2013**, *5*, 737–742.
[107] A. Herzog, A. Bergmann, H. S. Jeon, J. Timoshenko, S. Kühl, C. Rettenmaier, M. Lopez Luna, F. T. Haase, B. Roldan Cuenya, *Angewandte Chemie - International Edition* **2021**, *60*, 7426–7435.
[108] H. S. Jeon, J. Timosnenko, F. Scholten, I. Sinev, A. Herzog, F. T. Haase, B. R. Cuenya, *Journal of the American Chemical Society* **2019**, *141*, 19879–19887.
[109] X. Wang, Q. Chen, Y. Zhou, H. Li, J. Fu, M. Liu, *Advanced Sensor and Energy Materials* **2022**, *1*, 100023.
[110] B. Talukdar, S. Mendiratta, M. H. Huang, C. H. Kuo, Recent Advances in Bimetallic Cu-Based Nanocrystals for Electrocatalytic CO2 Conversion, **2021**.
[111] D. Kim, J. Resasco, Y. Yu, A. M. Asiri, P. Yang, *Nature Communications* **2014**, *5*, 4948.
[112] C. G. Morales-Guio, E. R. Cave, S. A. Nitopi, J. T. Feaster, L. Wang, K. P. Kuhl, A. Jackson, N. C. Johnson, D. N. Abram, T. Hatsukade, C. Hahn, T. F. Jaramillo, *Nature Catalysis* **2018**, *1*, DOI 10.1038/s41929-018-0139-9.
[113] Y. Lum, J. W. Ager, *Energy and Environmental Science* **2018**, *11*, 2935–2944.
[114] Z. Fang, W. Chen, Recent advances in formic acid electro-oxidation: From the fundamental mechanism to electrocatalysts, **2021**.
[115] R. Bhaskaran, B. G. Abraham, R. Chetty, Recent advances in electrocatalysts, mechanism, and cell architecture for direct formic acid fuel cells, **2022**.
[116] O. A. Petrii, The Progress in Understanding the Mechanisms of Methanol and Formic Acid Electrooxidation on Platinum Group Metals (a Review), **2019**.
[117] T. Yang, S. Hou, J. Xing, C. Liu, J. Ge, W. Xing, Formic acid electro-oxidation: Mechanism and electrocatalysts design, **2022**.
[118] S. J. Folkman, J. González-Cobos, S. Giancola, I. Sánchez-Molina, J. R. Galán-Mascarós, Benchmarking catalysts for formic acid/formate electrooxidation, **2021**.
[119] V. Grozovski, F. J. Vidal-Iglesias, E. Herrero, J. M. Feliu, *ChemPhysChem* **2011**, *12*, 1641–1644.
[120] A. Capon, R. Parson, *Journal of Electroanalytical Chemistry and Interfacial Electrochemistry* **1973**, *44*, 1–7.
[121] A. Capon, R. Parsons, *Journal of Electroanalytical Chemistry and Interfacial Electrochemistry* **1973**, *44*, 239–254.
[122] B. Beden, A. Bewick, C. Lamy, *Journal of Electroanalytical Chemistry* **1983**, *150*, 505–511.
[123] C. T. Campbell, G Ertl, H Kuipers, J. Segner, *The Journal of Chemical Physics* **1980**, *73*, 5862–5873.
[124] Y. X. Chen, M. Heinen, Z. Jusys, R. J. Behm, *Angewandte Chemie - International Edition* **2006**, *45*, 981–985.
[125] A. Cuesta, G. Cabello, M. Osawa, C. Gutiérrez, *ACS Catalysis* **2012**, *2*, 728–738.
[126] Y. X. Chen, M. Heinen, Z. Jusys, R. J. Behm, *Langmuir* **2006**, *22*, 10399–10408.
[127] Z. Liu, X. Zhang, *Electrochemistry Communications* **2009**, *11*, 1667–1670.
[128] Z. Li, Y. Chen, S. Ji, Y. Tang, W. Chen, A. Li, J. Zhao, Y. Xiong, Y. Wu, Y. Gong, T. Yao, W. Liu, L. Zheng, J. Dong, Y. Wang, Z. Zhuang, W. Xing, C. T. He, C. Peng, W. C. Cheong, Q. Li, M. Zhang, Z. Chen, N. Fu, X. Gao, W. Zhu, J. Wan, J. Zhang, L. Gu, S. Wei, P. Hu,

J. Luo, J. Li, C. Chen, Q. Peng, X. Duan, Y. Huang, X. M. Chen, D. Wang, Y. Li, *Nature Chemistry* **2020**, *12*, 764–772.
[129] A. Cuesta, M. Escudero, B. Lanova, H. Baltruschat, *Langmuir* **2009**, *25*, 6500–6507.
[130] K. Jiang, H. X. Zhang, S. Zou, W. B. Cai, *Physical Chemistry Chemical Physics* **2014**, *16*, 20360–20376.
[131] J. Y. Wang, H. X. Zhang, K. Jiang, W. B. Cai, *Journal of the American Chemical Society* **2011**, *133*, 14876–14879.
[132] Y. Wang, Y. Qi, D. Zhang, C. Liu, *Journal of Physical Chemistry C* **2014**, *118*, 2067–2076.
[133] N. Hoshi, K. Kida, M. Nakamura, M. Nakada, K. Osada, *Journal of Physical Chemistry B* **2006**, *110*, 12480–12484.
[134] W. Zheng, J. Qu, X. Hong, K. Tedsree, S. C. E. Tsang, *ChemCatChem* **2015**, *7*, 3826–3831.
[135] S. I. Choi, J. A. Herron, J. Scaranto, H. Huang, Y. Wang, X. Xia, T. Lv, J. Park, H. C. Peng, M. Mavrikakis, Y. Xia, *ChemCatChem* **2015**, *7*, 2077–2084.
[136] X. Xia, S. I. Choi, J. A. Herron, N. Lu, J. Scaranto, H. C. Peng, J. Wang, M. Mavrikakis, M. J. Kim, Y. Xia, *Journal of the American Chemical Society* **2013**, *135*, 15706–15709.
[137] R. Zerdoumi, O. Matselko, L. Rößner, B. Sarkar, Y. Grin, M. Armbrüster, *Journal of the American Chemical Society* **2022**, *144*, 8379–8388.
[138] H. X. Liu, N. Tian, M. P. Brandon, J. Pei, Z. C. Huangfu, C. Zhan, Z. Y. Zhou, C. Hardacre, W. F. Lin, S. G. Sun, *Physical Chemistry Chemical Physics* **2012**, *14*, 16415–16423.
[139] M. Shao, J. Odell, M. Humbert, T. Yu, Y. Xia, *Journal of Physical Chemistry C* **2013**, *117*, 4172–4180.
[140] T. Gunji, F. Matsumoto, *Inorganics* **2019**, *7*, 36.
[141] T. Shen, J. Zhang, K. Chen, S. Deng, D. Wang, Recent Progress of Palladium-Based Electrocatalysts for the Formic Acid Oxidation Reaction, **2020**.
[142] A. Nilsson, L. G. Pettersson, B. Hammer, T. Bligaard, C. H. Christensen, J. K. Nørskov, *Catalysis Letters* **2005**, *100*, 111–114.
[143] W. Zhong, Y. Qi, M. Deng, *Journal of Power Sources* **2015**, *278*, 203–212.
[144] A. Romero Hernández, E. M. Arce Estrada, A. Ezeta, M. E. Manríquez, *Electrochimica Acta* **2019**, *327*, 134977.
[145] N Naresh, F. G. Wasim, B. P. Ladewig, M Neergat, *Journal of Materials Chemistry A* **2013**, *1*, 8553–8559.
[146] C. Rettenmaier, R. M. Aran-Ais, J. Timoshenko, R. Rizo, H. S. Jeon, S. Kühl, S. W. Chee, A. Bergmann, B. Roldan Cuenya, *ACS Catalysis* **2020**, *10*, 14540–14551.
[147] X. Wen, S. Lerch, Z. Wang, B. Aboudiab, A. R. Tehrani-Bagha, E. Olsson, K. Moth-Poulsen, *Langmuir* **2020**, *36*, 1745–1753.
[148] Y. Sun, L. Zhang, H. Zhou, Y. Zhu, E. Sutter, Y. Ji, M. H. Rafailovich, J. C. Sokolov, *Chemistry of Materials* **2007**, *19*, 2065–2070.
[149] J. Solla-Gullón, V. Montiel, A. Aldaz, J. Clavilier, *Journal of Electroanalytical Chemistry* **2000**, *491*, 69–77.
[150] F. J. Vidal-Iglesias, R. M. Arán-Ais, J. Solla-Gullón, E. Garnier, E. Herrero, A. Aldaz, J. M. Feliu, *Physical Chemistry Chemical Physics* **2012**, *14*, 10258–10265.
[151] W. H. Ke, C. F. Hsia, Y. J. Chen, M. H. Huang, *Small* **2016**, 3530–3534.
[152] A. W. Von Hofmann, *Introduction to Modern Chemistry, Experimental and Theoretic: Embodying Twelve Lectures Delivered in the Royal College of Chemistry, London*, Walton and Maberley, **1865**.
[153] A. Wuttig, Y. Surendranath, *ACS Catalysis* **2015**, *5*, 4479–4484.
[154] G. Inzelt, A. Lewenstam, F. Scholz, *Handbook of reference electrodes*, (Ed.: F. S. György Inzelt, Andrzej Lewenstam), Springer Berlin Heidelberg, **2013**, pp. 1–344.
[155] a Bard, L Faulkner, *Russian Journal of Electrochemistry* **2002**, *38*, 1505–1506.
[156] R. M. Arán-Ais, F. Scholten, S. Kunze, R. Rizo, B. Roldan Cuenya, *Nature Energy* **2020**, *5*, 317–325.
[157] K. W. Kimura, R. Casebolt, J. Cimada Dasilva, E. Kauffman, J. Kim, T. A. Dunbar, C. J. Pollock, J. Suntivich, T. Hanrath, *ACS Catalysis* **2020**, *10*, 8632–8639.
[158] R. Casebolt, K. W. Kimura, K. Levine, J. A. Cimada DaSilva, J. Kim, T. A. Dunbar, J. Suntivich, T. Hanrath, *ChemElectroChem* **2021**, *8*, 681–688.
[159] H. S. Jeon, J. Timoshenko, C. Rettenmaier, A. Herzog, A. Yoon, S. W. Chee, S. Oener, U. Hejral, F. T. Haase, B. Roldan Cuenya, *Journal of the American Chemical Society* **2021**, *143*, 7578–7587.

[160] J. Timoshenko, B. Roldan Cuenya, In Situ/ Operando Electrocatalyst Characterization by X-ray Absorption Spectroscopy, **2021**.
[161] J. J. Velasco-Vélez, C. H. Chuang, D. Gao, Q. Zhu, D. Ivanov, H. S. Jeon, R. Arrigo, R. V. Mom, E. Stotz, H. L. Wu, T. E. Jones, B. Roldan Cuenya, A. Knop-Gericke, R. Schlögl, *ACS Catalysis* **2020**, *10*, 11510–11518.
[162] S. Rudi, C. Cui, L. Gan, P. Strasser, *Electrocatalysis* **2014**, *5*, 408–418.
[163] H. A. Gasteiger, S. S. Kocha, B. Sompalli, F. T. Wagner, Activity benchmarks and requirements for Pt, Pt-alloy, and non-Pt oxygen reduction catalysts for PEMFCs, **2005**.
[164] K. J. Mayrhofer, D. Strmcnik, B. B. Blizanac, V. Stamenkovic, M. Arenz, N. M. Markovic, *Electrochimica Acta* **2008**, *53*, 3181–3188.
[165] W. Jorisch, *Vacuum Technology in the Chemical Industry* **2014**, 1–14.
[166] G. Binnig, H. Rohrer, *Surface Science* **1983**, *126*, 236–244.
[167] E. Meyer, R. Bennewitz, H. J. Hug, *Scanning Probe Microscopy The Lab on a Tip*, Second Edi, (Ed.: G. T. in Physics), **2021**.
[168] C. Bai, *Scanning tunneling microscopy and its application*, Springer Science and Business Media, **2000**.
[169] W. Moritz, *Atomic structures of surfaces and interfaces*, Elsevier, **2018**, pp. 55–58.
[170] T. Shirasawa, *Surface analysis | low-energy electron diffraction*, 3rd ed., Elsevier Inc., **2019**, pp. 365–373.
[171] D. P. Woodruff, *Methods of Surface Structure Determination*, **2016**, pp. 98–214.
[172] H. Ilbach, D. Roy, J. Carette, J. Kirschner, M. Henzler, B. Feuerbacher, B. Fitton, H. Froitzheim, *Electron Spectroscopy for Surface Analysis*, **1977**, 130ff.
[173] M. A. Bañares, M. O. Guerrero-Pérez, J. L. G. Fierro, G. G. Cortez, *Journal of Materials Chemistry* **2002**, *12*, 3337–3342.
[174] H. Hertz, *Annalen der Physik* **1887**, *267*, 983–1000.
[175] A. Einstein, *Annalen der Physik* **1905**, *322*, 549–560.
[176] a. D. Mc Naught, a Wilkinson, *Iupac* **2012**, 1670.
[177] M. Benfatto, C. Meneghini in *Synchrotron Radiation: Basics, Methods and Applications*, Springer Berlin Heidelberg, **2015**, pp. 213–240.
[178] J. J. Rehr, J. J. Kas, M. P. Prange, A. P. Sorini, Y. Takimoto, F. Vila, Ab initio theory and calculations of X-ray spectra, **2009**.
[179] J. J. Rehr, R. C. Albers, *Reviews of Modern Physics* **2000**, *72*, 621–654.
[180] A. Martini, S. A. Guda, A. A. Guda, G. Smolentsev, A. Algasov, O. Usoltsev, M. A. Soldatov, A. Bugaev, Y. Rusalev, C. Lamberti, A. V. Soldatov, *Computer Physics Communications* **2020**, *250*, 107064.
[181] B. Ravel, M. Newville, *Journal of Synchrotron Radiation* **2005**, *12*, 537–541.
[182] D. Ferri, *Heterogeneous Catalysts* **2021**, 311–338.
[183] P. Hollins, **2006**, 1–17.
[184] C.-C. Chang, M.-S. Ku, *J. Phys. Chem. C* **2021**, 125–10919.
[185] W. J. Durand, A. A. Peterson, F. Studt, F. Abild-Pedersen, J. K. Nørskov, *Surface Science* **2011**, *605*, 1354–1359.
[186] J. H. Baricuatro, Y. G. Kim, C. F. Tsang, A. C. Javier, K. D. Cummins, J. C. Hemminger, *Journal of Electroanalytical Chemistry* **2020**, *875*, DOI 10.1016/j.jelechem.2020.114757.
[187] S. J. Raaijman, N. Arulmozhi, M. T. M. Koper, *Cite This: ACS Appl. Mater. Interfaces* **2021**, *13*, 48730–48744.
[188] Y. Hori, K. Kikuchi, S. Suzuki, *Chemistry Letters* **1985**, *14*, 1695–1698.
[189] H. Xie, T. Wang, J. Liang, Q. Li, S. Sun, *Nano Today* **2018**, *21*, 41–54.
[190] Y. Zhou, F. Che, M. Liu, C. Zou, Z. Liang, P. De Luna, H. Yuan, J. Li, Z. Wang, H. Xie, H. Li, P. Chen, E. Bladt, R. Quintero-Bermudez, T. K. Sham, S. Bals, J. Hofkens, D. Sinton, G. Chen, E. H. Sargent, *Nature Chemistry* **2018**, *10*, 974–980.
[191] Y. Jännsch, J. J. Leung, M. Hämmerle, E. Magori, K. Wiesner-Fleischer, E. Simon, M. Fleischer, R. Moos, *Electrochemistry Communications* **2020**, *121*, 106861.
[192] J. Lee, Y. Tak, *Electrochimica Acta* **2001**, *46*, 3015–3022.
[193] S Ishimaru, R Shiratsuchi, G Nogami, Pulsed Electroreduction of CO 2 on Cu-Ag Alloy Electrodes, tech. rep. 5, **2000**, pp. 1864–1867.

[194] Q. Lei, H. Zhu, K. Song, N. Wei, L. Liu, D. Zhang, J. Yin, X. Dong, K. Yao, N. Wang, X. Li, B. Davaasuren, J. Wang, Y. Han, *Journal of the American Chemical Society* **2020**, *142*, 4213–4222.
[195] T. Möller, F. Scholten, T. N. Thanh, I. Sinev, J. Timoshenko, X. Wang, Z. Jovanov, M. Gliech, B. Roldan Cuenya, A. S. Varela, P. Strasser, *Angewandte Chemie - International Edition* **2020**, *59*, 17974–17983.
[196] R. M. Arán-Ais, R. Rizo, P. Grosse, G. Algara-Siller, K. Dembélé, M. Plodinec, T. Lunkenbein, S. W. Chee, B. Roldan Cuenya, *Nature Communications* **2020**, *11*, 3489.
[197] P. Grosse, A. Yoon, C. Rettenmaier, S. W. Chee, B. Roldan Cuenya, *Journal of Physical Chemistry C* **2020**, *124*, 26908–26915.
[198] P. Grosse, A. Yoon, C. Rettenmaier, A. Herzog, S. W. Chee, B. Roldan Cuenya, *Nature Communications* **2021**, *12*, 6736.
[199] J. J. Navarro, S. Tosoni, J. P. Bruce, L. Chaves, M. Heyde, G. Pacchioni, B. Roldan Cuenya, *Journal of Physical Chemistry C* **2020**, *124*, 20942–20949.
[200] A. P. Lagrow, M. R. Ward, D. C. Lloyd, P. L. Gai, E. D. Boyes, *Journal of the American Chemical Society* **2017**, *139*, 179–185.
[201] H. Xiao, W. A. Goddard, T. Cheng, Y. Liu, *Proceedings of the National Academy of Sciences of the United States of America* **2017**, *114*, 6685–6688.
[202] F. Dattila, R. Garclá-Muelas, N. López, *ACS Energy Letters* **2020**, *5*, 3176–3184.
[203] T. C. Chou, C. C. Chang, H. L. Yu, W. Y. Yu, C. L. Dong, J. J. Velasco-Vélez, C. H. Chuang, L. C. Chen, J. F. Lee, J. M. Chen, H. L. Wu, *Journal of the American Chemical Society* **2020**, *142*, 2857–2867.
[204] B. Bornmann, J. Kläs, O. Müller, D. Lützenkirchen-Hecht, R. Frahm, *AIP Conference Proceedings* **2019**, *2054*, DOI 10.1063/1.5084609.
[205] A. L. Ankudinov, B Ravel, J. J. Rehr, S. D. Conradson, **1998**, *58*, 7565–7576.
[206] G. Ashiotis, A. Deschildre, Z. Nawaz, J. P. Wright, D. Karkoulis, F. E. Picca, J. Kieffer, *Journal of Applied Crystallography* **2015**, *48*, 510–519.
[207] F. Reikowski, F. Maroun, I. Pacheco, T. Wiegmann, P. Allongue, J. Stettner, O. M. Magnussen, *ACS Catalysis* **2019**, *9*, 3811–3821.
[208] B. S. Clausen, J. K. Nørskov, *Topics in Catalysis* **2000**, *10*, 221–230.
[209] B. S. Clausen, H. Topsøe, L. B. Hansen, P. Stoltze, J. K Nørskov, *Japanese Journal of Applied Physics* **1993**, *32*, 95–97.
[210] J. Timoshenko, Z. Duan, G. Henkelman, R. Crooks, A. Frenkel, *Annual Review of Analytical Chemistry* **2019**, *12*, DOI 10.1146/annurev-anchem-061318.
[211] J. Timoshenko, A. I. Frenkel, *Catalysis Today* **2017**, *280*, 274–282.
[212] J. Timoshenko, A. Halder, B. Yang, S. Seifert, M. J. Pellin, S. Vajda, A. I. Frenkel, *Journal of Physical Chemistry C* **2018**, *122*, 21686–21693.
[213] P. An, L. Wei, H. Li, B. Yang, K. Liu, J. Fu, H. Li, H. Liu, J. Hu, Y. R. Lu, H. Pan, T. S. Chan, N. Zhang, M. Liu, *Journal of Materials Chemistry A* **2020**, *8*, 15936–15941.
[214] M. Liu, Y. Pang, B. Zhang, P. De Luna, O. Voznyy, J. Xu, X. Zheng, C. T. Dinh, F. Fan, C. Cao, F. P. G. De Arquer, T. S. Safaei, A. Mepham, A. Klinkova, E. Kumacheva, T. Filleter, D. Sinton, S. O. Kelley, E. H. Sargent, *Nature 2016 537:7620* **2016**, *537*, 382–386.
[215] F. D. Speck, S. Cherevko, *Electrochemistry Communications* **2020**, *115*, 106739.
[216] P. De Luna, C. Hahn, D. Higgins, S. A. Jaffer, T. F. Jaramillo, E. H. Sargent, What would it take for renewably powered electrosynthesis to displace petrochemical processes?, **2019**.
[217] S. Chu, Y. Cui, N. Liu, The path towards sustainable energy, **2016**.
[218] C. Reller, R. Krause, E. Volkova, B. Schmid, S. Neubauer, A. Rucki, M. Schuster, G. Schmid, *Advanced Energy Materials* **2017**, *7*, 1–8.
[219] H. Hu, Y. Tang, Q. Hu, P. Wan, L. Dai, X. J. Yang, *Applied Surface Science* **2018**, *445*, 281–286.
[220] Y. Feng, Z. Li, H. Liu, C. Dong, J. Wang, S. A. Kulinich, X. Du, *Langmuir* **2018**, *34*, 13544–13549.
[221] D. Karapinar, C. E. Creissen, J. G. Rivera De La Cruz, M. W. Schreiber, M. Fontecave, Electrochemical CO2Reduction to Ethanol with Copper-Based Catalysts, **2021**.
[222] K. Liu, M. Ma, L. Wu, M. Valenti, D. Cardenas-Morcoso, J. P. Hofmann, J. Bisquert, S. Gimenez, W. A. Smith, *ACS Applied Materials and Interfaces* **2019**, *11*, 16546–16555.
[223] H. A. Hansen, C. Shi, A. C. Lausche, A. A. Peterson, J. K. Nørskov, *Physical Chemistry Chemical Physics* **2016**, *18*, 9194–9201.

[224] A. A. Peterson, J. K. Nørskov, *Journal of Physical Chemistry Letters* **2012**, *3*, 251–258.
[225] H. A. Hansen, J. B. Varley, A. A. Peterson, J. K. Nørskov, *Journal of Physical Chemistry Letters* **2013**, *4*, 388–392.
[226] R. B. Sandberg, J. H. Montoya, K. Chan, J. K. Nørskov, *Surface Science* **2016**, *654*, 56–62.
[227] J. W. Vickers, D. Alfonso, D. R. Kauffman, Electrochemical Carbon Dioxide Reduction at Nanostructured Gold, Copper, and Alloy Materials, **2017**.
[228] J. Gao, H. Zhang, X. Guo, J. Luo, S. M. Zakeeruddin, D. Ren, M. Grätzel, Selective C–C Coupling in Carbon Dioxide Electroreduction via Efficient Spillover of Intermediates As Supported by Operando Raman Spectroscopy, **2019**.
[229] H. Zhang, X. Chang, J. G. Chen, W. A. Goddard, B. Xu, M. J. Cheng, Q. Lu, *Nature Communications* **2019**, *10*, 1–9.
[230] Z. Xu, E. Lai, Y. Shao-Horn, K. Hamad-Schifferli, *Chemical Communications* **2012**, *48*, 5626–5628.
[231] S. H Wei, A. A. Mbaye, L. G. Ferreira, A. Zunger, *Physical Review B* **1987**, *36*, 4163–4185.
[232] P. P. Fedorov, S. N. Volkov, *Russian Journal of Inorganic Chemistry* **2016**, *61*, 772–775.
[233] D. Friebel, F. Mbuga, S. Rajasekaran, D. J. Miller, H. Ogasawara, R. Alonso-Mori, D. Sokaras, D. Nordlund, T. C. Weng, A. Nilsson, *Journal of Physical Chemistry C* **2014**, *118*, 7954–7961.
[234] P. Hirunsit, *Journal of Physical Chemistry C* **2013**, *117*, 8262–8268.
[235] Z. Liu, M. N. Hossain, J. Wen, A. Chen, *Nanoscale* **2021**, *13*, 1155–1163.
[236] E. Andrews, Y. Fang, J. Flake, *Journal of Applied Electrochemistry* **2018**, *48*, 435–441.
[237] S. Back, J. H. Kim, Y. T. Kim, Y. Jung, *ACS Applied Materials and Interfaces* **2016**, *8*, 23022–23027.
[238] F. Jia, X. Yu, L. Zhang, *Journal of Power Sources* **2014**, *252*, 85–89.
[239] W. Zhu, K. Zhao, S. Liu, M. Liu, F. Peng, P. An, B. Qin, H. Zhou, H. Li, Z. He, *Journal of Energy Chemistry* **2019**, *37*, 176–182.
[240] S. Shen, X. Peng, L. Song, Y. Qiu, C. Li, L. Zhuo, J. He, J. Ren, X. Liu, J. Luo, *Small* **2019**, *15*, 1902229.
[241] J. Gao, D. Ren, X. Guo, S. M. Zakeeruddin, M. Grätzel, *Faraday Discussions* **2019**, *215*, 282–296.
[242] X. W. Liu, F. Y. Wang, F. Zhen, J. R. Huang, *RSC Advances* **2012**, *2*, 7647–7651.
[243] Y. Zhao, X. Chang, A. S. Malkani, X. Yang, L. Thompson, F. Jiao, B. Xu, *Journal of the American Chemical Society* **2020**, *142*, 9735–9743.
[244] M Kuhn, T. K. Sham, *Physical Review B* **1994**, *49*, 1647–1661.
[245] A. I. Frenkel, V. S. Machavariani, A. Rubshtein, Y. Rosenberg, Y. Rosenberg, A. Voronel, E. A. Stern, *Physical Review B - Condensed Matter and Materials Physics* **2000**, *62*, 9364–9371.
[246] T. K. Sham, Y. M. Yiu, M Kuhn, K. H. Tan, *Physical Review B* **1990**, *41*, 11881–11886.
[247] D. Higgins, A. T. Landers, Y. Ji, S. Nitopi, C. G. Morales-Guio, L. Wang, K. Chan, C. Hahn, T. F. Jaramillo, *ACS Energy Letters* **2018**, *3*, 2947–2955.
[248] A. Singhal, M. R. Pai, R. Rao, K. T. Pillai, I. Lieberwirth, A. K. Tyagi, *European Journal of Inorganic Chemistry* **2013**, *2013*, 2640–2651.
[249] S. Jiang, K. Klingan, C. Pasquini, H. Dau, *Journal of Chemical Physics* **2019**, *150*, DOI 10.1063/1.5054109.
[250] S. Zhao, G. Chen, G. Zhou, L. C. Yin, J. P. Veder, B. Johannessen, M. Saunders, S. Z. Yang, R. De Marco, C. Liu, S. P. Jiang, *Advanced Functional Materials* **2020**, *30*, 1906157.
[251] C. M. Gunathunge, J. Li, X. Li, J. J. Hong, M. M. Waegele, *ACS Catalysis* **2020**, *10*, 6908–6923.
[252] G. L. Beltramo, T. E. Shubina, M. T. Koper, *ChemPhysChem* **2005**, *6*, 2597–2606.
[253] S. Jiao, X. Fu, H. Huang, Descriptors for the Evaluation of Electrocatalytic Reactions: d-Band Theory and Beyond, **2022**.
[254] T. K. Sham, A. Bzowski, M. Kuhn, C. C. Tyson, *Solid State Communications* **1991**, *80*, 29–32.
[255] G. Iijima, T. Inomata, H. Yamaguchi, M. Ito, H. Masuda, *ACS Catalysis* **2019**, *9*, 6305–6319.
[256] H. Shen, Q. Sun, *Journal of Physical Chemistry C* **2019**, *123*, 29776–29782.
[257] K. J. Lee, N. Elgrishi, B. Kandemir, J. L. Dempsey, *Nature Reviews Chemistry* **2017**, *1*, DOI 10.1038/s41570-017-0039.

[258] A. Li, S. A. Nicolae, M. Qiao, K. Preuss, P. A. Szilágyi, A. Moores, M. M. Titirici, *ChemCatChem* **2019**, *11*, 3602–3625.
[259] M. Zhu, J. Chen, L. Huang, R. Ye, J. Xu, Y. F. Han, *Angewandte Chemie - International Edition* **2019**, *58*, 6595–6599.
[260] N. Leonard, W. Ju, I. Sinev, J. Steinberg, F. Luo, A. S. Varela, B. Roldan Cuenya, P. Strasser, *Chemical Science* **2018**, *9*, 5064–5073.
[261] M. Newville, *Journal of Synchrotron Radiation* **2001**, *8*, 322–324.
[262] Y. C. Li, Z. Wang, T. Yuan, D. H. Nam, M. Luo, J. Wicks, B. Chen, J. Li, F. Li, F. P. G. De Arquer, Y. Wang, C. T. Dinh, O. Voznyy, D. Sinton, E. H. Sargent, *Journal of the American Chemical Society* **2019**, *141*, 8584–8591.
[263] Y. Gong, X. Liu, Y. Gong, D. Wu, B. Xu, L. Bi, L. Y. Zhang, X. Zhao, *Journal of Colloid and Interface Science* **2018**, *530*, 189–195.
[264] A. Capon, R. Parsons, *Journal of Electroanalytical Chemistry and Interfacial Electrochemistry* **1973**, *45*, 205–231.
[265] D. Sun, L. Si, G. Fu, C. Liu, D. Sun, Y. Chen, Y. Tang, T. Lu, *Journal of Power Sources* **2015**, *280*, 141–146.
[266] V. Grozovski, V. V. Climent, E. Herrero, J. M. Feliu, *ChemPhysChem* **2009**, *10*, 1922–1926.
[267] H. Miyake, T. Okada, G. Samjeské, M. Osawa, *Physical Chemistry Chemical Physics* **2008**, *10*, 3662–3669.
[268] M. Fayette, J. Nutariya, N. Vasiljevic, N. Dimitrov, *ACS Catalysis* **2013**, *3*, 1709–1718.
[269] M. Arenz, V. Stamenkovic, P. N. Ross, N. M. Markovic, *Surface Science* **2004**, *573*, 57–66.
[270] M. Arenz, V. Stamenkovic, T. J. Schmidt, K. Wandelt, P. N. Ross, N. M. Markovic, *Physical Chemistry Chemical Physics* **2003**, *5*, 4242–4251.
[271] R. Rizo, B. Roldan Cuenya, *ACS Energy Letters* **2019**, *4*, 1484–1495.
[272] X. Yu, P. G. Pickup, *Electrochemistry Communications* **2009**, *11*, 2012–2014.
[273] M Baldauf, D. M. Kolb, *Journal of Physical Chemistry* **1996**, *100*, 11375–11381.
[274] X. Zhang, H. Yin, J. Wang, L. Chang, Y. Gao, W. Liu, Z. Tang, *Nanoscale* **2013**, *5*, 8392–8397.
[275] M. Jin, H. Zhang, Z. Xie, Y. Xia, *Energy and Environmental Science* **2012**, *5*, 6352–6357.
[276] J. Solla-Gullón, V. Montiel, A. Aldaz, J. Clavilier, *Electrochemistry Communications* **2002**, *4*, 716–721.
[277] S. Zhang, Y. Shao, G. Yin, Y. Lin, *Angewandte Chemie - International Edition* **2010**, *49*, 2211–2214.
[278] L. Liu, W. Sun, W. Yang, Q. Li, J. K. Shang, *Scientific Reports* **2016**, *6*, 20878.
[279] Y. Tang, S. Zou, *Surfaces* **2019**, *2*, 372–386.
[280] X. Xiao, H. Jeong, J. Song, J. P. Ahn, J. Kim, T. Yu, *Chemical Communications* **2019**, *55*, 11952–11955.
[281] D. Liu, M. Xie, C. Wang, L. Liao, L. Qiu, J. Ma, H. Huang, R. Long, J. Jiang, Y. Xiong, *Nano Research* **2016**, *9*, 1590–1599.
[282] Fuping Li, W. Li, H. Liu, C. Liu, G. Dong, J. Liu, K. Peng, *Russian Journal of Physical Chemistry A* **2018**, *92*, 1550–1557.
[283] R. Jana, U. Subbarao, S. C. Peter, *Journal of Power Sources* **2016**, *301*, 160–169.
[284] Z. Liu, G. Fu, J. Li, Z. Liu, L. Xu, D. Sun, Y. Tang, *Nano Research* **2018**, *11*, 4686–4696.
[285] DandanTu, B. Wu, B. Wang, C. Deng, Y. Gao, *Applied Catalysis B: Environmental* **2011**, *103*, 163–168.
[286] H. Wang, Z. Liu, Y. Ma, K. Julian, S. Ji, V. Linkov, R. Wang, *Physical Chemistry Chemical Physics* **2013**, *15*, 13999–14005.
[287] H. Lu, Y. Fan, P. Huang, D. Xu, *Journal of Power Sources* **2012**, *215*, 48–52.
[288] Y. Feng, D. Bin, K. Zhang, F. Ren, J. Wang, Y. Du, *RSC Advances* **2016**, *6*, 19314–19321.
[289] W. Z. Hung, W. H. Chung, D. S. Tsai, D. P. Wilkinson, Y. S. Huang, *Electrochimica Acta* **2010**, *55*, 2116–2122.
[290] R. X. Wang, Y. J. Fan, Z. R. Liang, J. M. Zhang, Z. Y. Zhou, S. G. Sun, *RSC Advances* **2016**, *6*, 60400–60406.
[291] Q. Qin, J. Xie, Q. Dong, G. Yu, H. Chen, *New Journal of Chemistry* **2019**, *43*, 19242–19252.
[292] R. Rizo, R. M. Arán-Ais, E. Padgett, D. A. Muller, M. J. Lázaro, J. Solla-Gullón, J. M. Feliu, E. Pastor, H. D. Abruña, *Journal of the American Chemical Society* **2018**, *140*, 3791–3797.
[293] E. Antolini, E. R. Gonzalez, *Catalysis Today* **2011**, *160*, 28–38.

[294] M. Shao, *Electrocatalysis in Fuel Cells A Non-and Low-Platinum Approach*, (Ed.: M. Shao), Springer-Verlag London, **2013**.
[295] H. X. Zhang, S. H. Wang, K. Jiang, T. André, W. B. Cai, *Journal of Power Sources* **2012**, *199*, 165–169.
[296] M. D. Obradović, S. L. Gojković, *Electrochimica Acta* **2013**, *88*, 384–389.
[297] K. Momma, F. Izumi, *Journal of Applied Crystallography* **2011**, *44*, 1272–1276.
[298] D. J. Myers, X. Wang, M. C. Smith, K. L. More, *Journal of The Electrochemical Society* **2018**, *165*, F3178–F3190.
[299] K. Yasuda, A. Taniguchi, T. Akita, T. Ioroi, Z. Siroma, *Physical Chemistry Chemical Physics* **2006**, *8*, 746–752.
[300] L. D. Burke, *Journal of The Electrochemical Society* **1993**, *140*, 1292.
[301] L. S. Kibis, A. I. Titkov, A. I. Stadnichenko, S. V. Koscheev, A. I. Boronin, *Applied Surface Science* **2009**, *255*, 9248–9254.
[302] J. Kappler, N. Bârsan, U. Weimar, A. Dièguez, J. L. Alay, A. Romano-Roclriguez, J. R. Morante, W. Göpel, *Fresenius' Journal of Analytical Chemistry* **1998**, *361*, 110–114.
[303] P Domashevskaya, S. V. Ryabtsev, S Yu Turishchev, V. M. Kashkarov, Y. A. Yurakov, O. A. Chuvenkova, A. V. Shchukarev, É. P. Domashevskaya, XPS AND XANES Studies of SnOx Nanolayers, tech. rep., **2008**, pp. 80–91.
[304] M. A. Stranick, A. Moskwa, *Surface Science Spectra* **1993**, *2*, 50–54.
[305] F. J. Vidal-Iglesias, R. M. Arán-Ais, J. Solla-Gullón, E. Herrero, J. M. Feliu, *ACS Catalysis* **2012**, *2*, 901–910.
[306] R. M. Arán-Ais, F. J. Vidal-Iglesias, J. Solla-Gullón, E. Herrero, J. M. Feliu, *Electroanalysis* **2015**, *27*, 945–956.
[307] M. Hara, U. Linke, T. Wandlowski, *Electrochimica Acta* **2007**, *52*, 5733–5748.
[308] Y. Ishikawa, M. S. Liao, C. R. Cabrera, *Surface Science* **2000**, *463*, 66–80.
[309] M. Arenz, K. J. J. Mayrhofer, V. Stamenkovic, B. B. Blizanac, T. Tomoyuki, P. N. Ross, N. M. Markovic, *J. Am. Chem. Soc* **2005**, *127*, 6819–6829.
[310] N. Uwitonze, D. Zhou, J. Lei, W. Chen, X. Q. Zuo, J. Cai, Y. X. Chen, *Electrochimica Acta* **2018**, *283*, 1213–1222.
[311] S Garbarino, L. D. Burke, *International Journal of Electrochemical Science* **2010**, *5*, 828–851.
[312] A. S. Douk, H. Saravani, M. Farsadrooh, *International Journal of Hydrogen Energy* **2019**, *44*, 18028–18037.
[313] Z. Zhang, Y. Gong, D. Wu, Z. Li, Q. Li, L. Zheng, W. Chen, W. Yuan, L. Y. Zhang, *International Journal of Hydrogen Energy* **2019**, *44*, 2731–2740.
[314] W. F. Lin, T Iwasita, W Vielstich, *Journal of Physical Chemistry B* **1999**, *103*, 3250–3257.
[315] D. K. Lambert, *The Journal of Chemical Physics* **1991**, *94*, 6237–6242.
[316] T. Iwasita, F. C. Nart, *Progress in Surface Science* **1997**, *55*, 271–340.
[317] M. Newville, *Journal of Synchrotron Radiation* **2001**, *8*, 96–100.
[318] Q. Fan, M. Zhang, M. Jia, S. Liu, J. Qiu, Z. Sun, *Materials Today Energy* **2018**, *10*, 280–301.
[319] J. B. Greenblatt, D. J. Miller, J. W. Ager, F. A. Houle, I. D. Sharp, *Joule* **2018**, *2*, 381–420.
[320] *Fuel Cells Bulletin* **2006**, *2006*, 5.